

**POLITECNICO DI MILANO**  
Scuola di Ingegneria Industriale e dell'Informazione  
Corso di Laurea Magistrale in Ingegneria Aeronautica



**CFD ANALYSIS OF AN ENGINE AIR INTAKE  
FOR LIGHTWEIGHT HELICOPTERS**

**Relatore:**  
**Prof. Luigi VIGEVANO**

**Correlatori:**  
**Prof Dr.-Ing. Christian BREITSAMTER - TU München**  
**Dipl.-Ing. Florian KNOTH - TU München**

**Tesi di Laurea di:**

**Ermanno GROTTI**  
**Matr. 800507**

**Anno Accademico 2014-2015**





*Ai miei genitori*



## Sommario

Questa tesi è il risultato finale del lavoro svolto presso la Technische Universität München nell'ambito del progetto Erasums. Il lavoro è parte integrante del progetto "ATHENAI", condotto da Airbus Helicopters in collaborazione con la Technische Universität München. Obiettivo primario di questo progetto è l'analisi delle prestazioni aerodinamiche relative a specifiche prese d'aria del motore progettate per elicotteri e convertiplani. Il fine ultimo è dunque quello di migliorare le geometrie inizialmente concepite attraverso l'ottimizzazione delle forme. Il progetto "ATHENAI" si sviluppa a partire dal programma "Clean Sky", sovvenzionato dall'Unione Europea e da privati con il fine di sviluppare tecnologie innovative in grado di rivoluzionare l'impatto del trasporto aereo sull'ambiente.

Nello specifico, con il presente lavoro vengono analizzati gli effetti sul flusso d'aria prodotti da una presa d'aria installata su un elicottero bi-motore di ridotte dimensioni. La distribuzione di pressione sulla superficie esterna dell'elicottero e nella regione interna della presa d'aria è studiata per mezzo di simulazioni numeriche stazionarie realizzate attraverso la *Computational Fluid Dynamics*. Più nel dettaglio, nella prima parte del lavoro si affronta il problema riguardante le condizioni al contorno da imporre per la corretta definizione delle simulazioni: l'analisi viene effettuata utilizzando una geometria semplificata dell'elicottero, in cui la presa d'aria del motore viene sostituita da una carenatura. L'analisi prevede inoltre il confronto tra due possibili soluzioni in termini di accuratezza, stabilità e costo computazionale delle simulazioni; lo scopo è quello di determinare l'approccio più efficace. Sulla base delle conclusioni tratte dall'analisi, viene effettuata una nuova simulazione numerica realizzata con una geometria più completa dell'elicottero, in cui, rispetto alla configurazione iniziale, viene aggiunta la presa d'aria del motore. Le simulazioni numeriche vengono quindi confrontate con lo scopo di mettere in luce la dipendenza tra il flusso d'aria e l'impiego della presa d'aria del motore. I risultati ottenuti dalla simulazione effettuata con la geometria completa vengono inoltre validati attraverso il confronto con i valori sperimentali ottenuti da misurazioni effettuate in galleria del vento. La tesi si conclude infine con la descrizione di due possibili approcci da adottare per l'esecuzione di una simulazione numerica in cui due griglie vengono aggiunte alla geometria della presa d'aria, come peraltro già previsto da una delle varianti del progetto.

In conclusione, è possibile affermare che gli effetti sul flusso d'aria dovuti all'impiego della presa del motore sono solo locali: il campo di flusso viene infatti influenzato solamente in prossimità della presa d'aria stessa. Il confronto tra i dati sperimentali e quelli ottenuti attraverso la *Computational Fluid Dynamics* mostra inoltre una somiglianza molto stretta dei risultati, in particolare nella parte anteriore della superficie esterna del velivolo, dando così un'ulteriore conferma della corretta definizione delle simulazioni numeriche.

## Abstract

This dissertation represents the final result of the work performed at the Technische Universität München within the Erasmus program. The work has to be contextualised within the "ATHENAI" project, part of the EU/Industry "Clean Sky" program, whose primary target is to develop innovative technologies able to revolutionise the environmental footprint of air transport. The "ATHENAI" project is conducted as a collaboration between the Technische Universität München and Airbus Helicopters with the main purpose of taking into analysis several engine air intake shapes to be used for helicopters and tiltrotor aircraft. In addition to that, it aims at the optimisation of baseline geometries in order to improve aerodynamic performances.

The purpose of this thesis is to analyse the effects of an engine air intake, designed by Airbus Helicopters within the aforementioned project, on the air flow striking a lightweight twin-engine helicopter. The investigation is performed by means of stationary CFD simulations and deals with the flow structure and the pressure distribution both on the helicopter outer surface and in the engine air intake inner parts. The first part of the study is engaged with the problem concerning the correct specification of boundary conditions. In order to identify the most effective one, two distinct approaches are compared in terms of accuracy, stability and computational cost of the simulations, which are performed with a simplified geometry, featuring a closed surface in place of the engine air intake. Subsequently, the analysis' conclusions are employed to perform a new CFD simulation, using a more detailed geometry, equipped with the air intake. The effects of the engine air intake shapes on the flow field are then studied contrasting the CFD simulations; moreover, the results coming from the CFD simulation performed with the complete geometry are validated through a comparison with some experimental data taken from a wind tunnel campaign. Finally, the thesis provides the reader with some suggestions about the possible approaches to follow for CFD simulations of a flow striking a screen.

In conclusion, it is highlighted that the effect of the engine air intake installation on the flow field is local only: as a matter of fact, pressure distribution is affected in the vicinity of the air intake only. The numerical simulations are validated by the comparison between the CFD simulation and the experimental data: it in fact shows an excellent similarity of results, especially in the fore part of the helicopter surface.

# Contents

<b>List of Figures</b>	<b>VII</b>
<b>List of Tables</b>	<b>XIII</b>
<b>1 Introduction</b>	<b>1</b>
1.1 "Clean Sky" program . . . . .	1
1.2 "ATHENAI" project . . . . .	2
1.2.1 First experimental campaign . . . . .	3
1.3 Overview of the work . . . . .	6
1.3.1 Objectives of the work . . . . .	6
1.3.2 Phases of the work . . . . .	6
1.3.3 Organisation of chapters . . . . .	7
<b>2 Theoretical basics</b>	<b>9</b>
2.1 Navier-Stokes equations . . . . .	9
2.2 Turbulence models . . . . .	10
2.2.1 Statistical turbulence models . . . . .	11
2.2.2 Shear Stress Transport (SST) model . . . . .	12
2.2.3 $y^+$ parameter . . . . .	12
2.3 Structured and unstructured meshes . . . . .	13
2.3.1 Structured mesh . . . . .	13
2.3.2 Unstructured mesh . . . . .	14
2.3.3 Differences . . . . .	15
2.3.4 Hybrid mesh . . . . .	16
<b>3 Analysis of boundary conditions</b>	<b>17</b>
3.1 Description of the problem . . . . .	17
3.1.1 Geometry . . . . .	17
3.1.2 Mesh . . . . .	21
3.1.3 Settings . . . . .	21
3.1.4 Boundary conditions . . . . .	22
3.2 Choice of boundary condition on the outlet surface . . . . .	22
3.2.1 "Mass flow" boundary condition . . . . .	23
3.2.2 "Pressure" boundary condition . . . . .	26
3.3 Kriging model . . . . .	27
3.3.1 Kriging's theory . . . . .	27
3.3.2 Co-Kriging model . . . . .	29
3.4 Implementation of co-Kriging model . . . . .	30
3.4.1 "961.228 Pa" case . . . . .	31
3.4.2 Other cases . . . . .	33
3.4.3 Two expensive values . . . . .	34
3.4.4 Three expensive values . . . . .	36

3.5	Final considerations . . . . .	37
3.5.1	"974.405 Pa" case . . . . .	38
3.6	Comparison between boundary conditions . . . . .	39
3.6.1	Accuracy . . . . .	40
3.6.2	Stability . . . . .	57
3.6.3	Cost . . . . .	57
3.6.4	Conclusion . . . . .	58
<b>4</b>	<b>Simulation of the engine air intake</b>	<b>59</b>
4.1	Description of the problem . . . . .	59
4.1.1	Geometry . . . . .	59
4.1.2	Mesh . . . . .	64
4.1.3	Settings . . . . .	64
4.1.4	Boundary conditions . . . . .	64
4.2	Simulation . . . . .	66
<b>5</b>	<b>Analysis of results</b>	<b>71</b>
5.1	Data processing . . . . .	71
5.1.1	First analysis . . . . .	72
5.1.2	Second analysis . . . . .	72
5.2	Effect of engine air intake on the external flow . . . . .	73
5.3	Comparison between CFD and experimental data . . . . .	82
5.3.1	Flow structure . . . . .	82
5.4	Flow field in the engine air intake . . . . .	100
<b>6</b>	<b>Analysis of screens</b>	<b>103</b>
6.1	Screens of the engine air intake . . . . .	103
6.2	Reproduction of screens in CFD simulations . . . . .	104
6.3	Air flow through a screen . . . . .	105
6.4	Loss coefficient . . . . .	107
6.4.1	Reynolds number sensitivity . . . . .	108
6.4.2	Porosity sensitivity . . . . .	110
6.4.3	Normal loss coefficient . . . . .	111
6.4.4	Choice of the model . . . . .	114
6.4.5	Tangential loss coefficient . . . . .	115
<b>7</b>	<b>Conclusions</b>	<b>117</b>
7.1	Future research . . . . .	118
<b>A</b>	<b>Results of the co-Kriging model</b>	<b>121</b>
A.1	Monitor points . . . . .	121
A.1.1	Expensive values . . . . .	121
A.1.2	Cheap values . . . . .	122
A.2	Curves estimated with the co-Kriging model . . . . .	124
<b>B</b>	<b>Comparison between simulations</b>	<b>129</b>
B.1	Pressure and velocity distribution . . . . .	131
B.2	Pressure and forces acting on the helicopter surface . . . . .	149
<b>C</b>	<b>Loss coefficient model</b>	<b>155</b>
C.1	Definition of $K_0$ . . . . .	155
C.2	Definition of $K_{Re}$ . . . . .	155
C.3	Implementation of loss coefficient model . . . . .	157

<b>D Settings of CFD simulations</b>	<b>161</b>
D.1 Turbulence model . . . . .	161
D.2 Material . . . . .	161
<b>Bibliography</b>	<b>163</b>





# List of Figures

1.1	Test facility . . . . .	4
1.2	Wind tunnel model . . . . .	4
1.3	Engine air intake geometries . . . . .	5
2.1	Structured mesh . . . . .	14
2.2	Unstructured mesh . . . . .	15
2.3	Hybrid mesh . . . . .	16
3.1	Initially defined wind tunnel geometry . . . . .	18
3.2	Helicopter geometry used in the boundary conditions analysis . . . . .	19
3.3	Position of the helicopter within the wind tunnel . . . . .	19
3.4	Position of the helicopter within the wind tunnel - X-view . . . . .	20
3.5	Position of the helicopter within the wind tunnel - Y-view . . . . .	20
3.6	Position of the helicopter within the wind tunnel - Z-view . . . . .	20
3.7	Helicopter geometry mesh . . . . .	21
3.8	Wind tunnel geometry used in the CFD simulations . . . . .	23
3.9	Mass and momentum residuals - "Mass flow" case . . . . .	24
3.10	Turbulence residuals - "Mass flow" case . . . . .	24
3.11	Velocity u-component - New geometry outlet section . . . . .	25
3.12	Velocity u-component - Initial geometry outlet section . . . . .	25
3.13	Newton's method - Intervals of variation . . . . .	27
3.14	Pressure distribution on the wind tunnel outlet section - "Mass flow" simulation . . . . .	31
3.15	Mass and momentum residuals - "961.228 Pa" case . . . . .	32
3.16	Turbulence residuals - "961.228 Pa" case . . . . .	32
3.17	Monitor points - "961.228 Pa" case . . . . .	33
3.18	Co-Kriging model implementation - 2 expensive values . . . . .	36
3.19	Co-Kriging model implementation - 3 expensive values . . . . .	37
3.20	Mass and momentum residuals - "974.405 Pa" case . . . . .	38
3.21	Turbulence residuals - "974.405 Pa" case . . . . .	39
3.22	Monitor points - "974.405 Pa" case . . . . .	39
3.23	Pressure distribution - General investigation . . . . .	40
3.24	Velocity u-component distribution - General investigation . . . . .	41
3.25	Pressure distribution - Test section investigation . . . . .	41
3.26	Velocity u-component distribution - Test section investigation . . . . .	42
3.27	$C_p$ distribution - General investigation . . . . .	42
3.28	$\Delta C_p$ - General investigation . . . . .	43
3.29	$C_p$ distribution - Test section investigation . . . . .	43
3.30	$\Delta C_p$ - Test section investigation . . . . .	44
3.31	Percentage variation of forces - X-axis . . . . .	47
3.32	Percentage variation of forces - Y-axis . . . . .	47
3.33	Percentage variation of forces - Z-axis . . . . .	48

3.34	Percentage variation of moments - X-axis . . . . .	48
3.35	Percentage variation of moments - Y-axis . . . . .	49
3.36	Percentage variation of moments - Z-axis . . . . .	49
3.37	Velocity vectors at x = 1.50 m - "Mass flow" case . . . . .	50
3.38	Velocity vectors at x = 1.50 m - "961.228 Pa" case . . . . .	51
3.39	Velocity vectors at x = 1.50 m - "974.405 Pa" case . . . . .	51
3.40	Velocity vectors at x = 2.50 m - "Mass flow" case . . . . .	52
3.41	Velocity vectors at x = 2.50 m - "961.228 Pa" case . . . . .	52
3.42	Velocity vectors at x = 2.50 m - "974.405 Pa" case . . . . .	53
3.43	Velocity vectors at x = 3.50 m - "Mass flow" case . . . . .	53
3.44	Velocity vectors at x = 3.50 m - "961.228 Pa" case . . . . .	54
3.45	Velocity vectors at x = 3.50 m - "974.405 Pa" case . . . . .	54
3.46	Velocity v-component distribution on YZ planes . . . . .	55
3.47	Velocity v-component distribution on XY planes . . . . .	56
3.48	Velocity w-component distribution on YZ planes . . . . .	56
3.49	Velocity w-component distribution on XY planes . . . . .	57
4.1	Engine air intake overview . . . . .	60
4.2	Engine Air Intake (EAI) . . . . .	61
4.3	Engine Plenum Chamber (EPC) . . . . .	61
4.4	Engine Intake Duct (EID) . . . . .	62
4.5	Guide vanes . . . . .	62
4.6	Aerodynamic Interface Plane (AIP) . . . . .	63
4.7	Helicopter section overview . . . . .	63
4.8	Outlet section of the measurement tube . . . . .	65
4.9	Mass and momentum residuals - "Open air intake" case . . . . .	66
4.10	Turbulence residuals - "Open air intake" case . . . . .	66
4.11	Energy residuals - "Open air intake" case . . . . .	67
4.12	$C_P$ distribution on the helicopter surface . . . . .	68
4.13	$C_P$ distribution on the EID front surface . . . . .	68
4.14	$C_P$ distribution on the EID back surface . . . . .	69
5.1	Definition of lines on the helicopter surface - Comparison between CFD simulations	73
5.2	Definition of Line 1 - Comparison between CFD simulations . . . . .	74
5.3	$C_P$ distribution on Line 1 - Comparison between CFD simulations . . . . .	74
5.4	Definition of Lines 2-3 - Comparison between CFD simulations . . . . .	75
5.5	$C_P$ distribution on Line 2 - Comparison between CFD simulations . . . . .	75
5.6	$C_P$ distribution on Line 3 - Comparison between CFD simulations . . . . .	76
5.7	Definition of Lines 4-5 - Comparison between CFD simulations . . . . .	76
5.8	$C_P$ distribution on Line 4 - Comparison between CFD simulations . . . . .	77
5.9	$C_P$ distribution on Line 5 - Comparison between CFD simulations . . . . .	77
5.10	Definition of Lines 6-7 - Comparison between CFD simulations . . . . .	78
5.11	$C_P$ distribution on Line 6 - Comparison between CFD simulations . . . . .	78
5.12	Line 6 - $n = 0.95$ . . . . .	79
5.13	$C_P$ distribution on Line 7 - Comparison between CFD simulations . . . . .	79
5.14	Line 7 - $n = 0.10$ . . . . .	80
5.15	Definition of Lines 8-9 - Comparison between CFD simulations . . . . .	80
5.16	$C_P$ distribution on Line 8 - Comparison between CFD simulations . . . . .	81
5.17	$C_P$ distribution on Line 9 - Comparison between CFD simulations . . . . .	81
5.18	Definition of lines on the helicopter surface - Comparison with experimental data	83
5.19	Definition of lines on EID and EPC - Comparison with experimental data . . . . .	84
5.20	Fore and rear line on the EID - Comparison with experimental data . . . . .	84

5.21	Definition of Line 1 - Comparison with experimental data . . . . .	85
5.22	$C_P$ distribution on Line 1 - Comparison with experimental data . . . . .	85
5.23	Definition of Lines 2-3 - Comparison with experimental data . . . . .	86
5.24	$C_P$ distribution on Line 2 - Comparison with experimental data . . . . .	86
5.25	$C_P$ distribution on Line 3 - Comparison with experimental data . . . . .	87
5.26	Definition of Lines 4-5 - Comparison with experimental data . . . . .	87
5.27	$C_P$ distribution on Line 4 - Comparison with experimental data . . . . .	88
5.28	$C_P$ distribution on Line 5 - Comparison with experimental data . . . . .	88
5.29	Definition of Lines 6-7 - Comparison with experimental data . . . . .	89
5.30	$C_P$ distribution on Line 6 - Comparison with experimental data . . . . .	89
5.31	Line 6 - $s = 0.90$ . . . . .	90
5.32	$C_P$ distribution on Line 7 - Comparison with experimental data . . . . .	90
5.33	Line 7 - $s = 0.10$ . . . . .	91
5.34	Definition of Line 8 - Comparison with experimental data . . . . .	91
5.35	$C_P$ distribution on Line 8 - Comparison with experimental data . . . . .	92
5.36	Definition of Line 9 - Comparison with experimental data . . . . .	92
5.37	$C_P$ distribution on Line 9 - Comparison with experimental data . . . . .	93
5.38	Line 9 - $s = 0.15$ . . . . .	93
5.39	Line 9 - $s = 0.55$ . . . . .	94
5.40	Line 9 - $s = 0.65$ . . . . .	94
5.41	Line 9 - $s = 0.85$ . . . . .	95
5.42	Definition of EID lines - Comparison with experimental data . . . . .	95
5.43	$C_P$ distribution on Line 10 - Comparison with experimental data . . . . .	96
5.44	$C_P$ distribution on Line 11 - Comparison with experimental data . . . . .	96
5.45	Line 11 - $s = 0.85$ . . . . .	97
5.46	$C_P$ distribution on Line 12 - Comparison with experimental data . . . . .	97
5.47	$C_P$ distribution on Line 13 - Comparison with experimental data . . . . .	98
5.48	$C_P$ distribution on Line 14 - Comparison with experimental data . . . . .	98
5.49	$C_P$ distribution on Line 15 - Comparison with experimental data . . . . .	99
5.50	$C_P$ distribution on Line 16 - Comparison with experimental data . . . . .	99
5.51	$C_P$ distribution on Line 17 - Comparison with experimental data . . . . .	100
5.52	Velocity vectors in the EPC . . . . .	101
5.53	Velocity distribution in the EID . . . . .	102
5.54	Velocity distribution on the AIP . . . . .	102
6.1	Sensitivity analysis - Reynolds number dependency for $\beta = 0.300$ . . . . .	108
6.2	Sensitivity analysis - Reynolds number dependency for $\beta = 0.720$ . . . . .	109
6.3	Sensitivity analysis - Reynolds number dependency for $\beta = 0.758$ . . . . .	109
6.4	Sensitivity analysis - Reynolds number dependency for $\beta = 0.900$ . . . . .	109
6.5	Sensitivity analysis - Porosity dependency for $Re_w = 200$ . . . . .	110
6.6	Sensitivity analysis - Porosity dependency for $Re_w = 500$ . . . . .	110
6.7	Sensitivity analysis - Porosity dependency for $Re_w = 1500$ . . . . .	111
6.8	Sensitivity analysis - Porosity dependency for $Re_w = 2000$ . . . . .	111
6.9	Normal loss coefficient - Screen A . . . . .	112
6.10	Normal loss coefficient - Screen B . . . . .	112
6.11	Normal loss coefficient - Screen C . . . . .	113
6.12	Normal loss coefficient - Screen D . . . . .	113
6.13	Tangential loss coefficient - Screen B . . . . .	115
6.14	Tangential loss coefficient - Screen D . . . . .	116
A.1	Monitor points - "900 Pa" case supplying an expensive value . . . . .	121
A.2	Monitor points - "1050 Pa" case supplying an expensive value . . . . .	122

A.3	Monitor points - "900 Pa" case supplying a cheap value . . . . .	122
A.4	Monitor points - "1000 Pa" case supplying a cheap value . . . . .	122
A.5	Monitor points - "1050 Pa" case supplying a cheap value . . . . .	123
A.6	Monitor points - "1100 Pa" case supplying a cheap value . . . . .	123
A.7	Monitor points - "1200 Pa" case supplying a cheap value . . . . .	123
A.8	Co-Kriging model implementation with 5 intervals - 2 expensive values . . . . .	124
A.9	Co-Kriging model implementation with 10 intervals - 2 expensive values . . . . .	124
A.10	Co-Kriging model implementation with 30 intervals - 2 expensive values . . . . .	125
A.11	Co-Kriging model implementation with all values - 2 expensive values . . . . .	125
A.12	Mean Square Error - 2 expensive values . . . . .	125
A.13	Co-Kriging model implementation with 5 intervals - 3 expensive values . . . . .	126
A.14	Co-Kriging model implementation with 10 intervals - 3 expensive values . . . . .	126
A.15	Co-Kriging model implementation with 30 intervals - 3 expensive values . . . . .	126
A.16	Co-Kriging model implementation with all values - 3 expensive values . . . . .	127
A.17	Mean Square Error - 3 expensive values . . . . .	127
B.1	Planes in x-direction - Test section . . . . .	129
B.2	Planes in x-direction - Wind tunnel . . . . .	130
B.3	Planes in z-direction - Test section . . . . .	130
B.4	Relative static pressure distribution in the test section - "Mass flow" case . . . . .	133
B.5	Relative static pressure distribution in the test section - "961.228 Pa" case . . . . .	134
B.6	Relative static pressure distribution in the test section - "974.405 Pa" case . . . . .	134
B.7	Velocity u-component distribution in the test section - "Mass flow" case . . . . .	135
B.8	Velocity u-component distribution in the test section - "961.228 Pa" case . . . . .	135
B.9	Velocity u-component distribution in the test section - "974.405 Pa" case . . . . .	136
B.10	Relative static pressure distribution in the wind tunnel - "Mass flow" case . . . . .	136
B.11	Relative static pressure distribution in the wind tunnel - "961.228 Pa" case . . . . .	137
B.12	Relative static pressure distribution in the wind tunnel - "974.405 Pa" case . . . . .	137
B.13	Velocity u-component distribution in the wind tunnel - "Mass flow" case . . . . .	138
B.14	Velocity u-component distribution in the wind tunnel - "961.228 Pa" case . . . . .	138
B.15	Velocity u-component distribution in the wind tunnel - "974.405 Pa" case . . . . .	139
B.16	Relative static pressure distribution at x = 2.50 m - "Mass flow" case . . . . .	140
B.17	Relative static pressure distribution at x = 2.50 m - "961.228 Pa" case . . . . .	141
B.18	Relative static pressure distribution at x = 2.50 m - "974.405 Pa" case . . . . .	141
B.19	Velocity u-component distribution at x = 2.50 m - "Mass flow" case . . . . .	142
B.20	Velocity u-component distribution at x = 2.50 m - "961.228 Pa" case . . . . .	142
B.21	Velocity u-component distribution at x = 2.50 m - "974.405 Pa" case . . . . .	143
B.22	Relative static pressure distribution at x = 7.50 m - "Mass flow" case . . . . .	143
B.23	Relative static pressure distribution at x = 7.50 m - "961.228 Pa" case . . . . .	144
B.24	Relative static pressure distribution at x = 7.50 m - "974.405 Pa" case . . . . .	144
B.25	Velocity u-component distribution at x = 7.50 m - "Mass flow" case . . . . .	145
B.26	Velocity u-component distribution at x = 7.50 m - "961.228 Pa" case . . . . .	145
B.27	Velocity u-component distribution at x = 7.50 m - "974.405 Pa" case . . . . .	146
B.28	Relative static pressure distribution at x = 20.00 m - "Mass flow" case . . . . .	146
B.29	Relative static pressure distribution at x = 20.00 m - "961.228 Pa" case . . . . .	147
B.30	Relative static pressure distribution at x = 20.00 m - "974.405 Pa" case . . . . .	147
B.31	Velocity u-component distribution at x = 20.00 m - "Mass flow" case . . . . .	148
B.32	Velocity u-component distribution at x = 20.00 m - "961.228 Pa" case . . . . .	148
B.33	Velocity u-component distribution at x = 20.00 m - "974.405 Pa" case . . . . .	149
B.34	Force coefficient - X-axis . . . . .	150
B.35	Force coefficient - Y-axis . . . . .	150
B.36	Force coefficient - Z-axis . . . . .	151

B.37	Moment coefficient - X-axis . . . . .	151
B.38	Moment coefficient - Y-axis . . . . .	152
B.39	Moment coefficient - Z-axis . . . . .	152
B.40	Pressure field on the helicopter surface - "Mass flow" case . . . . .	153
B.41	Pressure field on the helicopter surface - "961.228 Pa" case . . . . .	153
B.42	Pressure field on the helicopter surface - "974.405 Pa" case . . . . .	154
C.1	Comparison between different screen typologies - Loss coefficient . . . . .	155
C.2	$K_{Re}$ - Circular-wire screens . . . . .	156
C.3	$K_{Re}$ - Silk-thread screens . . . . .	156
C.4	$K_{\theta}$ model - Engine air intake screen . . . . .	158
C.5	$K_{\theta}$ model - Engine screen . . . . .	158
C.6	$F_{\theta}$ model - Engine air intake screen . . . . .	159
C.7	$F_{\theta}$ model - Engine screen . . . . .	159



# List of Tables

3.1	Settings - "Analysis of boundary conditions" . . . . .	21
3.2	Interval - Second expensive value . . . . .	34
3.3	Intervals - Cheap values . . . . .	34
3.4	Mean values - Second expensive value . . . . .	34
3.5	Mean values - Cheap values . . . . .	35
3.6	Zero of the curves - Two expensive values . . . . .	35
3.7	Interval - Third expensive value . . . . .	36
3.8	Mean values - Third expensive value . . . . .	36
3.9	Zero of the curves - Three expensive values . . . . .	37
3.10	$C_{Fx}$ - X-force coefficient . . . . .	45
3.11	$C_{Fy}$ - Y-force coefficient . . . . .	45
3.12	$C_{Fz}$ - Z-force coefficient . . . . .	45
3.13	$C_{Mx}$ - X-moment coefficient . . . . .	46
3.14	$C_{My}$ - Y-moment coefficient . . . . .	46
3.15	$C_{Mz}$ - Z-moment coefficient . . . . .	46
3.16	Computational cost . . . . .	58
4.1	Settings - "Simulation of the engine air intake" . . . . .	64
4.2	Boundary conditions - Pressure and temperature . . . . .	65
5.1	EID lines - Position with reference to the AIP coordinate system . . . . .	72
6.1	Geometrical characteristics - Engine air intake screen . . . . .	103
6.2	Geometrical characteristics - Engine screen . . . . .	104
6.3	Geometrical characteristics of screens - Experimental data . . . . .	112
B.1	Relative static pressure - Comparison . . . . .	131
B.2	U-component of velocity - Comparison . . . . .	132
C.1	Loss coefficient model relative to the engine air intake screens . . . . .	157





# Chapter 1

## Introduction

*CFD Analysis of an Engine Air Intake for Lightweight Helicopters* represents the final report written on the basis of the work carried out at the Technische Universität München, from October 2014 till May 2015, within the *Erasmus* project. The whole study must be contextualised within the "ATHENAI" project, part of the EU/Industry "Clean Sky" program; therefore, it is integrated within the ongoing work performed by the Institute of Aerodynamics and Fluid Mechanics of the Technische Universität München in collaboration with Airbus Helicopters.

### 1.1 "Clean Sky" program

"Clean Sky" is the most challenging European research program ever developed in the aeronautical field, whose goal is to engineer breakthrough technologies to revolutionise the environmental performances of aircraft and, in general, air transport; the purpose is to reach less noisy and more fuel efficient aircraft, hence making a significant contribution in the achievement of the Single European Sky (SES) environmental objectives, that regulate the reduction of the aviation environmental footprint.

The Clean Sky JTI (Joint Technology Initiative) was born in 2008 and represents a unique example of Public-Private Partnership. Clean Sky JTI was born as an agreement between the European Commission and the industry world, with an initial budget of € 1.6 billion, contributed by the Commission and by the aeronautical industry for the same quantity. With regard to the industry, ITD (Integrated Technologies Demonstrators) Leaders commit up to 50%, Associates members up to 25% and Partners a minimum of 25%; what is remarkable about "Clean Sky" program is the participation as ITD Leaders of the most important European societies dealing in the aeronautical field as Airbus, Airbus Group, Airbus Helicopters, Fraunhofer, AleniaAermacchi, AgustaWestland, Safran, Thales, Saab, Dassault Aviation, Liebherr and Rolls-Royce.

In the 2001 report "European Aeronautics: A vision for 2020", a group of personalities pioneered an integrated vision of the European air transport system for the following 20 years. As its main target it established the importance to adapt to society's needs and to fasten the European leadership in the aeronautics field.

*Society's needs embrace the whole range of benefits that all citizens of Europe expect of the air transport industry now and in the future. These benefits are direct, as*

*in the quality and price of travel, and indirect, as in the preservation of security and safety in a globalised world. They encompass the personal needs of travellers and the collective needs of non-travellers who want to live in quiet streets, safe from pollution.*<sup>1</sup>

Moreover, the report suggested the foundation of the Advisory Council for Aeronautics Research in Europe (ACARE), the first European technology platform, that defined a set of strategic research objectives. The "Clean Sky" program is contributing to the reaching of two of the six ACARE's High Level Target Concepts (HLTCS), that are the realisation of:

- an ultra green air transport system, leading to an environmentally friendly air transport;
- a highly cost efficient air transport system, fastening European leadership in aeronautics;

**Objectives of the program** The main objective of the "Clean Sky" program is to speed up the development of breakthrough technologies and to shorten the time necessary for the commercialisation of new configurations tested on full-scale demonstrators. The program is testing and validating technologies that are required by the environmental targets set by ACARE, which have to be reached within 2020:

- 50% reduction of  $CO_2$  emission by means of drastic reduction of fuel consumption;
- 80% reduction of  $NO_x$  (nitrogen oxide) emission;
- 50% reduction of external noise;
- a green product life cycle: design, manufacturing, maintenance and disposal/recycling;

## 1.2 "ATHENAI" project

The "ATHENAI" (Aerodynamic Testing of Helicopter Novel Air Intakes) project belongs to the sub-project Green Rotorcraft Consortium (GRC), which is part of the Clean Sky JTI.

**Green Rotorcraft Consortium sub-project 2** The sub-project GRC2 of the Green Rotorcraft ITD (Integrated Technology Demonstrator) is led with the purpose of improving the aerodynamic performances of fuselages and engines installation on helicopter and tiltrotor aircraft. Within this research field, the investigation and optimisation of engines installation plays a key role in supporting the engine functioning in an efficient fuel consumption condition. The GRC2's study is extended to all the weight classes, from light to heavy, in order to cover the widest range of future helicopters. Numerical optimisations of several configurations are performed through CFD simulations and expected improvements of identified solutions are tested by means of experimental campaigns.

---

<sup>1</sup>Advisory Council for Aeronautics Research in Europe, Strategic Research Agenda, October 2004, p.4

**Objectives of the project** The "ATHENAI" project's main objective is to investigate several engine air intake concepts optimised within GRC2 and to enhance the baseline geometries by means of retrofittable components implementation or shape optimisation. Massive wind tunnel tests are carried out on a full-scale model of a lightweight twin-engine helicopter fuselage section at the Institute of Aerodynamics and Fluid Mechanics of the Technische Universität München (TUM): some of them have been already performed, some other are still ongoing. For this aim, the new wind tunnel model of the helicopter - including a fuselage cowling part, all the air intake components and the flow passages - has been designed, produced and instrumented.

The model is constructed in such a way that high degrees of flexibility as concerns easy comparison of different air intake components are possible. Aerodynamic performances of three baseline engine air intake configurations are analysed in detail in two distinct wind tunnel campaigns with the purpose of modifying the initial design, concentrating on flow guiding elements like fillets, vanes, spoilers and scoops. Flow field measurements are performed on the aerodynamic interface plane (AIP) with a five-hole pressure probing system; in addition, steady and unsteady pressure on cowling and air intake regions is recorded. Finally, turbulence level of the incoming flow is analysed by means of mean and fluctuating velocities measurements.

**Possible benefits** The aerodynamic optimisation of the engine intake and engine air duct elements is conducted with the purpose of enhancing the compressor inflow conditions which foster better engine working conditions. The evaluation of the inflow conditions is performed on the AIP, that is taken as the reference plane, on which, directly upstream of the compressor inlet, several parameters are analysed; an example is the distortion parameter DC60.

The enhancement of compressor inflow conditions is of extreme importance, since a reduction of total pressure losses would result in an increase of static pressure in the compressor inlet and in a consequent increase of thermal efficiency. A decrease in swirl and flow distortions would lead to a more uniform flow field at the compressor inlet and therefore would improve the output engines power. As a final result, a minor total amount of fuel would be necessary at constant power requirements for a given flight operating point, leading to fewer emissions. Furthermore, flow uniformity would foster stable engine conditions especially in proximity of the surge line.

### 1.2.1 First experimental campaign

A suction system has been employed during the first wind tunnel campaign in order to provide engine mass flow rates in the compressor inlet section; the mass flow rates have been set to reproduce the engine operation points in real helicopter flight conditions.

Four 5-hole pressure probing systems have been used to measure total pressure and three components of velocity in the AIP in four distinct positions instantaneously; each measurement system consists of four 5-hole probes and a traversing system, that has been used for azimuthal positioning of the probes. Therefore, a measurement grid has been obtained for the analysis of compressor inflow parameters such as DC60, average swirl angle and pressure drop in order to evaluate the intake geometries investigated during the wind tunnel campaign.

**General considerations** In order to fulfil local Mach number and Reynolds number similarities, a full-scale model (Figure 1.1) has been installed within the wind tunnel of the Institute of Aerodynamics and Fluid Mechanics of the TUM. The outer surface of the wind tunnel model is simplified, since both the complete empennage with the Fenestron® rotor system and the landing gear have not been provided in the model geometry; as a matter of fact, their influence on the intake flow field area is thought to be considerably small. The main rotor has not been included in the model due to lack of space and to its complexity. On the contrary, the air intake and the engine grids, that preserve the engine from foreign object damage and that influence the local flow field of the inlet region, as well as other geometric details, have been maintained on the wind tunnel model.

The size of the model is decreased by the wind tunnel test section as well as nozzle and collector dimensions. The free stream contraction is to be avoided in the transition between the nozzle exit and the collector entry; therefore, an overall size of 4.50 m in the main stream direction shall not be overtaken. Moreover, the height of the model has been limited due to blockage effects; only a section of the cabin and cowling is tested in order to meet the spatial restrictions. The ratio of sections at the nozzle exit to the entire model analysed is defined at a reasonable level of 7-8%. In Figure 1.2 an overview of the outer parts of the wind tunnel model is given.

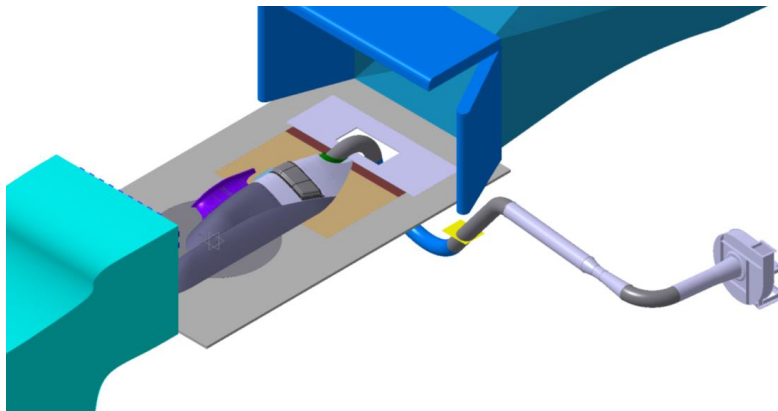


Figure 1.1: Test facility <sup>2</sup>

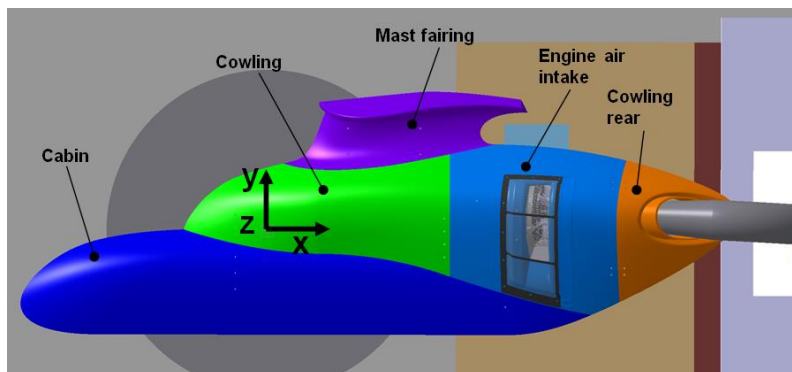


Figure 1.2: Wind tunnel model <sup>3</sup>

<sup>2</sup>Taken from [26]

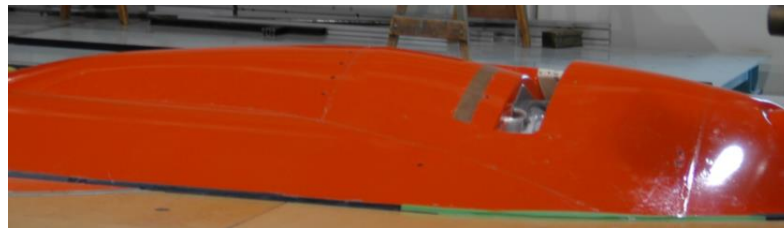
<sup>3</sup>Taken from [26]

**Experimental measurements** The geometric shapes tested in the first wind tunnel campaign have been designed and provided by the GRC Consortium. During the experimental measurements three different air intake geometries (Figure 1.3) have been tested according to a measurement matrix specified together with Airbus Helicopters Germany:

- the first air intake is designed as a static inlet. Limitations on the inlet area cross section are given by the engine plenum chamber dimensions;
- the second air intake is designed as a "semi-dynamic" inlet, featuring a ramp for recovery of dynamic pressure, in contrast to the first geometry. The optimisation of this variant is done for level flight conditions;
- the third air intake provides the same main geometry of the second variant, but it additionally features a scoop, whose function is to define a plane normal to the main flow direction that the incoming air has to pass to enter the engine air intake. In this way, it leads the free stream flow into the intake, regaining more dynamic pressure into static;



(a) First variant



(b) Second variant



(c) Third variant

Figure 1.3: Engine air intake geometries <sup>4</sup>

Two different engine plenum chambers have also been tested; the plenum chamber number two features an overall rounded shape compared to the first plenum chamber. The first air intake geometry has been tested with the first plenum chamber, whereas both the second and the third

<sup>4</sup>Taken from [26]

geometry have been investigated with the second plenum chamber. The first two combinations of air intakes and plenum chamber variations have been investigated with and without an outer and an inner foreign object damage screen.

The "Clean Sky" program description has been taken from [14], whereas [26] has been used as reference for the "ATHENAI" project; see [1, 2, 14, 16] for further information about the "Clean Sky" program.

## **1.3 Overview of the work**

### **1.3.1 Objectives of the work**

The main objective of the work is the study of interferences between the air flow and the first variant of engine air intakes designed by Airbus Helicopters within the ATHENAI project. The work has been carried out with the purpose of analysing the flow structure developed on the helicopter surface and in the engine air intake inner parts; given the importance assumed by the air intake geometry within the ATHENAI project, special attention is paid to the flow field at the air intake entrance, as the most critical conditions are expected. In addition to that, the work aims at the examination of the air intake installation influence on the flow field and at the validation of the results obtained by a CFD simulation by means of a comparison with the experimental data.

### **1.3.2 Phases of the work**

The work can be divided in four main phases, strictly connected with each other; the temporal chronology of the four phases does not necessarily correspond to the chapters organisation. The study has been performed by means of CFD simulations, conducted with the purpose of recreating the same conditions occurred during the first experimental campaign. For this reason, the wind tunnel model and the TUM's wind tunnel facility geometries have been reproduced and then used in the simulations. The so-called "ANSYS CFX" commercial software has been used for the simulations.

In the first phase an analysis of the boundary condition to impose on the outlet section of the wind tunnel geometry has been performed; this research has focused on the comparison between two different approaches, both able to keep the wind tunnel functioning in a stationary regime. The CFD simulations have been performed by means of a simplified helicopter geometry, on which the engine air intake has been kept closed.

In the second phase the air intake has been added to the geometry; the CFD simulation has been performed setting a certain engine operation point, in terms of ambient condition and engine mass flow rate.

In the third phase the problem regarding the CFD simulation of a screen stricken by an air flow has been studied. First of all, the kinematic and the thermodynamic properties of the air flow have been analysed. Subsequently, two possible approaches to simulate the presence of the screen within an air flow have been proposed, the first concerning the mesh definition of the screen and the second relative to the loss coefficient model implementation.

In the fourth phase the CFD simulations performed in the first and in the second phase have been compared in order to study the influence of the engine air intake installation on the air flow. Furthermore, the comparison between the CFD results obtained in the second phase and the experimental data has been made.

### 1.3.3 Organisation of chapters

The second chapter provides the reader with some theoretical basics, representing the fundamentals of Computational Fluid Dynamics. Firstly, Navier-Stokes equations and the relative closure problem are described, highlighting the meaning of each equation; the chapter then deals with the models used in CFD for the turbulence simulation and ends with a simple illustration of mesh typologies.

The third chapter is concerned with the choice of the boundary condition to impose on the wind tunnel outlet surface in order to guarantee the functioning in a stationary regime within a CFD simulation. The analysis is carried out through the comparison between two different approaches in terms of accuracy, stability and computational cost of the simulations. Pressure and velocity fields are in particular studied. The chapter also provides a description of geometries and settings employed in the CFD simulations, performed keeping the helicopter engine air intake closed; furthermore, the *Kriging* model, adopted within one of the two aforementioned approaches, is illustrated.

In the fourth chapter the CFD simulation of the helicopter equipped with the engine air intake is performed. Firstly, the geometries as well the boundary conditions are described; subsequently, part of the results are commented and shown by some pictures. The remaining results are illustrated in the fifth chapter, in which the comparison with the experimental data obtained by the wind tunnel campaign is made.

In the fifth chapter the CFD simulations examined in the two previous chapters are compared in order to investigate the relation between the engine air intake installation and the flow field around the helicopter surface. Moreover, the results obtained by the simulation illustrated in the fourth chapter are contrasted with the experimental data supplied by the first wind tunnel campaign. The most relevant flow structures are also analysed within this chapter.

The sixth chapter deals with the problem related to the CFD simulation of the complete helicopter geometry, on whose engine air intake two screens are added, in accordance with the Airbus Helicopters' design. Two different approaches are suggested. The first consists in the screen geometry meshing, the second concerns the loss coefficient model implementation, definable by means of experimental tests and mathematical models found in literature. Some kinematic and thermodynamic properties of a flow passing through a screen are also described.

The seventh chapter provides the reader with some conclusive comments, focused on the summary of the entire work and on the proposal of possible future researches.





## Chapter 2

# Theoretical basics

In this chapter the most important theoretical constructs related to the present dissertation will be presented; in particular, Navier-Stokes equations and the numerical methodologies used to model the turbulence of a flow in computational engineering will be considered. With regard to the last ones, Shear Stress Turbulence model, which is used in this work, will be analysed. These concepts represent the basis of the whole work and are, for this reason, extremely important. Finally, a description of the different typologies of meshes will be presented.

### 2.1 Navier-Stokes equations

Navier-Stokes equations are the basic governing equations for a flow in terms of mass, momentum and energy balance; the first and the third balance are represented by a scalar equation, while the second one by a vectorial equation.

**Law of conservation of mass** The law of conservation of mass states that the mass of a flow can be neither generated nor destroyed anywhere; that is to say, there must be an identity between the temporal variation of the mass within a certain volume  $V$  and the nett mass flow through the surface  $S$  of the volume  $V$ . Considering  $\rho$  and  $\mathbf{u}$  as regular functions of time and space, Equation 2.1 can be expressed in the local form, valid for every kind of flow. This equation is known as *continuity equation* of the flow [30].

$$\int_V \frac{\partial \rho}{\partial t} = - \oint_S \rho \mathbf{u} \cdot \hat{\mathbf{n}} \quad (2.1)$$

$$\frac{\partial \rho}{\partial t} + \nabla \cdot (\rho \mathbf{u}) = 0 \quad (2.2)$$

**Law of conservation of momentum** The law of conservation of momentum represents Newton's second law for a flow; it states that, in a whatever inertial reference system, the temporal variation of a particle flow's momentum is given by the sum of the forces acting on the particle itself. As a general observation, forces caused by pressure, viscosity and gravity are considered. The mathematical representation of this statement can be expressed as follows, by

defining  $\mathbf{\Omega}(\mathbf{u})$  as the viscous stress tensor.

$$\int_V \frac{\partial}{\partial t}(\rho \mathbf{u}) = - \oint_S \rho \mathbf{u}(\mathbf{u} \cdot \hat{\mathbf{n}}) - \oint_S P \hat{\mathbf{n}} + \oint_S \mathbf{\Omega}(\mathbf{u}) \cdot \hat{\mathbf{n}} + \int_V \rho \mathbf{g} \quad (2.3)$$

$$\frac{\partial(\rho \mathbf{u})}{\partial t} + \nabla \cdot (\rho \mathbf{u} \otimes \mathbf{u}) + \nabla P = \nabla \cdot \mathbf{\Omega}(\mathbf{u}) + \rho \mathbf{g} \quad (2.4)$$

**Law of conservation of energy** In the case of an ideal fluid, the law of conservation of energy states that the rate of variation of the total energy  $E^t$  within a portion of flow is equal to the power related to the forces acting on the portion of flow itself. However, in the case of a real fluid, the terms depending on heat conduction and on energy dissipation due to viscous friction must be considered [29]. Defining the heat flow as  $\mathbf{q}$ , the law of conservation of energy can be written as follows.

$$\int_V \frac{\partial E^t}{\partial t} = - \oint_S \mathbf{q} \cdot \hat{\mathbf{n}} - \oint_S P \mathbf{u} \cdot \hat{\mathbf{n}} + \oint_S \mathbf{u} \cdot \mathbf{\Omega}(\mathbf{u}) \cdot \hat{\mathbf{n}} + \int_V \rho \mathbf{g} \cdot \mathbf{u} \quad (2.5)$$

$$\frac{\partial E^t}{\partial t} + \nabla \cdot [(E^t + P) \mathbf{u}] = -\nabla \cdot \mathbf{q} + \nabla \cdot (\mathbf{u} \cdot \mathbf{\Omega}(\mathbf{u})) + \rho \mathbf{g} \cdot \mathbf{u} \quad (2.6)$$

**Closure of Navier-Stokes equations** The term  $\mathbf{q}$  is generally defined using Fourier's law ( $\mathbf{q} = -k\nabla T$ ) as a function of the temperature  $T$ ; moreover, total energy  $E^t$  can be expressed as the sum of density of the internal energy  $\rho e$  and of the kinetic one  $1/2\rho|\mathbf{u}|$ . Referring to the previous formulations, the unknowns of Navier-Stokes equations are pressure  $P$ , density  $\rho$ , velocity  $\mathbf{u}$ , temperature  $T$  and internal energy  $e$ , four scalar quantities and one vectorial quantity. However, Navier-Stokes equations are not sufficient to solve the problem, since they are constituted only by two scalar equations and one vectorial equation. The closure of the problem is obtained by using two additional scalar equations, the *equations of state*; they can be defined for example as follows.

$$P = P(e, \rho) \quad (2.7)$$

$$T = T(e, \rho) \quad (2.8)$$

Therefore, the combination of Navier-Stokes equations and the equations of state represents a closed problem.

## 2.2 Turbulence models

Turbulence exhibits as a fluctuation in the flow both in space and in time, when the viscous force becomes much larger than the inertial one. The problem related to turbulence modelling during a numerical analysis concerns the length scales involved in the phenomenon, that are generally smaller than the smallest finite volume mesh commonly used during a simulation. Since the computational cost of a Direct Numerical Simulation (DNS) increases as the cube of the Reynolds number [27], DNS results useless for flows characterised by a high Reynolds number; in order to fix this problem, different turbulence models have been developed. Most of them are statistical models; the only exceptions are represented by Large Eddy Simulation

(LES) and Detached Eddy Simulation (DES) models [7], that won't be used in this work.

### 2.2.1 Statistical turbulence models

Let us consider the velocity and the density of flow as given by the sum of an average,  $\overline{u_i}$  and  $\overline{\rho}$ , and a fluctuating component,  $u'_i$  and  $\rho'$  [7, 27]. The i-th component of velocity and the density can be written as follows.

$$u_i = \overline{u_i} + u'_i \quad \text{with} \quad \overline{u'_i} = 0 \quad (2.9)$$

$$\rho = \overline{\rho} + \rho' \quad \text{with} \quad \overline{\rho'} = 0 \quad (2.10)$$

Statistical turbulence models use this consideration to simplify the Navier-Stokes equations and to solve the so-called *Averaged Navier-Stokes Equations*. One of the possible approaches to derive Averaged Navier-Stokes Equations is to define the mean value of velocity and density applying the Favre average; mean and averaging value for a general fluctuating function are then defined as follows.

$$\tilde{a} = \frac{\overline{\rho a}}{\overline{\rho}} \quad (2.11)$$

$$a'' = a - \tilde{a} \quad (2.12)$$

As proposed in [25], averaging Navier-Stokes equations by means of Favre filter and neglecting the gravitational term, the following Averaged Navier-Stokes Equations are obtained.

$$\frac{\partial \overline{\rho}}{\partial t} + \nabla \cdot (\overline{\rho \mathbf{u}}) = 0 \quad (2.13)$$

$$\frac{\partial (\overline{\rho \mathbf{u}})}{\partial t} + \nabla \cdot (\overline{\rho \mathbf{u}} \otimes \mathbf{u}) + \nabla \overline{P} = \nabla \cdot \overline{\mathbf{\Omega}} + \nabla \cdot \mathbf{R} \quad (2.14)$$

$$\frac{\partial (\overline{\rho \tilde{E}})}{\partial t} + \nabla \cdot (\overline{\rho \mathbf{u} \tilde{E}}) + \nabla \cdot (\overline{P \mathbf{u}}) = \nabla \cdot (\overline{\mathbf{\Omega} \mathbf{u}}) + \nabla \cdot (\mathbf{R} \mathbf{u}) + \nabla \cdot (k \nabla \tilde{T} - \gamma \overline{\rho \mathbf{u}'' T''}) \quad (2.15)$$

where  $\tilde{E} = 1/2|\tilde{\mathbf{u}}|^2 + \tilde{T} + K$ , being K the turbulent kinetic energy. This operation introduces new unknowns in the momentum transport equation, leading the set of equations to be unclosed; in addition to the molecular diffusive fluxes there are, in fact, Reynolds stresses ( $R_{ij} = -\overline{\rho u'_i u'_j}$ ) too. These terms come from the non-linear convective term in Navier-Stokes equations: convective transport caused by turbulent velocity fluctuations will act to increase mixing in addition to that given by thermal fluctuations at molecular level. Given the impossibility to directly find Reynolds stresses, they are modelled by additional equations that allow us to achieve the closure of the problem; furthermore, turbulent heat flux,  $\overline{\rho T'' \mathbf{u}''}$ , and turbulent kinetic energy,  $1/2|\tilde{\mathbf{u}}''|^2$ , must be numerically modelled too. Some models commonly used are listed here.

- Zero Equation model
- k- $\epsilon$  model
- RNG k- $\epsilon$  model
- k- $\omega$  model

- BSL k- $\omega$  model
- Shear Stress Transport (SST) model
- Reynolds Stress model
- $\omega$  Reynolds Stress model
- BSL Reynolds Stress model

### 2.2.2 Shear Stress Transport (SST) model

Shear Stress Transport model belongs to the family of the k- $\omega$  turbulence models, where k and  $\omega$  respectively define the turbulent kinetic energy and the turbulent frequency. The main advantage of a k- $\omega$  model concerns the treatment of the viscous near-wall region and of the pressure gradient effects in low Reynolds number computations; however, for a basic method, the sensitivity to free-stream conditions is very high and the results obtained can differ significantly by setting different values of  $\omega$  at the inlet [7, 27].

**Wilcox model** The basic k- $\omega$  model, also called Wilcox model, solves two transport equations, one for the turbulent kinetic energy, k, and one for the turbulent frequency,  $\omega$ .

**Baseline (BSL) k- $\omega$  model** In order to solve the problems related to sensitivity to the free-stream conditions characterizing the Wilcox model, Baseline (BSL) k- $\omega$  model has been developed; it consists of a blending between the k- $\omega$  near the surface and the k- $\epsilon$  model in the outer region. The Wilcox model is multiplied by a blending function  $F_1$ , that is equal to one close to the wall and to zero outside the boundary layer, while the k- $\epsilon$  model by the function  $1 - F_1$ . The BSL model includes the advantages related to both the Wilcox model and the k- $\epsilon$  model; however, it still fails to compute the amount of flow separation.

**Shear Stress Transport (SST) model** SST model properly predicts the amount of flow separation under adverse pressure gradients in most of cases; the main reason is that it accounts for the transport of the turbulent shear stress, that leads to a correct prediction of the eddy-viscosity. The correct computation of the transport of the turbulent shear stress can be obtained by using a limiter to the formulation of the kinetic eddy-viscosity, as follows.

$$\nu_t = \frac{a_1 k}{\max(a_1 \omega, S F_2)} \quad (2.16)$$

where  $a_1$  is a fixed coefficient,  $F_2$  is another blending function, similar to  $F_1$ , that restricts the limiter to the wall boundary layer, while S is an invariant measure of the strain rate [7].

### 2.2.3 $y^+$ parameter

The total shear stress  $\tau$  is equal to the sum of the viscous stresses and the Reynolds stresses. On the wall, where the boundary condition  $\mathbf{u} = 0$  is considered, the Reynolds stresses are null

and the total shear stress is entirely given by the viscous stress; on the contrary, in a high-Reynolds-number free shear flow the viscous stress is negligible compared to Reynolds stresses. Therefore, the kinematic viscosity,  $\nu$ , and the wall shear stress,  $\tau_w$ , assume extreme importance close to the wall; these quantities are used to define two parameters, the *friction velocity*  $u_\tau$  and the *viscous length scale*  $\delta_\nu$ , that characterise the behaviour of the flow close to the wall.

$$u_\tau \equiv \sqrt{\frac{\tau_w}{\rho}} \quad (2.17)$$

$$\delta_\nu \equiv \nu \sqrt{\frac{\rho}{\tau_w}} = \frac{\nu}{u_\tau} \quad (2.18)$$

The distance from the wall measured in viscous lengths, called also wall units, is defined as *dimensionless wall distance*,  $y^+$  [11].

$$y^+ \equiv \frac{y}{\delta_\nu} = \frac{u_\tau y}{\nu} \quad (2.19)$$

The  $y^+$  parameter can be interpreted as a local Reynolds number; therefore, its magnitude can be used to determine the importance of viscous effects at a certain distance  $y$  from the wall [27].

## 2.3 Structured and unstructured meshes

The simplest classifications of meshes are based either on the connectivity of a mesh or on the type of elements employed for its generation. The most basic mesh classification is made considering connectivity as discriminating factor: on the base of this distinction, a mesh can be defined as *structured* or *unstructured*.

For a more complete description see [9, 12, 20]; in the following sub-sections only general information is given.

### 2.3.1 Structured mesh

A structured mesh is defined as a mesh for which it is possible to construct a mapping function able to transform the curvilinear mesh, belonging to the physical domain, to a uniform Cartesian mesh, that is the tool used by computers to store the data. As a general rule, a structured mesh is characterised by regular connectivities that can be simply expressed as a two or a three dimensional array; the regularity of connectivity allows us to save space, since relations between elements are directly obtained by the storage arrangement. In this way, a certain point's neighbours are easily identified and efficiently accessed, leading to fast CFD codes. On the other hand, this kind of mesh does not allow us to add elements into the mesh if a refinement in some regions is required.

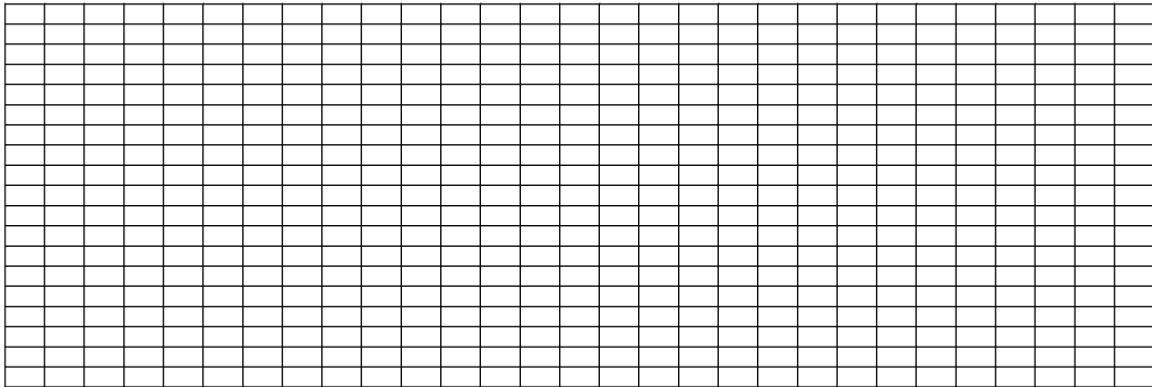


Figure 2.1: Structured mesh

**Generation of a structured mesh** The physical space is subdivided into a number of grid cells, quadrilaterals in 2D and hexahedra in 3D, in such a way that:

- the domain is entirely covered by the grid;
- there are no free spaces between the cells;
- the cells are not overlapping each other.

### 2.3.2 Unstructured mesh

Unstructured meshes do not present a mapping between the location where the elements are memorised and the way in which they are connected in the physical space, leading to the necessity of explicitly storing the neighbourhood connectivity. This means that extrapolating the position of a given point's neighbours is more expensive than in the case of a structured mesh; on the other hand, such a mesh allows for a wider freedom in the construction of a grid, refining or coarsening it where necessary.

**Octree method** An octree is a tree data structure in which each internal node is subdivided in eight exact parts. As written in [4], the Octree mesh algorithm implemented in ANSYS ICEM CFD, the software employed for meshes computation, guarantees refinement where necessary, but defines larger elements where possible, allowing for fast computation. The operations made by the algorithm can be itemised as follows.

- once the root tetrahedron, in which the whole geometry is enclosed, has been created, the mesher subdivides it until the required element dimensions are obtained;
- the mesher adjusts the mesh so that elements sharing an edge or a face do not differ in dimension by more than a factor of 2;
- the mesher ensures that each pair of adjacent elements will share an entire face;

- as the given geometry is not yet matched by the mesh, the mesher rounds the nodes of the mesh to the prescribed points, prescribed curves or model surfaces;
- the mesher removes every part of the mesh which cannot be reached by a user-defined material point without intersecting a surface;
- as final step, the mesh is smoothed by moving nodes, merging nodes, swapping edges and deleting bad elements.

**Delaunay method** In ANSYS ICEM CFD a Delaunay algorithm is implemented and used to create tetras from an already existing mesh, in this way allowing for a smoother transition in the volume element dimension.

A Delaunay triangulation for a set  $\mathbf{S}$  of points in a plane is defined as a triangulation such that no point in  $\mathbf{S}$  is inside the circumcircle of any triangle. Among all possible triangulations of a fixed set of points, Delaunay triangulations maximise the minimum angle of all the angles of the triangles. Every point set has almost one Delaunay triangulation; moreover, if and only if the point set does not have four cocircular points, its Delaunay triangulation is also unique.

For further information about Delaunay triangulations see [13, 36].

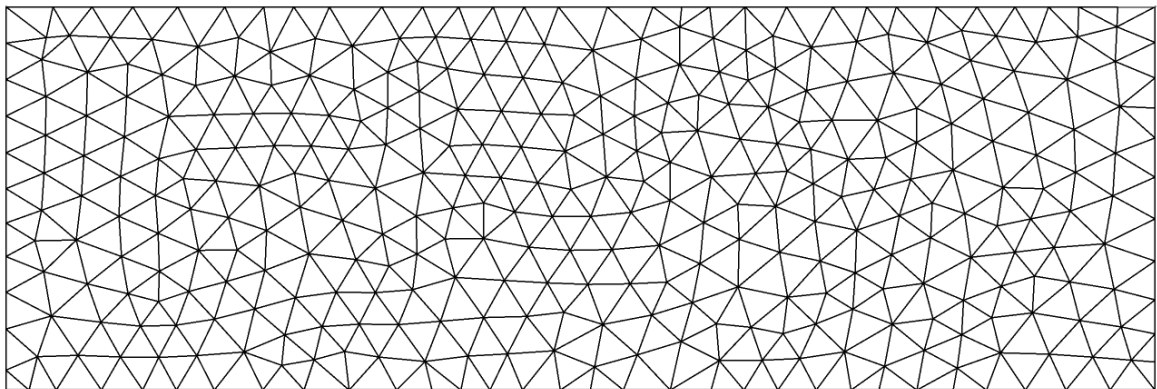


Figure 2.2: Unstructured mesh

### 2.3.3 Differences

**Unstructured mesh pros** As written in [20], unstructured meshes offer maximum flexibility, giving the possibility of putting a grid around a whatever geometry and adding resolution where it is needed. On the contrary, in a structured mesh, due to regular connectivity, it is often necessary to refine the mesh in small gradients regions in order to obtain the required resolution in other parts of the domain.

**Structured mesh pros** On the other hand, structured solvers generally run much faster than unstructured solvers. Moreover, even though unstructured meshes are much easier to create, it

often happens that creating an unstructured grid with a satisfying resolution takes the same time as creating a structured mesh with the same level of resolution. Finally, unstructured codes are often very dissipative compared to high resolution structured solvers; furthermore, unstructured codes are almost no more than second order in space, whereas structured solvers may have fifth or sixth order schemes.

### 2.3.4 Hybrid mesh

A hybrid mesh is a mesh that contains both structured and unstructured grids.

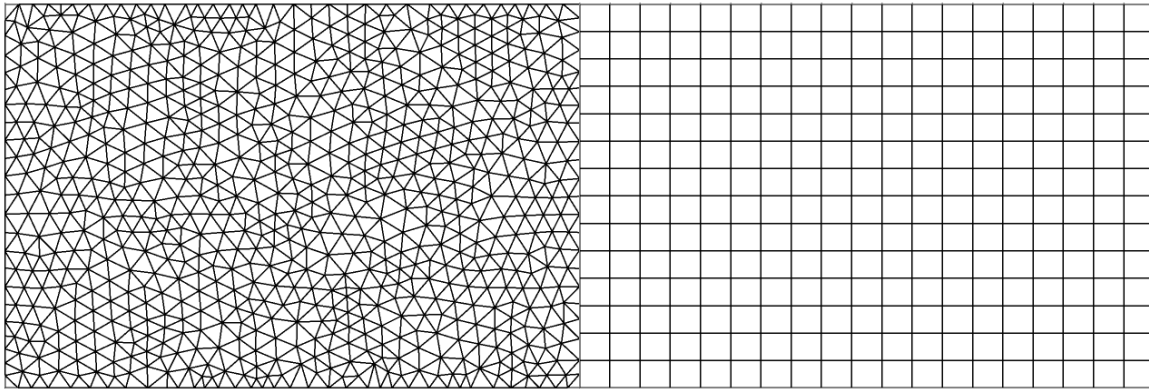


Figure 2.3: Hybrid mesh



## Chapter 3

# Analysis of boundary conditions

The primary objective of the work is to analyse the aerodynamic performances of the first variant of engine air intakes designed by Airbus Helicopters within the "ATHENAI" project; the study will be conducted by means of stationary CFD simulations, attempting to reproduce the same conditions occurred during the first experimental campaign. Therefore, the reproduction of the same configuration is required, including the helicopter model and the wind tunnel facility; the so-called "ANSYS CFX" software has been used for the computation.

This chapter will deal with the problem related to the boundary conditions specification in the CFD simulations; the analysis will especially concern the imposition of the boundary condition on the wind tunnel outlet surface, required to guarantee the wind tunnel working in a stationary regime. In order to speed up its execution, the study has been performed using a simplified helicopter geometry, on which the air intake has been kept closed. This has also allowed us to study the flow field generated by the helicopter external surface only, separating these effects from those caused by the engine air intake installation and by the engine mass flow rates, that will be studied in Chapter 4.

As previously mentioned, the simulations have been carried out with the primary purpose of analysing the boundary conditions; furthermore, they have been also exploited to contrast the obtained results with those presented in Chapter 4, that will also be used for a comparison with the experimental data coming from the first experimental campaign. In order to obtain comparable values, all the simulations must be performed attempting to re-create the conditions occurred within the wind tunnel at the moment of measurements. However, the starting of the wind tunnel measurements were subsequent to the CFD simulations; therefore, in the simulations described within this chapter, the reference temperature and pressure have been calculated using the *International Standard Atmosphere model* (ISA) at the altitude of Garching, the location of the wind tunnel.

### 3.1 Description of the problem

#### 3.1.1 Geometry

The geometry considered at the beginning of the work is represented in Figure 3.1; actually, this geometry will be slightly adapted for the simulations. The reasons will be explained in

the next section, but the geometry is anyway shown to introduce the problem related to the boundary conditions specification.

The real wind tunnel of the Institute of Aerodynamics and Fluid Mechanics of the Technische Universität München is a closed-loop format; the measurement campaign has been conducted with an open test section. For the CFD simulations, that will be described in the following sections, only the parts essential to reproduce the flow field around the helicopter section have been taken into account; the complexity of reproducing the real wind tunnel, in particular the corners and their vanes, has led to the choice of defining an open-loop wind tunnel, able anyway to recreate in the test section the same conditions in which the flow has to operate. Compared to the real geometry, a duct has also been added at the end of the diffuser in order to distance the outlet from a recirculation region originating just after the beginning of the diffuser itself; an additional extension of the duct was actually necessary to solve the problem, as explained in Section 3.2. A more detailed description of the wind tunnel geometry is given in Appendix B.

A representation of the helicopter section employed in the CFD simulations is shown in Figure 3.2. As previously explained in the preface, the wind tunnel model manufactured for the experimental campaign does not represent the entire helicopter, since it lacks the landing gear and also the main and the tail rotors; the same helicopter geometry is used in this set of CFD simulations, with the exception of the engine air intake, that is not taken into account yet. The tube at the end of the helicopter represents the conduct used during the experimental campaign to ensure the desired mass flow rate to the engine by means of the suction system. From Figure 3.3, 3.4, 3.5, 3.6 it is possible to see the position of the helicopter inside the wind tunnel; the coordinate system used during the CFD simulations is the common coordinate system employed for a wind tunnel: the x-axis (red) is directed in the longitudinal direction, the y-axis (green) in the right-left direction and the z-axis (blue) in the top-bottom direction.

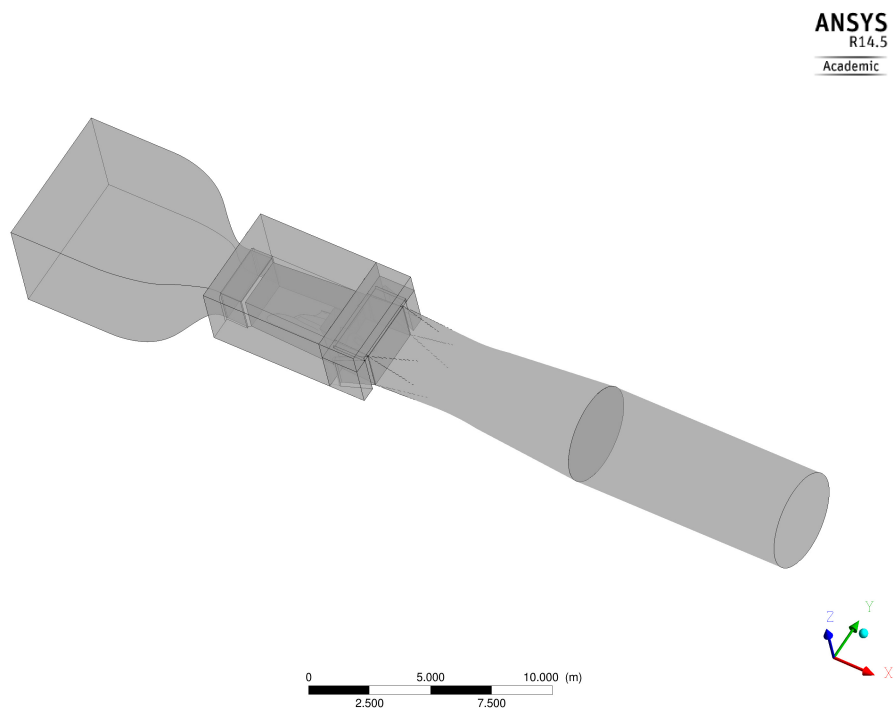


Figure 3.1: Initially defined wind tunnel geometry

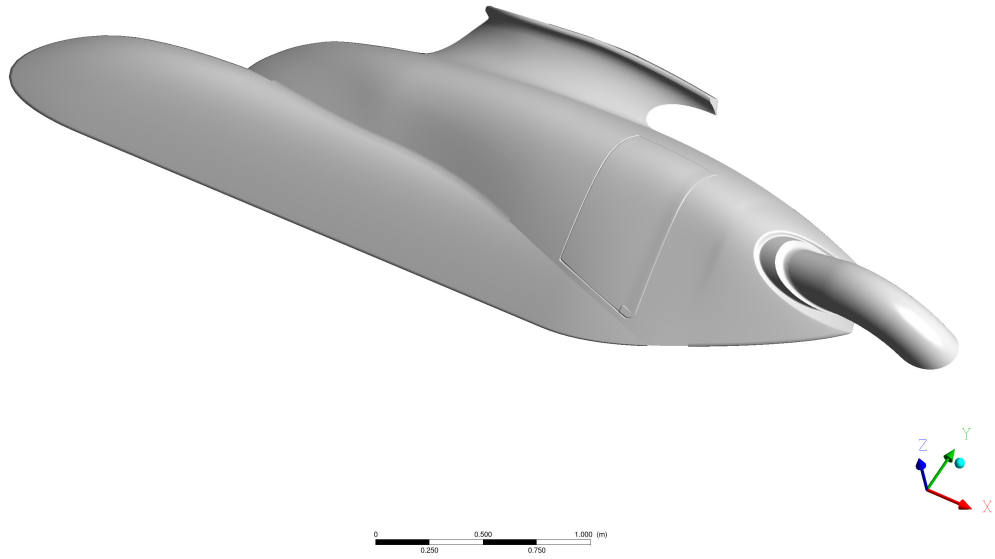


Figure 3.2: Helicopter geometry used in the boundary conditions analysis

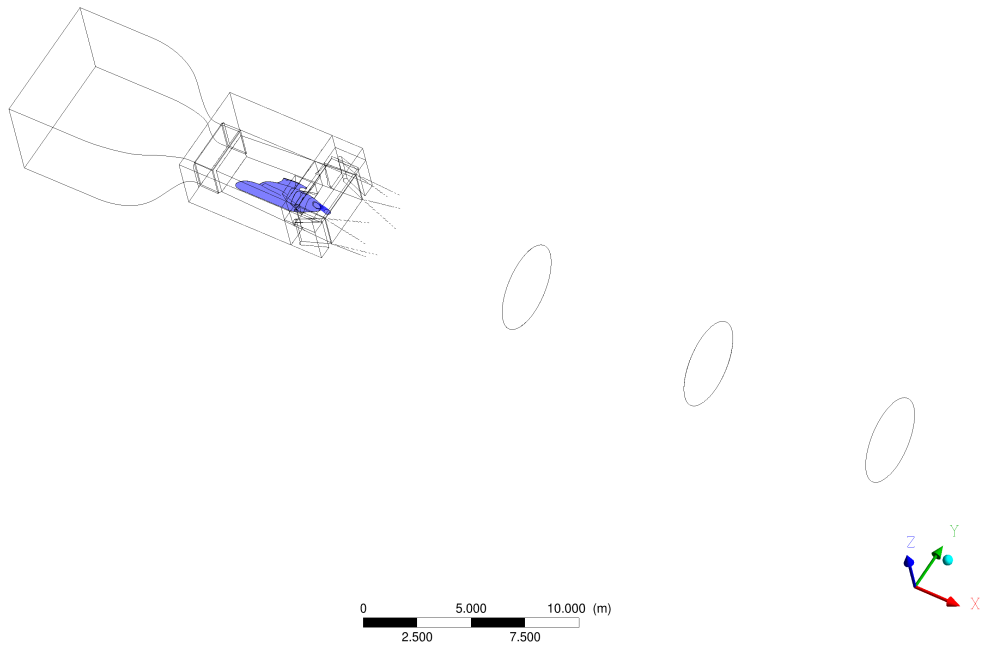


Figure 3.3: Position of the helicopter within the wind tunnel

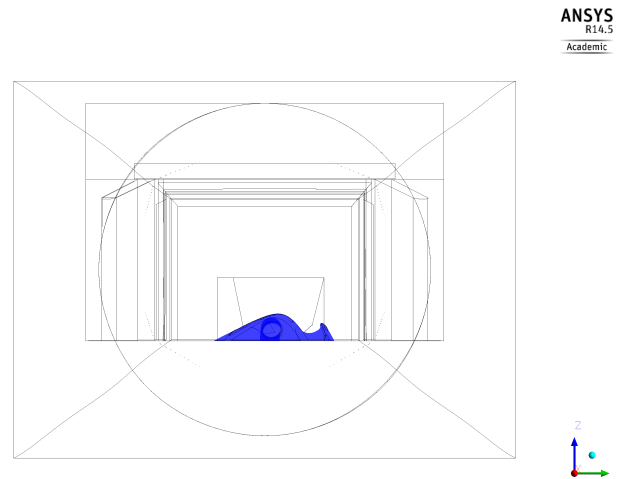


Figure 3.4: Position of the helicopter within the wind tunnel - X-view

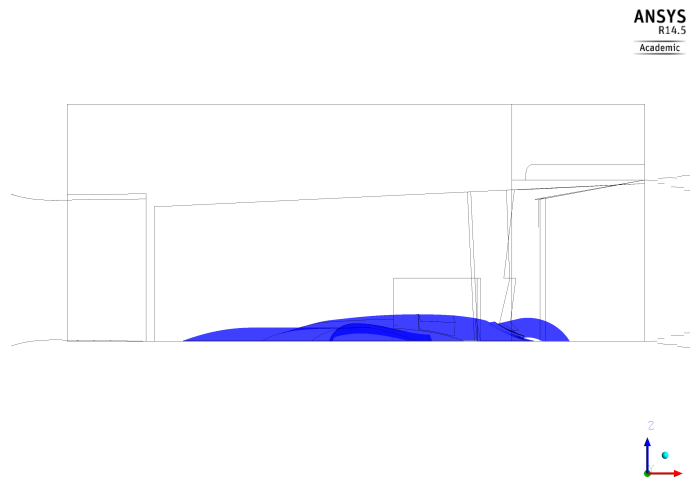


Figure 3.5: Position of the helicopter within the wind tunnel - Y-view

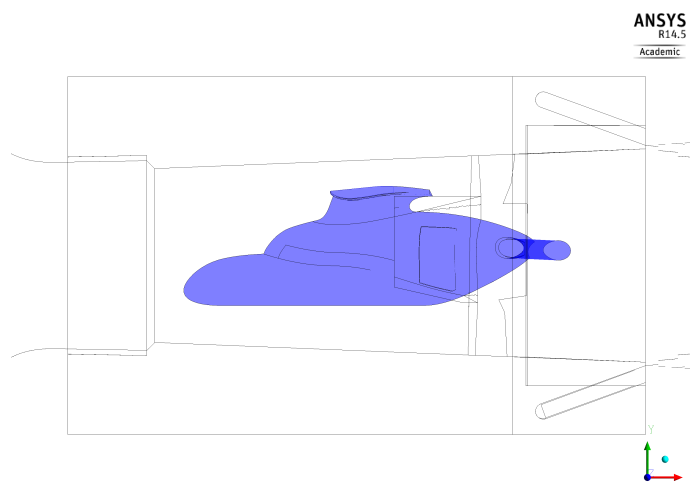


Figure 3.6: Position of the helicopter within the wind tunnel - Z-view

### 3.1.2 Mesh

The mesh of the wind tunnel geometry is almost exclusively of type "unstructured"; in this way it has been possible to obtain a good mesh resolution, despite the complexity of the shapes. On the contrary, the mesh of the helicopter section is almost totally "structured" (Figure 3.7), unlike the surface used to substitute the engine air intake.

The computation and the quality investigation of the wind tunnel geometry and of the helicopter section meshes is described in [18].

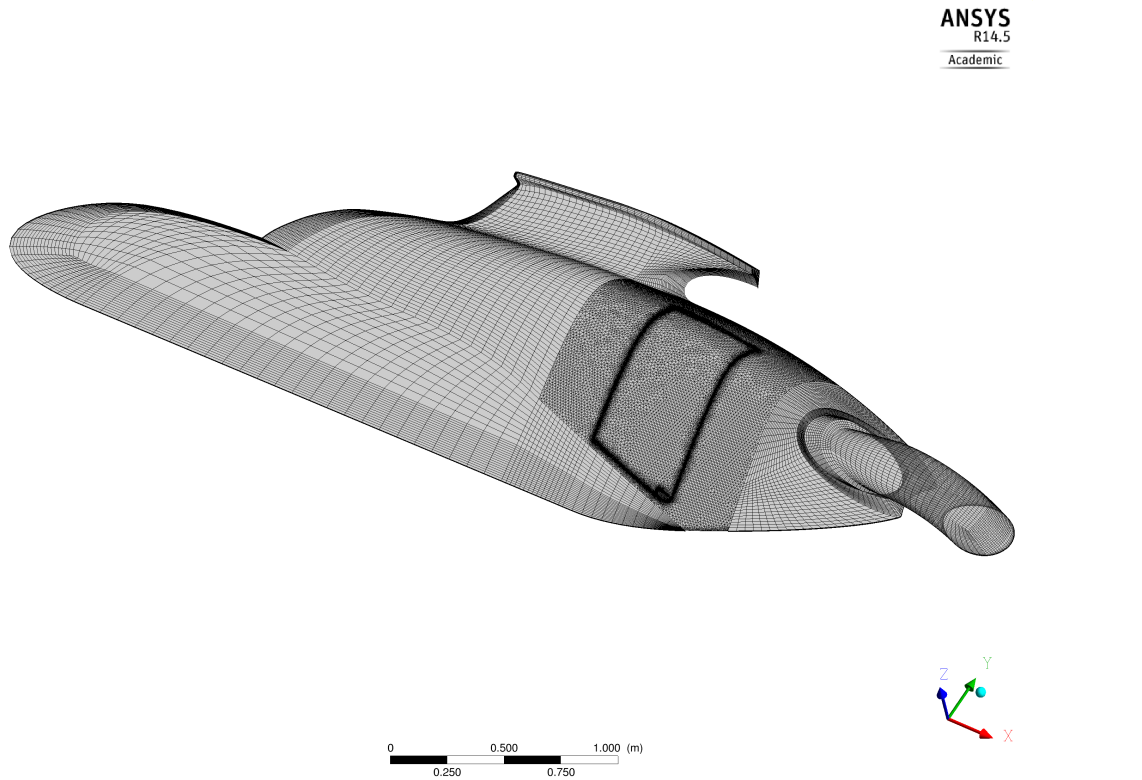


Figure 3.7: Helicopter geometry mesh

### 3.1.3 Settings

The settings used in the CFD simulations described in this chapter are summarised in Table 3.1; a similar table will also be used in the following chapter. A description of the items used in this table can be found in Appendix D.

Setting	Model
Turbulence	SST
Material	Air at 25°C

Table 3.1: Settings - "Analysis of boundary conditions"

This set of simulations have been performed using the properties of air at 25°C. The effect of air compressibility should be analysed; however, the Mach number characterising the flow is expected to remain around a value of 0.1, that allows us to neglect the effects given by air compressibility. The reference temperature has been defined equal to 285.02 K, whereas the reference pressure has been set to a value equal to 95667.10 Pa. Hereinafter, the term "pressure" will be referred to as "relative static pressure", if not differently specified.

### 3.1.4 Boundary conditions

On the wind tunnel inlet section a mass flow rate equal to 269.36 kg/s has been imposed. This value has been chosen in order to guarantee a given flow velocity on the section corresponding to the nozzle exit ( $x = 0.00$  m); this velocity corresponds to the maximum velocity specified by Airbus Helicopters for the first experimental campaign. The velocity measured at the nozzle exit is considered as the free-stream velocity and will be taken as reference for the velocity normalisation.

During the wind tunnel stationary working, the same mass flow rate must occur on the inlet and on the outlet sections; as previously anticipated, the present chapter will entirely be devoted to the fulfilment of this requirement. The choice of the boundary condition on the outlet section was much more complicated than in the case of the inlet one: as a matter of fact, CFX-Solver creates a physical wall on the outlet (inlet) surface when the flow tries to enter (exit) the domain and an "outlet" ("inlet") boundary type with a mass flow or a pressure boundary condition is set. Considering the geometry represented in Figure 3.1, the presence of the helicopter geometry within the wind tunnel test section and, in particular, the transition of the diffuser section from rectangular to circular lead the flow to create a recirculation area extending as far as the outlet surface. This is shown in Figure 3.12.

In this way, the mass flow cannot be imposed on the outlet section too, as the wall created by the software would change the geometry completely and the results would differ greatly from the case of the real outlet; however, in a stationary condition, the mass flow on the outlet must be equal to the one imposed on the inlet, since no fluid particles can exit the wind tunnel. As suggested by [6], two methods could be used to fix such a problem.

- move the outlet to a region far from the previous one, where the recirculation area is not present any more, by extending the flow domain further downstream.
- use an "opening" boundary type to describe the flow where simultaneous inflow and outflow may occur; artificial walls are not erected in this case, as both inflow and outflow are allowed.

## 3.2 Choice of boundary condition on the outlet surface

Both the methods above presented have been considered to solve the problem of boundary condition on the outlet surface: the comparison between the two approaches in terms of accuracy, stability and computational cost of the simulations will allow for the definition of the most effective one. The conclusions of the analysis will help to simulate a more complex geometry in

the most efficient way. The different measurement typologies will also allow us to validate the results obtained and, hence, to make sure of the negligible influence of the boundary condition type used to get the results on the flow field within the wind tunnel.

### 3.2.1 "Mass flow" boundary condition

A first simulation has been performed with an "outlet" boundary type, setting the same mass flow of the inlet section (269.36 kg/s) on the outlet one; due to the previously mentioned reason, the length of the conduct at the exit of the diffuser has been doubled. The new configuration is represented in Figure 3.8.

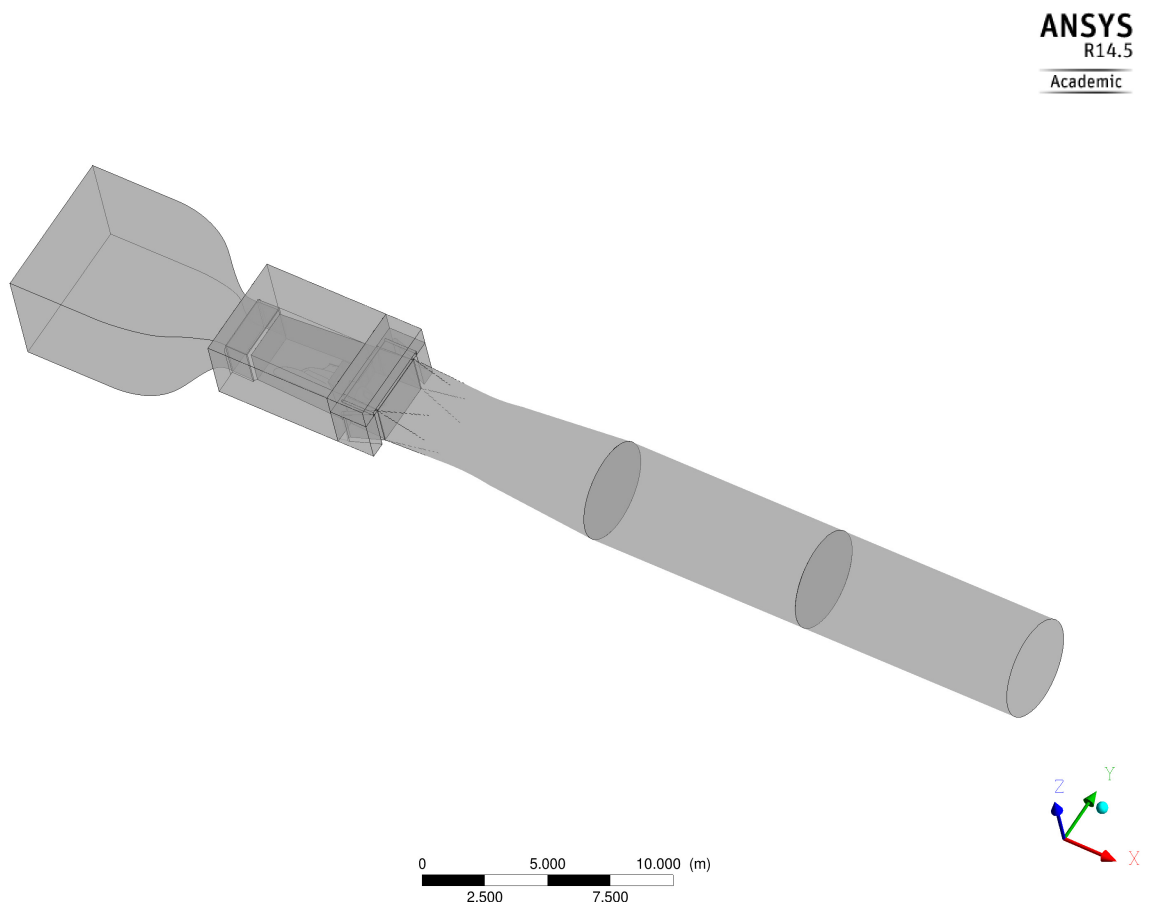


Figure 3.8: Wind tunnel geometry used in the CFD simulations

The results obtained by the simulation performed with the aforementioned boundary conditions have reached a quite good convergence. As suggested by [6], Root Mean Square (RMS) residual values larger than  $1E-04$  may be sufficient to obtain a qualitative understanding of the flow field, even if only a minimum value of  $1E-05$  generally corresponds to a good convergence level. In the present case, the simulation has obtained very good values only for the residuals relative to pressure  $P$  and to turbulent frequency  $\omega$ ; on the contrary, this does not occur for the three velocity components and the turbulent kinetic energy  $\epsilon$ , which present a poorer convergence ( $\sim 1E-3$ ). The RSM residuals are plotted in Figure 3.9, 3.10.

With the purpose of verifying that no artificial walls have been constructed during the

simulations, the absence of an inflow on the outlet section has been controlled a posteriori. Figure 3.11 shows that the u-component of velocity, normal to the outlet surface, is entirely positive on the section considered. This ensures that the recirculation area does not concern the region where the outlet has been moved. Figure 3.12 instead shows that the u-component of velocity is not entirely positive on the outlet section of the initially considered configuration, in particular in the upper side; this picture is explanatory for the choice of extending the conduct.

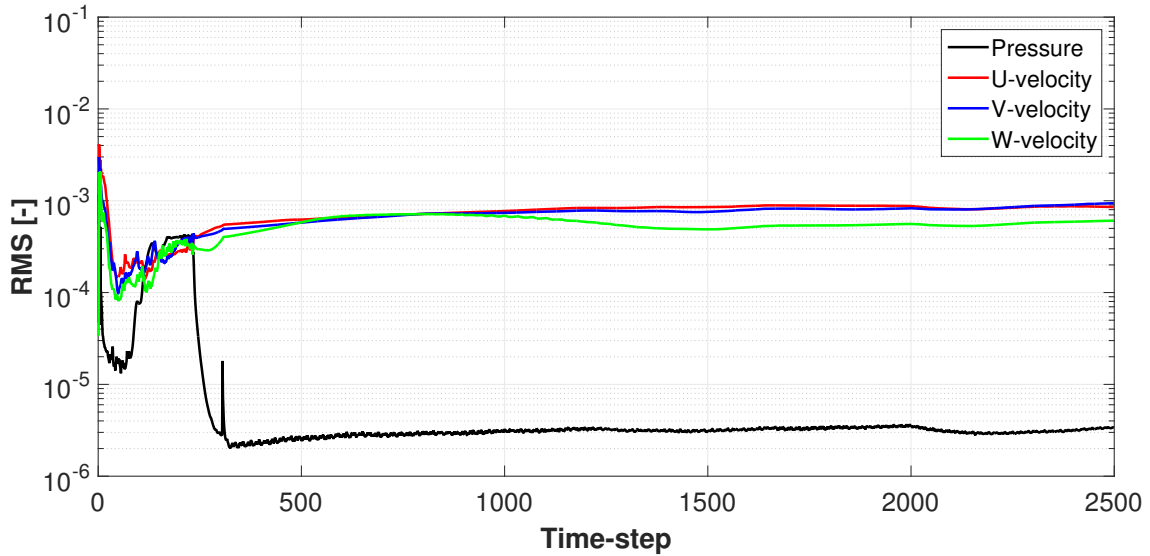


Figure 3.9: Mass and momentum residuals - "Mass flow" case

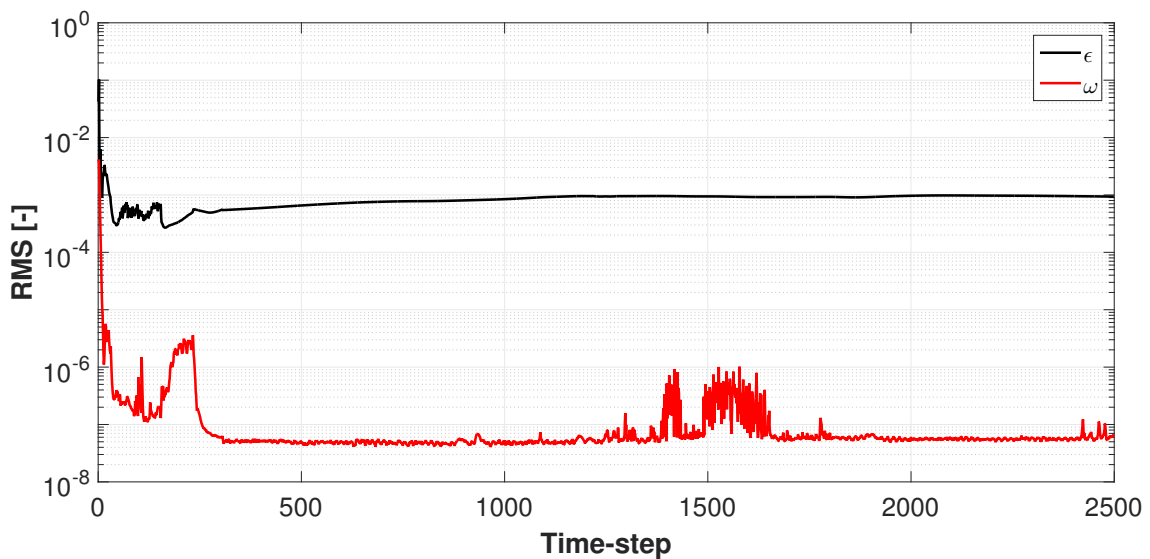


Figure 3.10: Turbulence residuals - "Mass flow" case



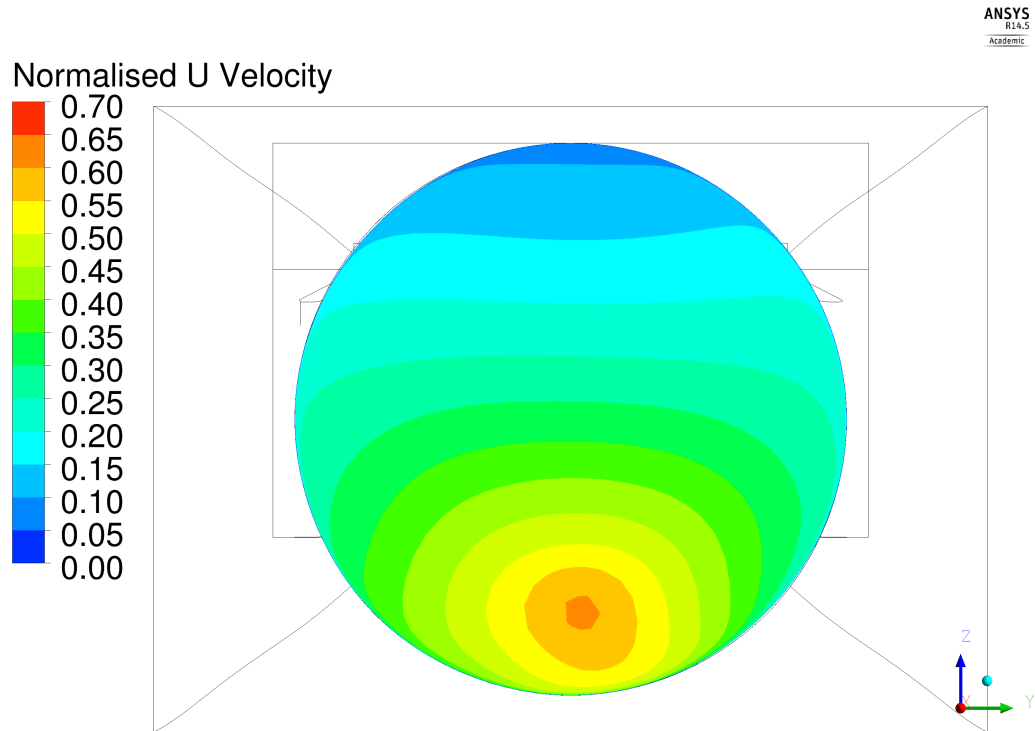


Figure 3.11: Velocity u-component - New geometry outlet section

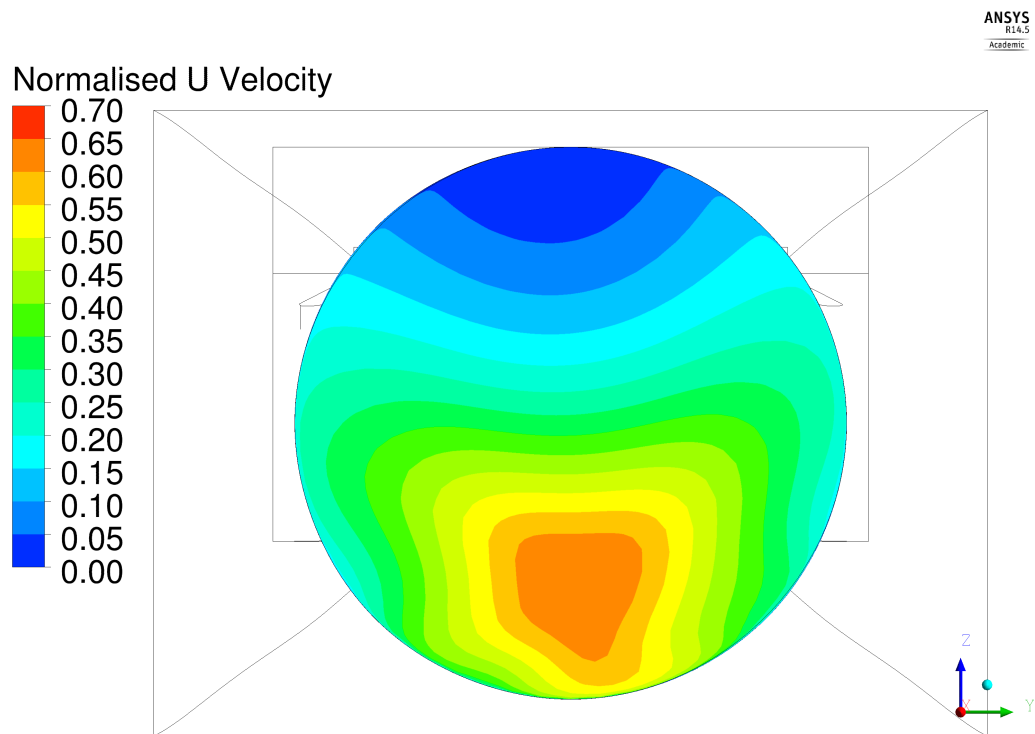


Figure 3.12: Velocity u-component - Initial geometry outlet section

### 3.2.2 "Pressure" boundary condition

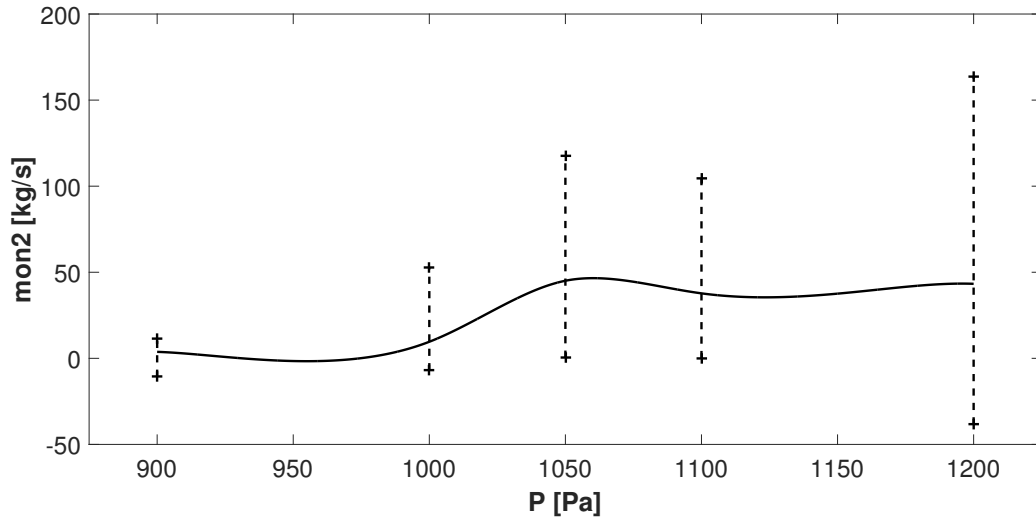
An "opening" boundary type has been considered for another set of simulations, in which the relative static pressure on the outlet section has been specified. Also in this case, the simulations have been conducted using the wind tunnel geometry represented in Figure 3.8; as a matter of fact, [6] suggests not to define the boundary of the domain to cross a recirculation zone, since only a poor approximation of the flow can be obtained by not modelling what is happening just outside the opening. Moreover, in the case of the present work, the geometry extension has helped the problem to be more stable and to reach, even though only in a few cases, a convergence considerable as acceptable, given the complexity of the problem.

The real challenge related to such an approach is to find the right value of relative static pressure to set on the outlet section so that the mass flow rate, at the end of the computation, is equal to that specified on the inlet one. In order to determine the correct boundary condition, the parameter `mon2`, representing the net mass flow between inlet and outlet, has been defined: it has allowed us to re-define the problem as the research of the zero of `mon2` itself, considered as a function of the relative static pressure imposed on the outlet section. It is expected that, for completely converged simulations, `mon2` crosses the x-axis (pressure-axis) just once; in other words, only one solution of the problem should be present. This follows from a simple physical interpretation of the problem: as a matter of fact, the higher the pressure defined on the outlet surface, the smaller the velocity and, as a consequence, the higher the `mon2` value.

As suggested by [18], the first attempt to solve such a problem has focused on the employment of Newton's method or a simpler method of the same family; however, these methods do not represent the best way to find the solution of the problem for the following reasons:

- Newton's method requires the computation of the first derivative of the function, that is actually impossible to obtain directly in CFX-Solver; an extremely expensive approach based on an external Fortran subroutine should be used;
- Newton's method family suffers the presence of local minima or maxima and abrupt variations of the first derivative in proximity of the zero. Given the impossibility to know the function trend a priori, this second point would be sufficient to exclude Newton's method family as a possible approach to solve the problem;
- due to the insufficient robustness of "pressure" boundary conditions, the convergence has resulted, as a general rule, absolutely poor; the oscillation of `mon2` has very often characterised the behaviour of these simulations. Only a few has reached quite constant values of `mon2` and of the residuals. In Figure 3.13, as an example, a curve with intervals of variation of the simulation at certain pressure values is represented.

Therefore, Newton's method employment has been considered inefficient for the present work, given the difficulty to obtain reliable values from the simulations. The solution of the problem was possible thanks to the co-Kriging model, belonging to the Kriging family, a set of methods of interpolation for spatial data, commonly used to predict the expected value for a point within a defined region, given a set of observations of some variables of interest [24]. As explained in detail in the next section, the features of this method make it absolutely suitable for the solution of the problem.

Figure 3.13: Newton's method - Intervals of variation <sup>1</sup>

### 3.3 Kriging model

Kriging is a model developed to approximate deterministic noise-free data, a special case of optimal linear prediction applied to random processes in space or random fields; Kriging is proven to be very useful for tasks concerning optimisation, design space exploration, visualisation, prototyping and sensitivity analysis. As an optimal linear interpolation model, Kriging requires the covariance structure of the random field to be known; when, as it is often the case, the covariance structure is unknown, it is estimated using the same data that would be used for interpolation [15, 34]. Differently from other interpolation algorithms, that estimate the value at a given location as a weighted sum of data values at surrounding locations, Kriging assigns weights making use of a data-driven weighting function. Some advantages of Kriging compared to other interpolation methods are listed here [10].

- it takes the presence of data clustering into account, giving individual points within a cluster less weights than isolated data;
- it estimates both interpolation error and response.

#### 3.3.1 Kriging's theory

Following [23], let us consider a set of design sites  $\mathbf{S} = [s_1 \dots s_m]^T$  with  $s_i \in \mathbb{R}^n$  and the relative responses  $\mathbf{Y} = [y_1 \dots y_m]$  with  $y_i \in \mathbb{R}^q$ . Let us adopt now a model  $\hat{y}$  that defines the deterministic response  $y(x) \in \mathbb{R}^q$  for an input  $x \in \mathcal{D} \subseteq \mathbb{R}^n$ , as the sum of a regression model  $\mathcal{F}$  and a random function expressing a stochastic process.

$$\hat{y}_\ell(x) = \mathcal{F}(\beta_{:, \ell}, x) + z_\ell(x), \quad \ell = 1, \dots, q \quad (3.1)$$

<sup>1</sup>The curve is taken from the "co-Kriging" approach described in Section 3.4; three expensive values have been used for the computation. The mean values used for the co-Kriging model have been computed considering all the values of the range. The intervals represented in the figure are limited by the minimum and the maximum values in the ranges defined in Table 3.3

Let us now define the regression model as a linear combination of  $p$  chosen functions  $f_j : \mathbb{R}^n \mapsto \mathbb{R}$ , using some regression parameters  $\beta_{k,\ell}$ .

$$\begin{aligned}\mathcal{F}(\beta_{:, \ell}, x) &= \beta_{1,\ell} f_1(x) + \dots + \beta_{p,\ell} f_p(x) \\ &= [f_1(x) \quad \dots \quad f_p(x)] \beta_{:, \ell} \\ &= \mathbf{f}(x)^T \beta_{:, \ell}\end{aligned}\tag{3.2}$$

The mean value of the random process  $z$  is assumed to be equal to zero. Defining  $\sigma_\ell^2$  as the process variance for the  $\ell$ -th component of the response and  $\mathcal{R}(\theta, w, x)$  as the correlation model with parameters  $\theta$ , the covariance between  $z(w)$  and  $z(x)$  can be computed as follows.

$$E[z_\ell(w)z_\ell(x)] = \sigma_\ell^2 \mathcal{R}(\theta, w, x), \quad \ell = 1, \dots, q\tag{3.3}$$

For the set of design sites the  $m \times p$  design matrix  $\mathbf{F}$ , with  $F_{ij} = f_j(s_i)$ , is written using  $\mathbf{f}(x)$  defined in Equation 3.2.

$$\mathbf{F} = [f(s_1) \quad \dots \quad f(s_m)]^T\tag{3.4}$$

Let us define  $\mathbf{R}$  as the matrix of stochastic process correlations between  $z$ 's at design sites and  $\mathbf{r}(x)$  as the vector of correlations between  $z$ 's at design sites and  $x$ .

$$R_{ij} = \mathcal{R}(\theta, s_i, s_j), \quad i, j = 1, \dots, m\tag{3.5}$$

$$\mathbf{r}(x) = [\mathcal{R}(\theta, s_1, x) \quad \dots \quad \mathcal{R}(\theta, s_m, x)]^T\tag{3.6}$$

In the special case of  $q = 1$ , it follows that  $\beta = \beta_{:,1}$  and  $\mathbf{Y} = \mathbf{Y}_{:,1}$ . Let us consider the following linear predictor.

$$\hat{y}(x) = \mathbf{c}^T \mathbf{Y}\tag{3.7}$$

Considering  $\mathbf{c} = \mathbf{c}(x) \in \mathbb{R}^m$ , the error can be computed defining the vector of errors at the design sites as  $\mathbf{Z} = [z_1 \quad \dots \quad z_m]^T$ . It is subsequently necessary to impose a relation in order to keep the predictor unbiased.

$$\begin{aligned}\hat{y}(x) - y(x) &= \mathbf{c}^T \mathbf{Y} - y(x) \\ &= \mathbf{c}^T (\mathbf{F} \beta + \mathbf{Z}) - (\mathbf{f}(x)^T \beta + z) \\ &= \mathbf{c}^T \mathbf{Z} - z + (\mathbf{F}^T \mathbf{c} - \mathbf{f}(x))^T \beta\end{aligned}\tag{3.8}$$

$$\mathbf{F}^T \mathbf{c}(x) = \mathbf{f}(x)\tag{3.9}$$

The last condition allows us to determine the mean squared error (MSE) of the predictor as

follows.

$$\begin{aligned}
\varphi(x) &= E \left[ (\hat{y}(x) - y(x))^2 \right] \\
&= E \left[ (\mathbf{c}^T \mathbf{Z} - z)^2 \right] \\
&= E \left[ z^2 + \mathbf{c}^T \mathbf{Z} \mathbf{Z}^T \mathbf{c} - 2\mathbf{c}^T \mathbf{Z} z \right] \\
&= \sigma^2 \left( 1 + \mathbf{c}^T \mathbf{R} \mathbf{c} - 2\mathbf{c}^T \mathbf{r} \right)
\end{aligned} \tag{3.10}$$

The constrained minimisation of a functional requires the employment of the Lagrange multipliers, that allow us to define the following Lagrangian function.

$$L(c, \lambda) = \sigma^2(1 + \mathbf{c}^T \mathbf{R} \mathbf{c} - 2\mathbf{c}^T \mathbf{r}) - \lambda^T (\mathbf{F}^T \mathbf{c} - \mathbf{f}) \tag{3.11}$$

Computing and considering the gradient with respect to  $\mathbf{c}$  of Equation 3.11 equal to zero, and defining  $\tilde{\boldsymbol{\lambda}} = -\boldsymbol{\lambda}/2\sigma^2$ , the following system of equations is obtained. This allows for the computation of the estimated response  $\hat{y}$ .

$$\begin{bmatrix} \mathbf{R} & \mathbf{F} \\ \mathbf{F}^T & \mathbf{0} \end{bmatrix} \begin{bmatrix} \mathbf{c} \\ \tilde{\boldsymbol{\lambda}} \end{bmatrix} = \begin{bmatrix} \mathbf{r} \\ \mathbf{f} \end{bmatrix} \tag{3.12}$$

$$\hat{y}(x) = \mathbf{r}^T \mathbf{R}^{-1} \mathbf{Y} - (\mathbf{F}^T \mathbf{R}^{-1} \mathbf{r} - \mathbf{f})^T (\mathbf{F}^T \mathbf{R}^{-1} \mathbf{F})^{-1} \mathbf{F}^T \mathbf{R}^{-1} \mathbf{Y} \tag{3.13}$$

From Equation 3.10 and 3.13, defining  $\mathbf{u} = \mathbf{F}^T \mathbf{R}^{-1} \mathbf{r} - \mathbf{f}$ , the estimated Mean Square Error of the predictor is computed as follows.

$$\varphi(x) = \sigma^2 \left[ 1 + \mathbf{u}^T (\mathbf{F}^T \mathbf{R}^{-1} \mathbf{F})^{-1} \mathbf{u} - \mathbf{r}^T \mathbf{R}^{-1} \mathbf{r} \right] \tag{3.14}$$

For further information see [10, 15, 23, 24, 34].

### 3.3.2 Co-Kriging model

Co-Kriging takes advantage of the correlation between fine and rough model values to improve the interpolation accuracy. As described in [15], let us consider two sets of design sites of dimensions  $d$  relative respectively to cheap and expensive simulators,  $\mathbf{S}_c = [x_1^c \ \dots \ x_{m_c}^c]$  and  $\mathbf{S}_e = [x_1^e \ \dots \ x_{m_e}^e]$ ; the associated values are defined by  $\mathbf{Y}_c = [y_1^c \ \dots \ y_{m_c}^c]$  and  $\mathbf{Y}_e = [y_1^e \ \dots \ y_{m_e}^e]$ . A co-Kriging model can be interpreted as developing two distinct Kriging models in sequence. Firstly, a Kriging model of the rough data ( $\mathbf{S}_c, \mathbf{Y}_c$ ) is defined; subsequently, a second Kriging model is constructed on the residuals of the fine and coarse data ( $\mathbf{S}_e, \mathbf{Y}_d$ ), defining  $\mathbf{Y}_d = \mathbf{Y}_e - \rho \mu_c(\mathbf{S}_e)$ .

Differently to Newton's method, co-Kriging appears ideal to exploit not only converged simulations, but also oscillating ones. Therefore, this method has been used to estimate the zero of mon2 defined as function of relative static pressure. For this reason, simulations with different pressures specified on the outlet surface have been performed; in the following section the criteria employed to distinguish between cheap and expensive values will be explained.

**ooDACE toolbox** Data interpolation has been made by means of *ooDACE toolbox* [17], a Matlab toolbox that implements based Kriging models, created by the Department of Information Technology (INTEC) of the University of Ghent (Belgium). The common employment of this toolbox is to develop a Kriging model of a dataset taken by computer simulations or measurements [15]. The toolbox can be downloaded from [35]; additional information about the ooDACE toolbox is available on [15, 35].

The interpolating curve, defined within the range of values that will be presented in the following section, has been computed using the co-Kriging model and the Matérn correlation function. With regard to the correlation function, the choice has been strongly suggested by [34]: the Matérn correlation function is defined by a parameter that allows for any degree of differentiability for the random field, including the exponential model as a special case and the Gaussian model as a limiting case. As a matter of fact, there is no possibility of knowing a priori the degree of smoothness of a process modelled as a random field; the Matérn model guarantees a great flexibility in the smoothness of the random field, allowing for the degree of smoothness itself to be estimated directly from the data.

### 3.4 Implementation of co-Kriging model

The "Mass flow" simulation has been used to define the value of pressure to specify as boundary condition on the outlet surface in a new simulation; thanks to the fact that in the "Mass flow" case the pressure distribution on the outlet surface was characterised by small variations, as shown in Figure 3.14, the area-averaged pressure has been computed and then employed as boundary condition on the outlet section in the first "pressure" simulation, trusting the possibility to find very similar results in terms of flow field. A pressure equal to 961.228 Pa has been found; the results coming from the new simulation are quite good, both in terms of residuals and of mon2 value. This has allowed us to define the first expensive value to employ in the co-Kriging model, even though the mass flow rate obtained at the end of the computation on the outlet section was not exactly the desired one. In Section 3.6 the comparison between the results obtained in the two simulations will be shown.

In order to create the dataset required for the co-Kriging model, several values of pressure have been imposed on the wind tunnel outlet surface as boundary condition. In particular, the following pressures have been considered: 900 Pa, 1000 Pa, 1050 Pa, 1100 Pa and 1200 Pa. For all the simulations an "Automatic TimeScale" has been chosen, with a "Timescale Factor" of 1.0; this choice has allowed us to obtain comparable results. Results relative to other pressures have been discarded due to very unstable simulations.

As shown in Figure A.3-A.7, in spite of the oscillating trends observed for all the aforementioned pressures, mon2 values can be considered quite consistent with the expected physical trend of the function; however, after a certain pressure mon2 values tend to stabilise around a given value. In order to obtain reliable results, co-Kriging model requires the employment of values coming from stable simulations; for this reason the simulations have been stopped after 500 time-steps, at the beginning of the instability, when the results have started to be not usable any more. The only exception is represented by the "900 Pa" case, whose computation has been terminated after 300 time-steps, since only a small oscillation was present and no additional

iterations were necessary; given the good quality of this case and trusting the possibility of obtaining a fully converged result, another simulation with the same boundary condition on the outlet section has been performed, increasing the number of time-steps to 800. Even though a complete convergence has not been reached (Figure A.1), the satisfying quality of the solution has allowed us to consider this simulation as the source of the second expensive value.

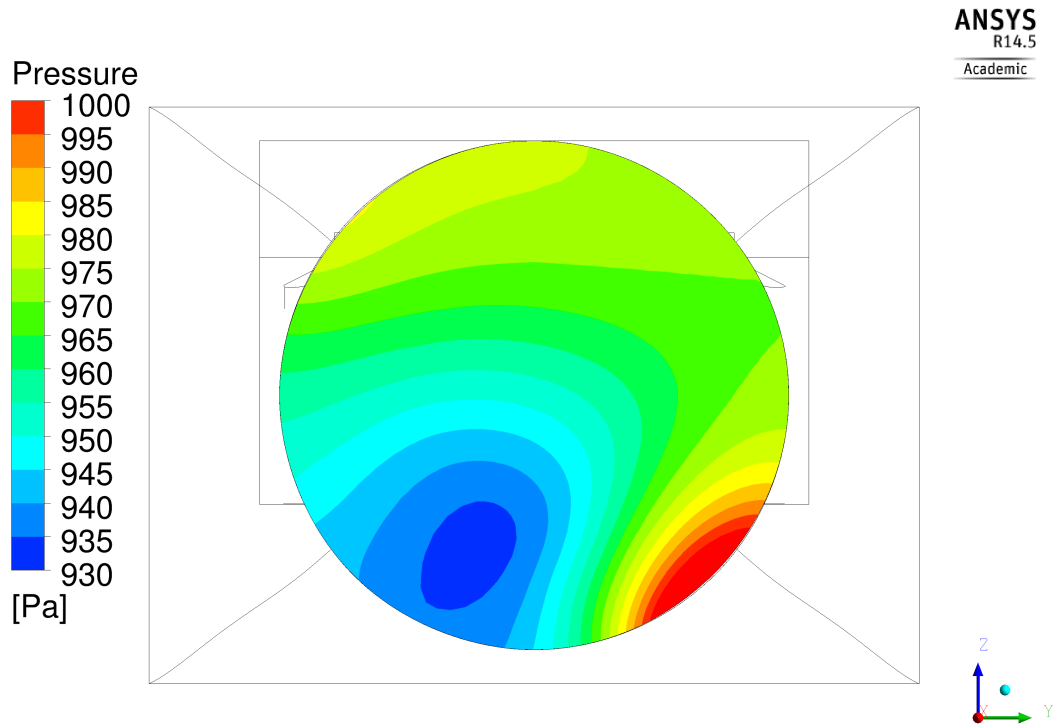


Figure 3.14: Pressure distribution on the wind tunnel outlet section - "Mass flow" simulation

### 3.4.1 "961.228 Pa" case

The "961.228 Pa" simulation has been performed using the results of the "Mass flow" simulation as initial condition. The analysis of convergence is presented in Figure 3.15, 3.16, 3.17; good residuals have been obtained in particular for pressure  $P$  and turbulent frequency  $\omega$ . In Figure 3.17, mon1 is a parameter representing the nett mass flow through the open sections of the wind tunnel test section.

The mon2 value obtained at the end of the simulation is equal to  $-1.511$  kg/s, indicating that a bigger mass flow rate occurs on the outlet compared to the one set on the inlet. Even though the value is not exactly equal to zero, it indicates that the solution of the problem,  $\text{mon2} = 0.0$  kg/s, is anyway close to 961.228 Pa. The solution is expected for a pressure higher than 961.228 Pa, since a lower velocity and, as a consequence, a smaller mass flow rate would be obtained on the outlet section.

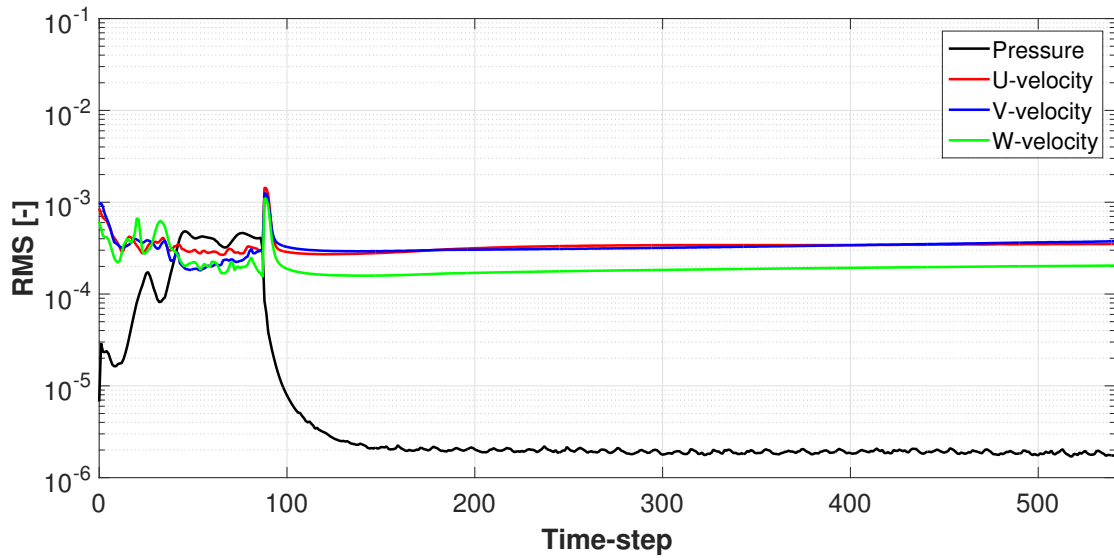


Figure 3.15: Mass and momentum residuals - "961.228 Pa" case

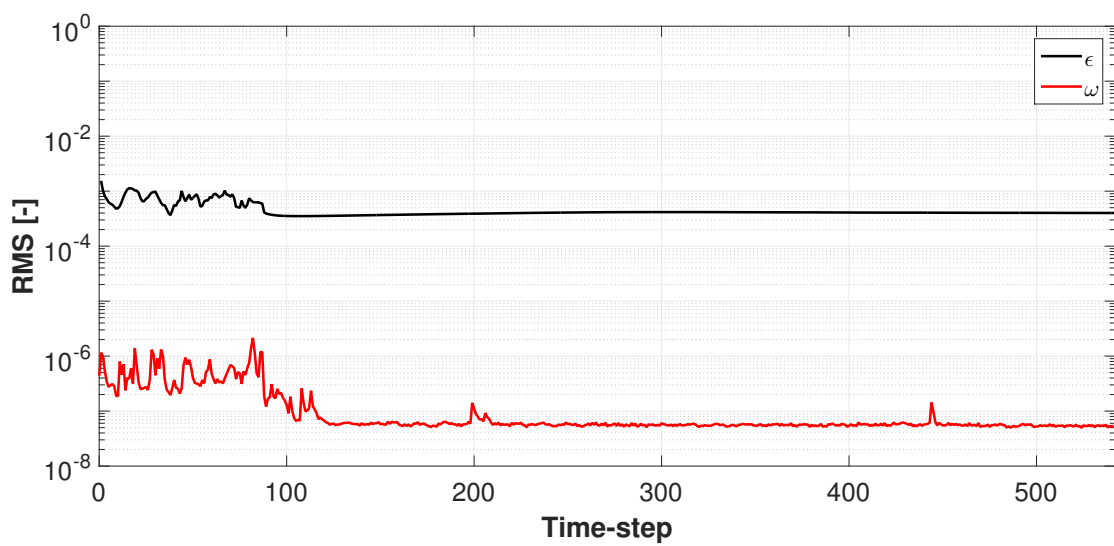


Figure 3.16: Turbulence residuals - "961.228 Pa" case



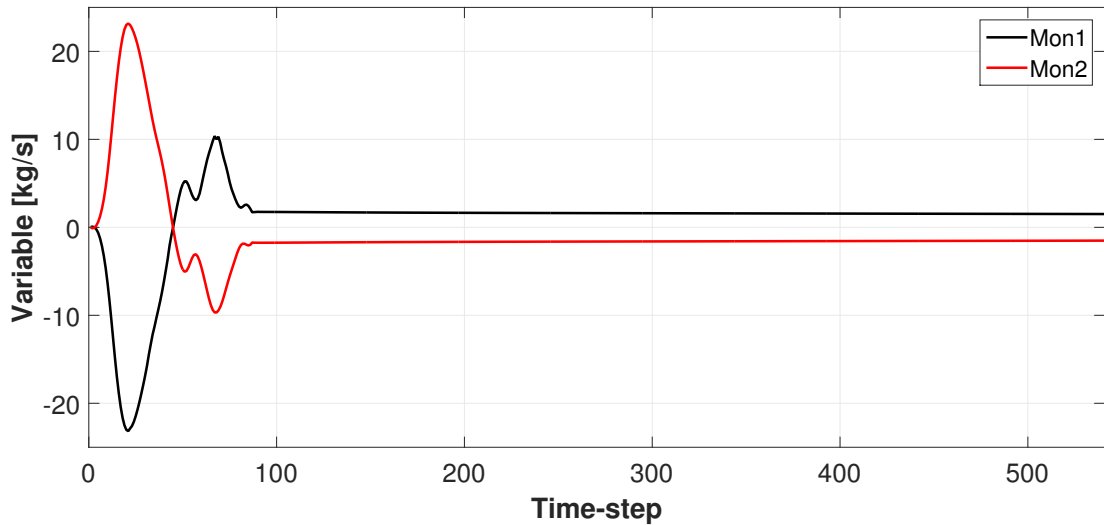


Figure 3.17: Monitor points - "961.228 Pa" case

### 3.4.2 Other cases

The results obtained in the "900 Pa", "1000 Pa", "1050 Pa", "1100 Pa" and "1200 Pa" cases have allowed us to create the dataset required for the co-Kriging model. The distinction between cheap and expensive values to use in the model was made considering not only the stability of the simulations as discriminant for the choice, but also the number of time-steps of the simulations:

- results obtained from simulations with few time-steps or with poor convergence have been considered as cheap values;
- results derived from converged simulations and achieved with a bigger number of time-steps have been taken as expensive values.

On the basis of these considerations and of Figure A.1, A.3-A.7, the "900 Pa" case simulated with a higher number of time-steps has supplied an expensive value, whereas all the other simulations have been used to compute a cheap value.

The oscillation of mon2 has however made the employment of the results related to these simulations difficult. The main problem consisted in finding the most efficient way to use the results inside the co-Kriging model; as a matter of fact, the oscillating trend has made it impossible to consider a single mon2 value for each simulation and, as a consequence, a mean value has been calculated within a range selected considering only oscillations with nearly constant amplitudes.

A disadvantage of the proceeding is represented by the lack of objectiveness in selecting the ranges, given that the lower extreme of the interval is chosen with the purpose of excluding the starting oscillation from the interval itself. For this reason and for the difficulty in using converged results, the analysis performed with the co-Kriging model will only be used to define the region where the solution of the problem is located; an extreme precision of the zero of mon2 obtained by this method cannot be guaranteed. The zero will be investigated and a specific simulation will anyway be conducted in order to check the accuracy of the solution.

Pressure [Pa]	Time-step	
	Min	Max
900	94	800

Table 3.2: Interval - Second expensive value

Pressure [Pa]	Time-step	
	Min	Max
900	94	300
1000	45	500
1050	78	500
1100	78	500
1200	70	500

Table 3.3: Intervals - Cheap values

### 3.4.3 Two expensive values

**Computation of cheap and expensive values** The relation between the number of values employed for the mean value computation and the mean value itself has been studied; for a single simulation, three different mean values have been calculated sampling data at the extremities of, respectively, 5, 10 and 30 intervals of constant amplitude. In addition, a fourth mean value has been computed considering all the values belonging to the entire intervals defined in Table 3.3: since more information is used for the computation, the curves associated to the fourth case will probably be the most accurate and, as a consequence, will be taken as reference. The mean values obtained for the four cases are summarised in the following tables.

Pressure [Pa]	mon2 [kg/s]			
	5 int	10 int	30 int	all values
900	5.478	6.365	4.495	3.763

Table 3.4: Mean values - Second expensive value

Pressure [Pa]	mon2 [kg/s]			
	5 int	10 int	30 int	all values
900	1.997	0.147	0.134	0.119
1000	9.609	9.624	11.776	11.871
1050	65.200	60.045	54.581	55.467
1100	42.028	41.654	46.234	46.445
1200	64.777	51.099	51.989	53.148

Table 3.5: Mean values - Cheap values

**Accuracy of computation** The mean values are strictly dependent on the number of values used in the computation; the dependency becomes stronger at high pressures, over the values at which the instability of the simulations starts. The implementation of the co-Kriging model in all the four cases allows us to define the curves represented in Figure 3.18: they exhibit different trends, as considerable differences are present in the values employed for the computation. However, the differences between the curves are probably mainly caused by the presence of only two expensive values, not sufficiently effective to constrain the correct curve shape.

With regard to the "900 Pa" case, an important consideration must be done both for the cheap and the expensive values. Considering that smaller mass flow rates are expected to correspond to higher pressures and remembering that a mon2 equal to -1.511 kg/s was found in the "961.228 Pa" case, the mean values computed for the "900 Pa" case could lead to inconsistent results, since negative values, lower than -1.511 kg/s, are expected. However, the general trend of the functions defined by the co-Kriging model and, in particular, their zero are probably not too much affected by that.

The four curves are very similar in the interval defined by 900 Pa and 961.228 Pa. However, since the zero of the real function is expected to be found for a pressure a little higher than 961.228 Pa, as previously explained, the curves have to accurately estimate the real function outside the aforementioned interval too. This probably does not occur. As a matter of fact, at high pressures the difference between the curves is of the order of some tens of kg/s, although that between the mean values relative to a given pressure is lower than few units: this leads to think that two expensive values are too little to obtain sufficiently precise results and that an additional expensive value, higher than 961.228 Pa, would force the curves to get closer to the real function. In Figure A.8-A.11 both the cheap and expensive values with the curve obtained are represented; the zeros relative to the four curves are reported in Table 3.6.

Pressure [Pa]	
5 int	974.939
10 int	969.714
30 int	966.004
all values	966.677

Table 3.6: Zero of the curves - Two expensive values

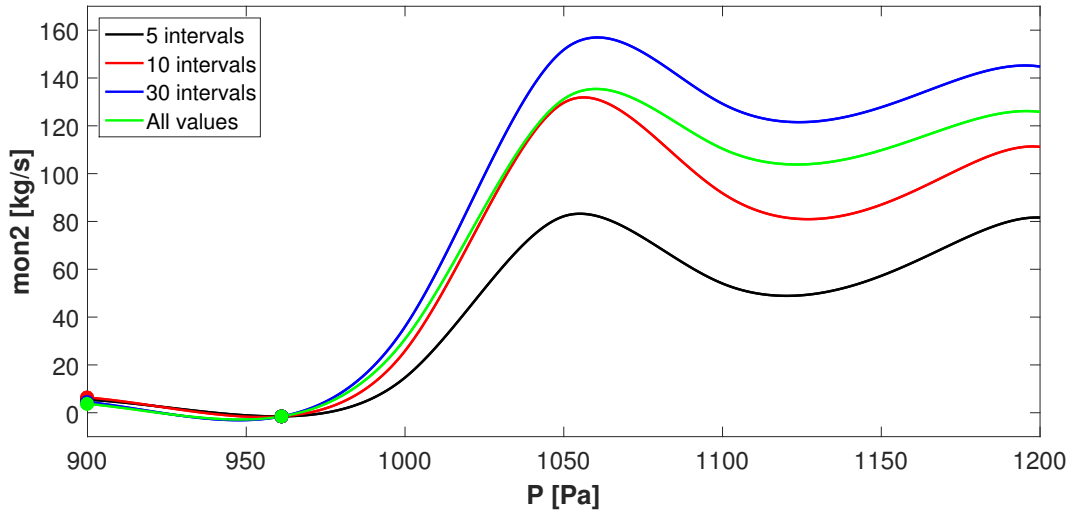


Figure 3.18: Co-Kriging model implementation - 2 expensive values

#### 3.4.4 Three expensive values

The choice of researching and employing another expensive value is rather forced. Given the good quality of the simulation performed in the "1050 Pa" case, the third expensive value has been computed, in the same way as the other values, simulating the "1050 Pa" for 1000 time-steps; the same settings in terms of time scale specified in the previously described simulations have been used. The mon2 trend obtained is shown in Figure A.2. The interval considered and the values of mon2 computed are reported, respectively, in Table 3.7 and in Table 3.8.

Pressure [Pa]	Time-step	
	Min	Max
1050	78	1000

Table 3.7: Interval - Third expensive value

Pressure [Pa]	mon2 [kg/s]			
	5	10	30	all values
1050	46.876	42.452	43.910	45.067

Table 3.8: Mean values - Third expensive value

The curves resulting from the employment of the third expensive value are represented in Figure 3.19: it is clear that the new set of values allows for the definition of curves much more

consistent with the data themselves. In this case the influence of pressure on the mass flow is probably better simulated; the values relative to the last simulation force the curves to increase quite slowly just after the zero of the function and to better follow the cheap values trend (compare Figure A.13-A.16 to Figure A.8-A.11). For these reasons, the reliability of the results obtained employing three expensive values is expected to be significantly greater compared to that achieved with only two expensive values.

Pressure [Pa]	
5 int	980.181
10 int	979.908
30 int	974.567
all values	974.405

Table 3.9: Zero of the curves - Three expensive values

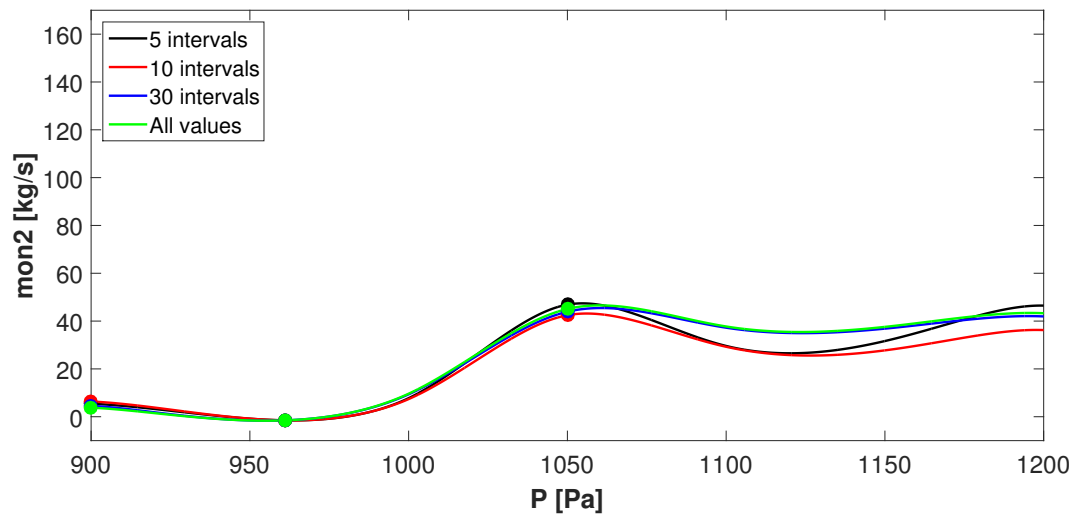


Figure 3.19: Co-Kriging model implementation - 3 expensive values

### 3.5 Final considerations

The result obtained calculating the mean values on the entire interval has been considered as the most reliable, given the greater amount of information employed in the computation. Therefore, a new simulation has then been performed specifying a pressure equal to 974.405 Pa on the wind tunnel outlet section in order to verify the accuracy of the result obtained by the co-Kriging model; the analysis of convergence and the representation of the results relative to this case will be presented in the following sub-section.

Without even taking into consideration this simulation, it is anyway possible to conclude the study performed with the co-Kriging model stating that an acceptable precision of the results

is expected, since the mon2 value computed in the "961.228 Pa" case is very close to zero and obtained by a quite well converged simulation; in this way, the function is forced to pass in the vicinity of the real zero. Moreover, with the employment of the third expensive value, the influence of pressure on the mass flow rate on the outlet section is hopefully better simulated too.

### 3.5.1 "974.405 Pa" case

The "974.405 Pa" simulation has led to a very good result in terms of mon2; with regard to the time scale, a "Physical TimeScale" equal to  $1E-4$  s has been used. The mon2 value at the end of the computation is very close to zero, as expected, even if fully converged results have not been obtained. As a matter of fact, despite the good trend of residuals (Figure 3.20, 3.21) and the close vicinity of mon2 to x-axis, the mon2 trend is anyway slightly oscillating, as shown in Figure 3.22.

The mon2 value obtained at the end of the computation is equal to "0.012" kg/s: given the difficulties encountered in stabilizing the "Pressure" simulations, the result can be considered as very satisfying. More accurate results could even be achieved, using the result obtained by the co-Kriging model as expensive value for the implementation of a new model. In Appendix A pressure and velocity distributions relative to the "974.405 Pa" simulation are compared with those of the "Mass flow" and "961.228 Pa" cases.

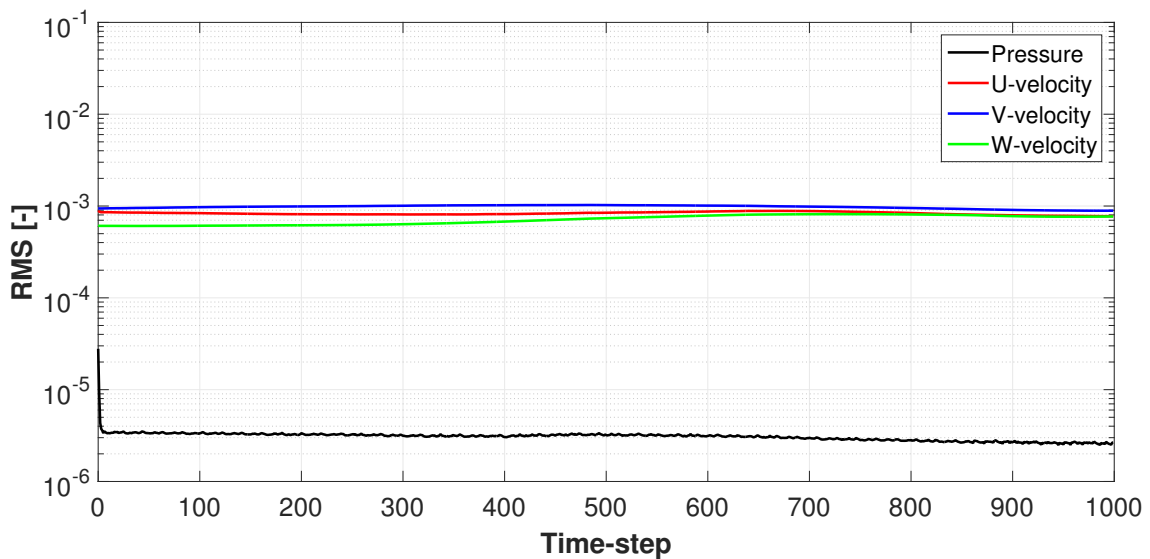


Figure 3.20: Mass and momentum residuals - "974.405 Pa" case

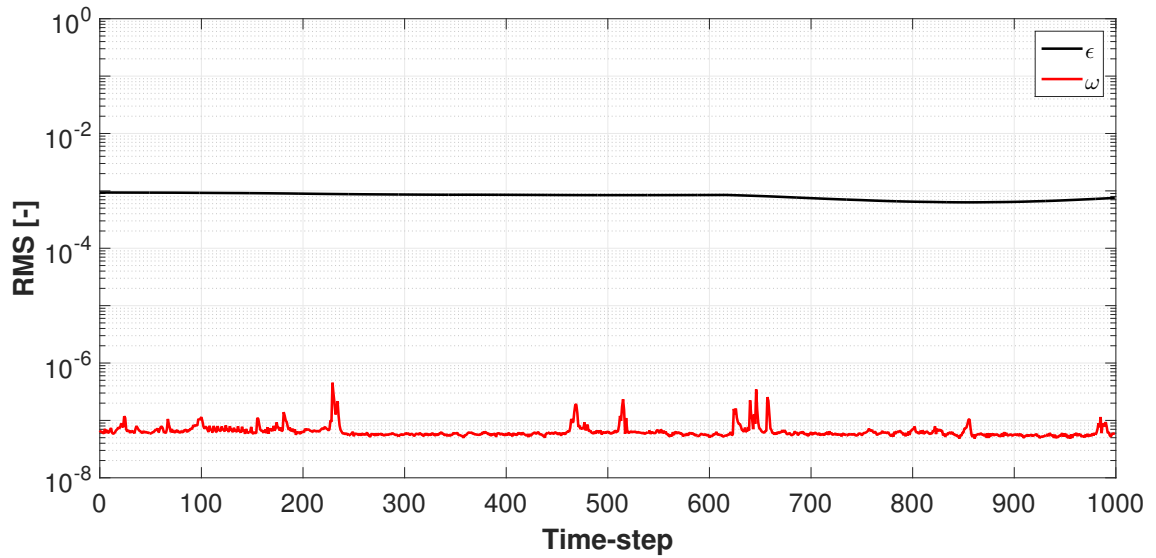


Figure 3.21: Turbulence residuals - "974.405 Pa" case

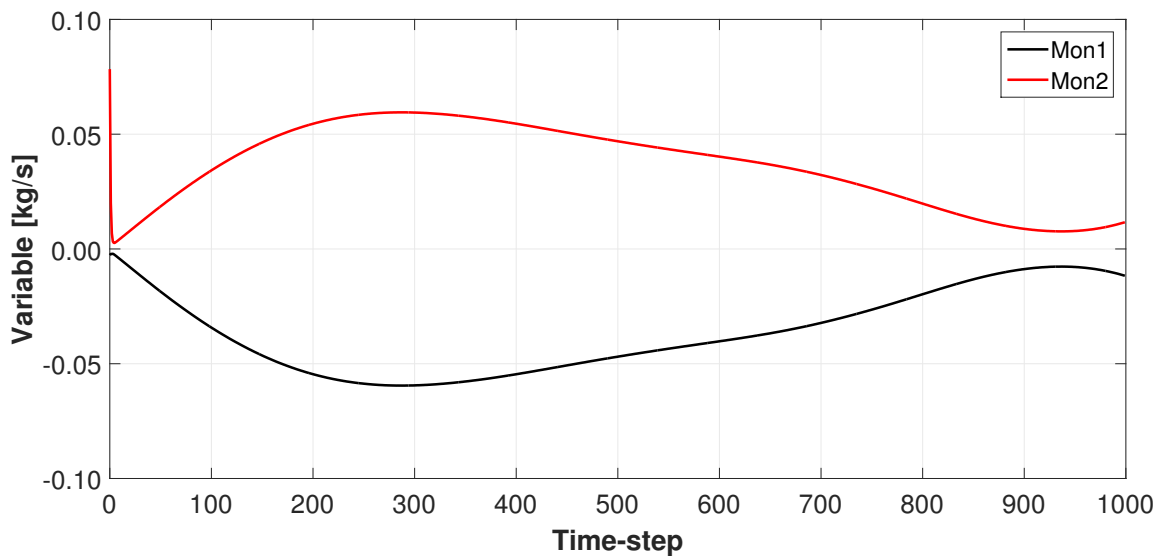


Figure 3.22: Monitor points - "974.405 Pa" case

### 3.6 Comparison between boundary conditions

It is now possible to conclude the analysis of boundary conditions. The final step will concern the contrast between the two approaches described in this chapter. The comparison will involve on the one hand the "Mass flow" boundary condition, with the namesake simulation, and on the other hand the "Pressure" boundary condition, represented by the "961.228 Pa" and the "974.405 Pa" cases. With regard to the "Pressure" boundary condition, "961.228 Pa" and "974.405 Pa" simulations have been considered. The analysis will be conducted with the purpose of determining the most effective approach; in order to perform a complete investigation, the study will concern accuracy, stability and cost of the simulations. Conclusions will be helpful for the proceeding of the work.

### 3.6.1 Accuracy

**Pressure and u-component of velocity** As first comparison, the area-averaged value of pressure and of the u-component of velocity have been considered; the mean values have been evaluated on planes spaced out by 2.50 m (Figure 3.23, 3.24), defined starting from the center of the coordinate system located at the nozzle exit, with regard to a general analysis of the wind tunnel, and on planes spaced out by 0.25 m (Figure 3.25, 3.26) for a more specific study on the wind tunnel test section. See Figure B.1, B.2 for an overview of the planes considered. "961.228 Pa"

**General investigation** The distributions of pressure are in good agreement, except in proximity of  $x = 7.50$  m and in the interval between  $x = 12.50$  m and  $x = 25.00$  m. In this region, the "Mass flow" simulation exhibits an extended area of separated flow, caused by a significant adverse gradient of pressure; the same pressure trend occurs also in the "974.405 Pa" case, unlike the "961.228 Pa" one, where a slighter gradient of pressure causes a smaller recirculation area, both along the x and the z-direction. It follows that, in the "961.228 Pa" simulation, the pressure significantly increases, unlike the other two cases, in which only a slight pressure growth occurs. The region of separated flow relative to the three simulations can be seen in Figure B.13, B.14, B.15, where the distribution of the u-component of velocity on the plane located at  $y = 0.00$  m is shown.

In order to explain the pressure differences within the aforementioned regions, the distributions of pressure and u-component of velocity on two planes positioned at  $x = 7.50$  m and  $x = 20.00$  m are analysed in Appendix B (Figure B.22-B.33).

The distribution of the u-component of velocity along the wind tunnel is also very similar in the three cases. A specific comment on the wind tunnel test section will be provided in the following sub-paragraph.

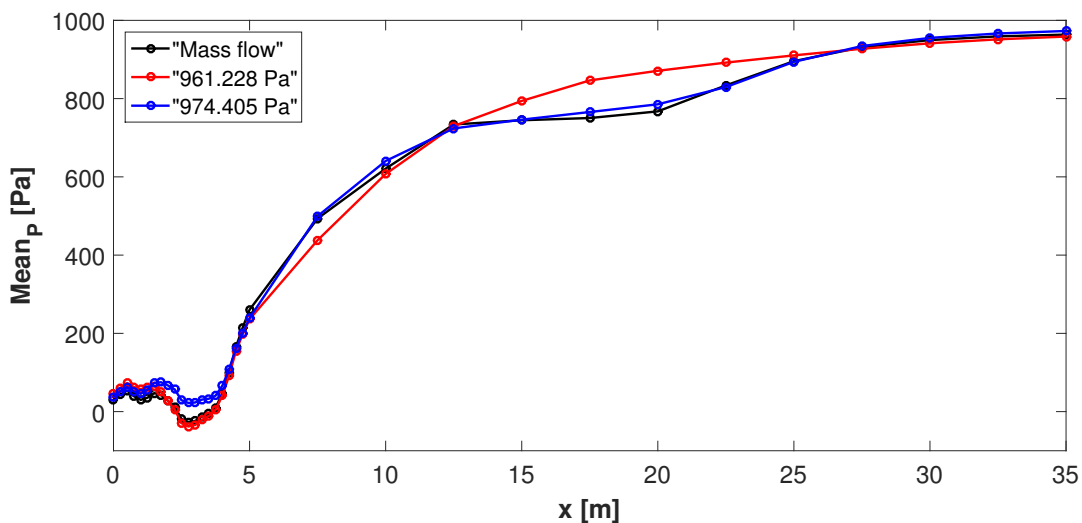


Figure 3.23: Pressure distribution - General investigation



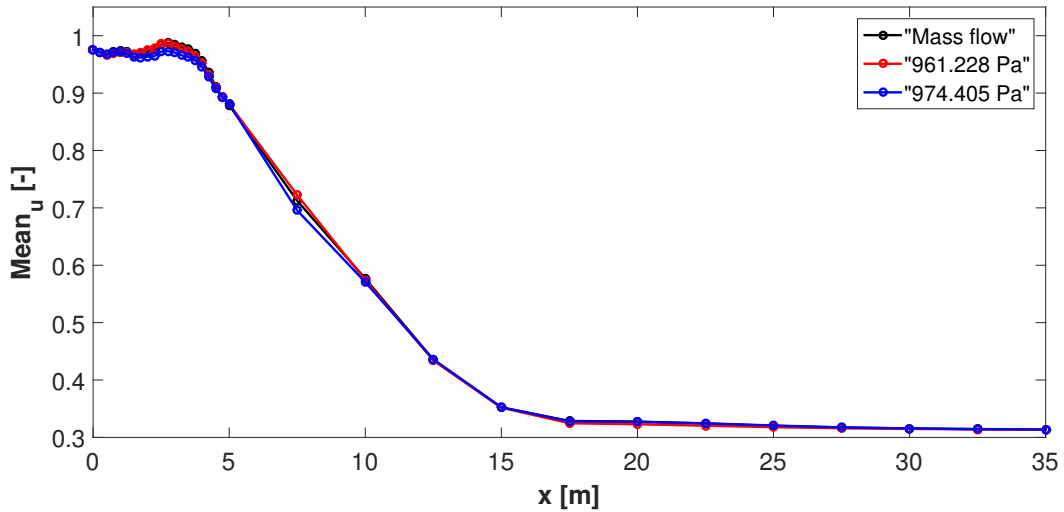


Figure 3.24: Velocity u-component distribution - General investigation

**Test section investigation** With regard to the analysis focused on the wind tunnel test section, the comparison is shown in Figure 3.25, 3.26. Within the test section, the differences between the curves relative to the pressure distribution are small. However, in this case, a more in-depth investigation is conducted for evaluating the similarity of the results. The approach followed is the analysis of pressure coefficient.

As for the general investigation, the distribution of pressure and u-component of velocity on the plane located at  $x = 2.50$  m, where the biggest discrepancy between the curves is present, is studied in Appendix B (Figure B.16-B.21).

An analogous consideration can be made for the u-velocity distribution; only a small deviation is found in the region included between  $x = 1.50$  m and  $x = 4.00$  m, where the helicopter section is located, in the "974.405 Pa" simulation. This is shown in Figure 3.26.

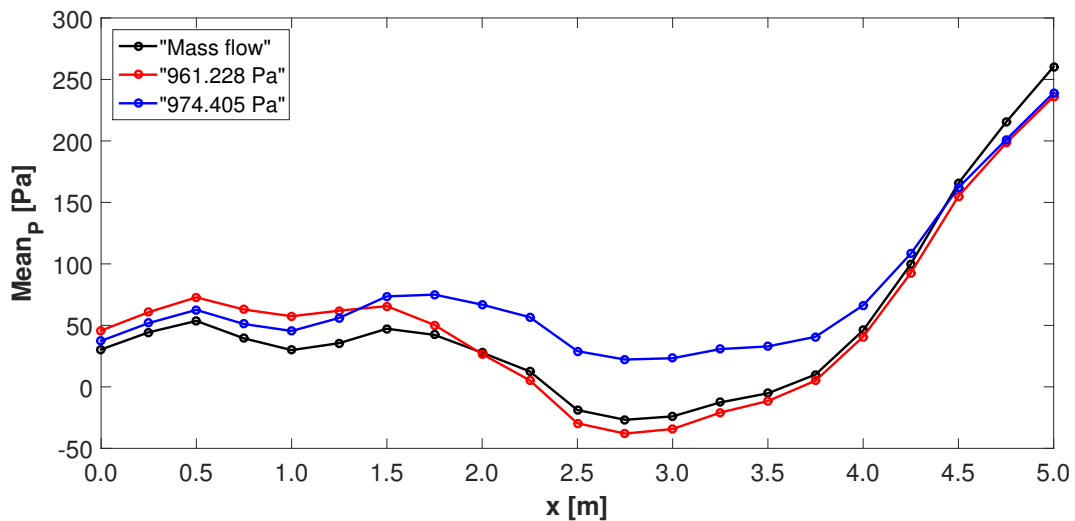


Figure 3.25: Pressure distribution - Test section investigation

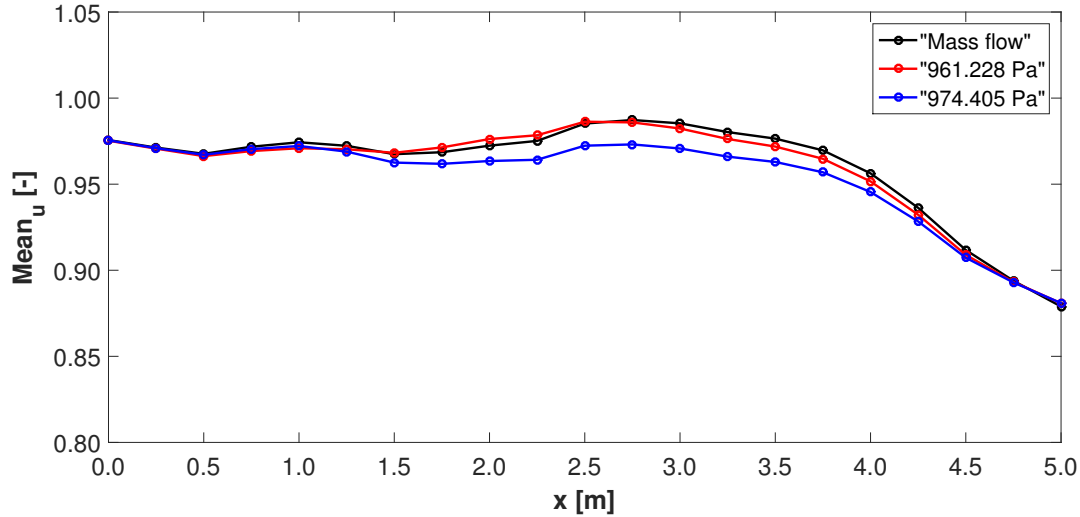


Figure 3.26: Velocity u-component distribution - Test section investigation

**Pressure coefficient** The pressure coefficient is computed using the mean dynamic pressure measured at the nozzle exit as reference.

$$C_p = \frac{p - p_{ref}}{q_{ref}} \quad (3.15)$$

In Figure 3.27-3.30 the pressure coefficient,  $C_p$ , and the difference of the same coefficient,  $\Delta C_p$ , with respect to the "Mass flow" case are represented. Obviously, the distribution of pressure coefficient is very similar to the relative static pressure one. As shown in Figure 3.28, 3.30, the  $\Delta C_p$  is in general very small; this means that relative static pressures are very similar in comparison with the reference dynamic pressure. However, it is important to highlight that in the "961.228 Pa" case the difference is smaller within the test section, unlike the rest of the wind tunnel, where it assumes higher values; the opposite occurs in the "974.405 Pa" case.

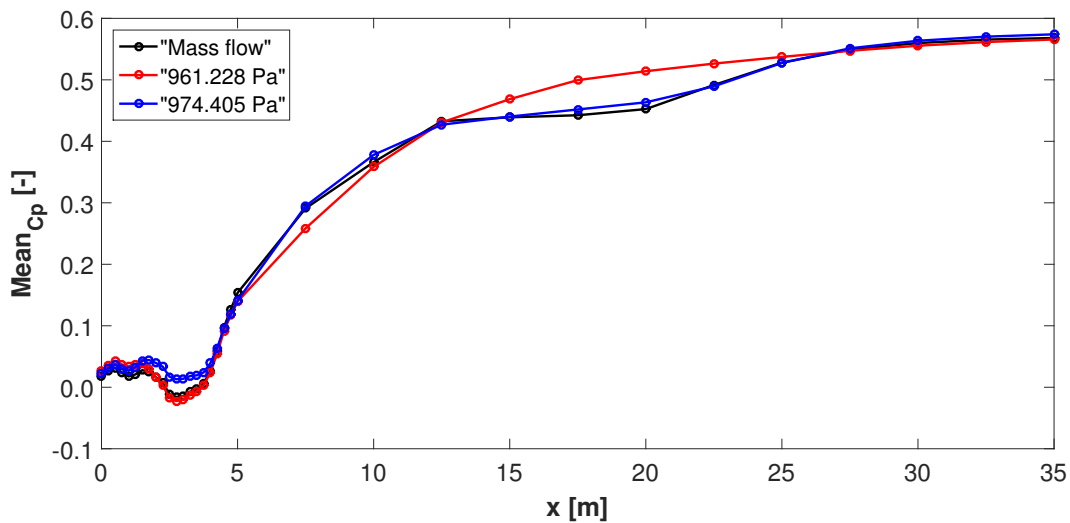
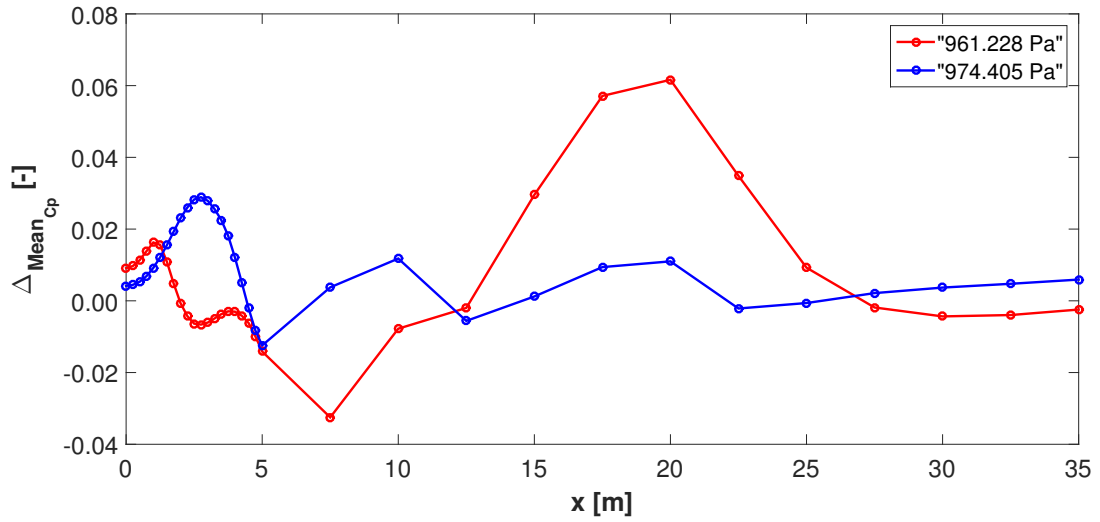
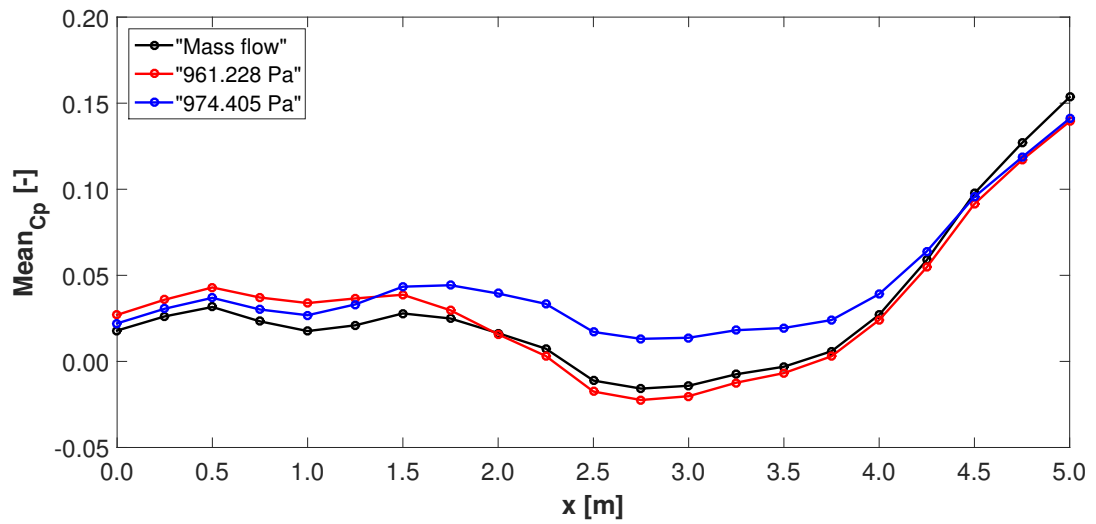


Figure 3.27:  $C_p$  distribution - General investigation

Figure 3.28:  $\Delta C_p$  - General investigationFigure 3.29:  $C_p$  distribution - Test section investigation

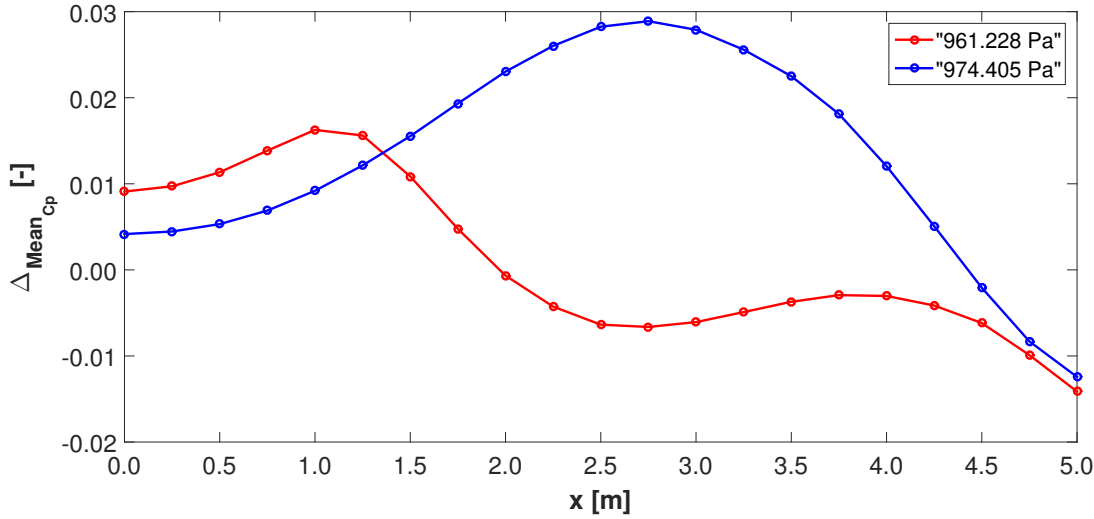


Figure 3.30:  $\Delta C_p$  - Test section investigation

**Forces and moments** The analysis of the simulations' accuracy is completed considering forces and moments acting on the surface of the helicopter geometry. Each single part of the helicopter surface has been analysed; the term "Cover" refers to the fairing employed to close the engine air intake. In Table 3.10-3.15 the values obtained are presented; in this study forces and moments are taken into analysis by means of dimensionless coefficients, computed as the ratio to the dynamic pressure of reference and to the helicopter projected surface; with regard to moments, a unitary length has been taken as reference for the computation.

The percentage variation is computed in comparison with the "Mass flow" simulation. With regard to the "961.228 Pa" case, the difference is generally lower than 20%, showing good similarity of results in the two cases; the biggest discrepancies are found on the rear part of the helicopter, on the "Exhaust" in particular. As a general conclusion about the "961.228 Pa" case, forces and moments acting on the helicopter section are similar compared to those of the "Mass flow" simulation.

Higher percentage variations occur in the "974.405" case. The most significant are found on the cabin and on cowling fore part; on the contrary, very similar forces and moments are computed on the mast fairing and on the cowling rear part. The values relative to a given force or moment are considerably more variable in this simulation, in terms of both sign and value; therefore, pressure distribution around the helicopter surface is expected to somehow differ compared to the other two simulations, in the front side of the helicopter especially, as Figure B.42 shows. Actually, it is possible to come to the same conclusion by observing Figure 3.28, 3.30, in which it is shown that  $\Delta C_p$  maximum is in proximity of the helicopter surface for the "974.405 Pa" case.

<b>Part</b>	<b>"Mass flow"</b>	<b>"961.228 Pa"</b>	<b>"974.405 Pa"</b>
Cabin	1.960 E-3	2.174 E-3	1.693 E-3
Cowling (fore)	1.354 E-3	1.442 E-3	1.756 E-3
Cowling (rear)	-4.030 E-3	-3.763 E-3	-4.185 E-3
Exhaust	-0.736 E-3	-0.497 E-3	-0.673 E-3
Mast fairing	1.345 E-3	1.477 E-3	1.328 E-3
Cover	1.184 E-3	1.376 E-3	1.024 E-3
<b>Total</b>	1.076 E-3	2.209 E-3	0.944 E-3

Table 3.10:  $C_{Fx}$  - X-force coefficient

<b>Part</b>	<b>"Mass flow"</b>	<b>"961.228 Pa"</b>	<b>"974.405 Pa"</b>
Cabin	-6.767 E-3	-6.736 E-3	-4.948 E-3
Cowling (fore)	1.994 E-3	2.080 E-3	1.360 E-3
Cowling (rear)	0.548 E-3	0.389 E-3	0.491 E-3
Exhaust	-0.302 E-3	-0.489 E-3	-0.380 E-3
Mast fairing	4.770 E-3	4.982 E-3	4.659 E-3
Cover	-2.499 E-3	-2.191 E-3	-2.837 E-3
<b>Total</b>	-2.257 E-3	-1.965 E-3	-1.654 E-3

Table 3.11:  $C_{Fy}$  - Y-force coefficient

<b>Part</b>	<b>"Mass flow"</b>	<b>"961.228 Pa"</b>	<b>"974.405 Pa"</b>
Cabin	10.290 E-3	8.417 E-3	3.666 E-3
Cowling (fore)	6.632 E-3	6.883 E-3	4.094 E-3
Cowling (rear)	-10.714 E-3	-9.953 E-3	-11.159 E-3
Exhaust	-2.159 E-3	-1.485 E-3	-2.013 E-3
Mast fairing	18.388 E-3	19.601 E-3	16.686 E-3
Cover	15.840 E-3	17.890 E-3	12.679 E-3
<b>Total</b>	38.278 E-3	41.350 E-3	23.953 E-3

Table 3.12:  $C_{Fz}$  - Z-force coefficient

<b>Part</b>	<b>"Mass flow"</b>	<b>"961.228 Pa"</b>	<b>"974.405 Pa"</b>
Cabin	-3.060 E-3	-2.461 E-3	-1.212 E-3
Cowling (fore)	1.068 E-3	1.105 E-3	0.669 E-3
Cowling (rear)	-0.442 E-3	-0.443 E-3	-0.464 E-3
Exhaust	-0.209 E-3	-0.142 E-3	-0.193 E-3
Mast fairing	11.202 E-3	11.987 E-3	10.135 E-3
Cover	0.207 E-3	0.314 E-3	0.008 E-3
<b>Total</b>	<b>8.767 E-3</b>	<b>10.361 E-3</b>	<b>8.944 E-3</b>

Table 3.13:  $C_{M_x}$  - X-moment coefficient

<b>Part</b>	<b>"Mass flow"</b>	<b>"961.228 Pa"</b>	<b>"974.405 Pa"</b>
Cabin	-26.229 E-3	-24.081 E-3	-11.674 E-3
Cowling (fore)	-22.110 E-3	-22.984 E-3	-15.619 E-3
Cowling (rear)	47.972 E-3	44.655 E-3	49.929 E-3
Exhaust	9.915 E-3	6.616 E-3	9.172 E-3
Mast fairing	-50.189 E-3	-53.756 E-3	-45.354 E-3
Cover	-56.124 E-3	-63.715 E-3	-44.799 E-3
<b>Total</b>	<b>-96.767 E-3</b>	<b>-113.403 E-3</b>	<b>-58.346 E-3</b>

Table 3.14:  $C_{M_y}$  - Y-moment coefficient

<b>Part</b>	<b>"Mass flow"</b>	<b>"961.228 Pa"</b>	<b>"974.405 Pa"</b>
Cabin	-12.973 E-3	-12.962 E-3	-8.169 E-3
Cowling (fore)	7.431 E-3	7.827 E-3	5.813 E-3
Cowling (rear)	2.666 E-3	1.977 E-3	2.425 E-3
Exhaust	-1.567 E-3	-2.554 E-3	-1.969 E-3
Mast fairing	12.534 E-3	13.124 E-3	12.185 E-3
Cover	-9.094 E-3	-8.085 E-3	-10.343 E-3
<b>Total</b>	<b>-1.004 E-3</b>	<b>-0.673 E-3</b>	<b>-0.060 E-3</b>

Table 3.15:  $C_{M_z}$  - Z-moment coefficient

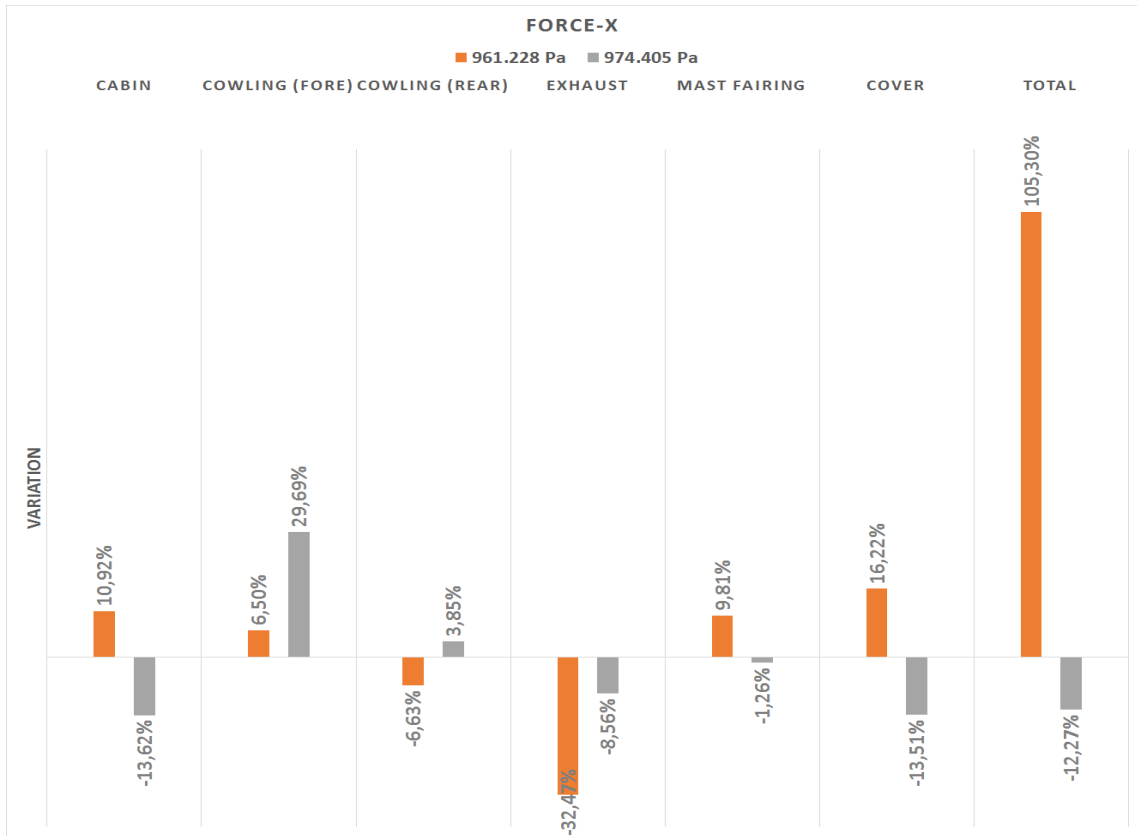


Figure 3.31: Percentage variation of forces - X-axis



Figure 3.32: Percentage variation of forces - Y-axis

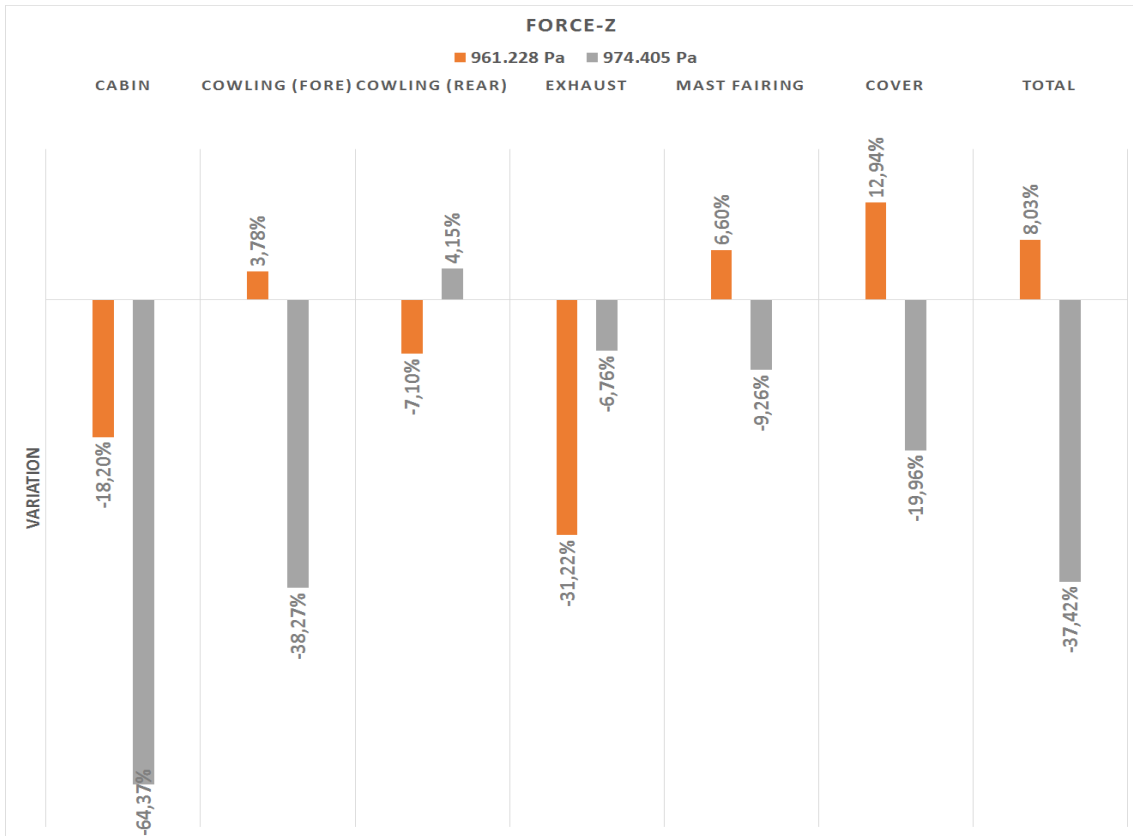


Figure 3.33: Percentage variation of forces - Z-axis

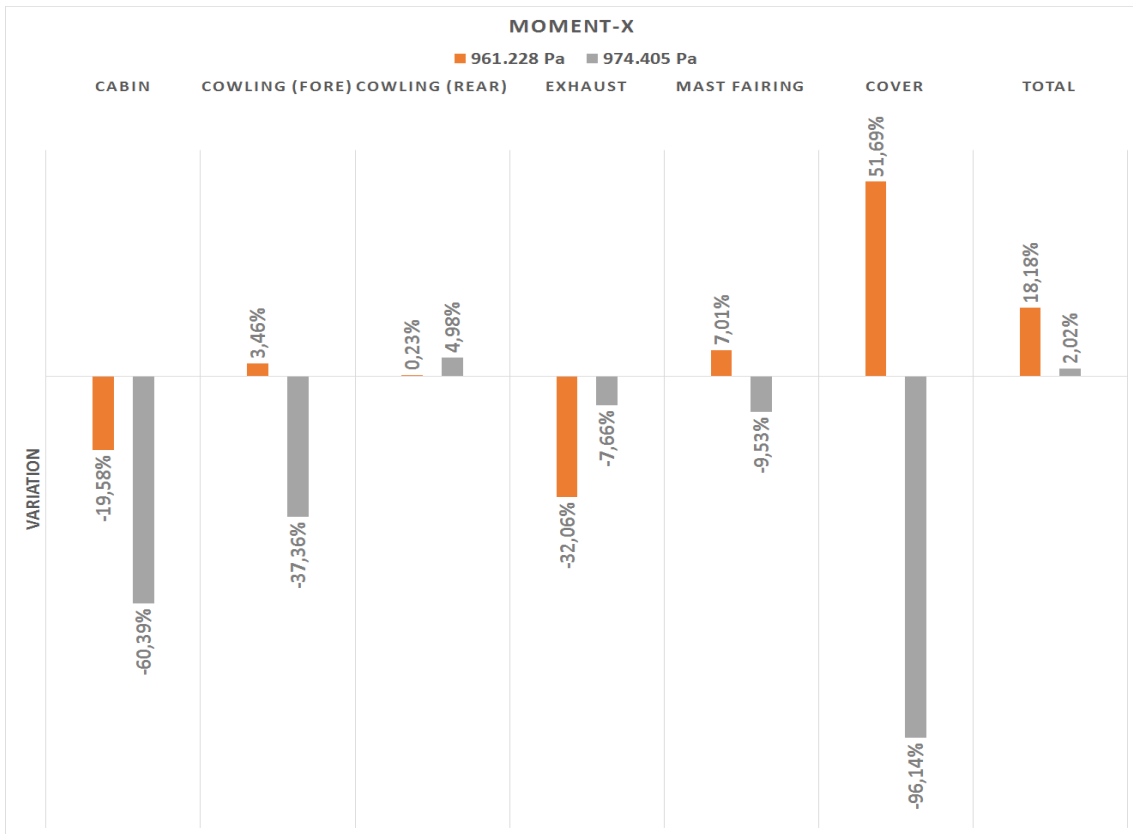


Figure 3.34: Percentage variation of moments - X-axis



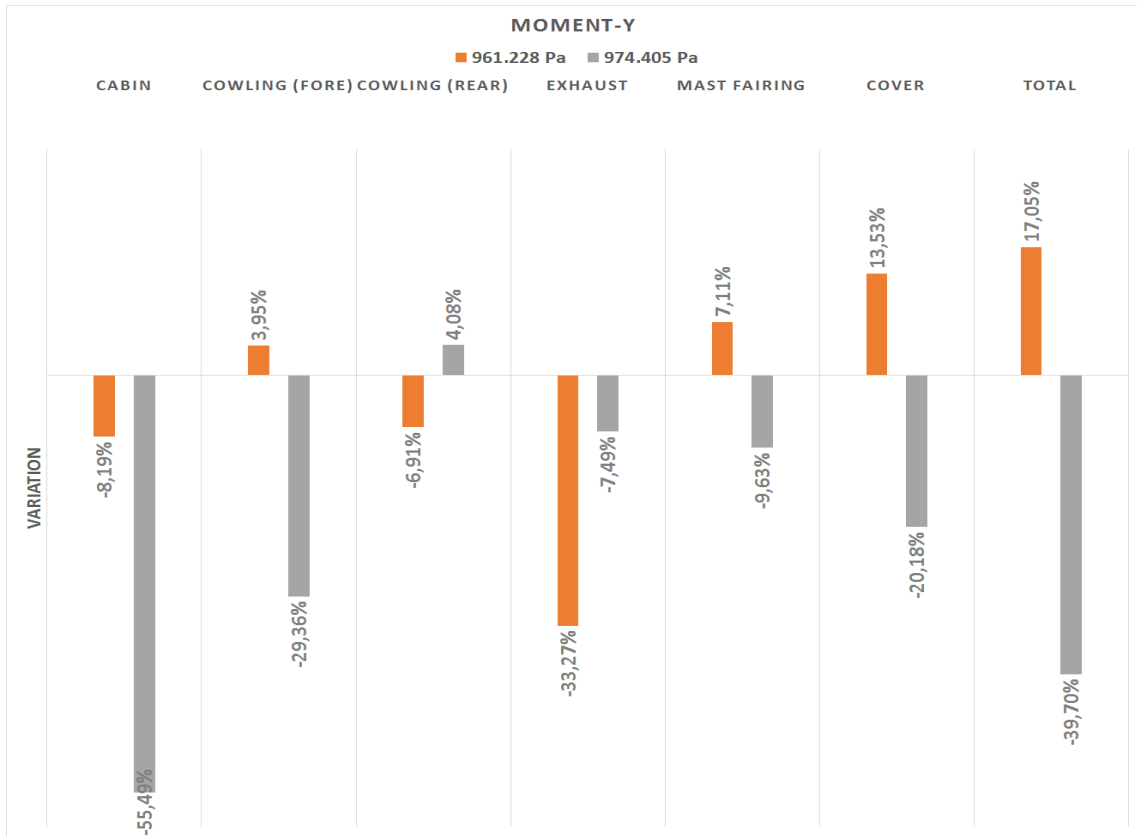


Figure 3.35: Percentage variation of moments - Y-axis

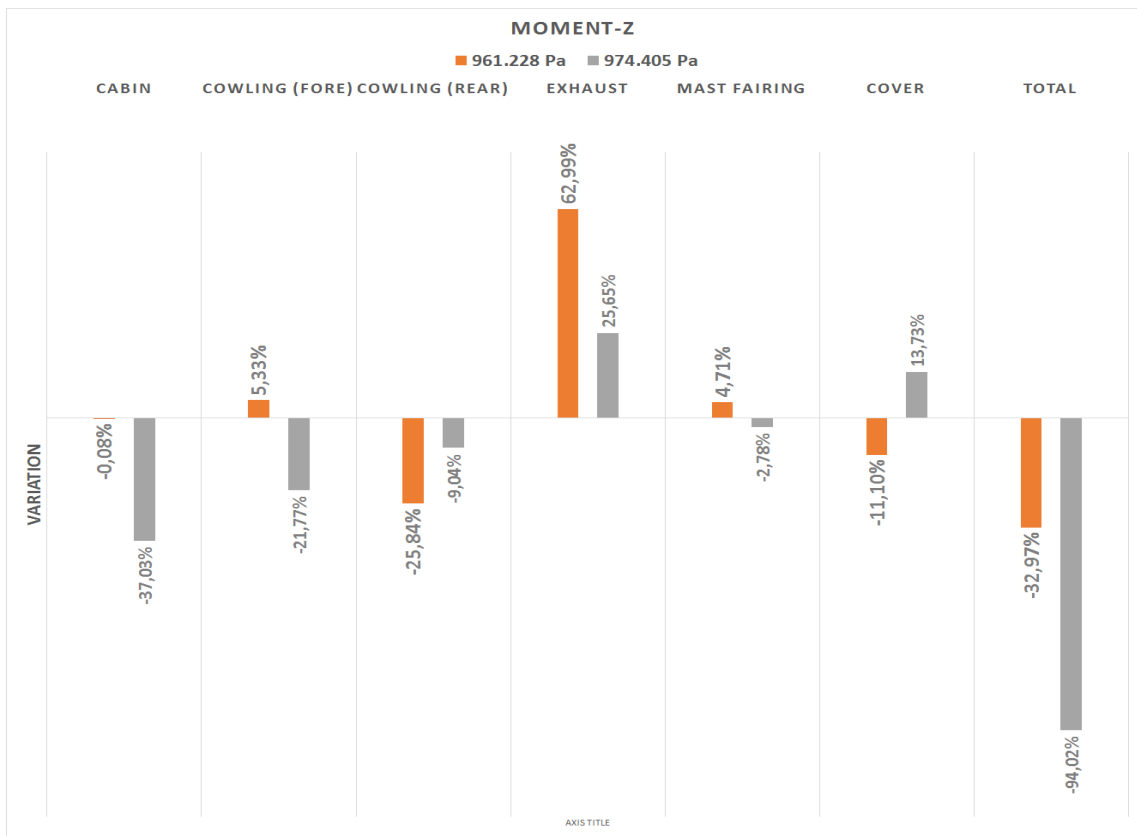


Figure 3.36: Percentage variation of moments - Z-axis

**Flow structure** It is clear that the flow field simulated within the test section in the "974.405 Pa" case shows greater differences compared to the "Mass flow" case, than in the "961.228 Pa" one. The pressure distributions on the helicopter surface are very similar in the three simulations, as shown in Figure B.40, B.41, B.42, even though both the "961.228 Pa" and the "974.405 Pa" cases exhibit small differences in force and moment distributions that are better evaluable in Figure 3.31-3.36. The distributions of pressure and u-component of velocity inside the test section differentiate as well, as seen in Figure 3.23-3.30 and in Figure B.16-B.21.

However, it is still not clear why this occurs. For this reason, the flow structure will be analysed by means of Figure 3.37-3.45; only the test section of the wind tunnel will be considered, since, for the purposes of the present work, the accuracy of flow field assumes greater importance within the test section than in the other parts of the wind tunnel. Subsequently, the v and the w-component of velocity will be analysed using Figure 3.46-3.49. The curves are defined computing the mean values on some planes cutting the helicopter geometry along the x and the z-direction. See Figure B.1, B.3 in Appendix B for a better comprehension.

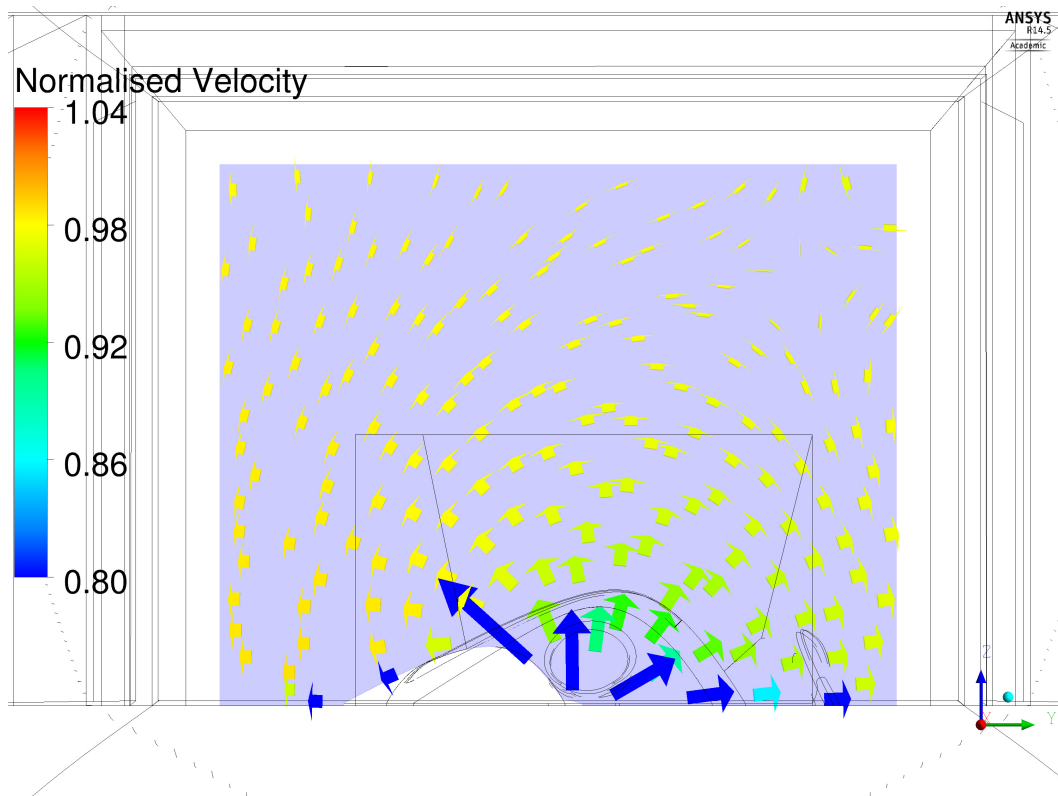
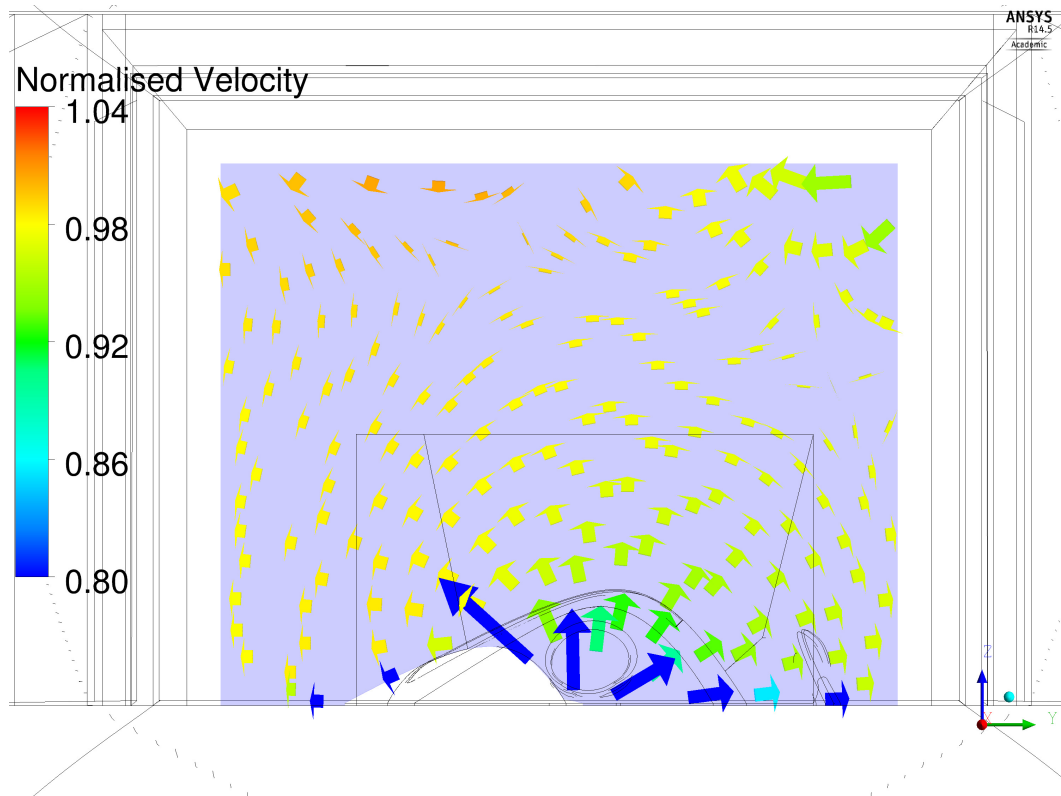
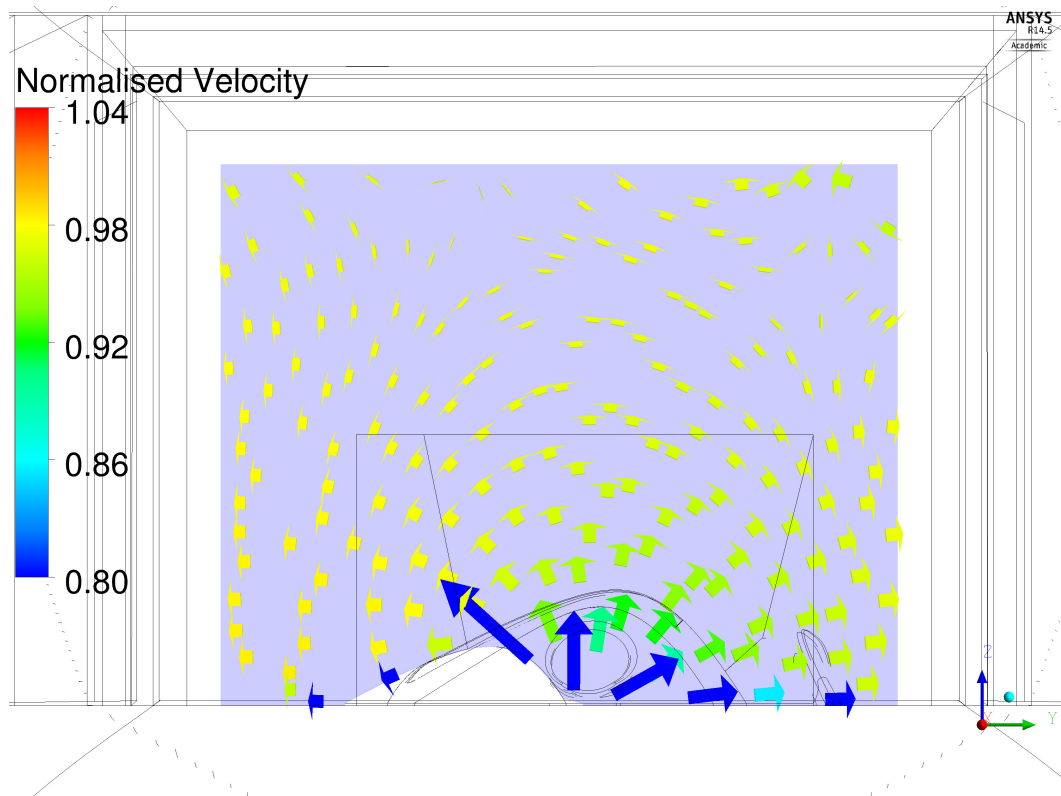


Figure 3.37: Velocity vectors at  $x = 1.50$  m - "Mass flow" case

Figure 3.38: Velocity vectors at  $x = 1.50$  m - "961.228 Pa" caseFigure 3.39: Velocity vectors at  $x = 1.50$  m - "974.405 Pa" case

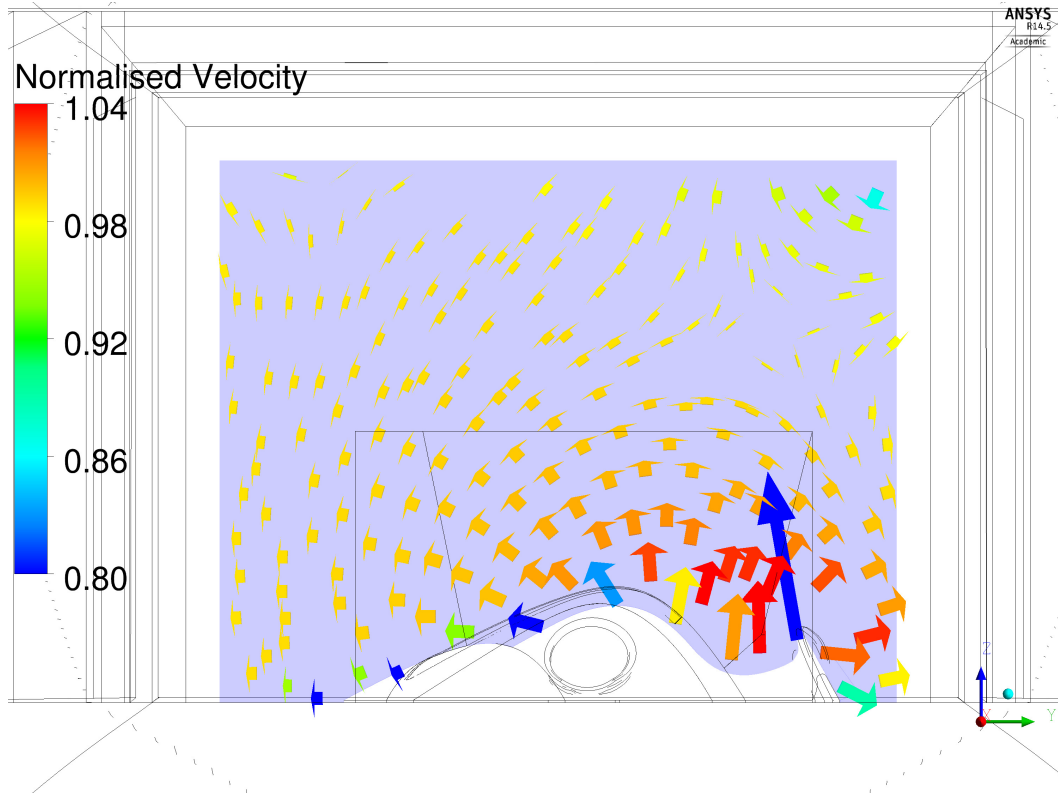


Figure 3.40: Velocity vectors at  $x = 2.50$  m - "Mass flow" case

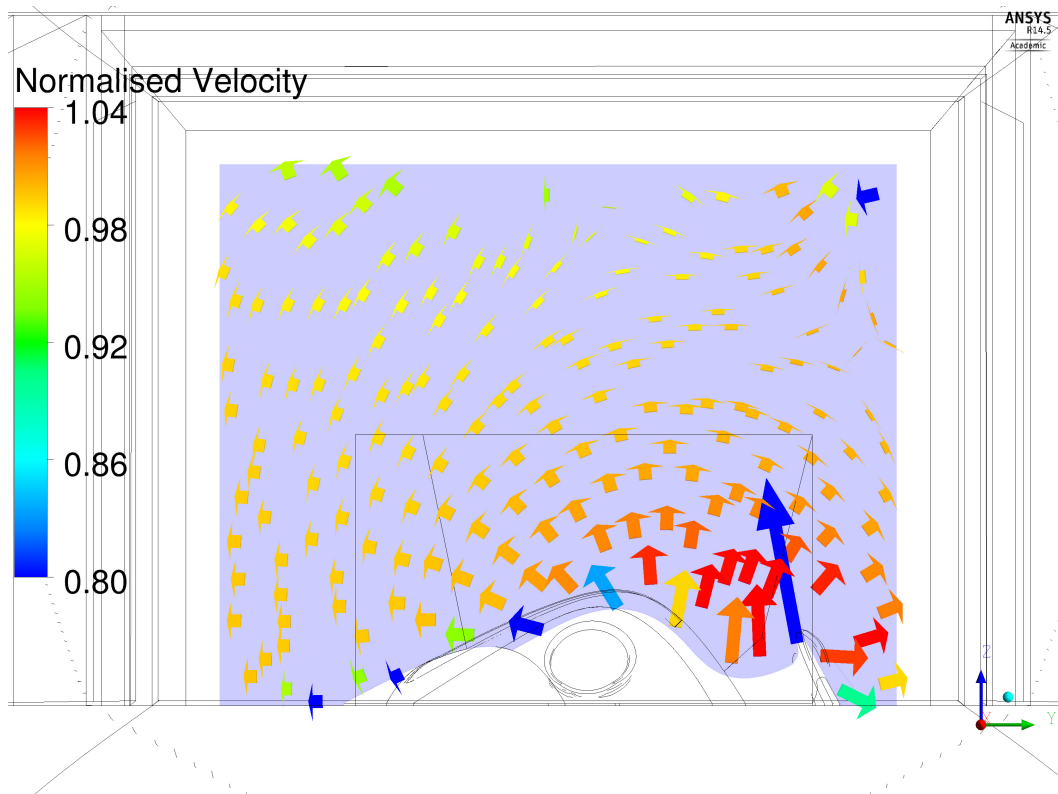
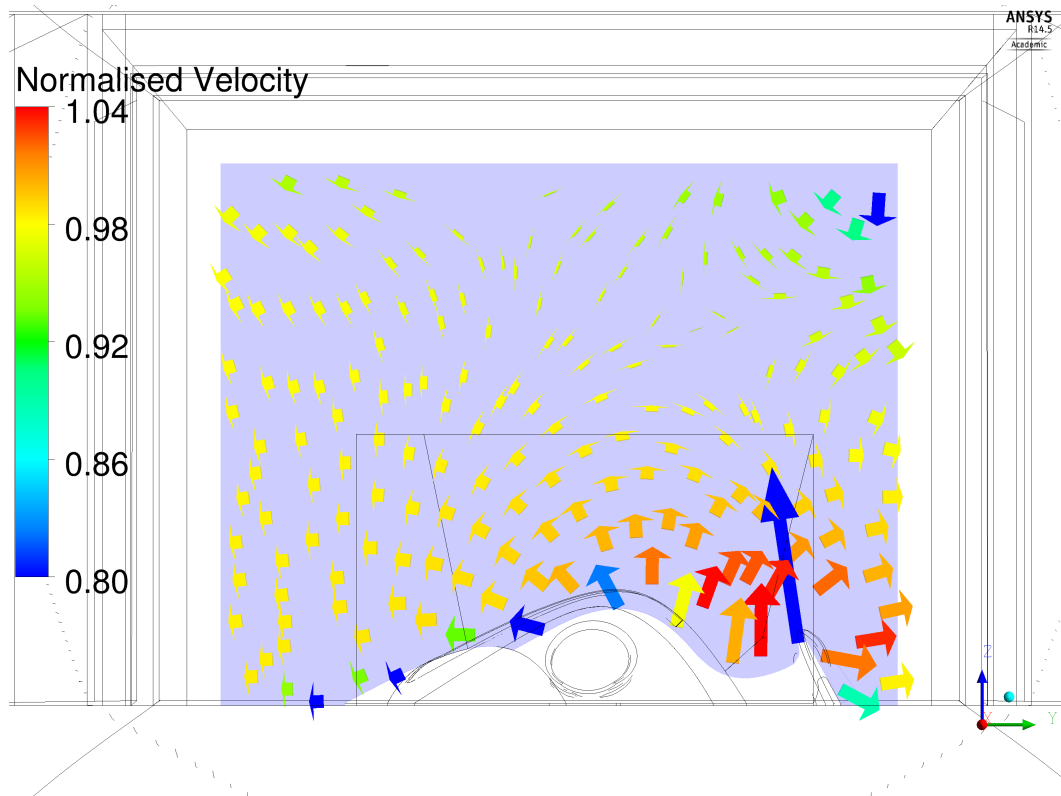
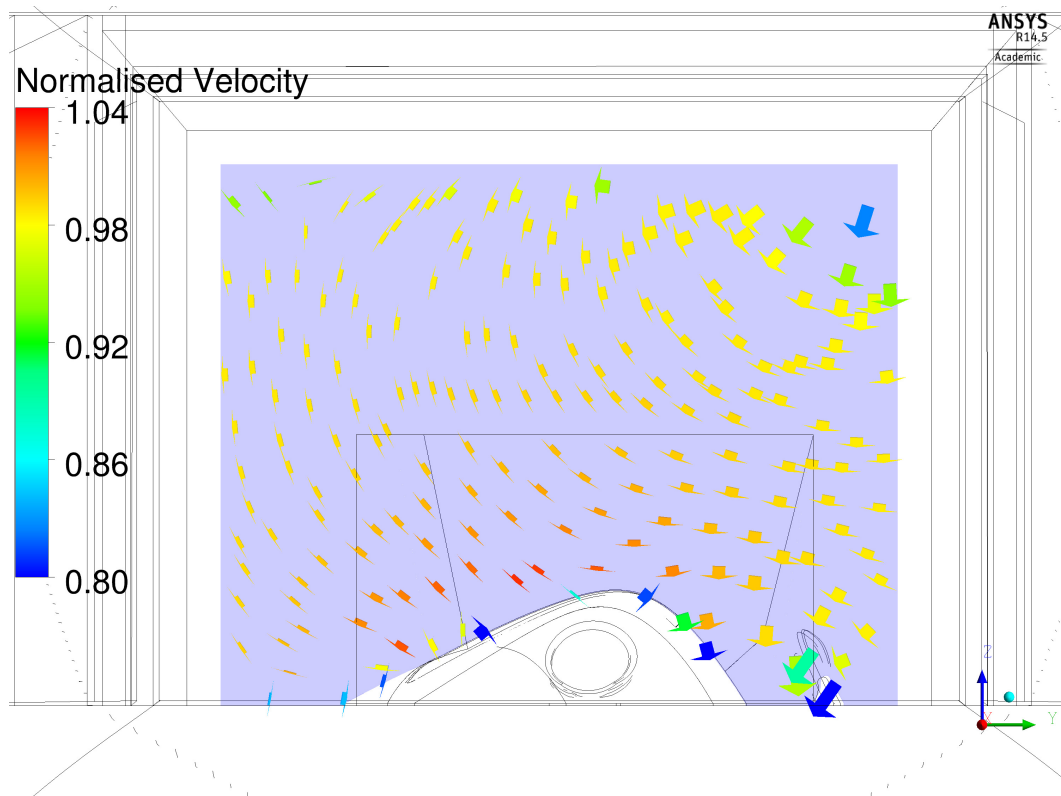


Figure 3.41: Velocity vectors at  $x = 2.50$  m - "961.228 Pa" case

Figure 3.42: Velocity vectors at  $x = 2.50$  m - "974.405 Pa" caseFigure 3.43: Velocity vectors at  $x = 3.50$  m - "Mass flow" case

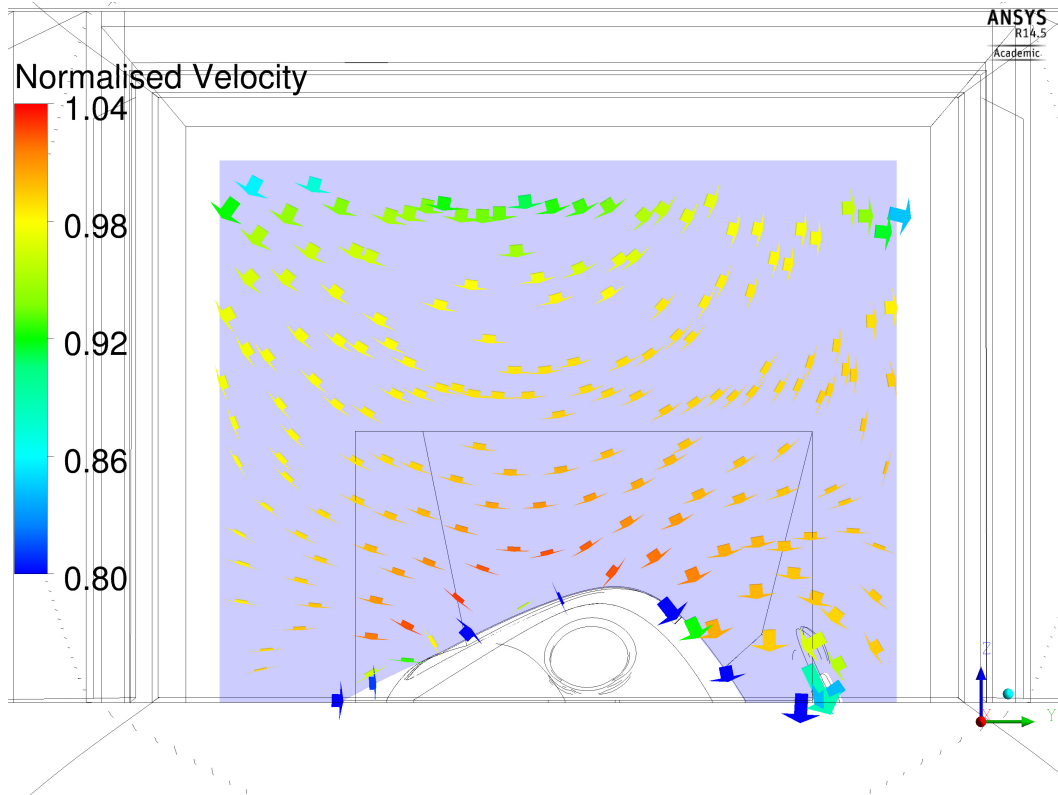


Figure 3.44: Velocity vectors at  $x = 3.50$  m - "961.228 Pa" case

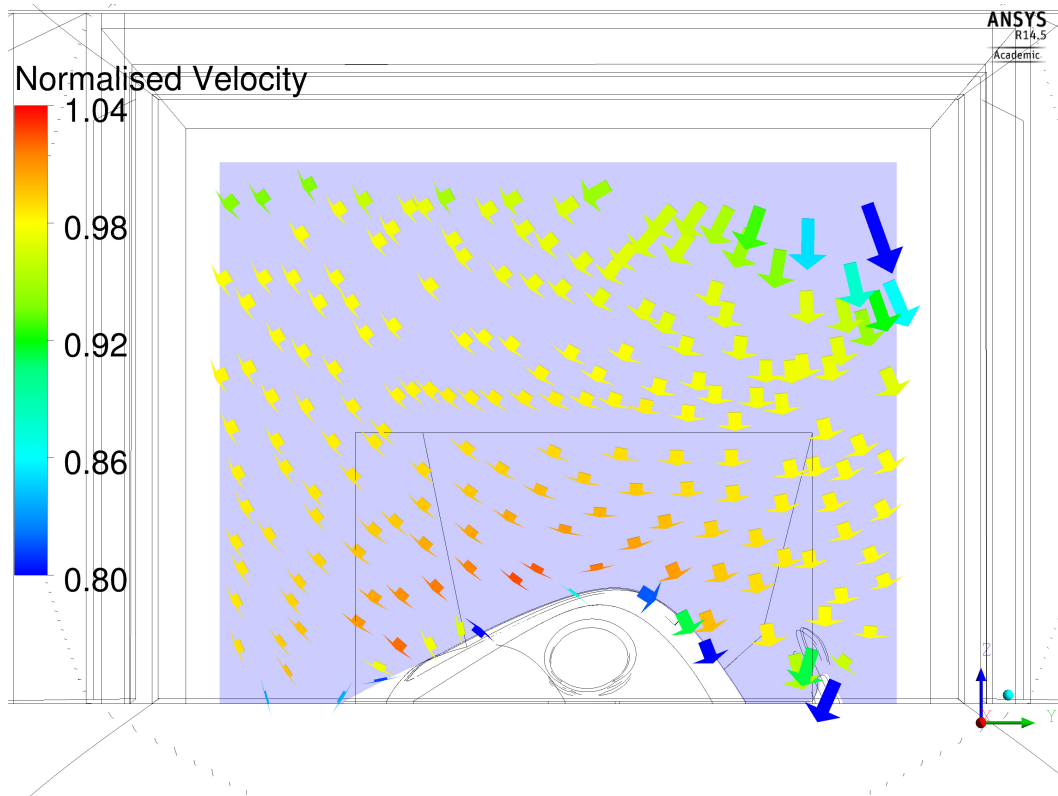


Figure 3.45: Velocity vectors at  $x = 3.50$  m - "974.405 Pa" case

Figure 3.37-3.45 show that velocity is mostly directed along the x-direction in the sections' upper side; on the contrary, the v and the w-component of velocity become more significant on the bottom of the test section, where the helicopter is located.

The flow structure is very similar in the lower side of the plane, closed to the helicopter surface. As the distance is increased in the z-direction, the difference between the three simulations becomes wider; this is probably due to the absence of a wall on the top of the test section that makes the correct reproduction of the flow field in that region difficult. This is also confirmed by the inhomogeneous velocity distribution in the upper side of the surface.

Furthermore, the analysis shows that velocity distribution is quite similar in the "Mass flow" and in the "974.405 Pa" cases, in particular in terms of flow direction, in the upper side of the test section. On the contrary, the "974.405 Pa" simulation differs from the other two in the lower side, in the central part of the helicopter surface especially, where the air flow is slightly slower: this leads to higher pressures on the cabin and on the cowling fore part in particular, as confirmed by Figure B.42, and consequently to different forces and moments on the aforementioned surfaces, as evaluable in Figure 3.31-3.36. The velocity vector distribution is very similar in the fore and in the central part of the helicopter in particular, when moving along the x-direction; on the contrary, in the rear part of the test section, the "961.228 Pa" case differently simulates the velocity, thus confirming the previously made observation on the forces and moments computation's discrepancies in the rear part of the helicopter.

**v-component of velocity** The v-component of velocity reproduced in the "961.228 Pa" case clearly differs from that of the other two simulations. The difference is wider in the upper side of the test section especially, whereas a good similarity is verified in the lower side (Figure 3.47). Analogous considerations can be made for the computation on the YZ planes: the same trend is exhibited in the initial part of the test section by all the simulations, while on the final sections the curve relative to the "961.228 Pa" simulation distances itself from the other two (Figure 3.46). As a general conclusion, the v-component of velocity is slightly influenced by the boundary condition imposed on the wind tunnel outlet section; furthermore, the differences between the curves are very small compared to reference velocity.

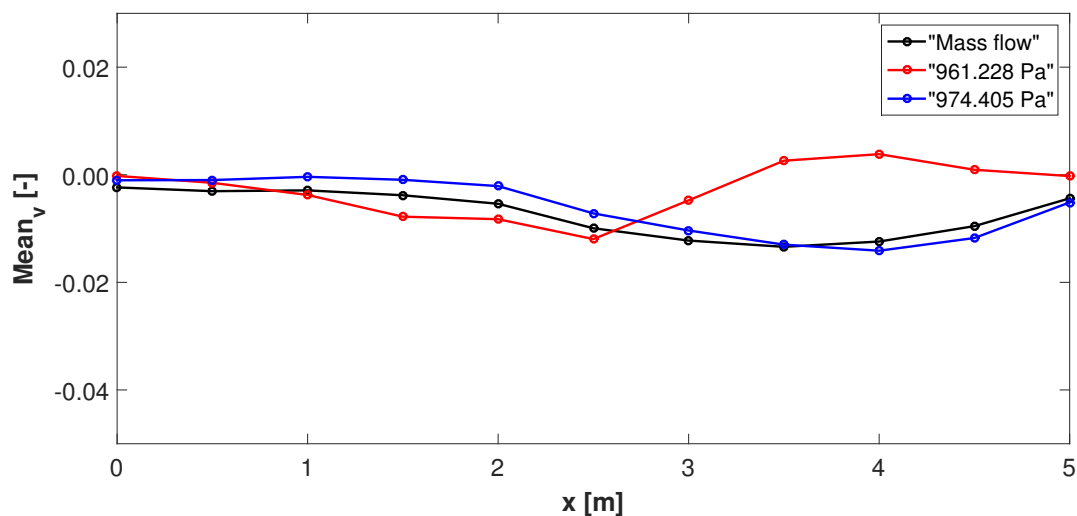


Figure 3.46: Velocity v-component distribution on YZ planes

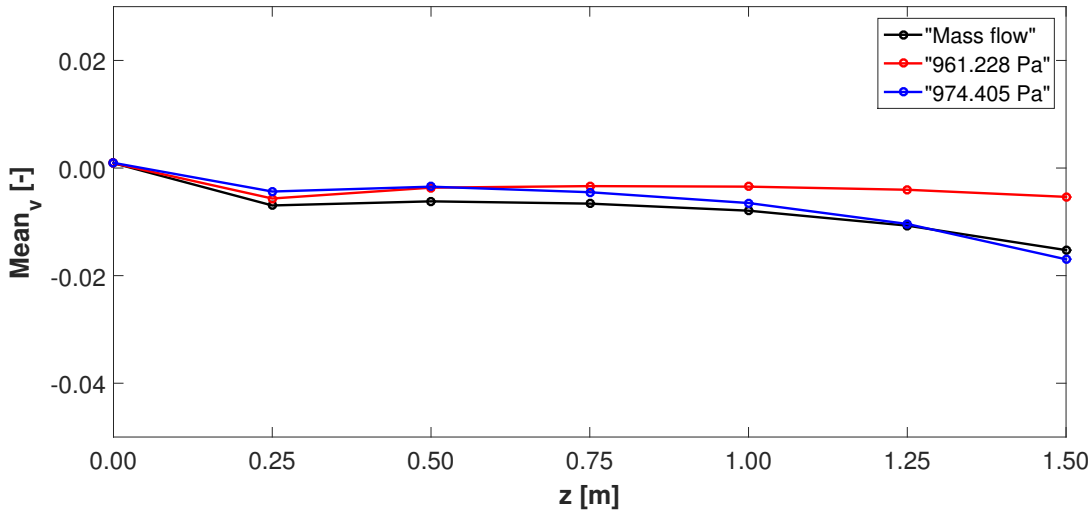


Figure 3.47: Velocity v-component distribution on XY planes

**w-component of velocity** Analogous considerations can be made with regard to the w-component of velocity simulated in the "974.405 Pa" case: in the upper side of the test section the velocity in the z-direction differs compared to "Mass flow" and "961.228 Pa" cases, especially in the region above  $z = 0.5$  m (Figure 3.49). Different trends are also found for the mean values computed on the YZ planes, in the final part of the test section especially (Figure 3.48). As a conclusion, the w-component of velocity is slightly dependent on the boundary condition specified on the outlet section; the differences found in the simulations are moreover negligible compared to reference velocity.

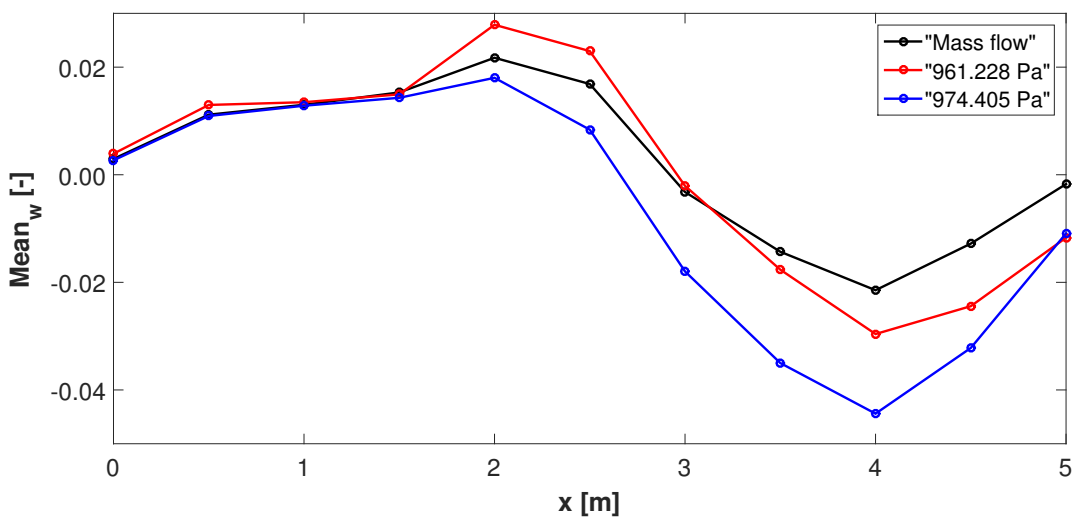


Figure 3.48: Velocity w-component distribution on YZ planes



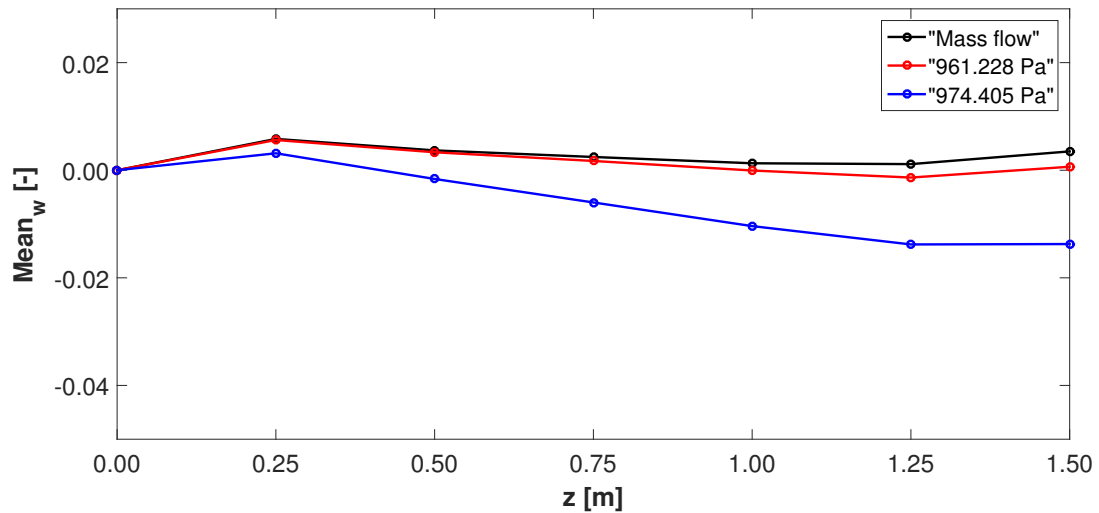


Figure 3.49: Velocity w-component distribution on XY planes

### 3.6.2 Stability

The stability of the simulations have also been analysed, performing a comparison between "Mass flow", "961.228 Pa" and "974.405 Pa" cases. With regard to the "Mass flow" simulation, the computation has been completed without particular problems; even if lower values of residuals are generally desired, given the complexity of the geometry, the level of convergence obtained can be accepted. On the contrary, several difficulties have been encountered setting a pressure as boundary condition on the wind tunnel outlet section. Most of the simulations have started to oscillate after a few time-steps; the simulations campaign has been concluded without any fully converged simulation.

The convergence problem relative to "961.228 Pa" and "974.405 Pa" cases comes from the fact that when the flow is coming into the domain, the boundary condition does not constrain the momentum allowed to flow through the boundary; as a consequence, any momentum flow satisfies the static pressure condition. Severe robustness problem can be caused, as suggested by [6].

### 3.6.3 Cost

The last parameter to analyse for the present investigation is the computational cost required to obtain the results. In Table 3.16 the time for each simulation to be completed has been collected; in addition, in order to get comparable values, the computation of the mean time for a single time-step has been performed.

The mean time required to complete a single time-step is the parameter on which to focus. The value referred to the "Mass flow" case is lower than the other values; in some cases, it is even more than twice smaller. Therefore, the "Mass flow" boundary condition matches a good computation stability with a likewise good computation velocity.

Case	Total time [s]	Total time-steps	Mean time [s]
Mass flow	1.023E+06	2500	409.2
900 Pa	5.005E+05	800	625.6
961.228 Pa	2.342E+05	542	432.1
1050 Pa	6.113E+05	1000	611.3
900 Pa	1.694E+05	300	564.7
1000 Pa	4.368E+05	500	873.6
1050 Pa	3.174E+05	500	634.8
1100 Pa	3.786E+05	500	757.2
1200 Pa	4.158E+05	500	831.6
974.405 Pa	6.865E+05	1000	686.5

Table 3.16: Computational cost

### 3.6.4 Conclusion

The results obtained with the "Mass flow" simulation and those computed with the co-Kriging model are similar, as demonstrated by the investigation on accuracy of results conducted within this section; actually, focusing on the comparison between the "Mass flow" case and the "974.405 Pa" case, the first simulation is probably more accurate, given the higher grade of convergence reached at the end of the computation. Anyway, the parameter represented by accuracy cannot be used as the only discriminating factor in the definition of the best approach to follow. The similarity of the results obtained with the two different approaches is of great importance because, whichever method is used, the results obtained are a good reproduction of wind tunnel experiments.

However, the analysis related to stability and cost have evidently highlighted that the "co-Kriging" approach is not competitive compared to the simulation conducted with the "Mass flow" boundary condition: a remarkable amount of time and simulations was necessary to deal with the difficulty encountered in reaching convergence of results. On the contrary, in the case of the "Mass flow" approach only one simulation is needed to have consistent results.

Given its preeminence in terms of computational cost and stability, and most probably in terms of accuracy too, "Mass flow" approach will be adopted as the only method for the simulation of the complete helicopter geometry.

---

## Chapter 4

# Simulation of the engine air intake

In the present chapter the engine air intake is added to the helicopter geometry and its influence on the flow will be analysed through a new stationary CFD simulation; the results obtained will be compared with those given by the "Mass flow" simulation and will be presented in Chapter 5. With the purpose of simulating the engine influence, an engine mass flow rate has been imposed at the compressor entry face. In the experimental measurements this is achieved by means of a suction system incorporating a venturi meter, pipes and a fan; as a matter of fact, the analysis represents the attempt of investigating the highest engine mass flow rate reproduced during the first wind tunnel campaign.

The engine air intake adopted for the simulation represents the first variant developed by Airbus Helicopters within the "ATHENAI" project; a representation is given in the preface. The engine comprises two different screens, one located at the air intake entrance and one inside the plenum chamber. Actually, in this simulation, the screens will not be considered in order to simplify the definition of the problem and to keep the computational cost within acceptable values; in Chapter 6 the flow striking a screen will be investigated; two possible approaches for the simulation of such a configuration by means of the CFD will be briefly described.

### 4.1 Description of the problem

#### 4.1.1 Geometry

The geometry of the wind tunnel used in the simulation is the same previously described in Chapter 3. The geometry of the helicopter differs from that of Chapter 3 for the employment of the engine air intake (Figure 4.1); in place of the surface previously defined as "Cover", the air intake is installed with the purpose of feeding the engine. On the helicopter outer surface the air flow is mainly directed towards the x-axis; in proximity of the air intake, it is then sucked towards the bottom, into the inner part of the intake itself. Firstly, the flow enters the plenum chamber (Figure 4.3), a box fostering the flow field homogeneity at the compressor inlet in all the flight conditions and improving engine functioning near the surge line. Subsequently, the air is led to flow in a duct, fixed by means of fastening elements to the plenum chamber surfaces having the normal approximately directed towards the x-axis. In this way, the air is forced to flow only within the duct, whose purpose is to deflect the main flow from a radial to an axial

direction. Moreover, the duct is crossed by twelve guide vanes (Figure 4.5: note that no flow is possible in the guide vanes' empty spaces, since they are delimited by the duct), aimed at the enhancement of the flow quality at the compressor inlet: they channel the air flow towards the ring-shaped duct (Figure 4.4) connecting the air intake to the suction system employed during the experimental measurements. Great importance is assumed by the aerodynamic interface plane (Figure 4.6), taken as reference for the flow conditions at the compressor inlet. Figure 5.52, 5.53, 5.54 allow for an easier comprehension of the flow field inside the engine air intake and of the relative geometry; a representation of the engine air intake installed on the helicopter is given in Figure 4.7.

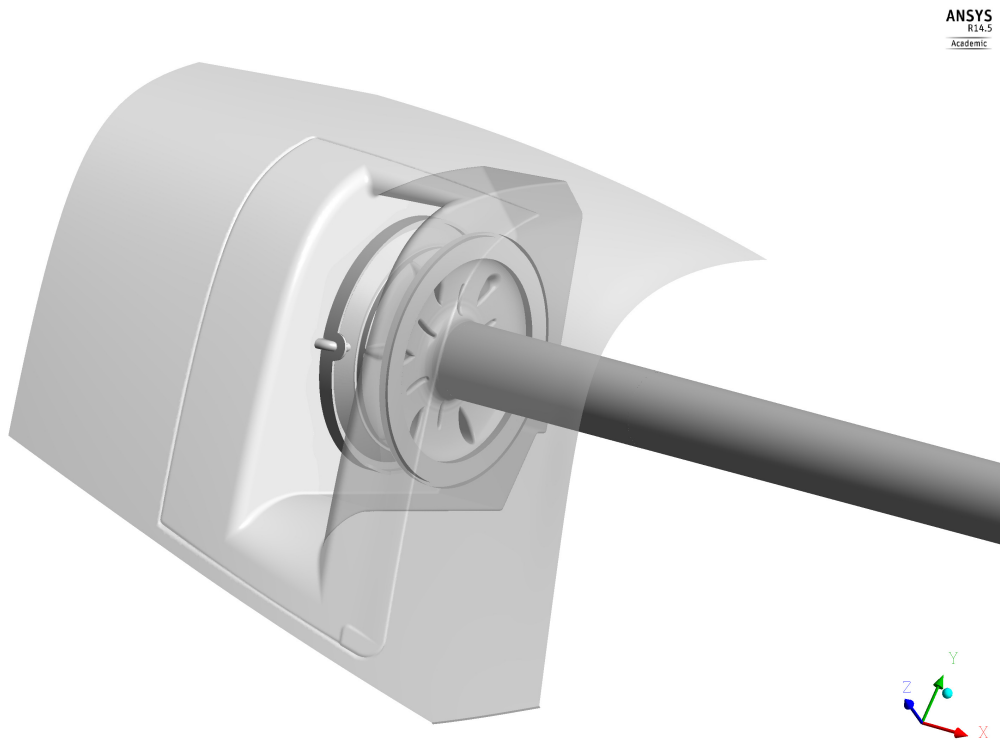


Figure 4.1: Engine air intake overview

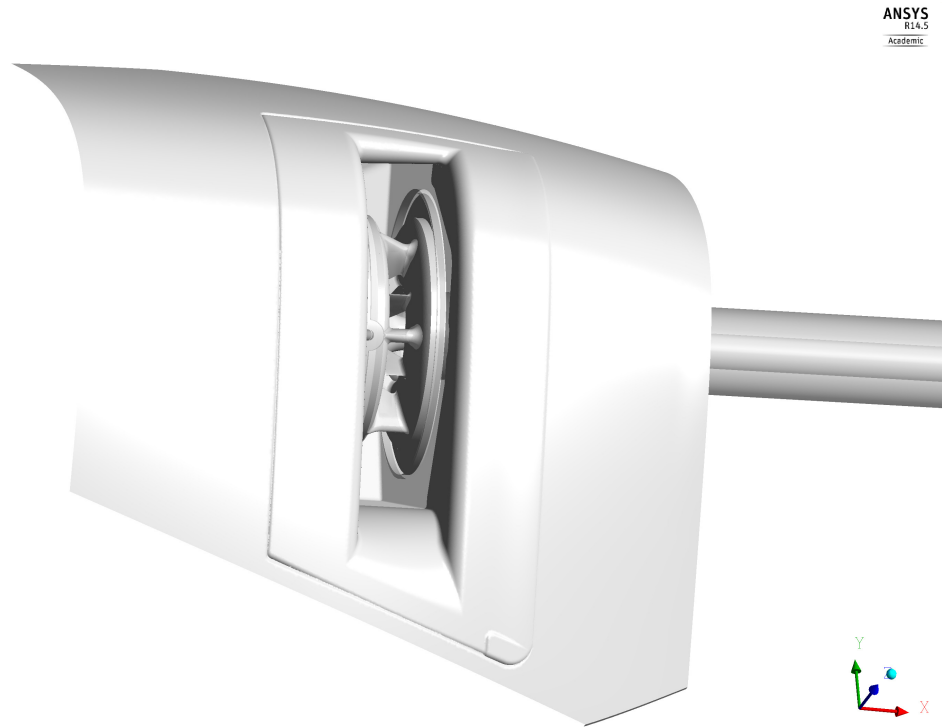


Figure 4.2: Engine Air Intake (EAI)

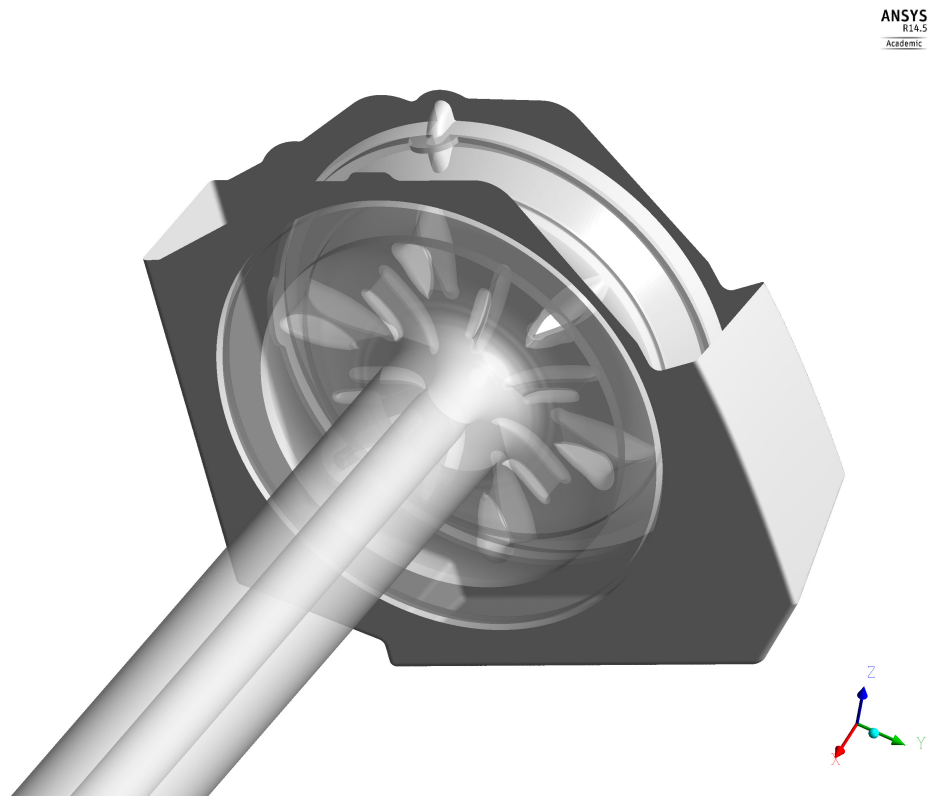


Figure 4.3: Engine Plenum Chamber (EPC)

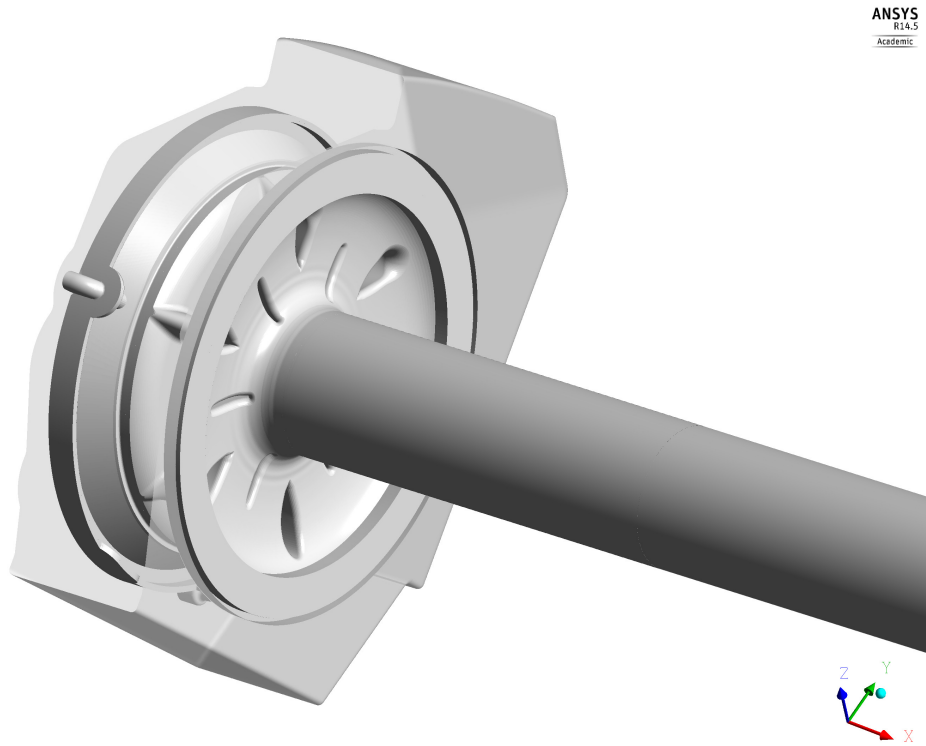


Figure 4.4: Engine Intake Duct (EID)

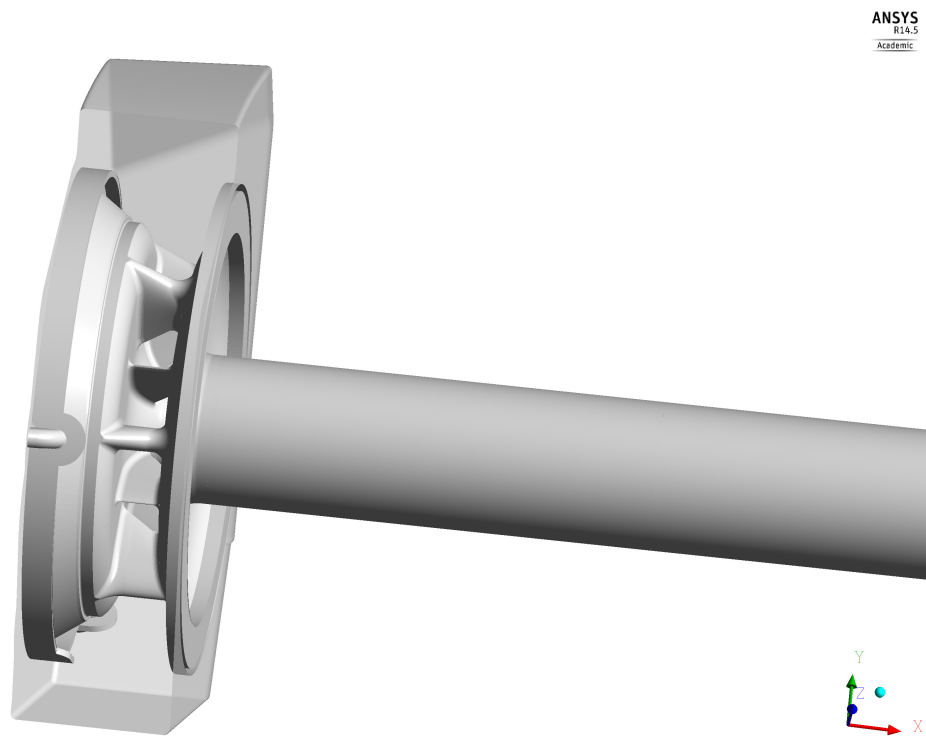


Figure 4.5: Guide vanes

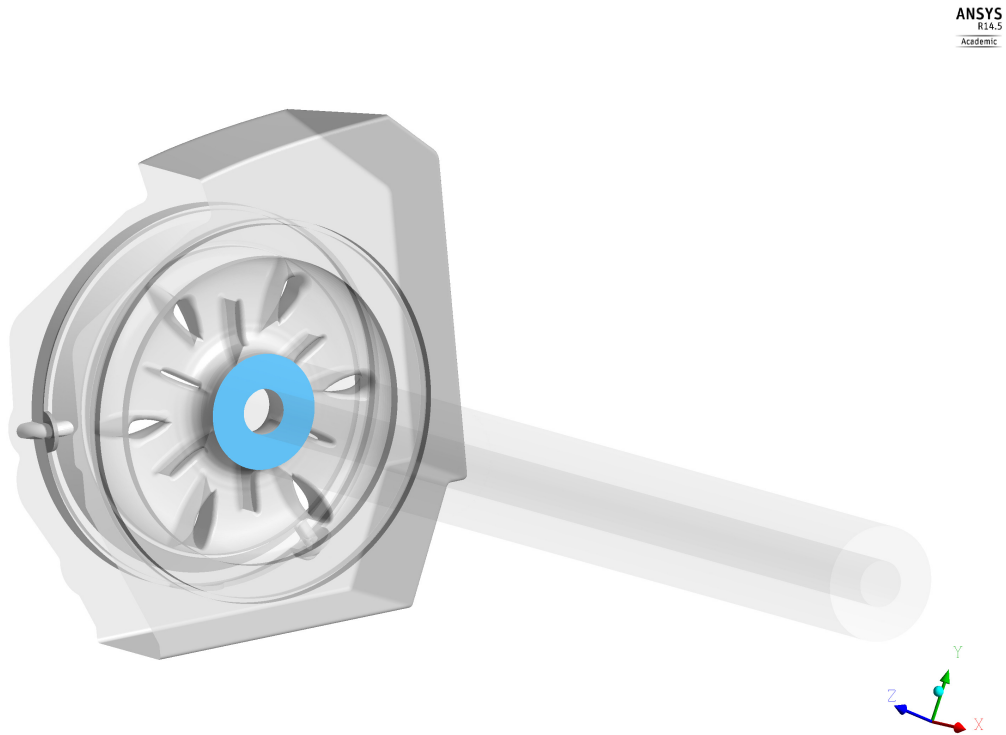


Figure 4.6: Aerodynamic Interface Plane (AIP)

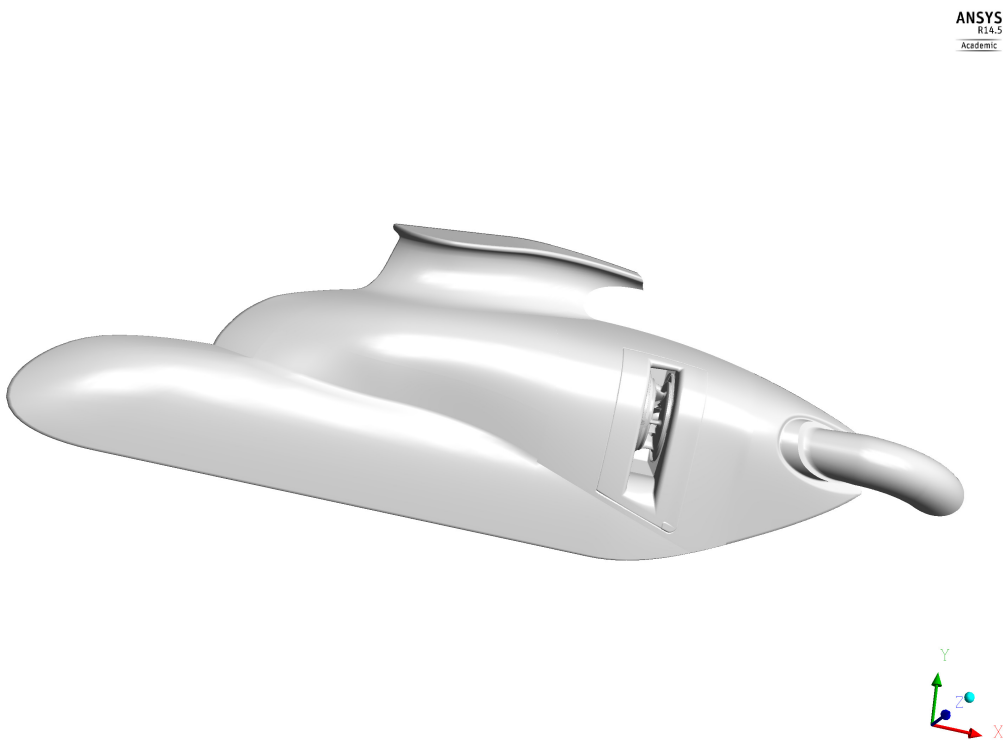


Figure 4.7: Helicopter section overview

### 4.1.2 Mesh

The wind tunnel and the helicopter outer surface meshes have not been modified compared to those used in the previous set of simulations.

The engine air intake meshes are created as part of [22] and have been almost totally created with a structured mesh; the EPC represents an exception with respect to this choice, since, due to the complexity of its geometry, an unstructured mesh has been preferred in this case. With the purpose of obtaining results as accurate as possible for a comparison with the experimental data, a particular attention has been paid to the EID and to the EPC, where a considerable number of surface pressure measurements have been made during the first wind tunnel campaign; additionally, flow field measurements have been conducted on the AIP using a five-hole pressure probing system.

### 4.1.3 Settings

The settings defined for the simulations described in this chapter are summarised in Table 4.1.

Setting	Model
Turbulence	SST
Material	Air Ideal Gas

Table 4.1: Settings - "Simulation of the engine air intake"

In the simulation of the complete helicopter geometry a fluid model able to reproduce the air compressibility was required, given that, even before the simulation, the Mach number characterising the flow inside the air intake was expected to be higher than 0.3.

### 4.1.4 Boundary conditions

The boundary condition imposed on the wind tunnel inlet section is the same used in the simulations described in Chapter 3, that is a mass flow rate equal to 269.36 kg/s. Even in the case of this simulation, the same mass flow rate defined on the inlet section has been imposed on the outlet one in order to satisfy the wind tunnel functioning in a stationary regime. A "Mass flow" boundary condition has been employed, as suggested by the conclusions of the analysis described in Section 3.6.

The suction system employment has been simulated imposing a mass flow rate on the measurement tube outlet section as boundary condition (Figure 4.8). The maximum mass flow rate reproduced during the first experimental campaign performed in the Technische Universität München's wind tunnel has been chosen in order to make a comparison with the experimental data; this rate had previously been calculated with the purpose of obtaining a specified free stream Mach number in the ISA conditions, taking Garching's altitude as reference. Starting from the corrected mass flow rate,<sup>1</sup> the computation of the right mass flow has allowed us to fulfil

<sup>1</sup>The corrected mass flow is defined as the mass flow that would pass through a section if the ambient air conditions were equal to the reference ones.



the Mach number similarity condition for real total pressure and temperature, characterising the ambient conditions during the experimental measurements.

The computation has been performed by means of Equation 4.1. The ambient conditions have been measured at the nozzle exit, where static pressure and temperature are equal to the stationary air ones; on the contrary, total values differ, even though the difference can actually be neglected, given the very low Mach number characterising the air flow field in this region. Reference pressure ( $P_{ref}$ ) and temperature ( $T_{ref}$ ), and real pressure (P) and temperature (T) are summarised in Table 4.2; P and T represent the ambient conditions measured during the experimental test. The mass flow  $\dot{m}$  computed through Equation 4.1, as well as pressure P and temperature T have then been used in the CFD simulation in order to obtain values comparable with the experimental ones.

$$\dot{m} = \dot{m}_{corr} \sqrt{\frac{T_{ref}}{T}} \frac{P}{P_{ref}} \quad (4.1)$$

$P_{ref}$ [Pa]	$T_{ref}$ [K]	P [Pa]	T [K]
95667.10	285.02	96704.06	304.75

Table 4.2: Boundary conditions - Pressure and temperature

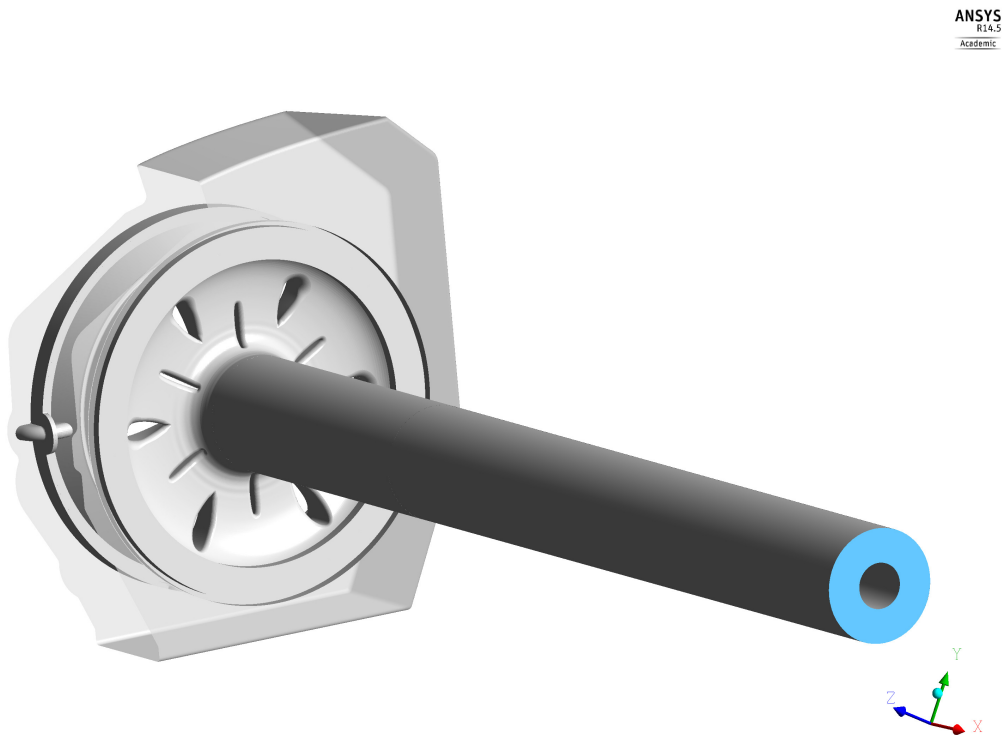


Figure 4.8: Outlet section of the measurement tube

## 4.2 Simulation

The CFD simulation has been performed using a "Physical Timescale" equal to  $1E-5$  s for 150 time-steps and a "Local Timescale" with a factor equal to 1 for other 800 time-steps. The results in terms of residuals are shown in Figure 4.9, 4.10, 4.11: good values have been obtained for pressure  $P$  and turbulence frequency  $\omega$ ; those relative to velocity, enthalpy and turbulence kinetic energy are anyway satisfying. As a conclusion, an acceptable convergence grade has been reached, even though the geometry complexity has not allowed for an easy reproduction of the flow field.

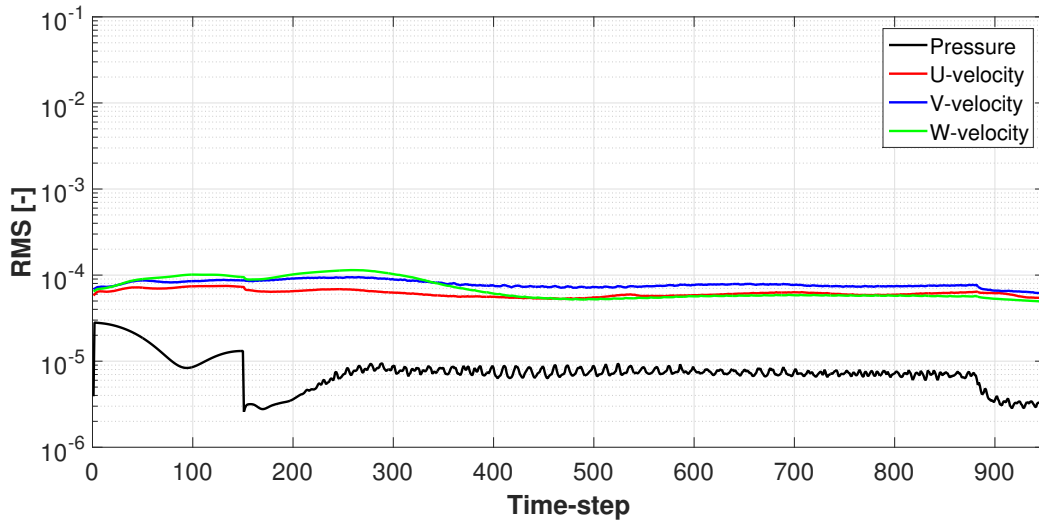


Figure 4.9: Mass and momentum residuals - "Open air intake" case

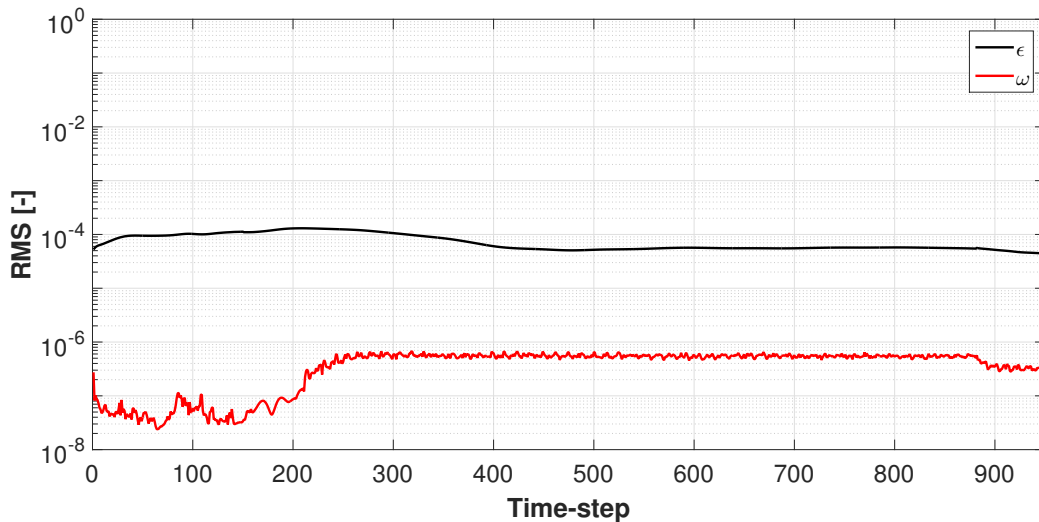


Figure 4.10: Turbulence residuals - "Open air intake" case

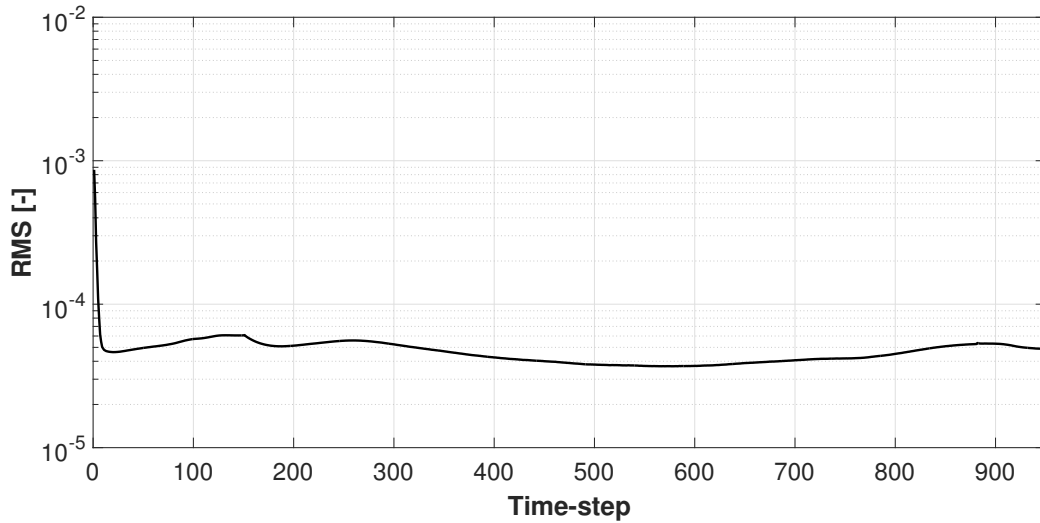


Figure 4.11: Energy residuals - "Open air intake" case

**$C_P$  distribution** In this paragraph the  $C_P$  distribution on the helicopter and on the EID surfaces is shown by means of Figure 4.12, 4.14, 4.13; the  $C_P$  is calculated using the dynamic pressure measured at the nozzle exit as reference, as defined in Section 5.1. The lines defined for the comparison described in Chapter 5 are represented on the same pictures in order to allow for the extrapolation from the distribution on the whole geometries of the trends plotted in Figure 5.22, 5.24, 5.25, 5.27, 5.28, 5.30, 5.32, 5.35, 5.37, 5.43, 5.44, 5.46-5.51; with the same purpose, the legend is defined in such a way that the range extremities are the same employed in Chapter 5 in the previously mentioned pictures.

The  $C_P$  is almost constant on the helicopter surface; only on the mast fairing and in the inner part of the intake the air flow slightly accelerates, leading to lower  $C_P$  values. The values are confined in a limited range around the zero; this means that the pressure does not distance itself from the reference value. On the front side of the EID the  $C_P$  distribution is not constant; since negative  $C_P$  values are present, the flow is faster than the reference velocity. A different distribution characterises the back side of the EID. On the one hand, the  $C_P$  values are comparable to the front side ones in the outer part; on the other hand, much lower values are present in the inner part. In this region, the flow is in fact strongly accelerated in order to follow the geometry curvature; as a consequence, the pressure undergoes a significant decrease.

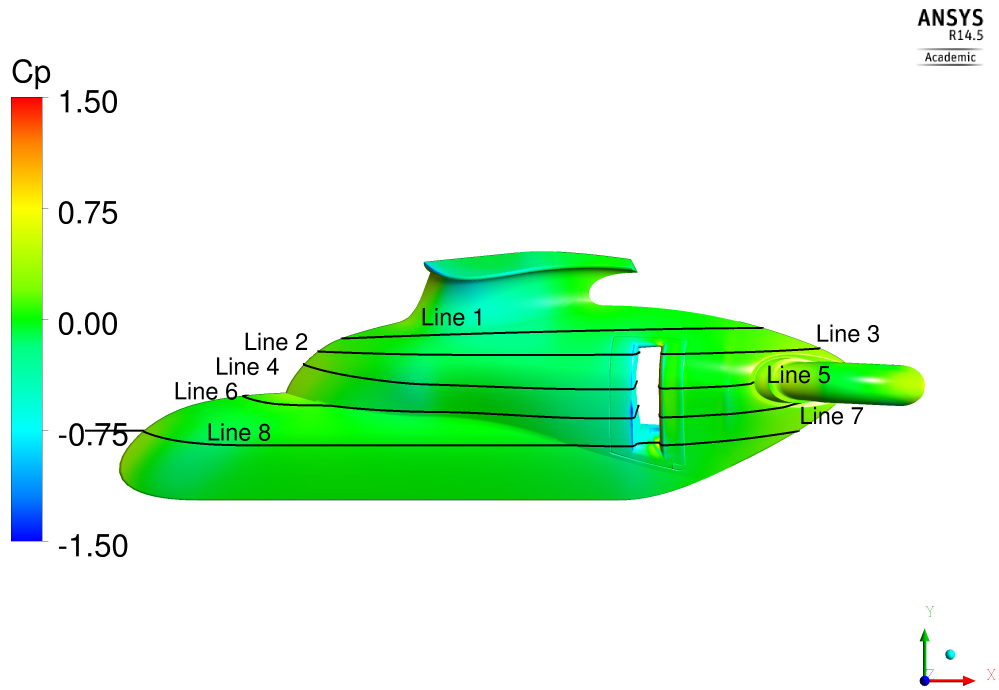


Figure 4.12:  $C_P$  distribution on the helicopter surface

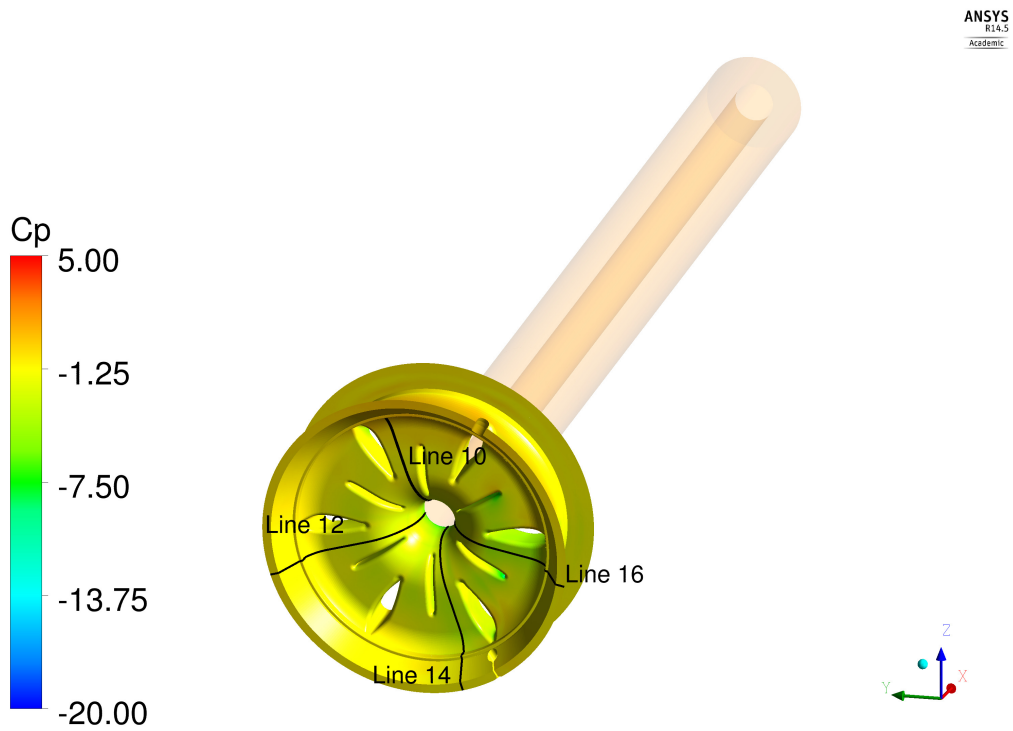


Figure 4.13:  $C_P$  distribution on the EID front surface

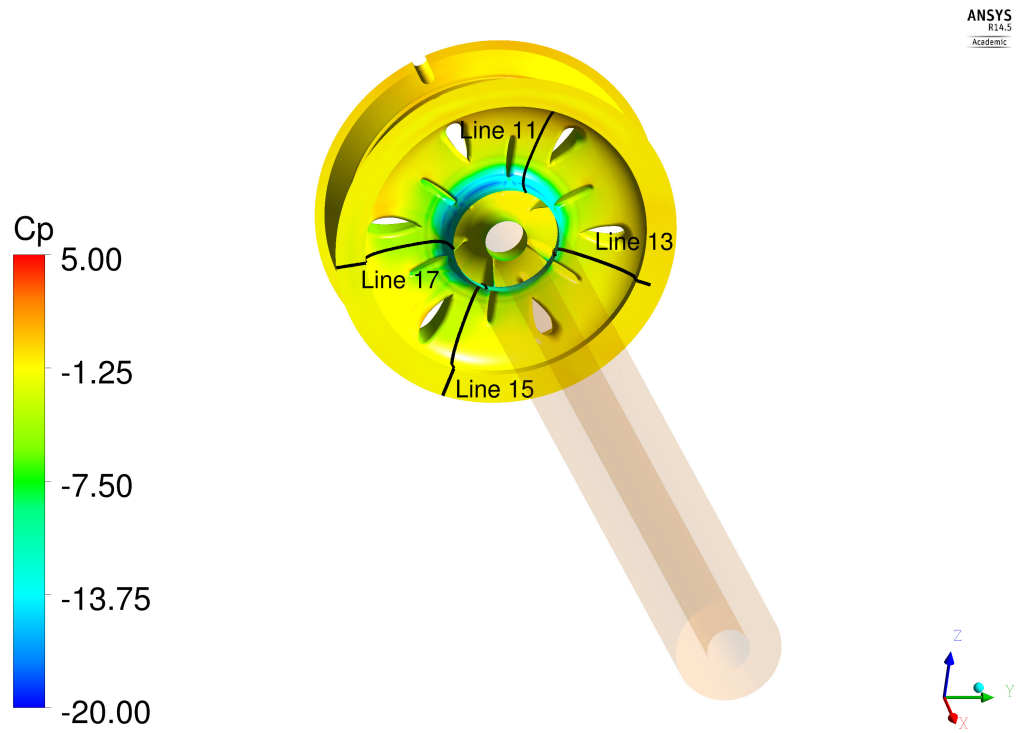


Figure 4.14:  $C_P$  distribution on the EID back surface



---

## Chapter 5

# Analysis of results

Two distinct analyses will be carried out in this chapter: on the one hand, the engine mass flow influence on pressure distribution around the helicopter section will be studied, whereas, on the other hand, CFD and experimental data will be compared for the numerical simulations validation. With regard to the first analysis, the CFD values obtained by the simulation performed with the simplified helicopter geometry, until now called "Mass flow" case (Chapter 3), will be compared with the results taken from the simulation performed with the complete helicopter geometry, previously shown in Chapter 4; with respect to the second analysis, the CFD data coming from the simulations described in Chapter 4 will be compared to the experimental data of the first wind tunnel campaign taken from [21].

### 5.1 Data processing

In both the analyses pressure distribution has been studied. In the first case only the flow around the helicopter section has been considered, given the lack of the engine air intake geometry in the simulation performed keeping the air intake closed. On the contrary, in the second case the flow inside the EID has been taken into account too. Pressure distribution is studied along lines, whose individuation has allowed us to obtain more effective comparisons based on numerical values. For each line a new coordinate has been defined with the purpose of plotting the pressure referred to a certain point in a very simple way, instead of using a general XYZ coordinate system; the definition of coordinates is described in the following sub-sections.

In order to compare simulations performed with different values of reference pressure, the results will be presented in terms of pressure coefficient  $C_P$ . For each simulation, both numerical and experimental,  $C_P$  has been defined as the ratio of relative static pressure to the mean dynamic pressure measured at the nozzle exit. With regard to the second analysis, the pressure  $P$  reported in Table 4.2 is used as reference pressure both for CFD and experimental results; with regard to the first analysis, as different reference pressure and temperature had been set in the two CFD simulations, it has been checked if the results were anyway comparable, that is to say if the differences between the  $C_P$  trends were very little conditioned by the reference values used. The check has been performed using mean dynamic pressure, measured at the nozzle exit, as parameter; since similar values have been found in both the simulations, the discrepancies observable between the  $C_P$  trends are mostly caused by the difference in geometry.

### 5.1.1 First analysis

Nine lines are used for the analysis regarding the engine mass flow rate influence on the air flow around the helicopter surface; they are represented in Figure 5.1. In order to avoid the problem relative to the lack of engine air intake geometry in one of the two simulations, the lines have been defined in such a way that the air intake is excluded by the analysis. A new coordinate  $n$  has been computed considering a single line as a polygonal chain defined by a certain number of points on which the pressure was known; the partial length of the line, calculated at a given point with reference to one of the extremities, has then been divided by the total length. Therefore, the  $n$ -coordinate will range between 0 and 1. Figure 5.2, 5.4, 5.7, 5.10, 5.15 help the reader to immediately visualise the real position on the line of a certain  $n$ -coordinate and, hence, to comprehend the pressure distribution more easily.

### 5.1.2 Second analysis

Seventeen lines have been used for the second analysis, eight on the helicopter surface, one on the EPC and eight on the EID. With regard to the first eight, represented in Figure 5.18, they are very similar to those used in the first analysis: they have been elongated in order to take into account also the engine air intake. The lines relative to the EID have been defined cutting the EID itself with planes rotated by given angles  $\varphi$  (Table 5.1), measured with reference to the AIP coordinate system, represented in Figure 5.19. In this coordinate system the x-axis is oriented along the engine mid axis and the z-axis towards the guide vane defined as "number 1"; the y-axis creates a right-handed trihedron with the other axes. As shown in Figure 5.19, the EID is symmetrical and could be divided in six equal parts; the lines definition is made in such a way that the four lines on the front side and the four lines on the EID back side are exactly equal. Figure 5.19 gives an example of the EID lines: on the front side of the geometry, Lines 10, 12, 14 and 16 are located, on the back side, Lines 11, 13, 15, 17.

With regard to the lines located on the helicopter surface and on the EID, the coordinates are defined in the same way as the first analysis; they are called  $s$  in order to distinguish the two analyses. The coordinate relative to the EPC line,  $\phi$ , is calculated as the ratio of the angle  $\varphi$  defined with respect to the AIP coordinate system to a full circle of 360 degrees. Table 5.1 presents the  $\phi$ -coordinates relative to the EID lines: it provides a better understanding of the connection between  $C_P$  distributions on EID and on EPC. Also in this case, Figure 5.21, 5.23, 5.26, 5.29, 5.34, 5.36, 5.42 help the reader understand the results more easily.

Line	$\varphi$ [deg]	$\phi$ [-]
10 - 11	45	0.125
12 - 13	135	0.375
14 - 15	225	0.625
16 - 17	288	0.800

Table 5.1: EID lines - Position with reference to the AIP coordinate system



## 5.2 Effect of engine air intake on the external flow

The engine mass flow rate influence is insignificant far from the region where the engine air intake is located; both the curves follow the same trend and are almost overlapping. Only in proximity of the air intake the influence becomes more evident. In the "closed air intake" case the flow is not accelerated given the continuity of the geometry and the  $C_P$  remains, as a consequence, almost constant. In the "open air intake" case the flow is affected by the presence of the intake and is accelerated in proximity of the intake entrance (Figure 5.31): the higher the mass flow rate, the more the flow is sucked into the engine, leading to even more significant acceleration and, consequently, to even more pronounced  $C_P$  drops. This can be seen in Figure 5.5, 5.8, 5.11, 5.16, at  $n$  confined between 0.9 and 1.0. The second analysis will show that a stagnation point is present on the back side of the air intake (Figure 5.33): above, the flow is again accelerated and another  $C_P$  drop is present, as Figure 5.25, 5.28, 5.32, at  $s$  included between 0.1 and 0.2, and Figure 5.35, at  $s$  equal to 0.8, show. Such a flow phenomenon is not observed in the "closed air intake" case.

On Lines 2, 4, 6, 8 at  $n = 0.9 \sim 1.0$  and on Lines 3, 5, 7, 9 at  $n = 0.1 \sim 0.2$ , a significant  $C_P$  drop is directly followed by a likewise strong increase. In these cases the flow is affected by the presence of some small steps in the geometry, that lead to an expansion of the flow and to a following compression. The phenomenon is well visualised in Figure 5.12, 5.14. The pictures are taken from the "open air intake" case; the figures are explanatory also for the other lines located on the helicopter outer surface and for the "closed air intake" simulation as well.

ANSYS  
R14.5  
Academic

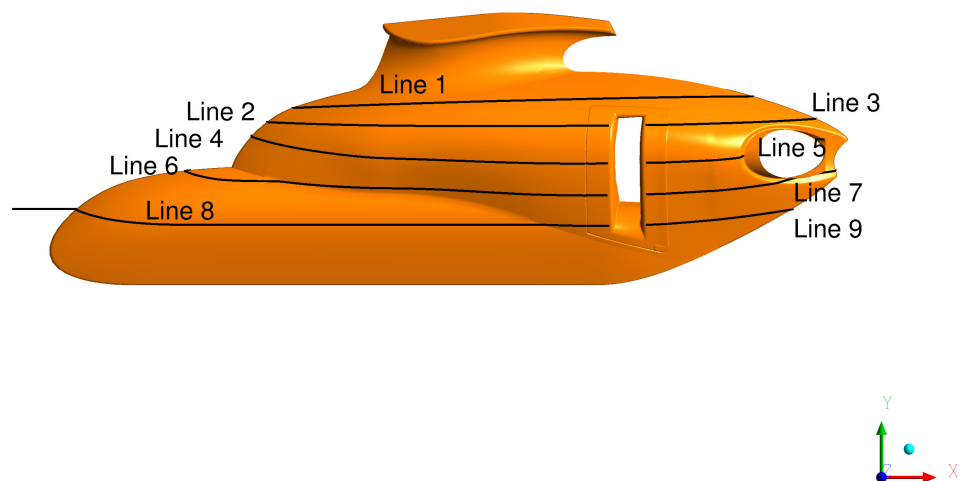


Figure 5.1: Definition of lines on the helicopter surface - Comparison between CFD simulations

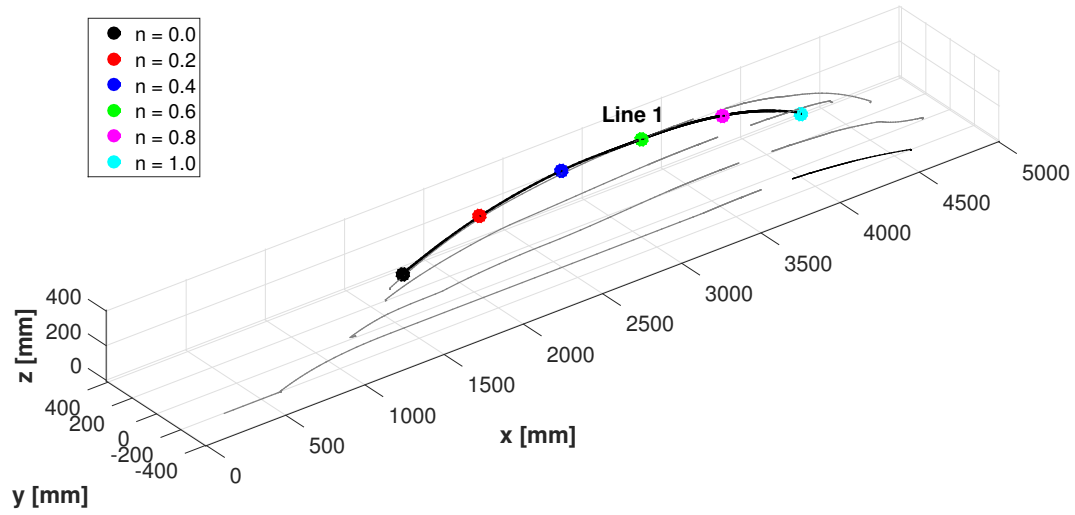


Figure 5.2: Definition of Line 1 - Comparison between CFD simulations

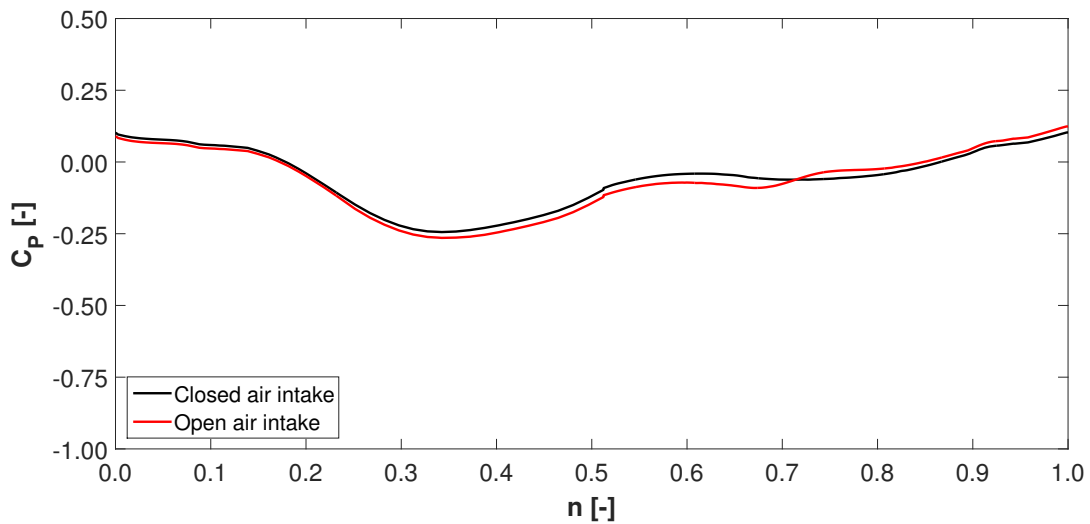


Figure 5.3:  $C_p$  distribution on Line 1 - Comparison between CFD simulations

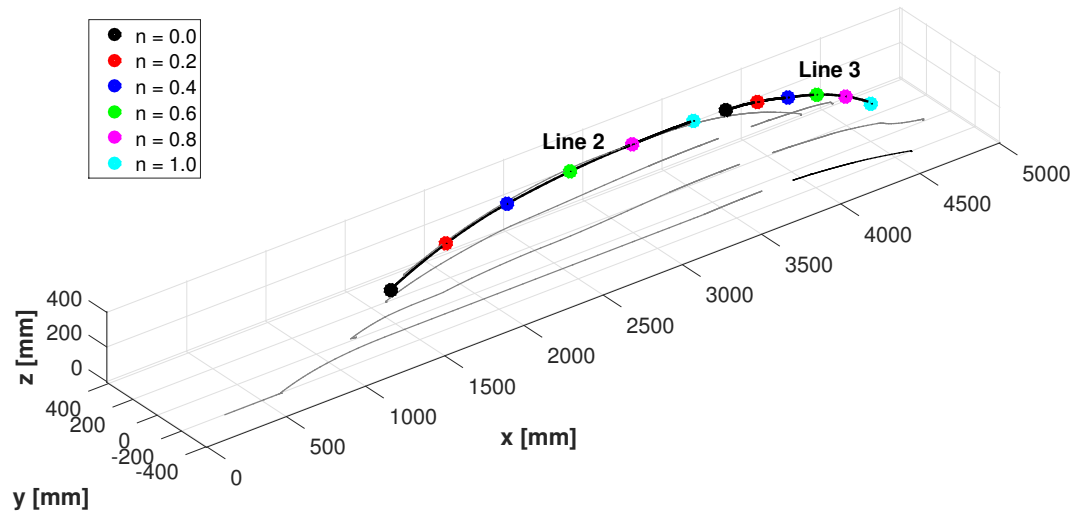
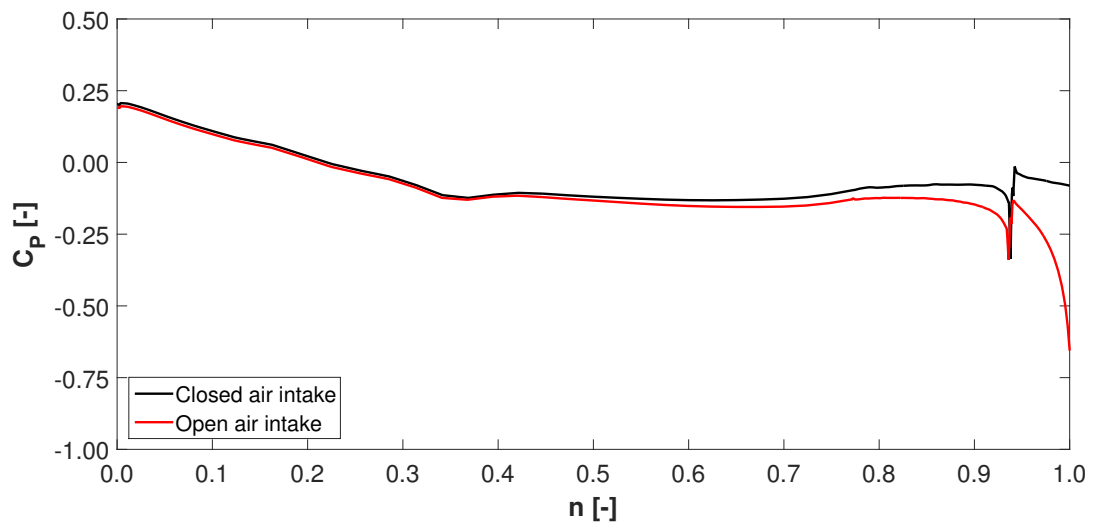


Figure 5.4: Definition of Lines 2-3 - Comparison between CFD simulations

Figure 5.5:  $C_p$  distribution on Line 2 - Comparison between CFD simulations

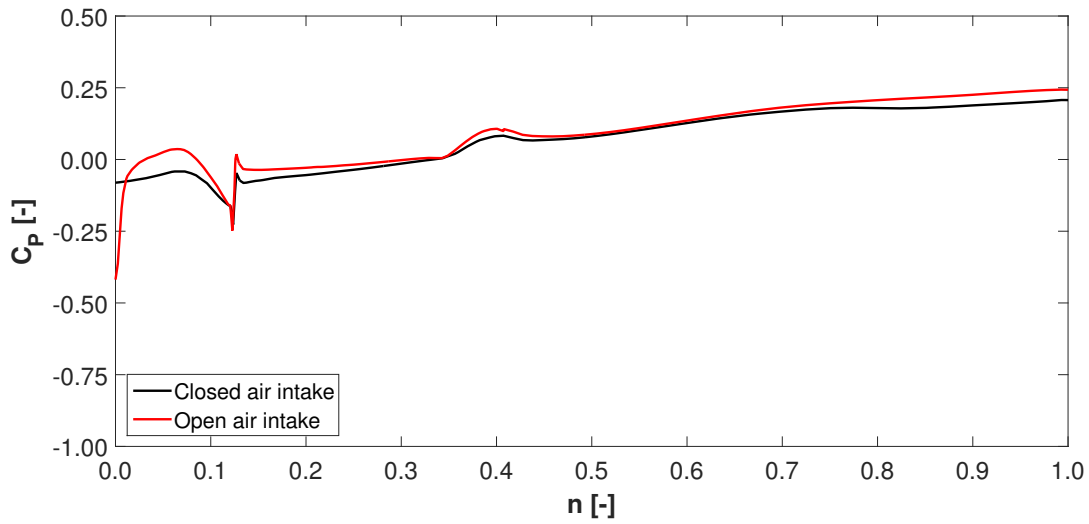


Figure 5.6:  $C_p$  distribution on Line 3 - Comparison between CFD simulations

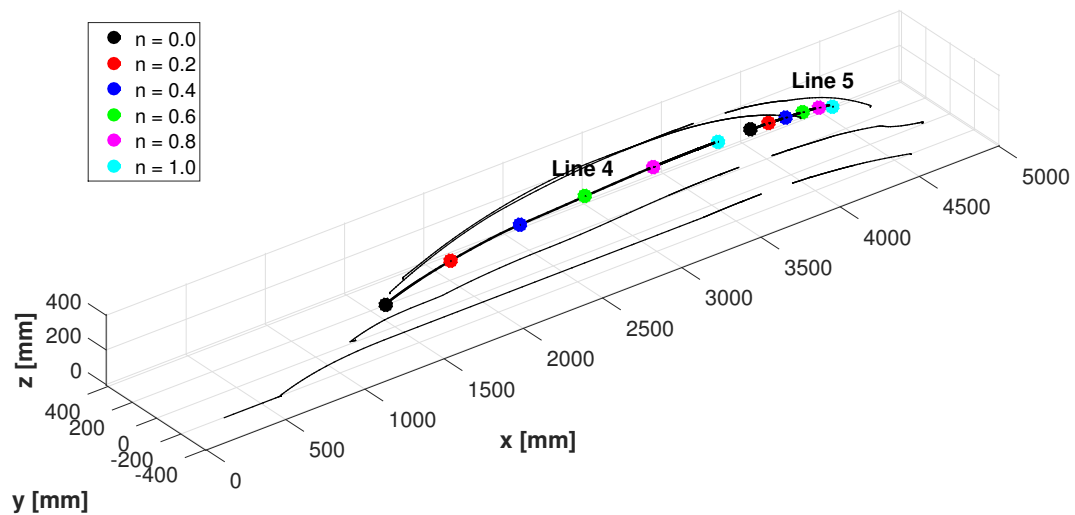


Figure 5.7: Definition of Lines 4-5 - Comparison between CFD simulations

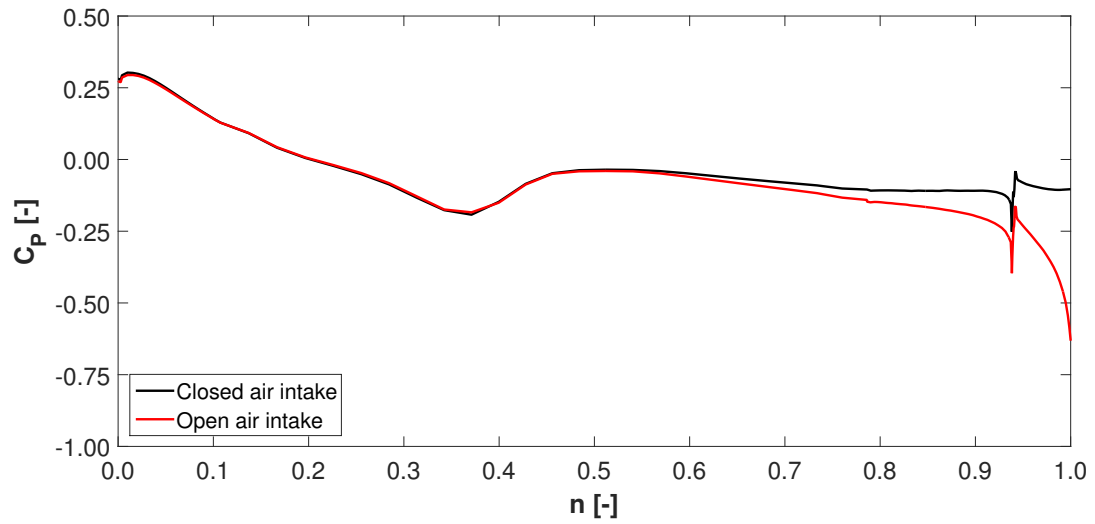


Figure 5.8:  $C_P$  distribution on Line 4 - Comparison between CFD simulations

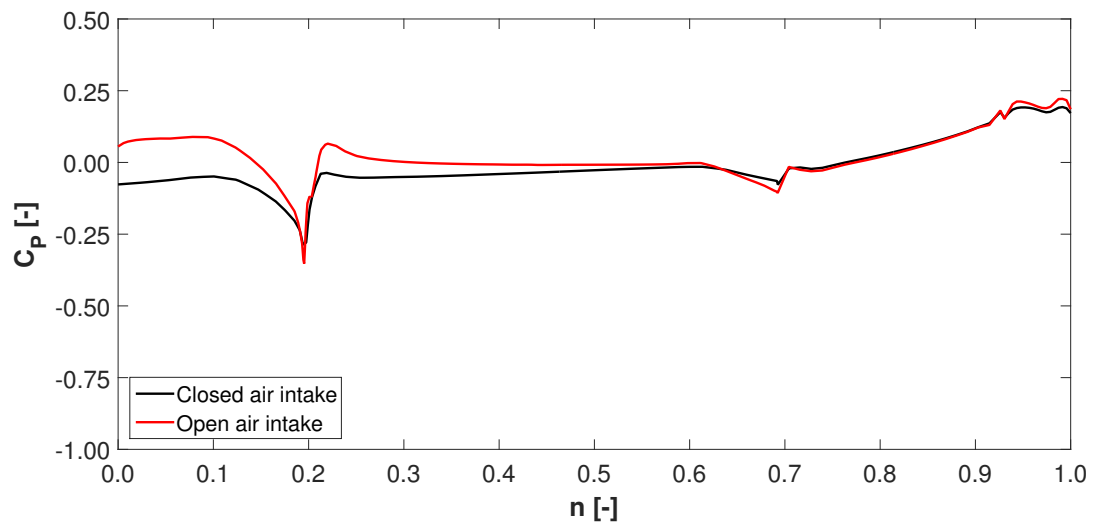


Figure 5.9:  $C_P$  distribution on Line 5 - Comparison between CFD simulations

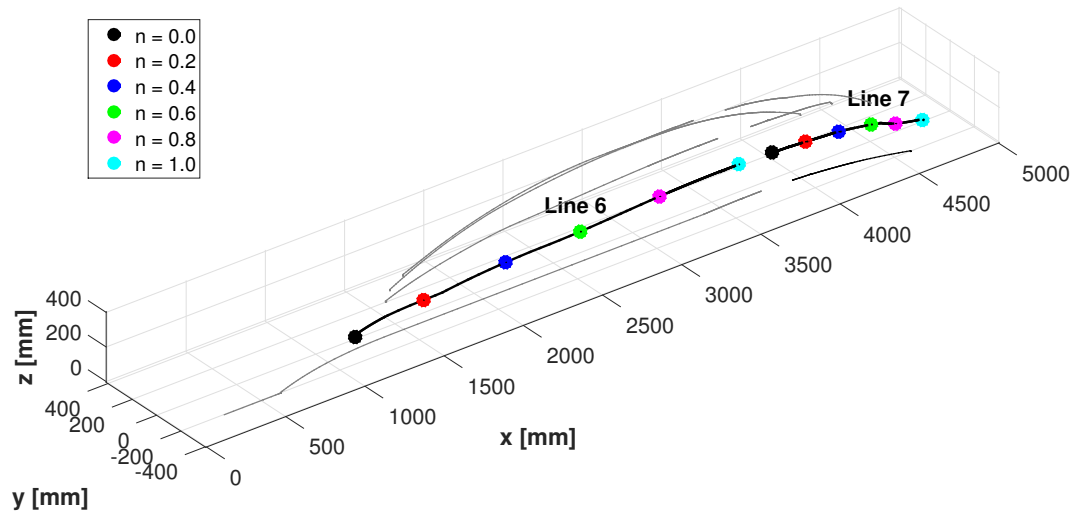


Figure 5.10: Definition of Lines 6-7 - Comparison between CFD simulations

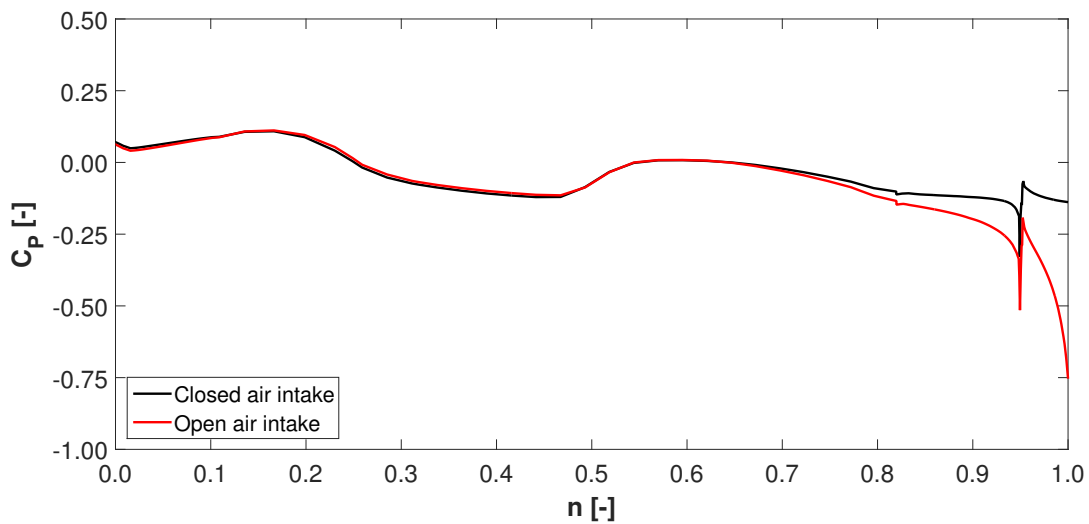
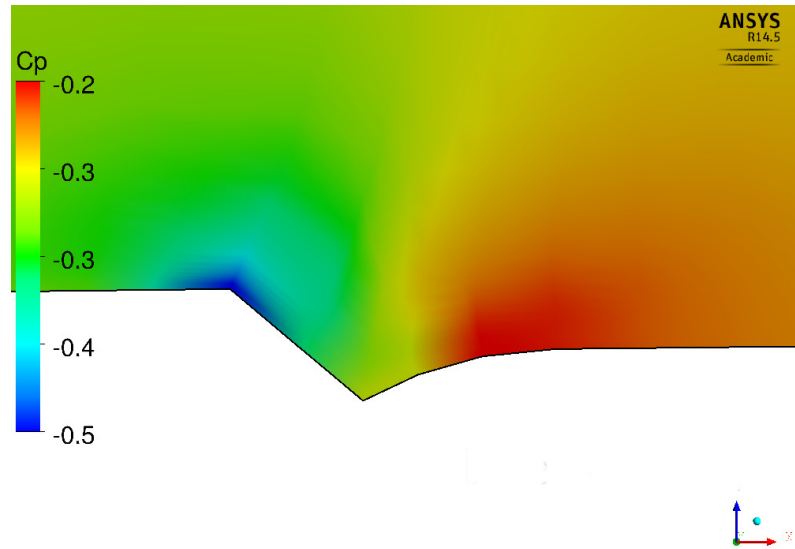
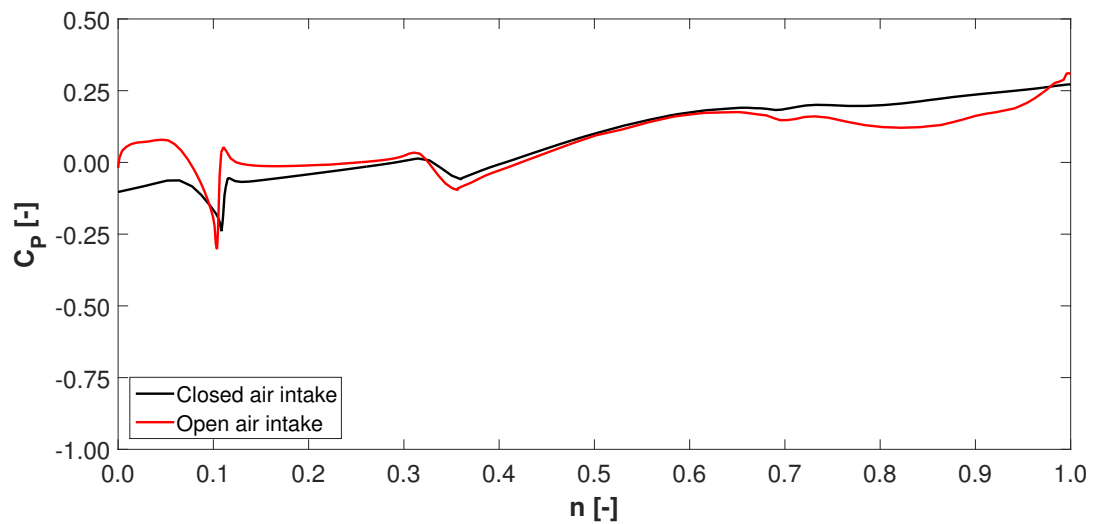


Figure 5.11:  $C_P$  distribution on Line 6 - Comparison between CFD simulations

Figure 5.12: Line 6 -  $n = 0.95$ Figure 5.13:  $C_p$  distribution on Line 7 - Comparison between CFD simulations

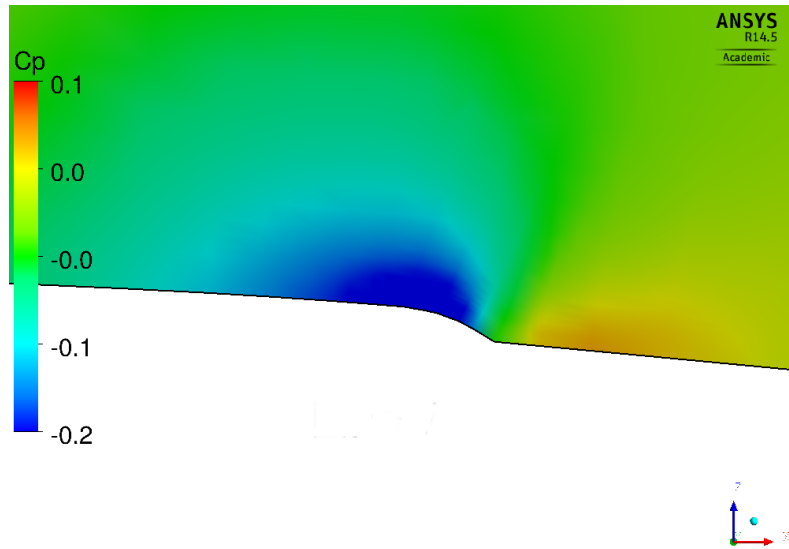
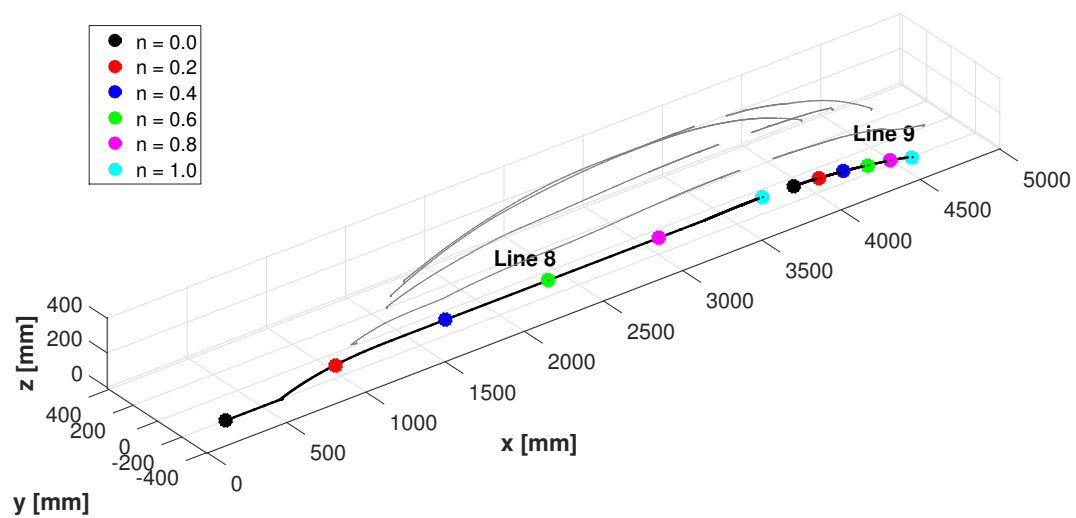
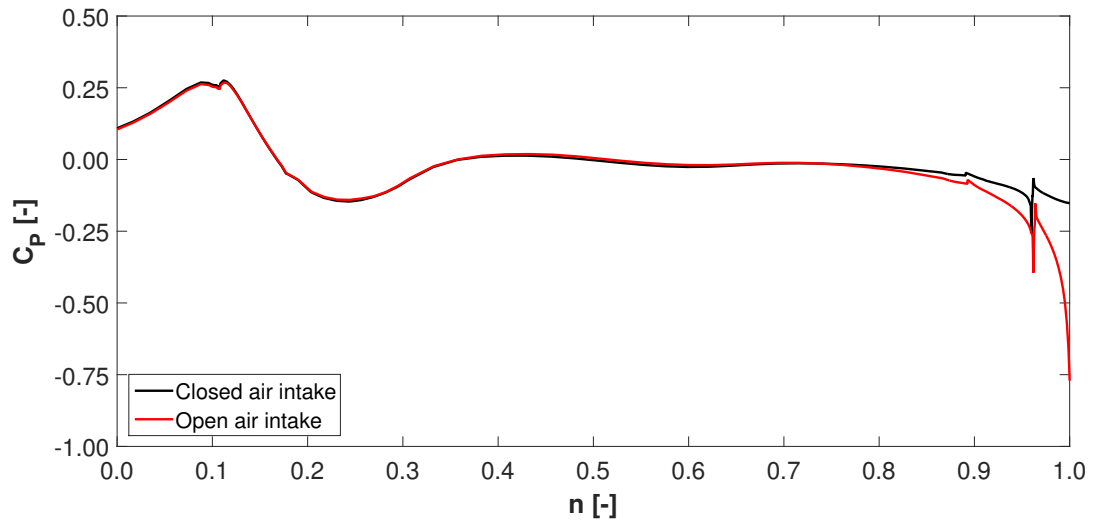
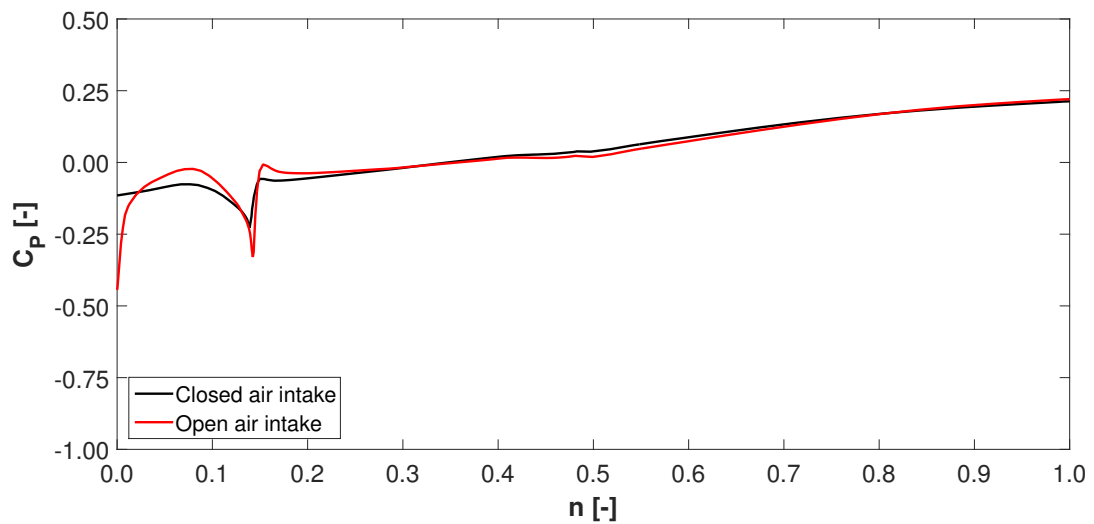
Figure 5.14: Line 7 -  $n = 0.10$ 

Figure 5.15: Definition of Lines 8-9 - Comparison between CFD simulations



Figure 5.16:  $C_p$  distribution on Line 8 - Comparison between CFD simulationsFigure 5.17:  $C_p$  distribution on Line 9 - Comparison between CFD simulations

### 5.3 Comparison between CFD and experimental data

With regard to the lines positioned on the helicopter surface, Figure 5.22, 5.24, 5.25, 5.27, 5.28, 5.30, 5.32, 5.35 show that there is a very good similarity between the CFD results and the experimental data. The CFD distributions strictly follow the experimental ones in the forward side of the helicopter: in this region the flow is slightly accelerated due to the curvature of the geometry and the  $C_P$  undergoes a faint drop. Even inside the intake and in the following region, in the rear part of the helicopter, the CFD is able to accurately simulate the flow and to reproduce even complicated flow structures. Only in the region preceding the air intake, definable in the interval between  $s = 0.7$  and  $s = 0.9$  in Figure 5.24, 5.27, 5.30, the difference is wider: in this region, in the CFD simulation, the flow is already affected by the presence of the air intake, that causes an acceleration and a consequent drop in the  $C_P$  distribution. On the contrary, the experimental data exhibit a constant trend of the  $C_P$ , indicating a constant velocity.

Compared to the experimental data, the CFD is able to properly simulate the  $C_P$  distribution on the EPC line (Figure 5.37); some small differences are present, in particular in the central part of the line, but the results are anyway satisfying given the difficulty of faithfully simulating the flow in this region due to the complexity of the geometry.

The  $C_P$  distribution on the EID lines is represented in Figure 5.43, 5.44, 5.46-5.51. The  $C_P$  exhibits a quite constant trend in the first part of the line, both in the fore and in the rear side of the EID; in this region the comparison between the CFD simulation and the experimental test shows a very good similarity in the results. In the last part of the line, for  $s$  higher than 0.6, the behaviour of flow differentiates in the front and in the back side of the EID, even though both of them manifest a negative  $C_P$ . In the fore part, the  $C_P$  slightly decreases and the CFD results do not completely follow the experimental values. On the contrary, in the rear part, the flow is accelerated with higher intensity, the  $C_P$  undergoes a more accentuate drop and a slight flow separation occurs (Figure 5.45); nevertheless, the CFD values remain closer to the experimental ones.

#### 5.3.1 Flow structure

**Engine air intake** On Line 6, at  $s$  higher than 0.9, the  $C_P$  exhibits a significant drop, to which an almost constant trend follows (Figure 5.30). In this region the air flow encounters the intake and is sucked into the engine: it is then accelerated leading to a strong reduction of static pressure. However, part of the flow separates from the wall and a recirculation area develops in the flow field (Figure 5.31). On Line 7, at  $s$  equal to 0.1, corresponding to the wall located in the back side of the intake, a stagnation point is present (Figure 5.32, 5.33): the air flow below enters the engine, whereas the one above is accelerated following the shape of the helicopter geometry. This explains why, in this region, the pressure undergoes a strong increase and a following drop. An analogous situation is found also on Lines 2-3, 4-5 and 8.

**Engine plenum chamber** Figure 5.37 shows that, in proximity of  $s$  equal to 0.15, a significant  $C_P$  drop occurs: in this region, part of the flow crashes against the external surface of the intake and is strongly decelerated, while part of it enters the EPC and deviates its trajectory in order to

follow the intake entrance curvature (Figure 5.38). However, the flow is not completely able to keep attached to the surface, leading to a small separation and to a consequent pressure growth. Proceeding along Line 9, other considerable  $C_P$  variations are found at  $s$  included between 0.5 and 0.7, where two distinct vortexes are present. The reader should note that, in this region, the flow direction is actually opposed to the line direction (compare Figure 5.52 with Figure 5.36); the following description will account for the first one. With regard to the first vortex, the flow initially accelerates and separates, leading to the vortex formation and causing a marked  $C_P$  decrease followed by a rapid increase, and later decelerates and re-attaches to the EPC surface, producing an additional pressure growth (Figure 5.39). With regard to the second one, due to a vortex contraction, the flow is firstly forced to increase its velocity, causing a drop in the  $C_P$  trend, and is again accelerated after it has re-attached to the surface (Figure 5.40). At the end of Line 9, in the neighbourhood of  $s$  equal to 0.9, the  $C_P$  undergoes a significant growth caused by the flow lines crashing against the external part of the air intake (Figure 5.41).

**Engine intake duct** As previously illustrated, in the final part of Lines 11, 13, 15 and 17, defined in the back side of the EID, due to the wall curvature, a slight flow separation occurs. As a matter of fact, the mass flow rate required to feed the engine and the relatively small duct cross section in which the air is forced to flow lead the flow to accelerate and to reach Mach numbers close to 0.6. The pressure is firstly subject to a drop, corresponding to the flow acceleration, and, later, to a little growth leading to the flow separation. The velocity distribution in this region is shown in Figure 5.45.

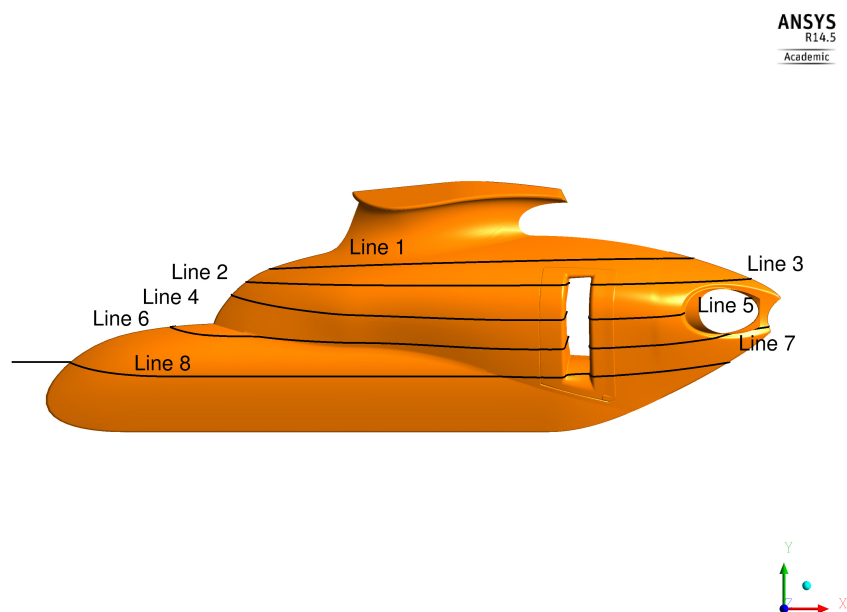


Figure 5.18: Definition of lines on the helicopter surface - Comparison with experimental data

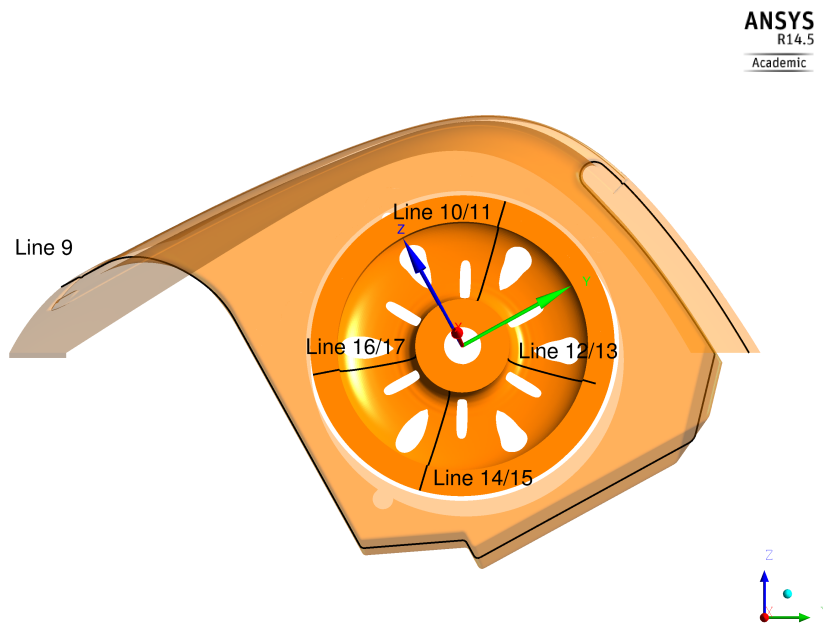


Figure 5.19: Definition of lines on EID and EPC - Comparison with experimental data

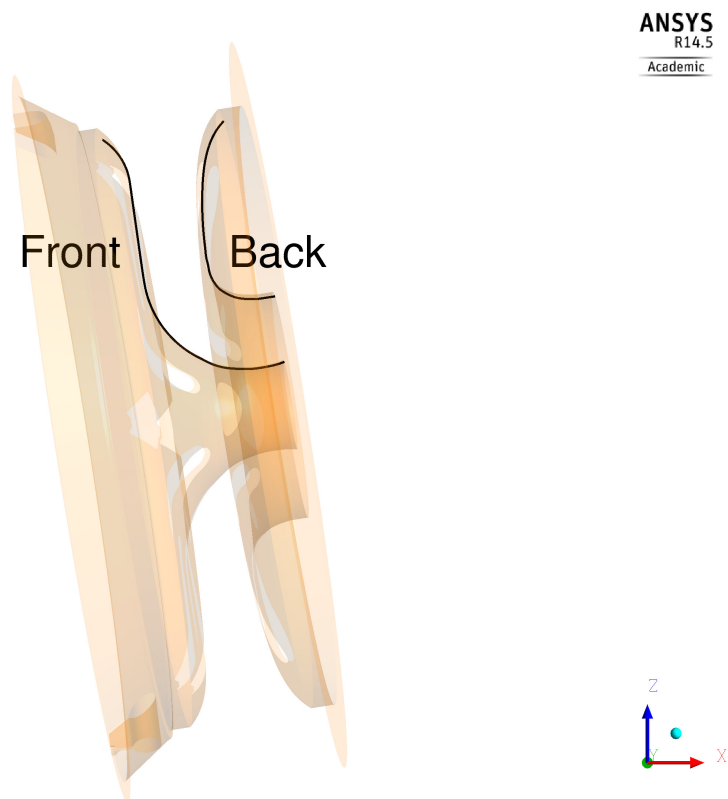


Figure 5.20: Fore and rear line on the EID - Comparison with experimental data

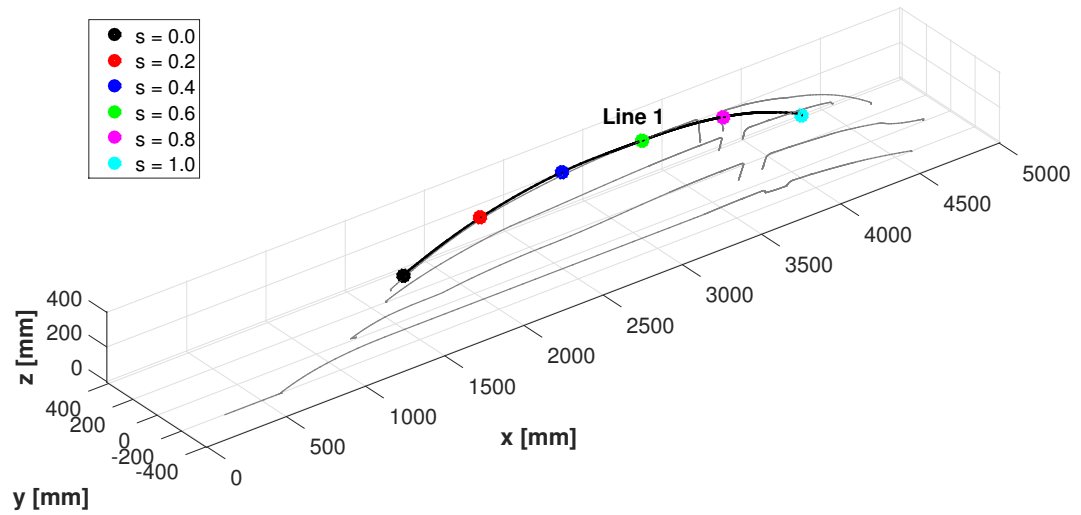
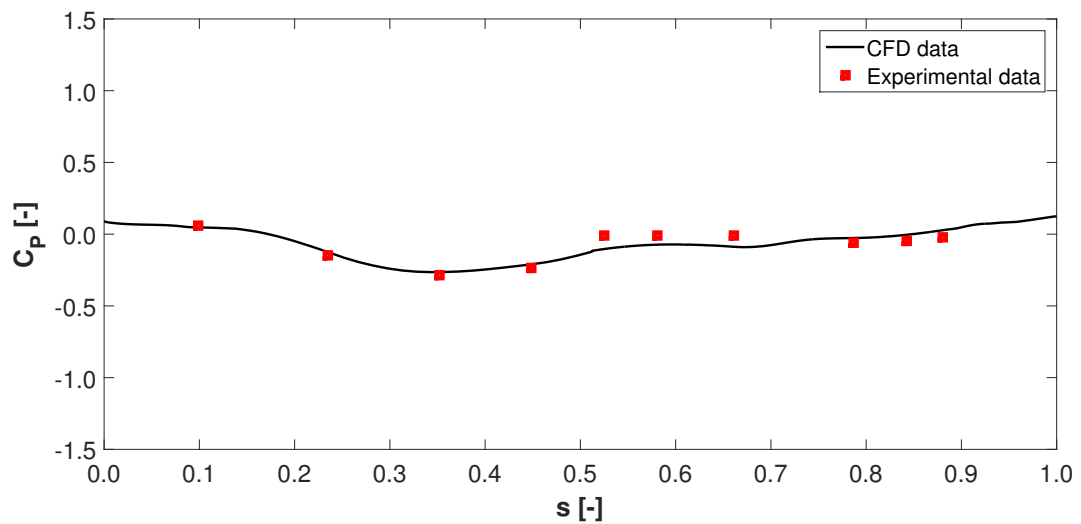


Figure 5.21: Definition of Line 1 - Comparison with experimental data

Figure 5.22:  $C_p$  distribution on Line 1 - Comparison with experimental data

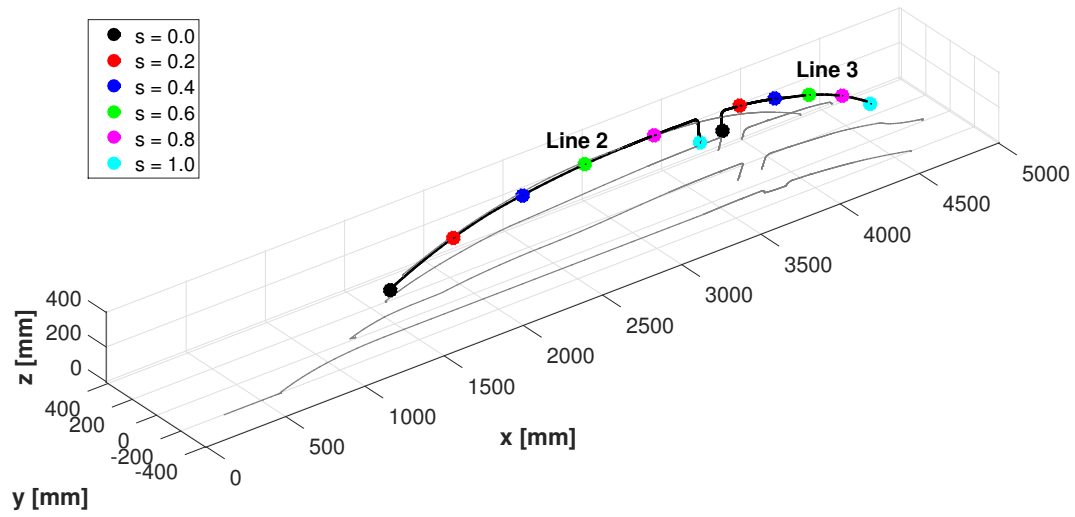


Figure 5.23: Definition of Lines 2-3 - Comparison with experimental data

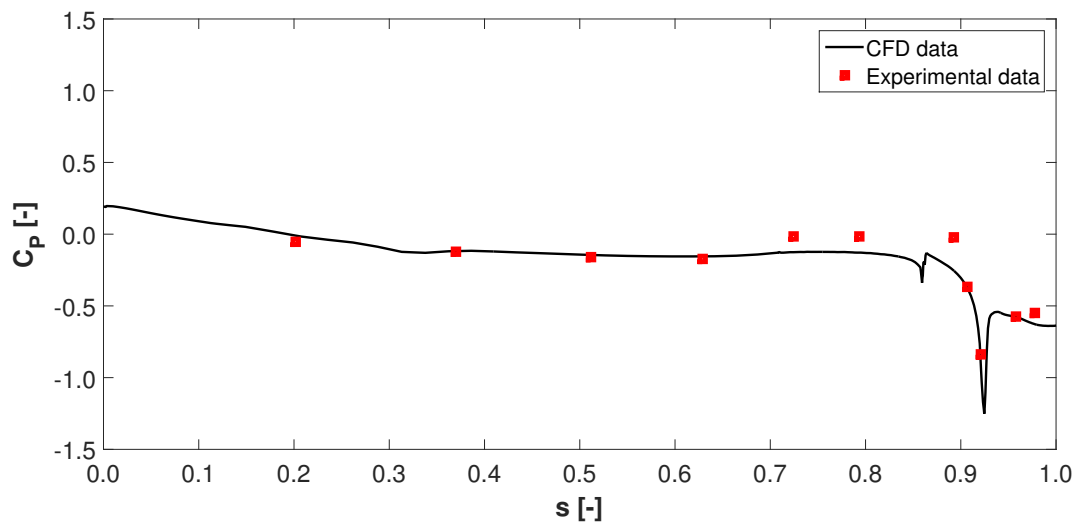


Figure 5.24:  $C_p$  distribution on Line 2 - Comparison with experimental data

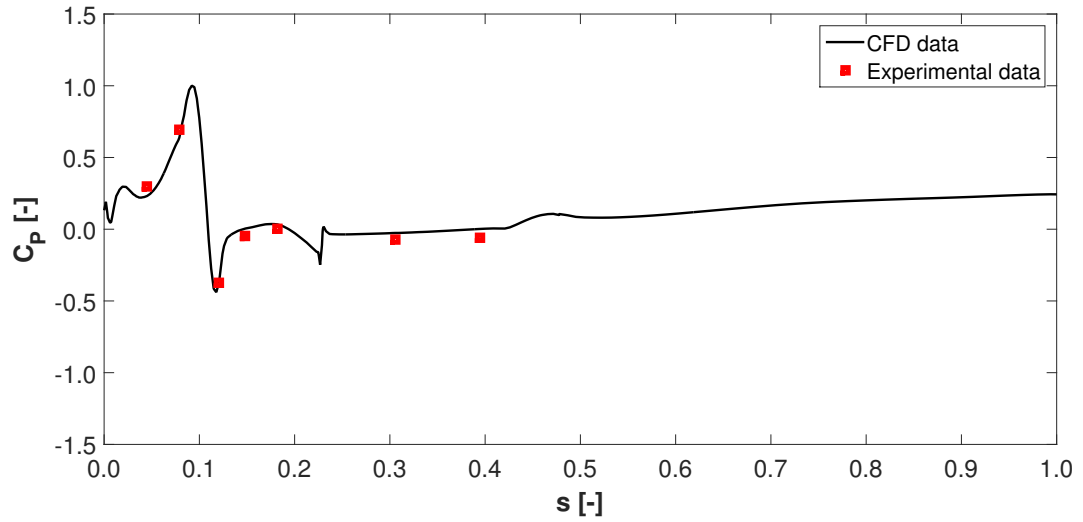


Figure 5.25:  $C_P$  distribution on Line 3 - Comparison with experimental data

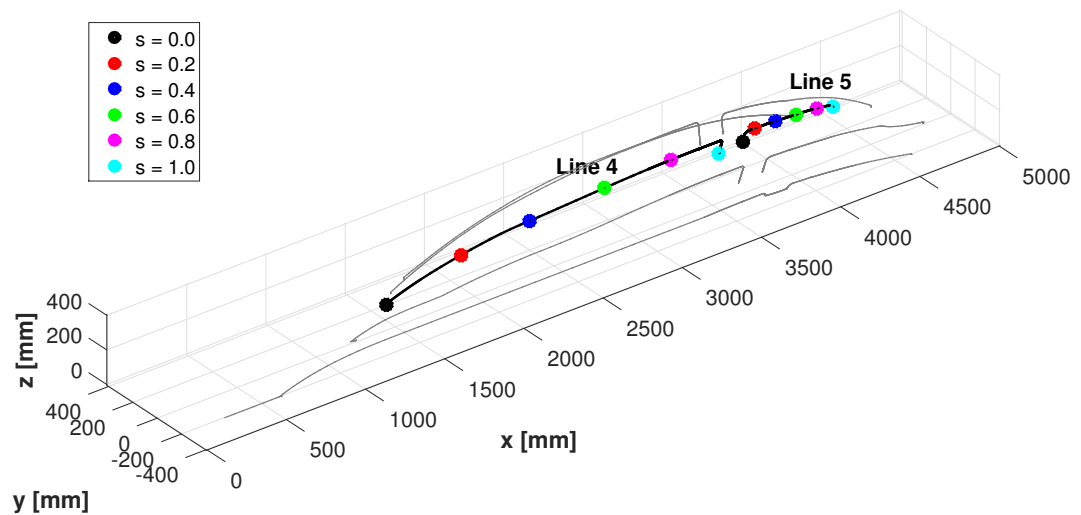


Figure 5.26: Definition of Lines 4-5 - Comparison with experimental data

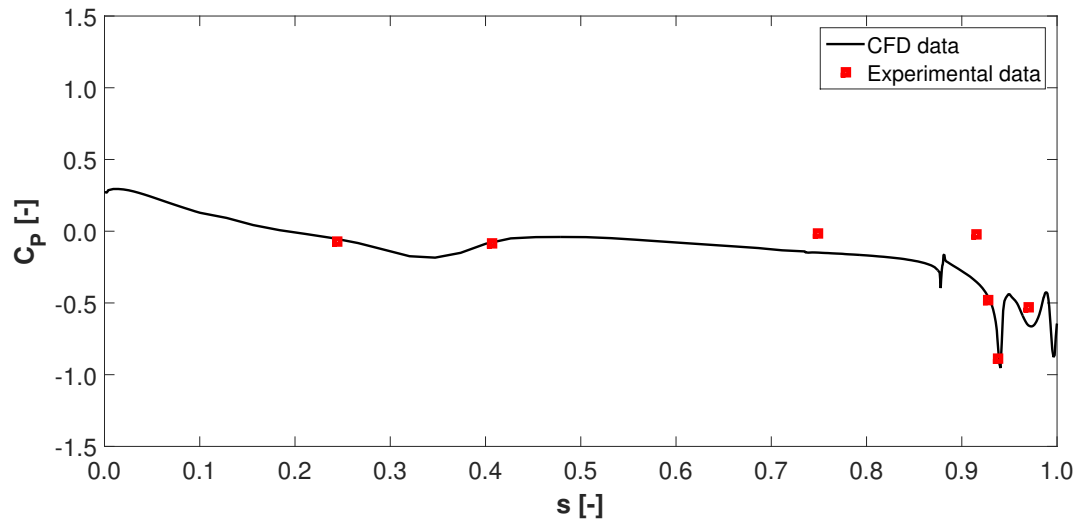


Figure 5.27:  $C_P$  distribution on Line 4 - Comparison with experimental data

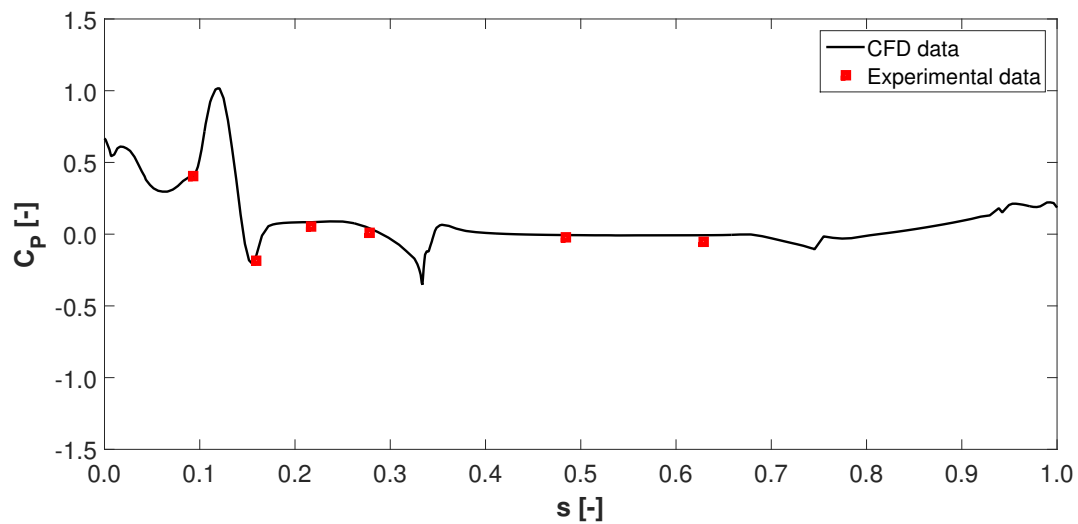


Figure 5.28:  $C_P$  distribution on Line 5 - Comparison with experimental data



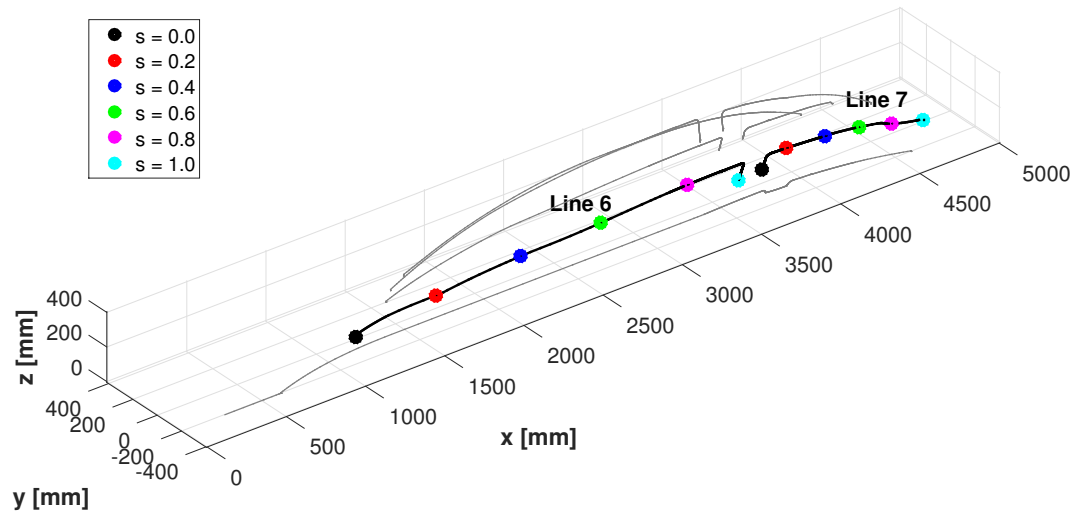
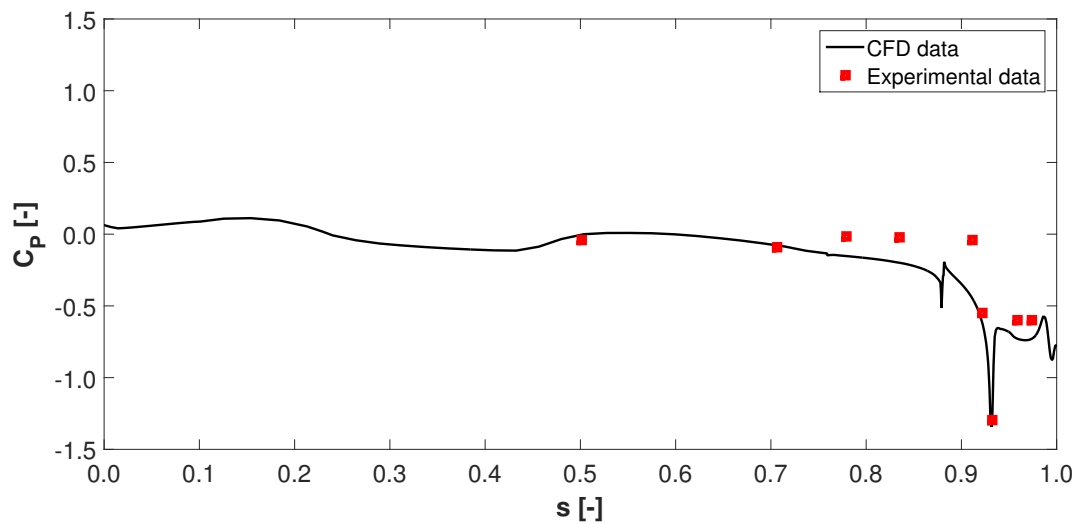


Figure 5.29: Definition of Lines 6-7 - Comparison with experimental data

Figure 5.30:  $C_p$  distribution on Line 6 - Comparison with experimental data

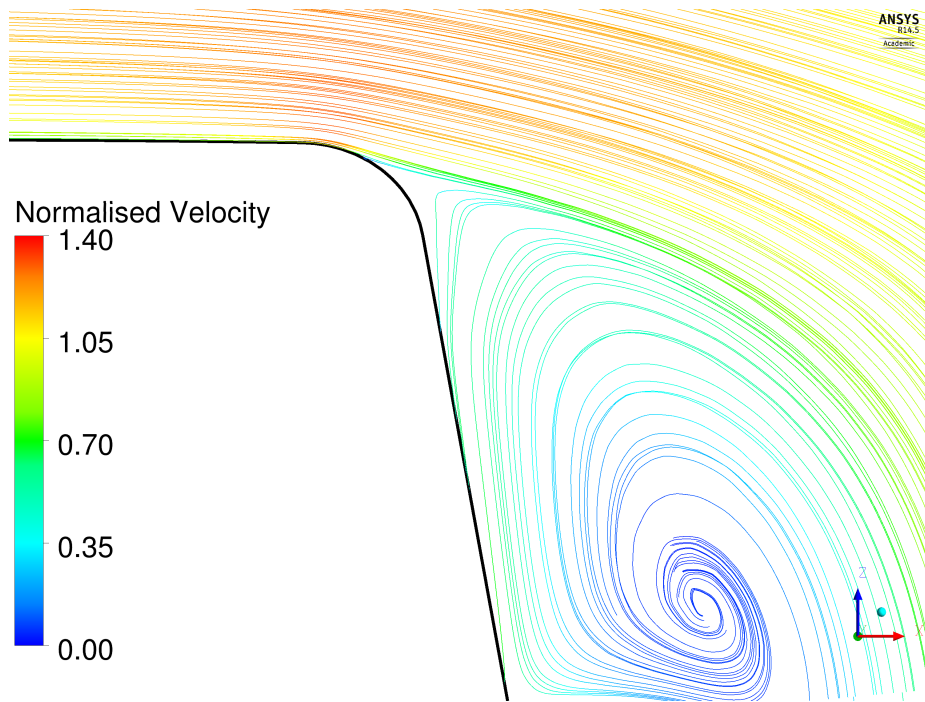


Figure 5.31: Line 6 -  $s = 0.90$

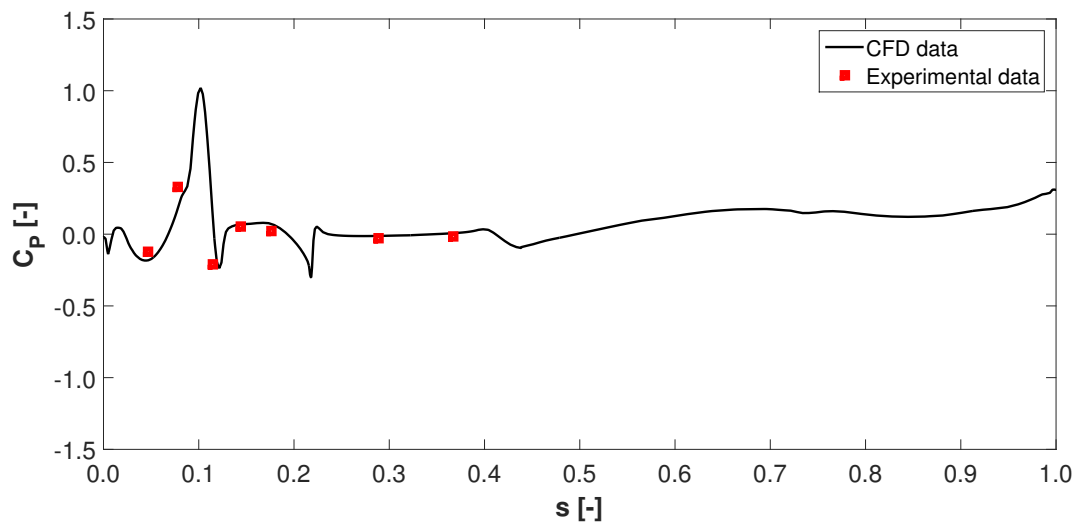


Figure 5.32:  $C_p$  distribution on Line 7 - Comparison with experimental data

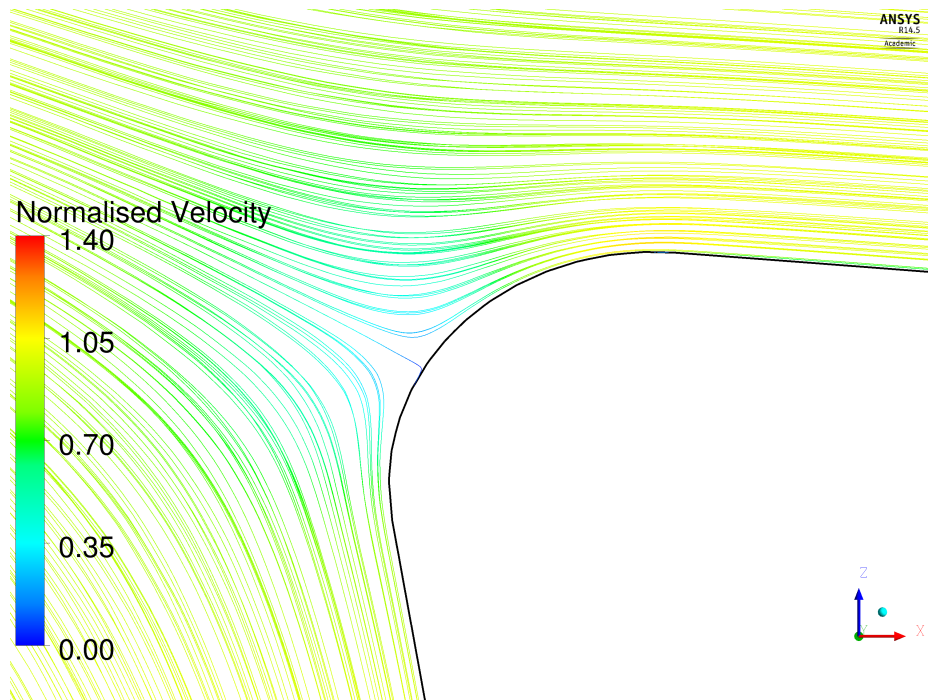


Figure 5.33: Line 7 -  $s = 0.10$

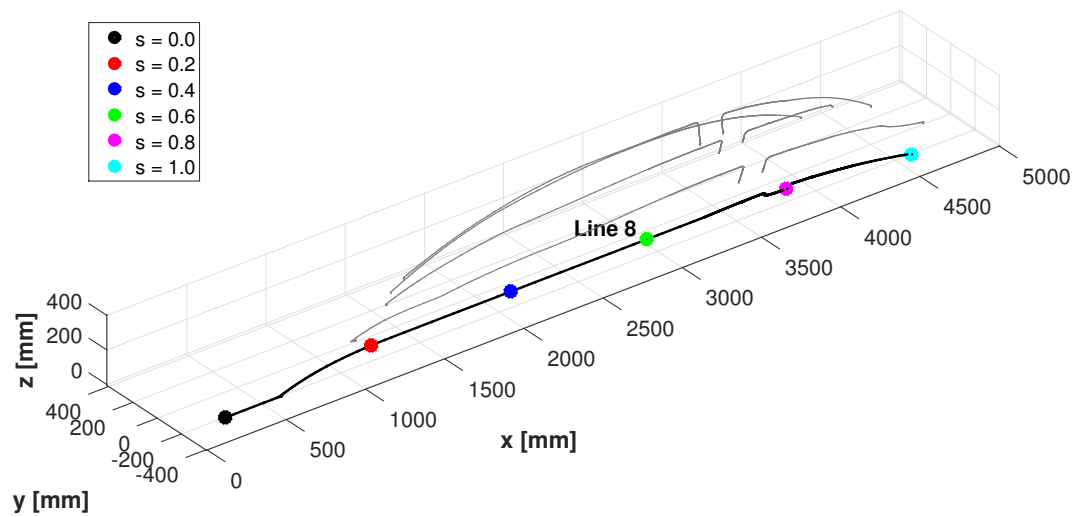


Figure 5.34: Definition of Line 8 - Comparison with experimental data

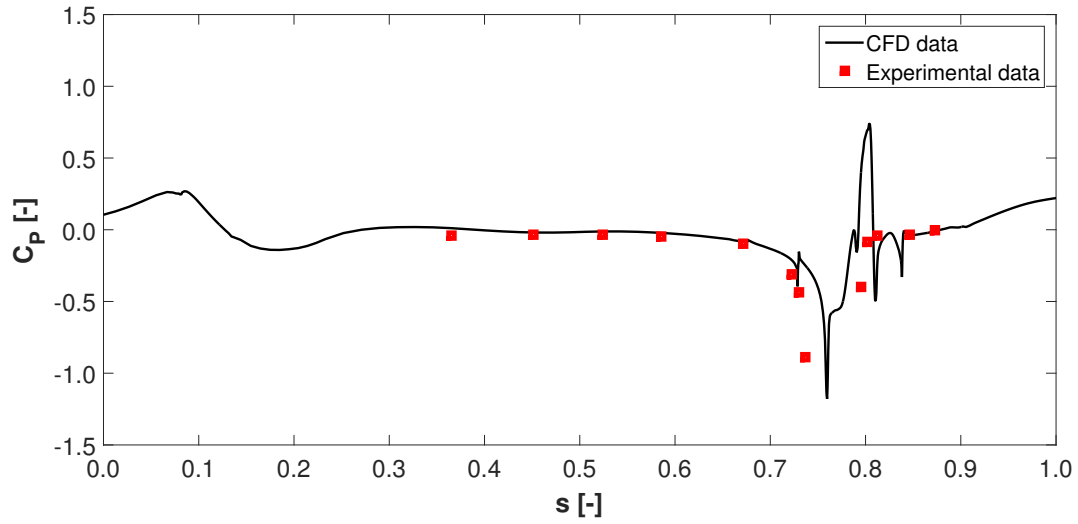


Figure 5.35:  $C_p$  distribution on Line 8 - Comparison with experimental data

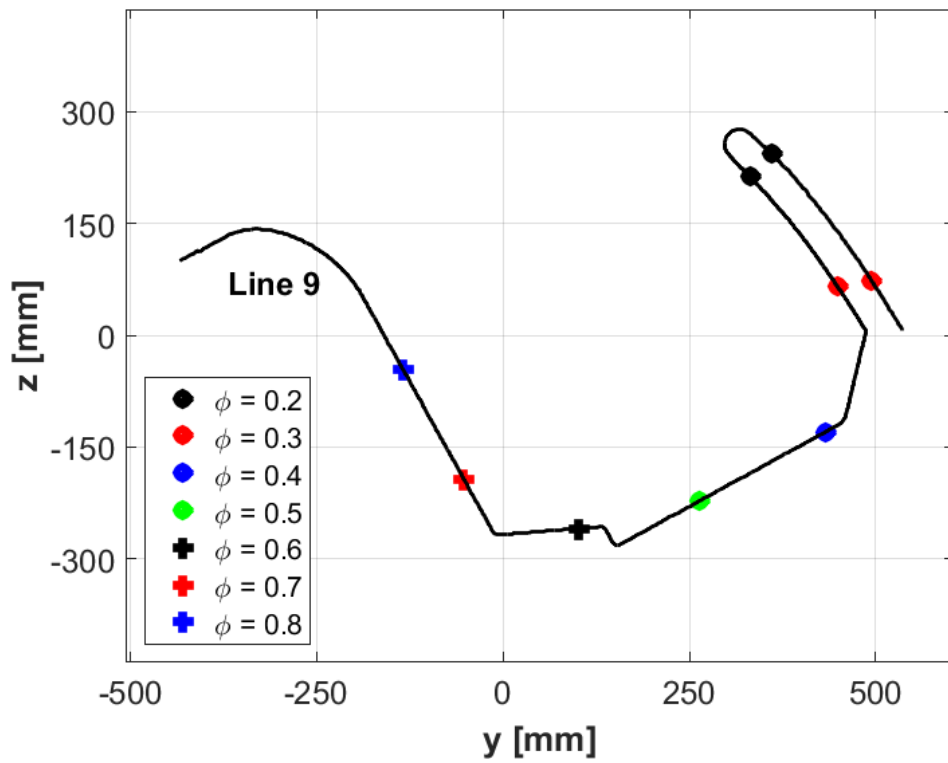
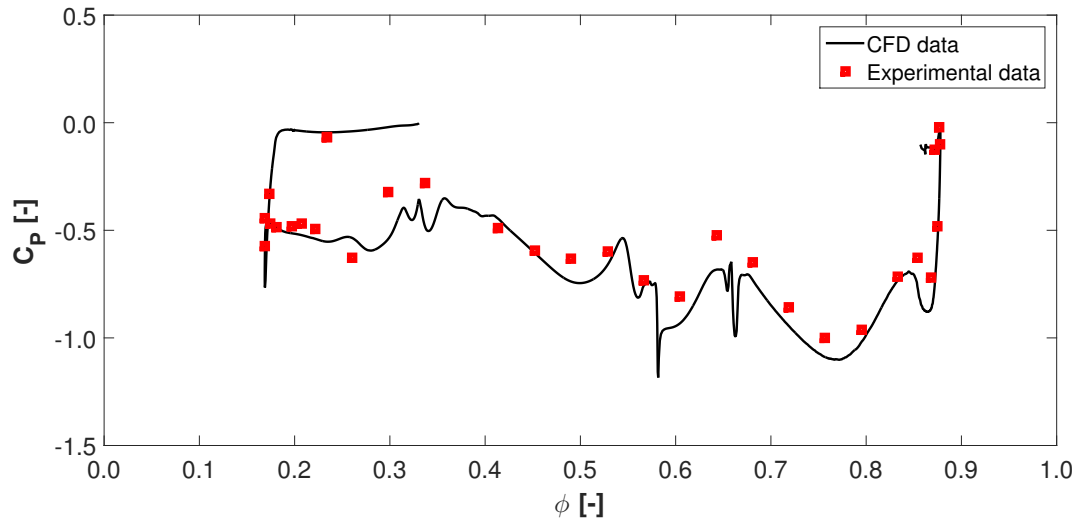
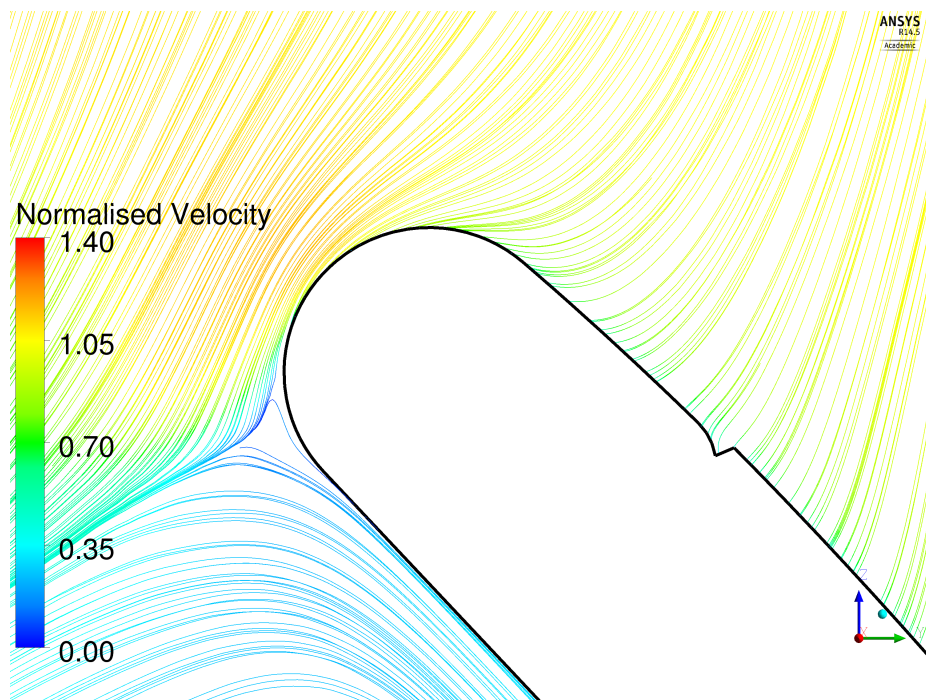
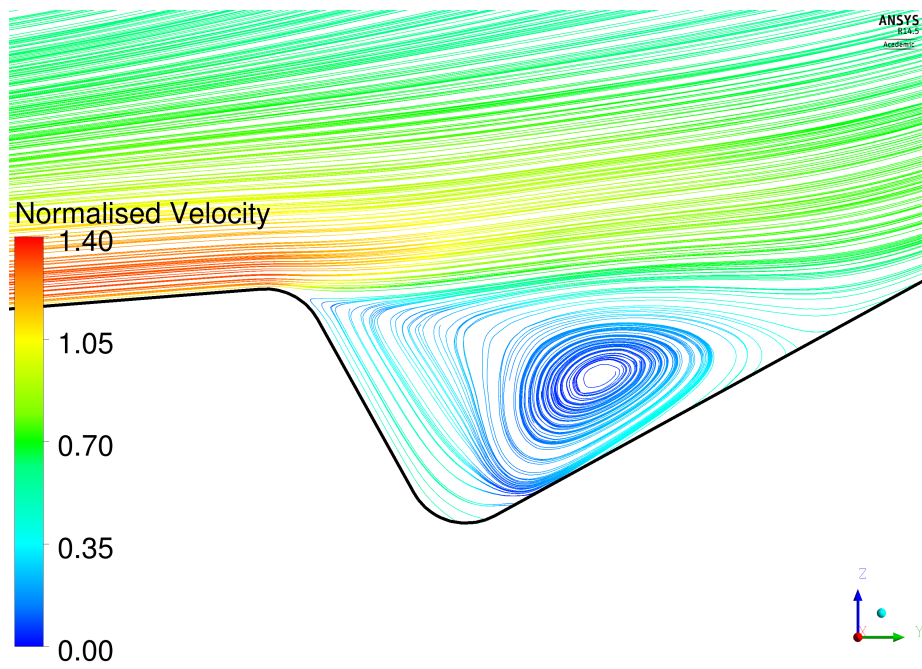
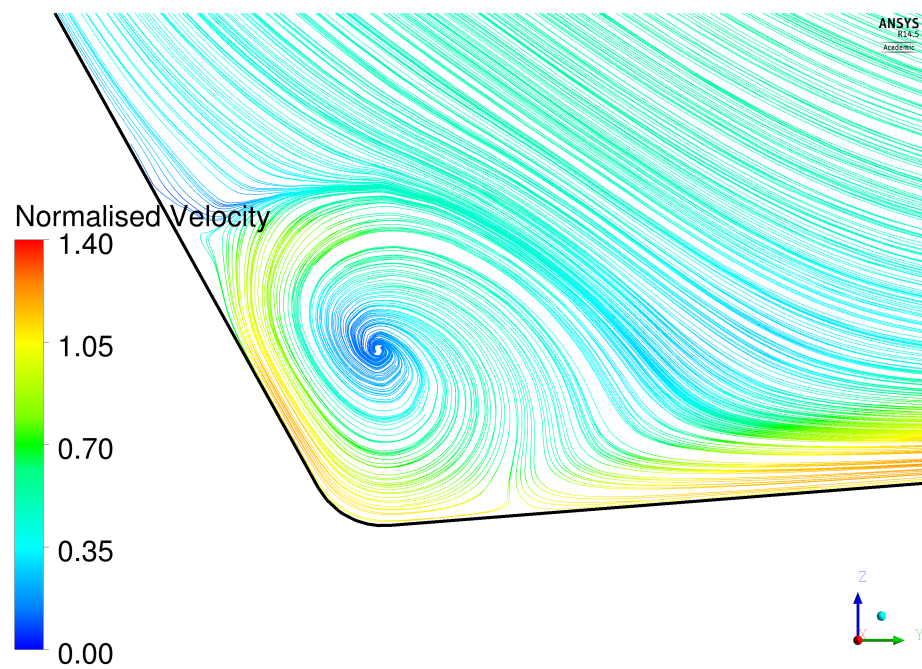


Figure 5.36: Definition of Line 9 - Comparison with experimental data

Figure 5.37:  $C_p$  distribution on Line 9 - Comparison with experimental dataFigure 5.38: Line 9 -  $s = 0.15$

Figure 5.39: Line 9 -  $s = 0.55$ Figure 5.40: Line 9 -  $s = 0.65$



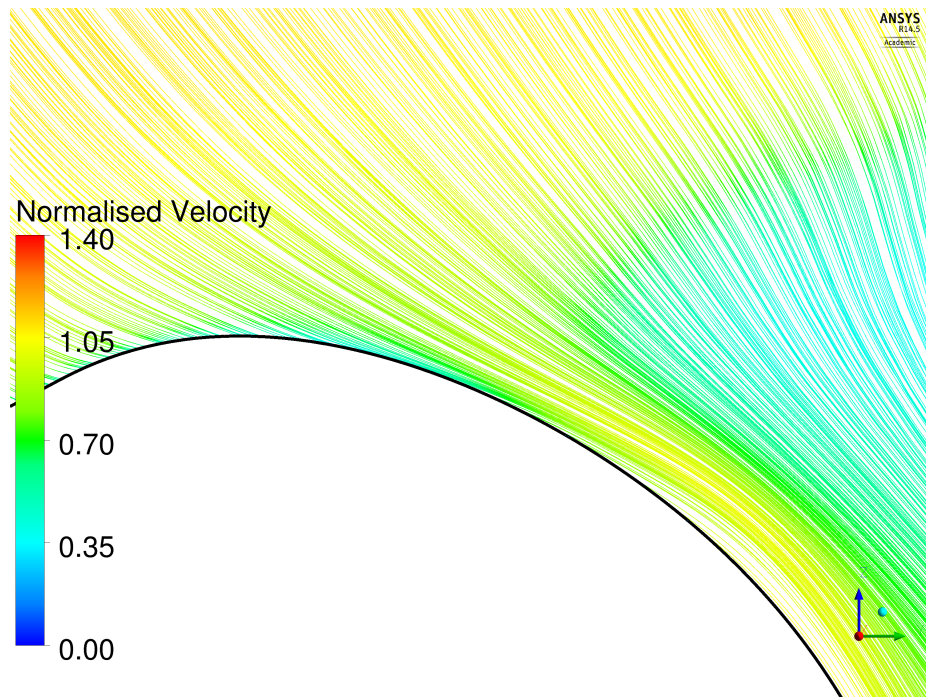
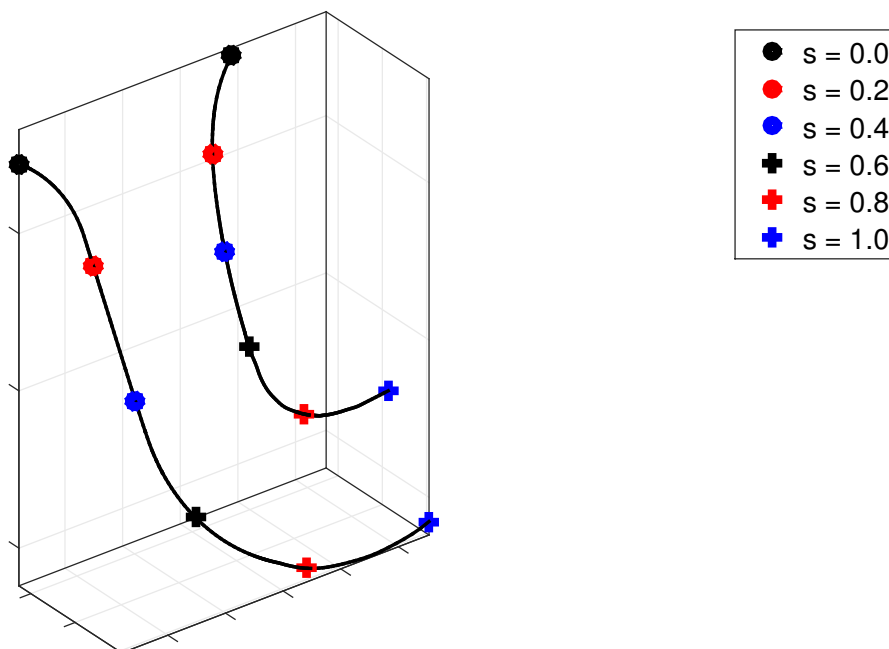
Figure 5.41: Line 9 -  $s = 0.85$ 

Figure 5.42: Definition of EID lines - Comparison with experimental data

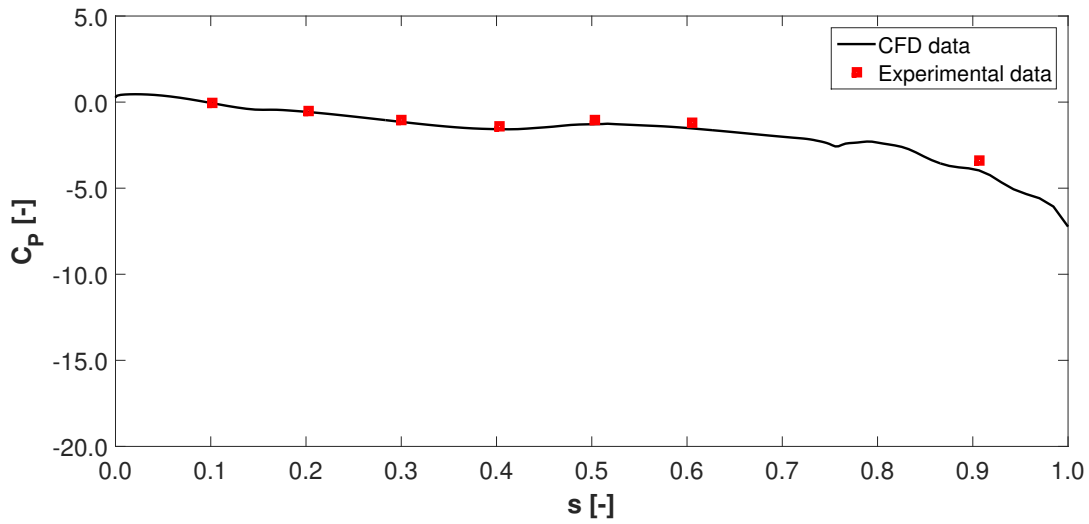


Figure 5.43:  $C_P$  distribution on Line 10 - Comparison with experimental data

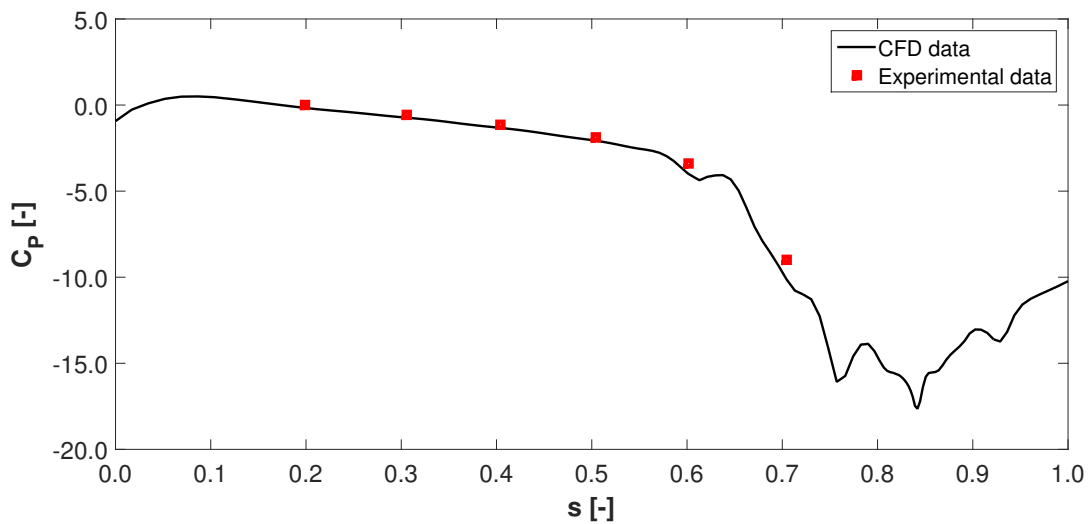
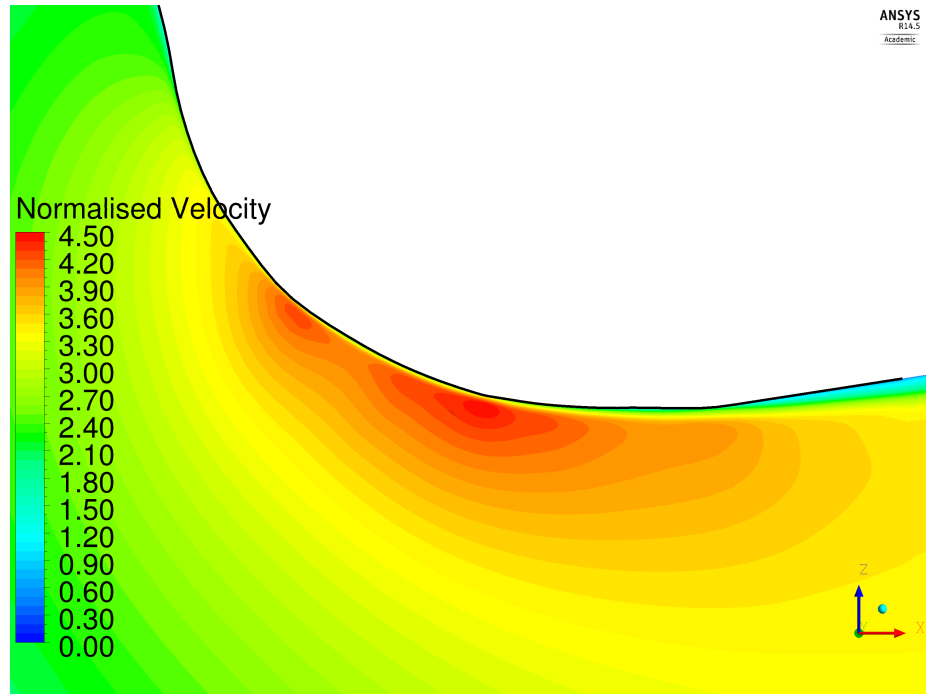
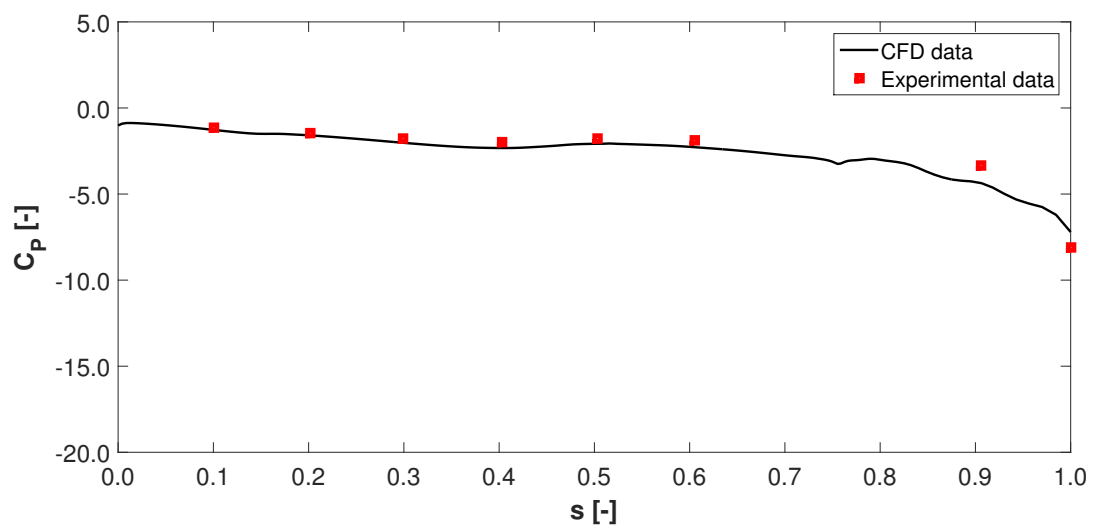


Figure 5.44:  $C_P$  distribution on Line 11 - Comparison with experimental data



Figure 5.45: Line 11 -  $s = 0.85$ Figure 5.46:  $C_p$  distribution on Line 12 - Comparison with experimental data

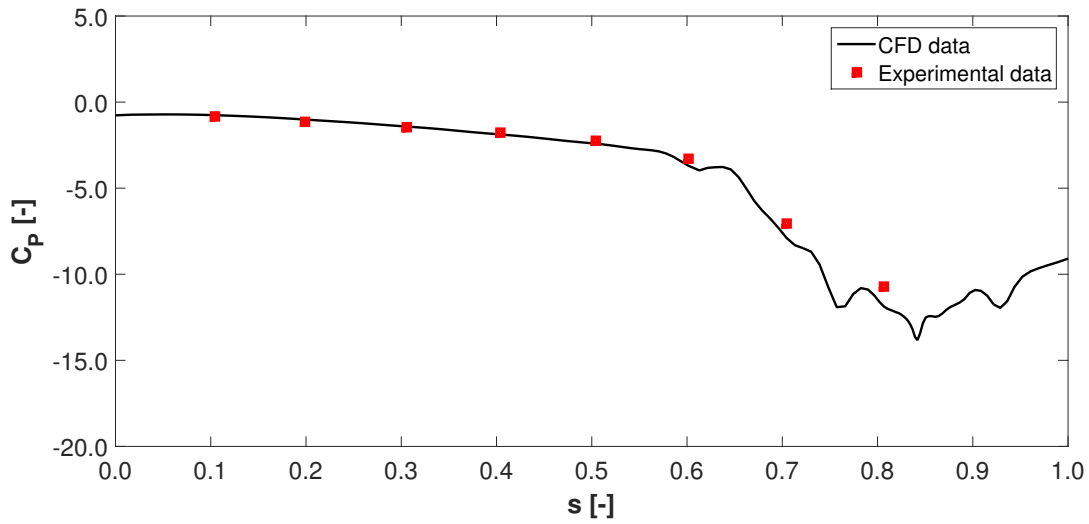


Figure 5.47:  $C_P$  distribution on Line 13 - Comparison with experimental data

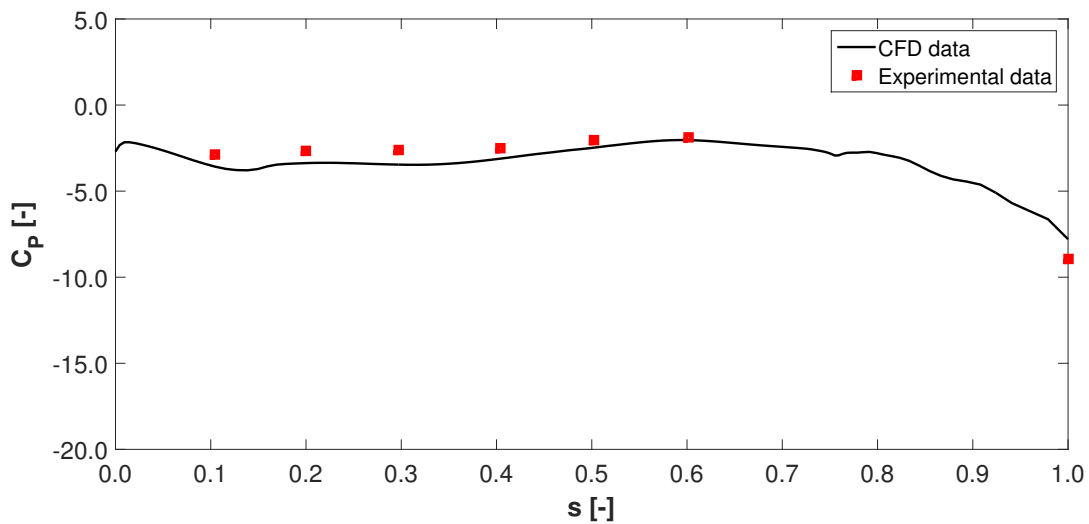


Figure 5.48:  $C_P$  distribution on Line 14 - Comparison with experimental data

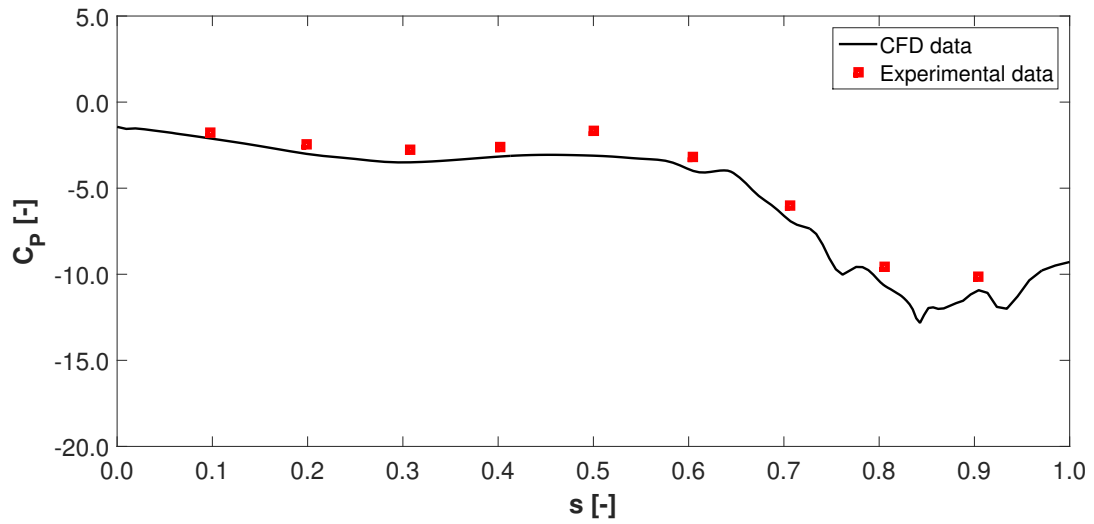


Figure 5.49:  $C_P$  distribution on Line 15 - Comparison with experimental data

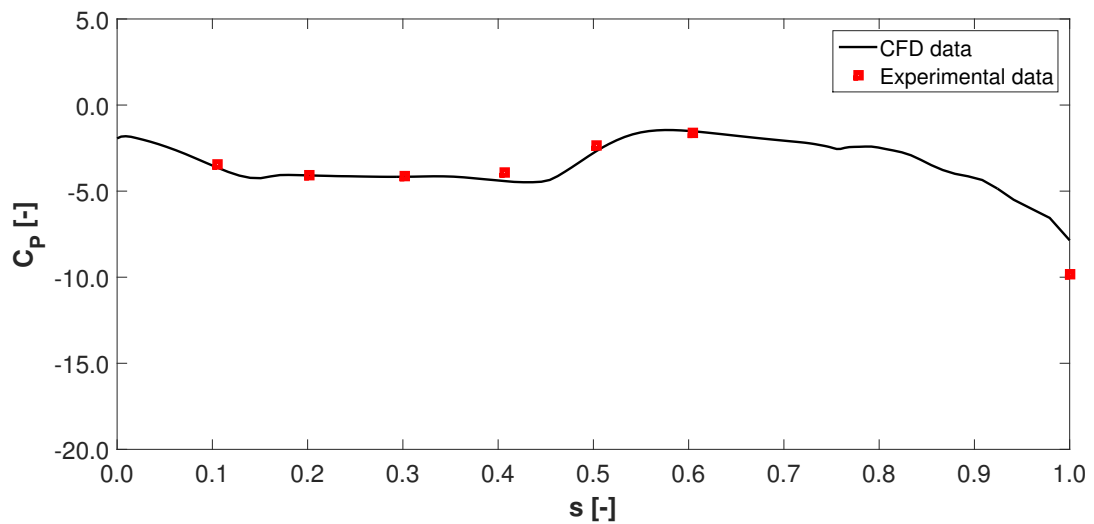


Figure 5.50:  $C_P$  distribution on Line 16 - Comparison with experimental data

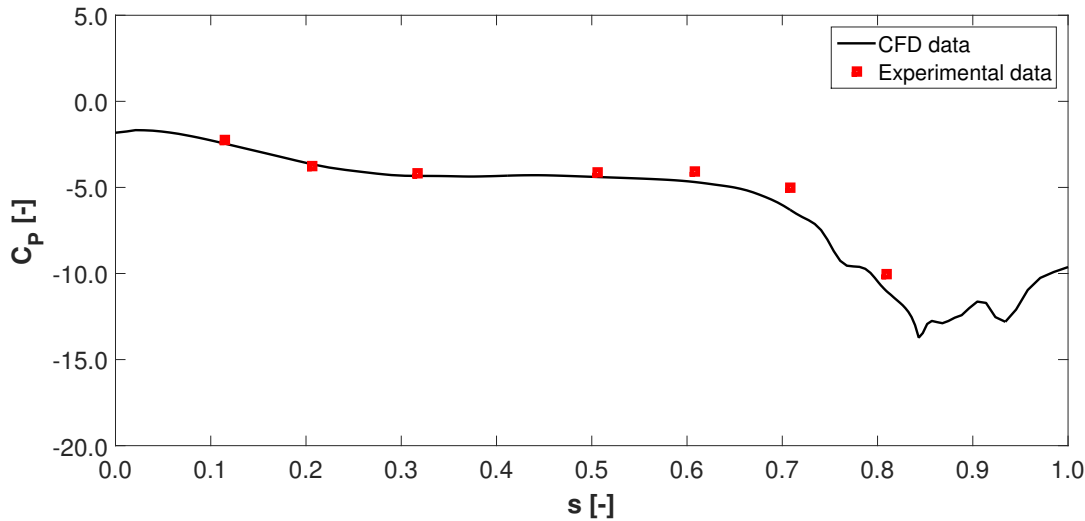


Figure 5.51:  $C_P$  distribution on Line 17 - Comparison with experimental data

## 5.4 Flow field in the engine air intake

In Section 5.3 the good quality of the results obtained by means of the CFD simulation is proved; the performed analysis allows us to study the flow field in the inner volume of the engine air intake and to expect an accurate reproduction of the flow. The investigation will concern the engine plenum chamber, the engine intake duct and the aerodynamic interface plane.

**Engine plenum chamber** Figure 5.52 is explanatory for the air flow field in the EPC. The flow enters the EPC from the top, where the intake is located; here, it is decelerated, coming into the EID at low velocity. Moreover, the picture shows that the air approaches the EID from all directions, since part of the flow circulates in the EPC and arrives in the EID passing through the lateral and the lower entrances: the velocity of the flow immediately entering the EID is higher than that circulating in the EPC. The effects of the velocity distribution in this region are notable in Figure 5.43, 5.44, 5.46-5.51, which show lower pressures on Line 14, 15, 16 and 17, where the highest velocities are present; this consideration is valid at low  $s$  only.

**Engine intake duct** The plane used to obtain Line 10 and 11 is here employed as an example to show the velocity distribution inside the EID (Figure 5.53); the bottom side of the plane is approximately corresponding to the region where Line 14 and 15 are located. The picture shows that the flow enters the EID at low velocity, as above illustrated: however, it is quite clear

that velocity at EID's bottom entry is higher than on the top, as confirmed by the comparison between Figure 5.48, 5.49 and 5.43, 5.44. The flow is subsequently accelerated as the suction effect becomes stronger, approaching the AIP at Mach number close to 0.6; on the AIP the flow field presents higher velocities in the upper side of the plane, leading to lower pressures as shown in the previously mentioned pictures. Figure 5.53 moreover shows that a small flow separation occurs at the entry of the ring-shaped duct, as previously described.

**Aerodynamic interface plane** The study of velocity distribution on the AIP assumes great importance, as the AIP is taken as reference for the flow conditions at the compressor entry. The velocity field is not completely homogeneous, since higher velocities are present in correspondence to the EPC's entry, as a result of the flow field in the EPC itself. The highest gradient is notable in the external part of the surface, where the influence of the flow field in the EPC is greater; on the contrary, in the internal part a more uniform velocity field is present. As further element highlighting the CFD simulation's accuracy, maximum velocity occurring on the AIP, taken both from the numerical simulation and the wind tunnel measurements, is studied: as a matter of fact, the difference between the numerical and the experimental values is equal to 11.85%.

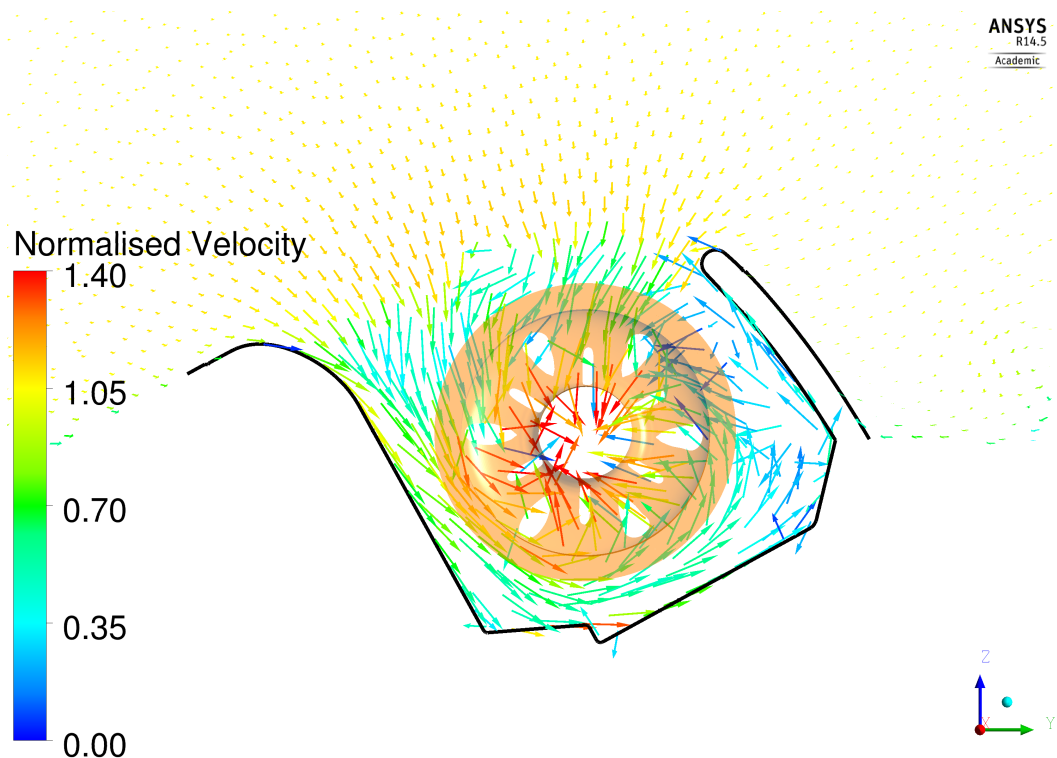


Figure 5.52: Velocity vectors in the EPC

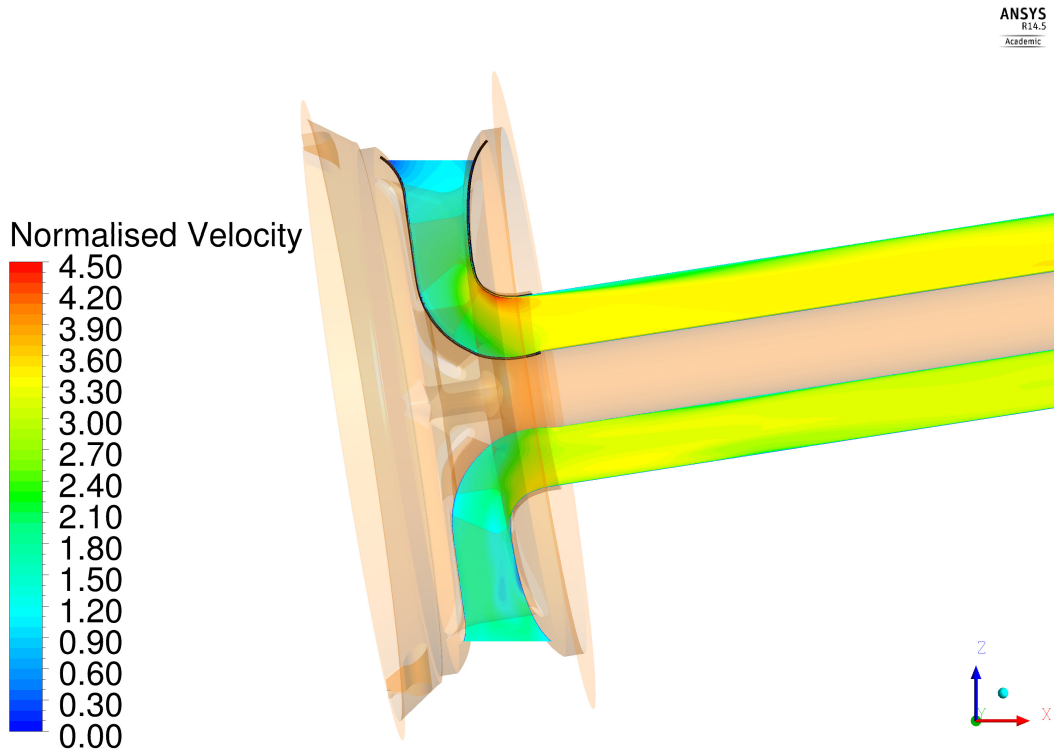


Figure 5.53: Velocity distribution in the EID

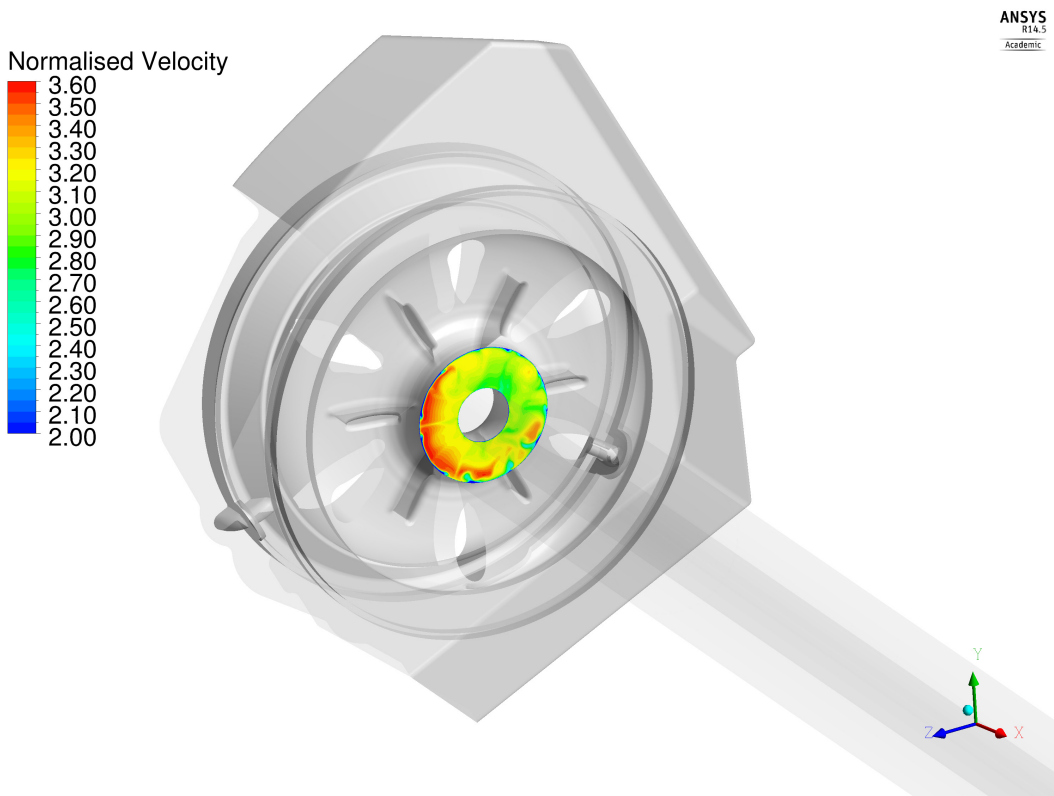


Figure 5.54: Velocity distribution on the AIP

## Chapter 6

# Analysis of screens

In this chapter the employment of screens in CFD simulations will be studied. As previously illustrated in Chapter 4, the engine air intake developed by Airbus Helicopter would include the presence of two screens, one at the air intake entrance and one within the plenum chamber. In the first part, a description concerning the properties of a flow striking a screen will be provided; in the final part, the analysis will more specifically treat the numerical simulations.

With regard to the last part of the chapter, two different approaches for the CFD simulation of a flow striking a screen will be described. The description will especially focus on the study of a loss coefficient model, defined starting from mathematical models and experimental data taken from literature; the screens of the Airbus Helicopter's design will be employed as reference.

### 6.1 Screens of the engine air intake

The so-called "engine air intake screen" is installed on the top of the engine air intake with the target of protecting the engine against foreign object damage. At the rearward side of the engine air intake the grid features an offset, a sort of grid by-pass available in case of grid blockage or in case of icing. The second screen, defined as "engine screen" in the project, is installed within the plenum chamber at the intake duct entrance; its purpose is to increase the quality of the flow approaching the plenum chamber, guaranteeing a more uniform velocity, as well as protecting the engine against foreign objects.

**Engine air intake screen** The screen installed on the engine air intake consists of woven round wires. The geometrical specification of the grid is summarised in Table 6.1; the wire diameter is given in terms of a dimensionless parameter obtained by the ratio to the distance between the wires axes.

wire diameter	0.180
grid porosity	0.720

Table 6.1: Geometrical characteristics - Engine air intake screen

**Engine screen** The characteristics of the screen installed directly on the engine differ from those of the engine air intake screen. The engine screen consists of welded wires with a dimensionless diameter equal to 0.147 and a rectangular open area; in this specific case the dimensionless diameter has been calculated as the ratio to the distance that horizontally separates the wires axes. The geometrical specification of the grid are summarised in Table 6.2.

wire diameter	0.147
grid porosity	0.758

Table 6.2: Geometrical characteristics - Engine screen

## 6.2 Reproduction of screens in CFD simulations

The interdependence of the screen's geometrical characteristics, in particular the porosity and the wires' weaving, and the flow striking the screen is very strong. For this reason, it is important to accurately reproduce the geometry of the screens, in terms of wire dimensions and shapes, weaving and porosity. The attempt to faithfully recreate the geometry of the screens in ANSYS ICEM CFD is very expensive in terms of time; it probably would require a specific analysis, that cannot be performed in this work, given the different goals originally predetermined.

A possible alternative approach for the simulation of a screen stricken by an air flow is here described. The reproduction of the screen presence can be made using a porous domain, helpful to model flows where the geometry is too complex to be resolved with a grid, as explicitly stated in [5]. For such a type of domain a loss coefficient model, both for longitudinal and transversal directions, must be specified. As a consequence, it is clearly necessary to study and develop a loss coefficient model able to properly represent the screens' characteristics. This study will be presented in the following sub-sections; the engine air intake screen and the engine screen will be taken into account for the analysis.

**Directional loss model in ANSYS CFX-Solver** Momentum sources are used to model directional losses in porous regions under the specification of the stream-wise direction; in ANSYS CFX they are implemented as a force per unit volume acting on the fluid. Considering a stream-wise oriented coordinate system  $(x', y', z')$  such that the  $x'$ -axis is directed towards the stream-wise direction and the  $y', z'$ -axes define the transverse plane, the momentum losses are given by the following equations [7].

$$S_{M,x'} = -\frac{\mu}{K_{perm}^S} u_{x'} - K_{loss}^S \frac{\rho}{2} |\mathbf{u}| u_{x'} \quad (6.1)$$

$$S_{M,y'} = -\frac{\mu}{K_{perm}^T} u_{y'} - K_{loss}^T \frac{\rho}{2} |\mathbf{u}| u_{y'} \quad (6.2)$$

$$S_{M,z'} = -\frac{\mu}{K_{perm}^T} u_{z'} - K_{loss}^T \frac{\rho}{2} |\mathbf{u}| u_{z'} \quad (6.3)$$

In Equation 6.1, 6.2, 6.3  $K_{perm}^S$  and  $K_{perm}^T$  are the stream-wise and transverse permeabilities, that are actually not taken into account in the present case, and  $K_{loss}^S$  and  $K_{loss}^T$  are the



stream-wise and transverse quadratic loss coefficients.

See [7] for further information.

### 6.3 Air flow through a screen

The first step accomplished during the analysis was concerned with the study of a flow passing through a screen; in particular, the main kinematic and thermodynamics properties, such as static pressure, total pressure, velocity and turbulence, have been studied and a significant amount of data and theories have been taken from literature. The flow deflection caused by the presence of the screen has also been analysed.

**Pressure drop** As stated by [3], the higher the Mach number, the higher both the static pressure drop and the total pressure loss, until the highest obtainable Mach number is reached; this Mach number corresponds to the choked condition, since an additional increase in velocity does not lead to a Mach number increase ahead of the screen. Chocking of the flow occurs when a Mach number equal to one is entirely obtained across the openings in the screen; the choking condition defines the Mach number limit value that can occur in the flow ahead of the screen. There exist two different possibilities.

- if the total pressure ahead of the screen is kept constant, no additional increase in mass flow rate is possible.
- if the total pressure ahead of the screen is increased, the mass flow rate can be increased; the increase in mass flow rate will be accompanied by large losses. Therefore, it is desirable to be careful in the selection of screen mesh and wire diameter in order to avoid the approaching of choking Mach number at maximum operating velocity.

The speed at which the choking occurs can be related to the screen variables by the following equation, where  $m$  is defined as the wires number per inch and  $d$  as the wire diameter also measured in inches. The equation is derived from the continuity equation, the adiabatic law and Bernoulli's equation for compressible flow.

$$1 - 2md + m^2d^2 = \frac{M_{choke}}{0.579 (1 + 0.2M_{choke}^2)^3} \quad (6.4)$$

In [31] screens of several porosities are tested and a regression analysis of results is carried out to obtain a mathematical relation between screen pressure  $P$ , u-component of velocity and porosity  $\beta$ , respectively expressed in Pascal, feet per minute and decimal percentage.

$$P = \frac{u^{1.50}}{42.8 \cdot 10^{2.59\beta}} \quad (6.5)$$

The equation shows that screen pressure increases with velocity, whereas it decreases with increasing porosity. This relation is ideally valid only for porosities defined between 0.30 and 0.55, even if it can probably be extended in either direction for a quantity equal to 0.10 with reasonable confidence.

**Flow deflection** As stated in [33], a stream approaching a screen at some angle with respect to its normal is deflected towards the normal passing through it. Defining  $\theta$  as the angle of incidence, measured from the normal, and  $\psi$  as the corresponding angle of exit from the screen, it is found that  $\psi$  is lower than  $\theta$ . It is assumed that, when  $\theta$  approaches zero, the flow deviation is small; therefore, defining as  $\alpha$  the limiting value of  $\psi/\theta$  as  $\theta$  approaches zero, the empirical relation between  $\alpha$  and  $K_{\theta=0}$ , a parameter that will be defined in the following sub-section, can be expressed as in Equation 6.6.

$$\alpha = \frac{1.1}{\sqrt{1 + K_{\theta=0}}} \quad (6.6)$$

It follows that, for a given screen over a nominal velocity range, the ratio of the angle of flow exit to the angle of flow incidence is approximately constant.

**Velocity** As stated in [28], the flow resistance of a wire screen is approximately proportional to the square of the speed. Consequently, the resistance in a flow which manifests a local variation in speed is greater at points in which the velocity is higher: the velocities are then comparable after the passage through the screen. However, this comparableness is always obtained at the expense of a great pressure drop in the screen.

With reference to  $\theta = 0$ , a moderate velocity difference,  $\Delta u$ , is approximately lowered to  $\delta u$  by a factor estimable as follows.

$$\frac{\delta u}{\Delta u} = \frac{1}{1 + K_{\theta=0}} \quad (6.7)$$

**Turbulence** The amount of turbulence at a given point in a stream is generally defined in terms of the root mean square of the velocity fluctuations at that point. The longitudinal and the lateral components of the fluctuations, denoted by  $u'$  and  $v'$  respectively, and the corresponding intensities,  $u'/U$  and  $v'/U$ , are commonly measured separately.

The damping produced by a screen is defined as the ratio between the intensity characterising the stream in a certain point after it has passed through the screen and the intensity at the same point in the absence of the screen. This ratio is called *reduction factor* and is usually denoted by  $f$ . Referring the subscript 2 to the intensity at a given point after the flow's passage through the screen and 1 to the intensity at the same point with the screen absent, the reduction factor is defined as follows.

$$f_u = \frac{(u'/U)_2}{(u'/U)_1} \quad (6.8)$$

$$f_v = \frac{(v'/U)_2}{(v'/U)_1} \quad (6.9)$$

The following considerations are based on the assumptions that the flow upstream of the screen is isotropic and homogeneous, that the turbulence level is small compared to the mean free-stream level and that the fluid is incompressible. The reduction factors can also be calculated in the following way, by using potential flow theory and accounting for boundary conditions on both sides of the screen.

$$f_u = \frac{1 + \alpha - \alpha K}{1 + \alpha + K} \quad (6.10)$$

$$f_v = \alpha \quad (6.11)$$

**Integral scale** The integral scale is defined as follows.

$$L_y = \int_0^\infty \frac{\overline{u_1 u_2}}{u_1' u_2'} dy \quad (6.12)$$

In Equation 6.12  $\overline{u_1 u_2}$  represents the mean product of the longitudinal fluctuations at points 1 and 2 separated by a lateral distance  $y$ , whereas  $u_1'$  and  $u_2'$  are the root mean square values of  $u_1$  and  $u_2$ . The equation shows that damping reduces the energy of all frequencies of the  $u$ -component of turbulence by the same factor, as the integral scale is not modified when turbulence is damped by a screen.

See [32, 33] for additional information about turbulence modification of a flow passing through a screen.

## 6.4 Loss coefficient

Since flow through a screen can occur only in the free spaces between wires, the resistance given by a screen depends on its porosity, defined as the ratio of open area to total area; the resistance is often expressed as function of the pressure drop occurring when the flow is perpendicular to the plane of the screen. Defining  $K_s$  as the *pressure-drop coefficient*, also called *loss coefficient*, depending on screen porosity and on Reynolds number computed using the wire diameter as reference length, the pressure drop is generally defined as in the expression reported in [33].

$$\Delta p = \frac{1}{2} \rho u^2 K_s \quad (6.13)$$

However, in more general terms, the angle of incidence of the approaching flow relative to the screen plane must be taken into account too. Therefore, within the following paragraphs, given the importance of using a complete loss model in order to get realistic results from a CFD simulation, both the normal and the tangential loss coefficient will be analysed as function of the angle of incidence.

**Loss coefficient models** All the loss coefficient models found in literature do not take into account the dependency on the angle of incidence of the flow approaching the screen; as a matter of fact, the pressure drop coefficient  $K_s$  is generally defined as function of porosity and Reynolds number only. Hence, the angle of incidence will be considered only later, in a successive analysis. Hereby, a list of mathematical models found in literature is given.

- <sup>1</sup>  $K_s = K_0 \left[ 0.785 \left( \frac{Re_w}{241} + 1.00 \right)^{-4} + 1.01 \right] (1 - \beta_s) + \frac{(1 - \beta_s)^2}{\beta_s^2}$
- <sup>2</sup>  $K_s = \left( \frac{1 - 0.95\beta_s}{0.95\beta_s} \right)^2 + \frac{55.2}{Re_w}$
- <sup>3</sup>  $K_s = K_{Re} K_0 (1 - \beta_s) + \frac{(1 - \beta_s)^2}{\beta_s^2}$

---

<sup>1</sup>from [8]

<sup>2</sup>from [32]

<sup>3</sup>from [19]

In the previous models  $\beta_s$ ,  $Re_w$ ,  $K_0$  and  $K_{Re}$  represent respectively screen porosity, Reynolds number defined using the wire diameter as reference length, a coefficient taking the screen typology into account and a coefficient taking the Reynolds number dependency into account;  $K_0$  and  $K_{Re}$  will be defined in Appendix C.

The similarity between the first and the third loss coefficient models is of great importance; they differ slightly only for the way in which the dependency on Reynolds number is treated. This will be better shown in the following two sub-paragraphs, where the loss coefficient dependency on Reynolds number and on screen porosity is analysed; the study and the following model implementation will take the engine air intake screens as reference.

### 6.4.1 Reynolds number sensitivity

The following graphs represent the loss coefficient trend computed as function of the Reynolds number, for four distinct porosity values. A special attention should be paid for Figure 6.2, 6.3, where the results relative to the porosities of interest are plotted, that are  $\beta = 0.720$  and  $\beta = 0.758$  for the engine air intake screen and the engine screen respectively. The reader will also note that different y-axes are employed in the figures in order to guarantee a better comprehension of loss coefficient trends; however, the same intervals width has been defined.

The difference between the curves relative to the first and the third model is very small, as expected; this is true in particular when high porosity values are considered. Moreover, it is important to underline that the dependency on Reynolds number is quite small, especially over  $Re = 500$ , where it becomes totally negligible. The second curve is shifted towards lower values, and also the trend is quite different from the one relative to the other two models; for the screen porosities of interest the difference is significant. Moreover, the dependency on Reynolds number is rather marked, at low values especially.

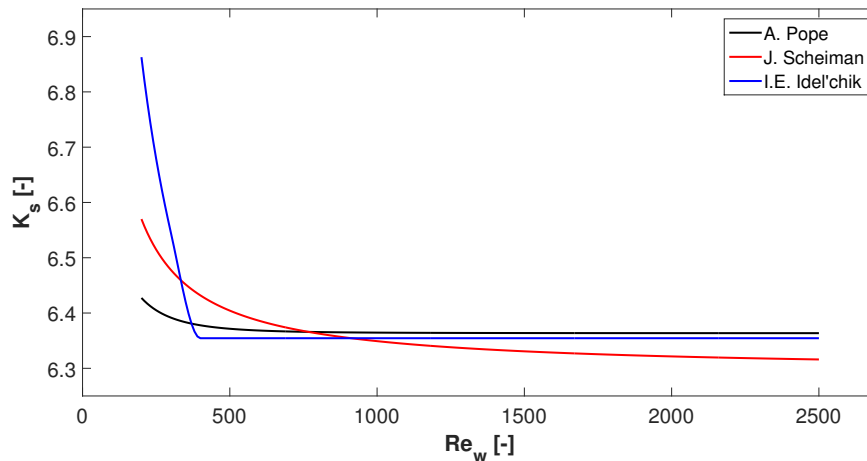
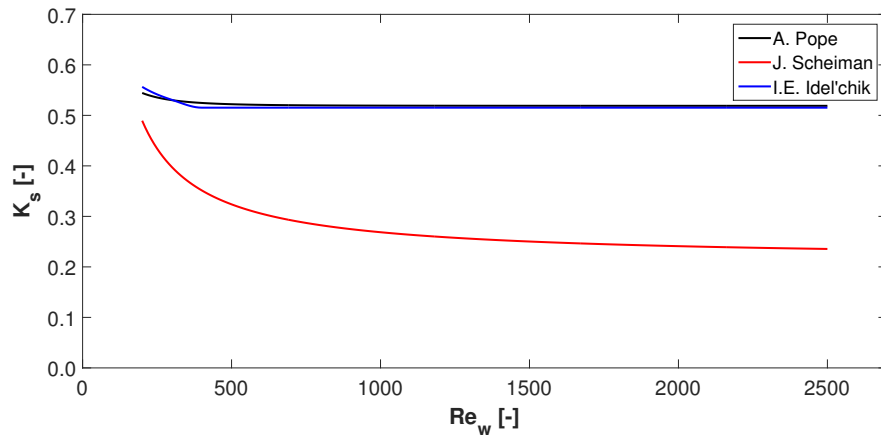
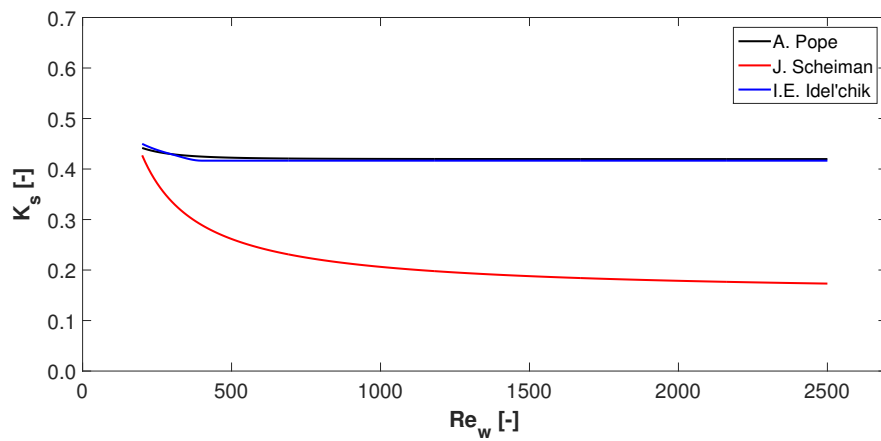
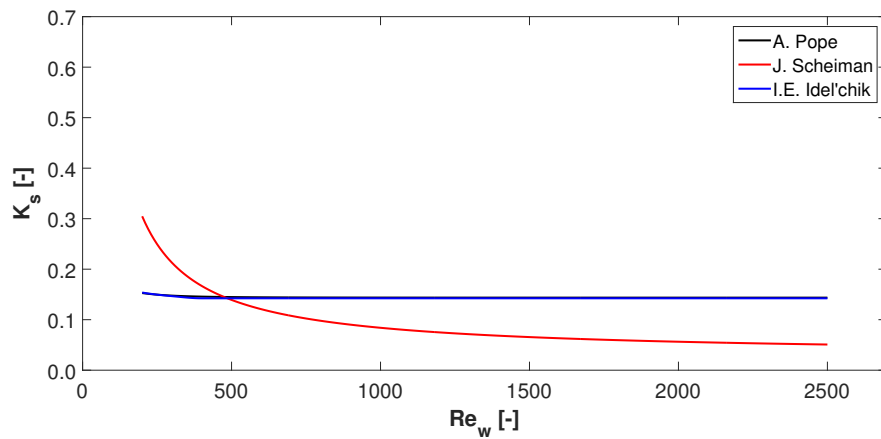


Figure 6.1: Sensitivity analysis - Reynolds number dependency for  $\beta = 0.300$

Figure 6.2: Sensitivity analysis - Reynolds number dependency for  $\beta = 0.720$ Figure 6.3: Sensitivity analysis - Reynolds number dependency for  $\beta = 0.758$ Figure 6.4: Sensitivity analysis - Reynolds number dependency for  $\beta = 0.900$

### 6.4.2 Porosity sensitivity

The following graphs represent the loss coefficient trend computed as function of the screen porosity, for four distinct Reynolds numbers. Figure 6.7, 6.8 are important for the analysis, since they treat Reynolds numbers that are estimated to be characterising the flow in the region surrounding the engine screens.

In this case the curves relative to the first and the third model are overlapping, since porosity dependency is taken into account exactly in the same way; just a small variation is present in the first figure, due to the different way in which Reynolds number dependency is taken into account at low Reynolds numbers. The curve relative to the second model is quite close to the other two and the trend is also very similar.

From this analysis it can be claimed that the dependency between loss coefficient and screen porosity is rather strong, in particular when screen porosity is low. Therefore, the choice of loss coefficient model to implement in the CFD simulation should account for this relation.

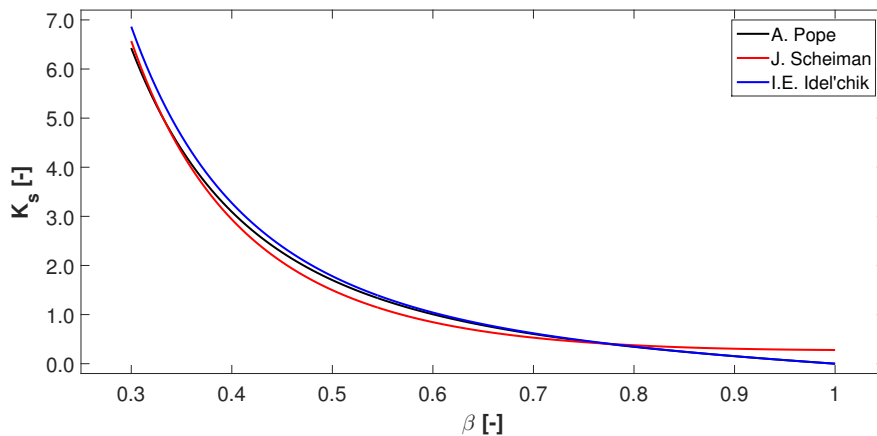


Figure 6.5: Sensitivity analysis - Porosity dependency for  $Re_w = 200$

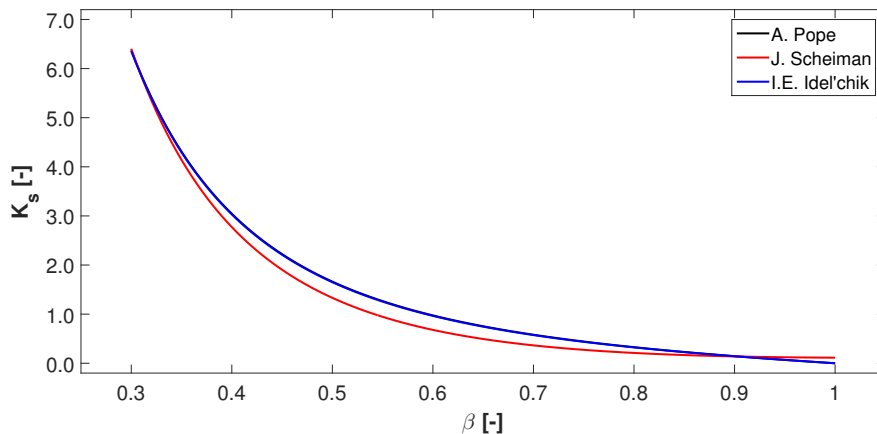
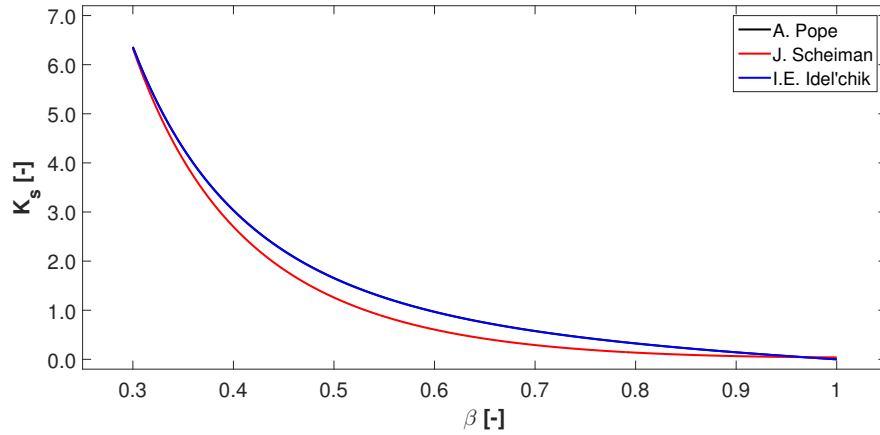
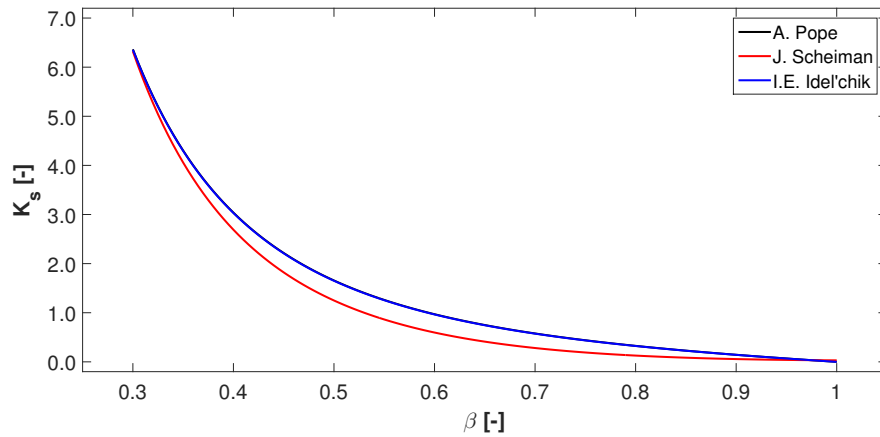


Figure 6.6: Sensitivity analysis - Porosity dependency for  $Re_w = 500$

Figure 6.7: Sensitivity analysis - Porosity dependency for  $Re_w = 1500$ Figure 6.8: Sensitivity analysis - Porosity dependency for  $Re_w = 2000$ 

### 6.4.3 Normal loss coefficient

As previously illustrated, when the flow approaches the screen with an angle  $\theta$  to the normal direction, it will leave the screen with an angle  $\psi$  lower than  $\theta$ . For an arbitrary angle  $\theta$ , two distinct loss coefficients are defined, one referred to the normal and one to the tangential direction, usually indicated respectively by  $K_\theta$  and  $F_\theta$ ; both of them are function of  $\theta$  as well of screen porosity and Reynolds number. In this sub-section the normal coefficient will be analysed.

In [33] the normal coefficient  $K_\theta$ , obtained experimentally, is used to define an empirical relation between  $f = K_\theta / \cos^2 \theta$  and  $g = Re_w \cos \theta$ , of the type  $f = h(g)$ , that is valid independently of the value of  $\theta$ . This indicates that the pressure drop depends on the normal component of the flow even though the flow approaches the screen with the angle  $\theta$  and leaves with the angle  $\psi$ .

The relation is obviously working also in the case of  $\theta$  equal to 0 degrees; this condition represents the case previously studied relative to the sensitivity analysis of Reynolds number. This equation allows us to compare the loss coefficient models described on Page 107 with the experimental data given by [33], since, in the case of  $\theta$  equal to 0 degrees, the relation is reduced to  $K_\theta = h(Re_w)$ , as in Figure 6.1-6.4. Experimental data relative to screens with the

same porosities of interest have not been found in literature; therefore, the comparison has been performed considering four different screens, whose geometrical characteristics are summarised in Table 6.3. Also in this case, different y-axes have been defined; a proper interpretation of the figures is left to the reader.

Screen	Wires per millimeter	Wire diameter [mm]	Pore size [mm]	Porosity [-]
A	0.157	0.6350	5.7150	0.810
B	0.945	0.1905	0.8687	0.672
C	0.787	0.4318	0.8382	0.436
D	1.575	0.1778	0.4572	0.519

Table 6.3: Geometrical characteristics of screens - Experimental data

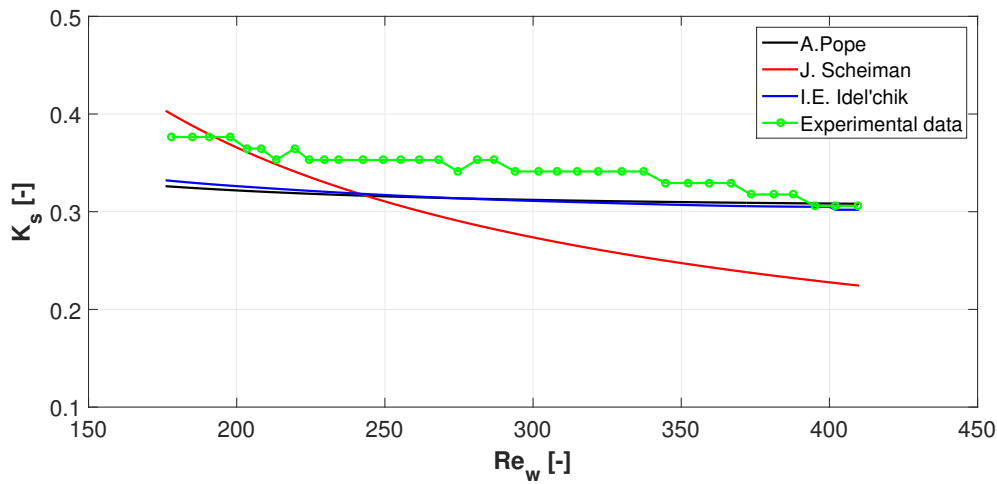


Figure 6.9: Normal loss coefficient - Screen A

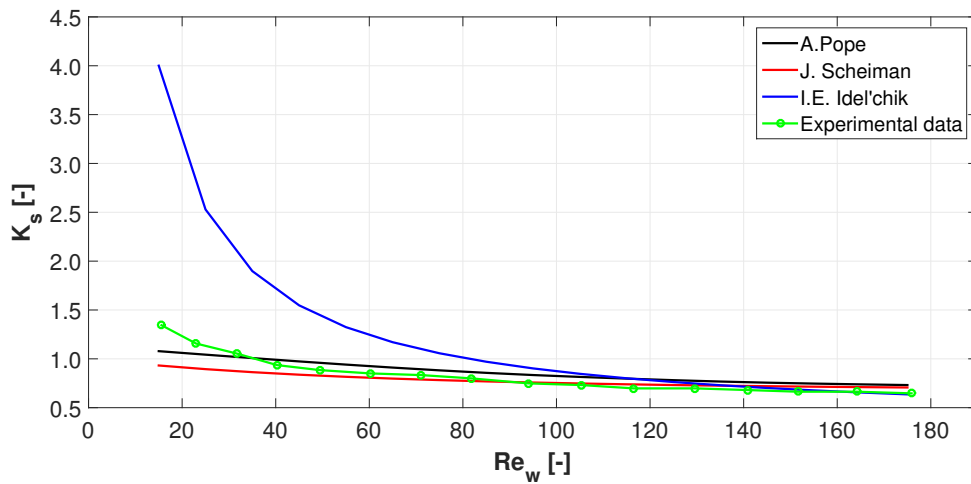


Figure 6.10: Normal loss coefficient - Screen B



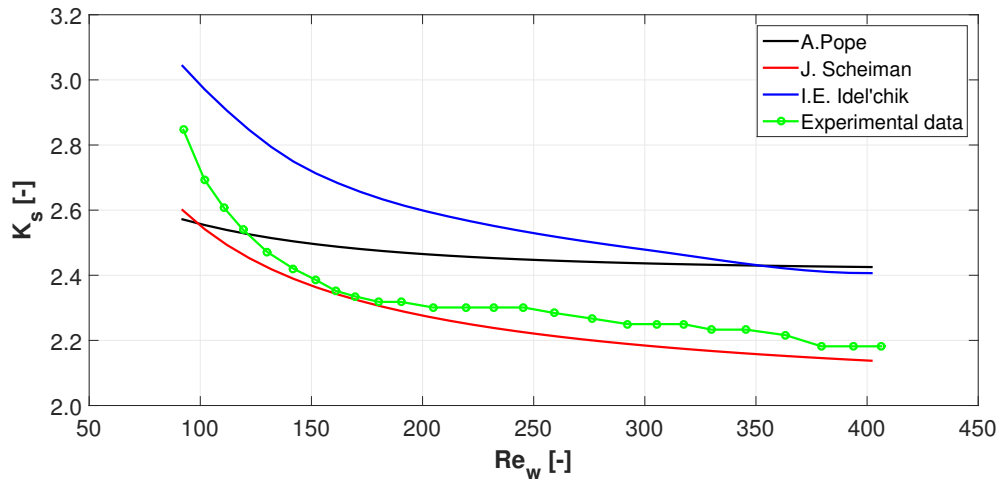


Figure 6.11: Normal loss coefficient - Screen C

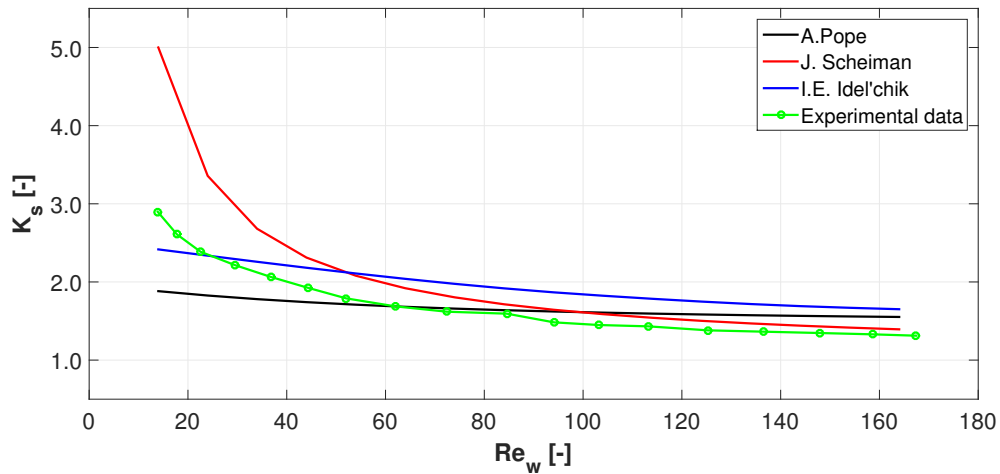


Figure 6.12: Normal loss coefficient - Screen D

Figure 6.9-6.12 show that the first (blue curve) and the third (green curve) model are able to follow quite well the experimental data distribution relative to high screen porosities; on the contrary, the second model (red curve) works more correctly at low values. This observation is of absolute importance for the final choice of loss coefficient model, since the screens used in the engine design can be placed within the screens band characterised by high porosity values; however, it must be remembered that, in the aforementioned images, the curves are defined for significantly smaller Reynolds numbers than those of interest. The reader will note that the correspondence between the models illustrated on Page 107 and the experimental data is equivalent to the correspondence between the aforementioned models and the function  $h$  of Page 111; this comes from the fact that the empirical relation is derived from the experimental values.

The transition from the case of  $\theta$  equal to 0 degrees, that has until now been studied with

three different models, to the case of a general  $\theta$  is instant. First of all, a simple consideration must be made. Assuming the correctness of the first and the third model at high porosity values, when the input variable  $g = Re_w \cos \theta$  of the function  $h$  is sufficiently high, the output can be considered as constant.

As a consequence, considering the general relation  $K_\theta / \cos^2 \theta = f(Re_w \cos \theta)$  valid for any  $\theta$ , it is true that, for sufficiently high Reynolds numbers and low  $\theta$  angles

$$K_{\theta=0} = K_\theta / \cos^2 \theta \quad (6.14)$$

$K_{\theta=0}$  defines the normal loss coefficient in the specific case of  $\theta$  equal to 0 degrees. Therefore, under the aforementioned conditions and for the specific case of high porosity values, the general normal loss coefficient can be defined as function of  $\theta$ .

$$K_\theta = K_{\theta=0} \cos^2 \theta \quad (6.15)$$

#### 6.4.4 Choice of the model

The final choice of loss coefficient model to implement in the CFD simulation of the flow striking the real engine air intake geometry developed by Airbus Helicopters must consider the sensitivity analysis and the comparison with the experimental data described in this section. The choice cannot be independent of the specific configuration considered, but, on the contrary, it must account for both the geometrical features of the screen and the flow properties, velocity and direction in particular. For this reason, figures relative to  $\beta = 0.720$  and  $\beta = 0.758$ , and to  $Re_w = 1500$  and  $Re_w = 2000$ , concerning the sensitivity analyses of Reynolds number and porosity respectively, assume great importance for a possible CFD simulation of the engine air intake; with regard to the comparison with the experimental data, attention has been paid to screens A and B due to their similarity in terms of porosity with those provided in the Airbus Helicopters' design.

As previously stated, the first and the third model allow us to compute very similar values to the experimental data in the case of high porosity screens at low Reynolds number; this is shown in Figure 6.9, 6.10. In the specific case of the considered engine air intake, the range within which the Reynolds number is actually expected to be is shifted towards higher values, between circa 1500 and 2000. However, this does not represent a real problem since the loss coefficient assumes a constant trend at high Reynolds numbers; this supposition, coming from Figure 6.9, 6.10 as well from Figure C.2, C.3, completely agrees with the trend obtained by the first and the third model, shown in Figure 6.2, 6.3. Therefore, under these considerations, the first and the third mathematical model constitute the best available way to simulate as faithfully as possible the pressure loss caused by the considered screens; even though the same results would be obtained by both of them, the model taken from [8] should be preferred to that defined in [19] thanks to the ease of implementation of the term relative to Reynolds number dependency. In Appendix C the trend of both the normal and the tangential loss coefficient, defined as function of the approaching angle  $\theta$ , will be shown.

### 6.4.5 Tangential loss coefficient

The tangential coefficient  $F_\theta$  is given by Equation 6.16, that is derived in [33] by the flow momentum modification occurring through the screen.

$$F_\theta = 2 \frac{\cos \theta}{\cos \psi} \sin(\theta - \psi) \quad (6.16)$$

The necessity of knowing the angle of incidence for both the incoming and the leaving flow makes Equation 6.16 difficult to be applied, given the impossibility of knowing the angle  $\psi$  a priori; a relation depending only on  $\theta$  would be desirable. Thanks to the experimental data, [33] defines a relation between  $r = F_\theta/\theta$  and  $K_\theta$ , under the assumption that  $\theta$  and  $\psi$  are small.

$$\frac{F_\theta}{\theta} = \frac{4K_\theta}{8 + K_\theta} \quad (6.17)$$

It is now possible to compare the curve  $F_\theta/\theta - K_\theta$  computed by the model chosen in the previous paragraph with the one obtained by the experimental data. The comparison will be used to demonstrate the applicability of the relation in the range defined by 0 and 45 degrees. Any relations have not been found in the literature for higher angles; a specific investigation should be performed with the purpose of having a complete model available.

The following graphs show the comparison between the model described by Equation 6.17 and the experimental data; they are referred to screens B and D. Unfortunately, any data regarding the tangential coefficient have not been found in [33] for screens C and, in particular, A. Figure 6.13, 6.14 show that the model described by Equation 6.17 represents the experimental data quite faithfully: the trend is properly modelled, even if the computed values are a little bit lower than the experimental ones.

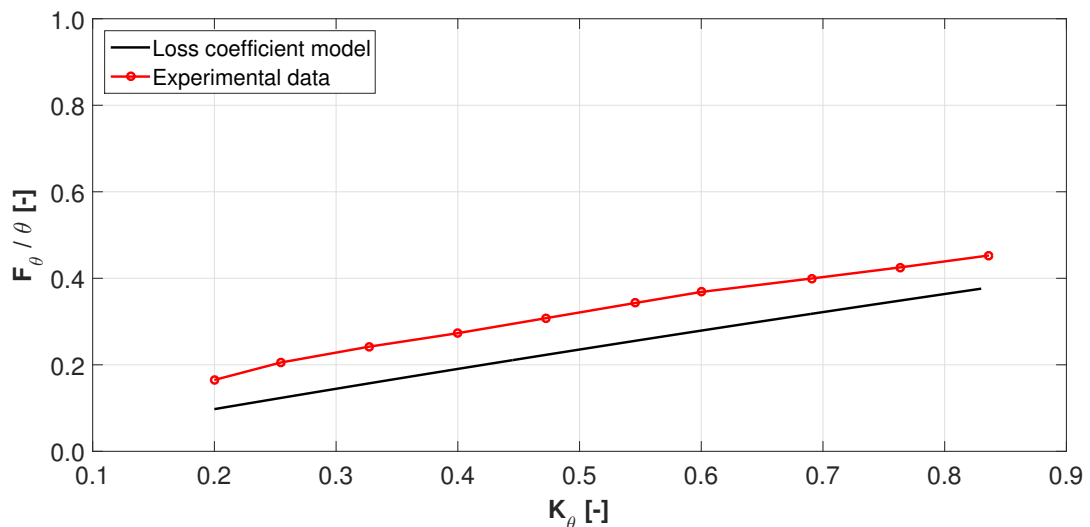


Figure 6.13: Tangential loss coefficient - Screen B

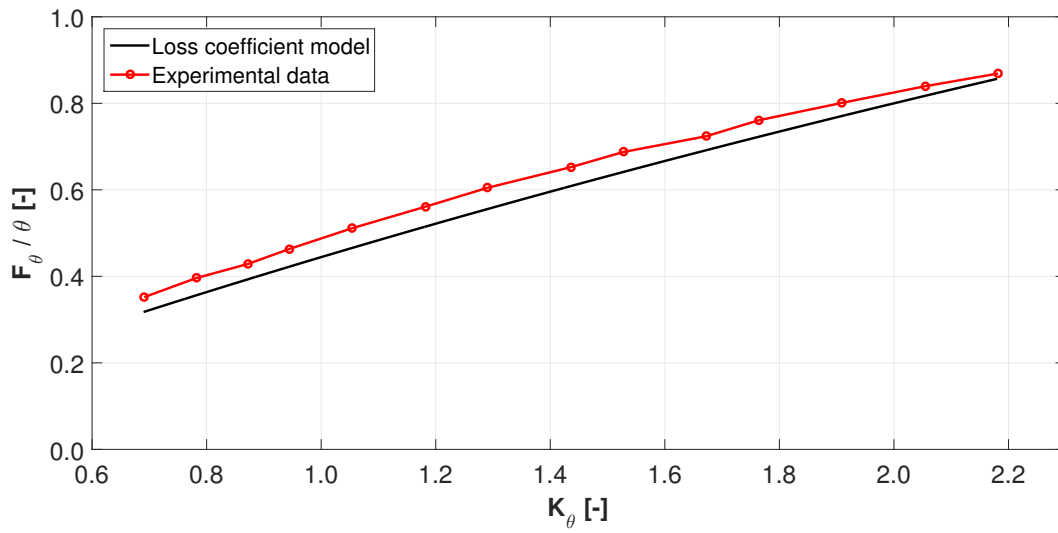


Figure 6.14: Tangential loss coefficient - Screen D

## Chapter 7

# Conclusions

The thesis is the result of the work performed at the Institute of Aerodynamics and Fluid Mechanics of the Technische Universität München within the "ATHENAI" project, whose target is to analyse and to enhance several engine air intake geometries for helicopters and tiltrotor aircraft. The "ATHENAI" project is part of the EU/Industry "Clean Sky" program, born with the purpose of meeting the important requirements imposed by the environment protection. The study described in this dissertation has been carried out with the primary objective of investigating the relation between the engine air intake installation on a lightweight twin-engine helicopter and the air flow field. The analysis has focused on the helicopter outer surface and on the inner region of the air intake, and has been executed by means of stationary CFD simulations, in which a reproduction of the TUM's wind tunnel facility has been employed.

In the first part of the work, an analysis concerning the boundary conditions specification has been performed in order to guarantee the wind tunnel functioning in a stationary regime; the study has been carried out by means of CFD simulations employing a simplified helicopter geometry, on which the engine air intake has been substituted by a fairing. Two different approaches have been employed: one consisting in the direct imposition of the same mass flow rate both on the inlet and on the outlet wind tunnel sections, and one consisting in the specification on the outlet section of the static pressure required to guarantee the same mass flow imposed on the inlet one. The correct static pressure has been calculated by means of the so-called co-Kriging model. The study has proved the greater effectiveness, in terms of stability and computational cost, of the "Mass flow" boundary condition compared to the "co-Kriging" approach: as a matter of fact, a unique, stable simulation is opposed to the need of simulating different configurations and to the difficulty of reaching converged results. The analysis has also allowed us to demonstrate the accuracy of the results: very similar flow fields have in fact been obtained through both the procedures.

This has guaranteed not only a greater speed of analysis, but also the possibility of studying the relation between the engine air intake and the flow field. This has been done comparing the results with those obtained by the stationary CFD simulation of a more accurate helicopter geometry, on which the engine air intake has been defined. The study has revealed that the effects are local only, since significant differences in the  $C_P$  distribution are found exclusively in the vicinity of the air intake entrance, whereas a very similar trend is obtained on the remaining part of the helicopter surface.

Subsequently, the comparison between the experimental data, supplied by a wind tunnel campaign previously conducted, and the numerical results, coming from the simulation of the more accurate geometry, has allowed for the validation of the CFD simulations: with this purpose, pressure coefficient has been studied. The investigation has shown a marked similarity of results in particular in the fore part of the helicopter surface; satisfying results have also been obtained in the region corresponding to the rear part of the helicopter surface and to the air intake entrance, despite the complexity of the flow structure. The pressure coefficient exhibits an almost constant trend in the fore and rear parts of the helicopter surface, whereas a significant drop is present in the vicinity of the air intake entrance due to a flow acceleration. Numerical results comparable to the experimental ones are obtained in the plenum chamber too; in this region, some vortices are present and the flow is continuously accelerated and decelerated, leading to a fluctuating  $C_P$  trend. The numerical and the experimental data are finally compared in the air intake internal duct; similar results are found especially on the back side of the conduct, whereas wider differences are observable on the front part. The pressure coefficient shows an almost constant trend in the part of the duct closer to the air intake entrance; on the contrary, in the most internal part, the flow is accelerated and the pressure undergoes a significant drop.

The validation of the numerical results has allowed us to study the flow field in the engine air intake inner volume. The study has shown that the flow is deflected at the engine air intake entry and then decelerated in proximity of the plenum chamber, a box fostering the flow field homogeneity at the compressor inlet in all the flight conditions and improving engine functioning near the surge line. The analysis has moreover revealed that part of the flow circulates in the plenum chamber before the intake duct is reached, whereas part of it directly enters. The intake duct acts as a flow deflector forcing the air from a radial to an axial direction: in this region a strong acceleration occurs and Mach numbers close to 0.60 are reached. At the exit, an adverse pressure gradient leads the flow to separate, influencing in this way the velocity distribution in the following region: on the aerodynamic interface plane the velocity field is in fact not completely homogeneous, since higher velocities are present in correspondence to the plenum chamber entry. The study has finally been completed with the comparison between the maximum velocity value computed in the numerical simulation and that measured in the wind tunnel campaign: the result has shown a percentage difference equal to 11.85%, giving a further confirmation of the simulations' accuracy.

## 7.1 Future research

**Engine working conditions dependency** Only one engine mass flow rate in a defined ambient condition has been analysed; this is not sufficient for a complete investigation of the effects on pressure distribution caused by the engine mass flow rate and by the ambient conditions in which the helicopter operates. Therefore, the suggestion is to investigate the dependency between the air flow field and the engine operation conditions more in detail, with the purpose of finding possible critical states.

**Screens employment** The engine air intake employed in the CFD simulations is simplified compared to the geometry designed by Airbus Helicopters within the "ATHENAI" project. The

real model would include two screens, one in the vicinity of the air intake entrance and one in the inner part; however, they have not been considered, as the time required for the numerical simulations would have increased significantly. The real air intake geometry could be studied in a future work, making a more precise investigation possible, in which the working conditions of the real configuration could be effectively analysed. In the numerical simulation the screens could be taken into account in two possible ways: by computing the screen mesh or by implementing a loss coefficient model, as proposed in Chapter 6. The first possibility, on the one hand, would require a big work time in order to obtain acceptable meshes, whereas, on the other hand, would give precise results. On the contrary, the second possibility could be implemented very quickly, but, at the same time, would not guarantee great accuracy; moreover, it would require the validation of the model described in Chapter 6 at high  $\theta$  angles.

**Different engine air intake models** The analysis performed has been focused only on a single air intake model, even if two others have been designed by Airbus Helicopters within the "ATHENAI" Project. The same approach employed for the analysis described in this thesis could be used to study the other air intake variants and a comparison between the performances offered by all the models could be performed; this would be strongly suggested in order to find pros and cons relative to each geometry and, if possible, to come to an optimisation of the baseline geometries.





## Appendix A

# Results of the co-Kriging model

### A.1 Monitor points

Mon1 and mon2 trends as function of the time-step are here represented for each simulation employed for the co-Kriging model implementation; the importance of the following graphs is related to the possibility of observing the simulations stability. The pictures are divided between "Expensive values" and "Cheap values". In all the graphs the same y-axis is used in order to facilitate the comprehension of the following general rule: the higher the pressure imposed on the outlet surface as boundary condition, the higher the mon2. The reader will also note that this tendency is more accentuated in the vicinity of the solution and becomes slighter at higher pressures, when the simulations are less stable. The figures seem anyway to confirm that only one solution of the problem can be found.

#### A.1.1 Expensive values

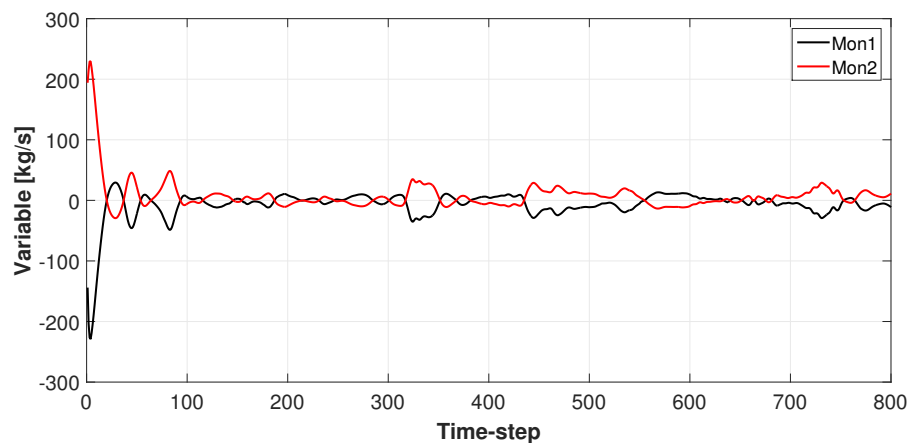


Figure A.1: Monitor points - "900 Pa" case supplying an expensive value

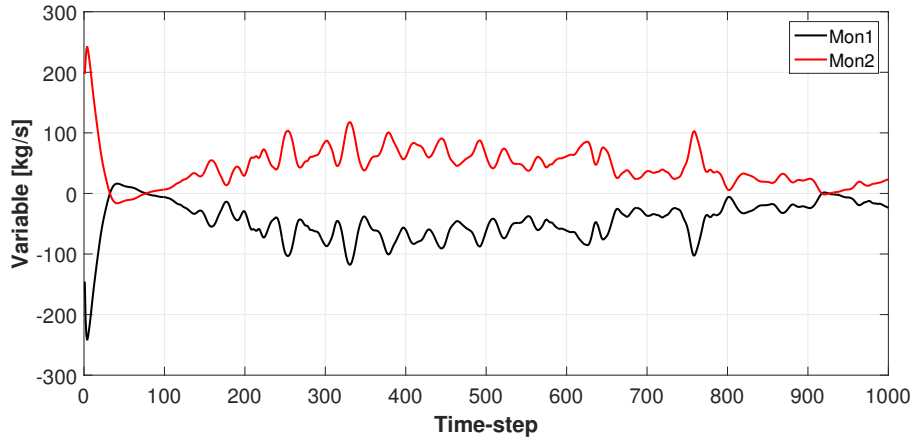


Figure A.2: Monitor points - "1050 Pa" case supplying an expensive value

### A.1.2 Cheap values

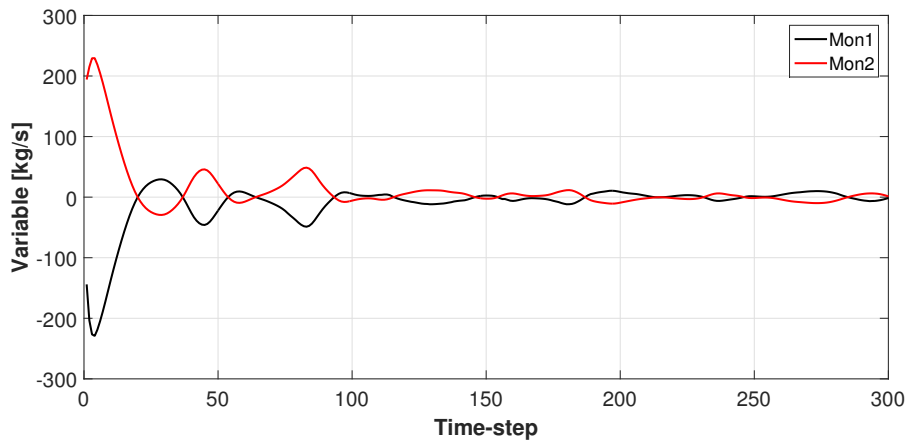


Figure A.3: Monitor points - "900 Pa" case supplying a cheap value

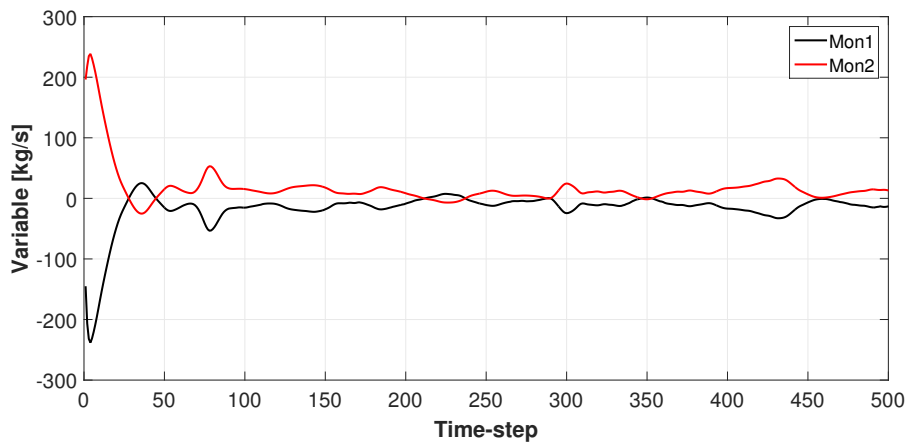


Figure A.4: Monitor points - "1000 Pa" case supplying a cheap value

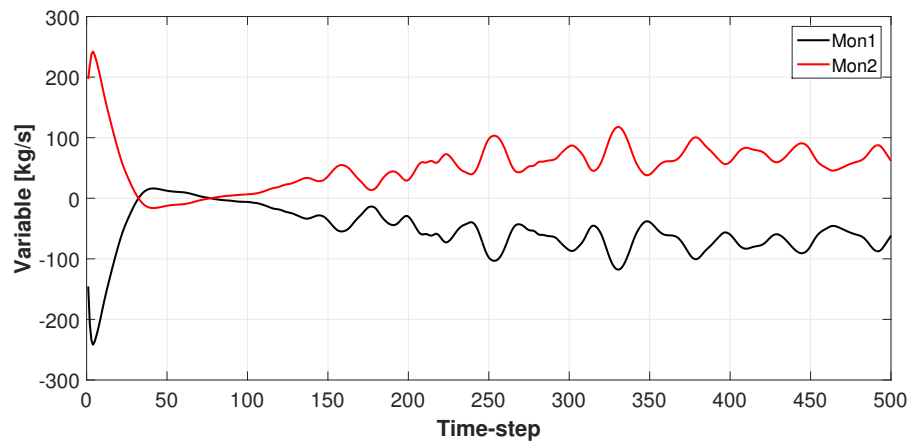


Figure A.5: Monitor points - "1050 Pa" case supplying a cheap value

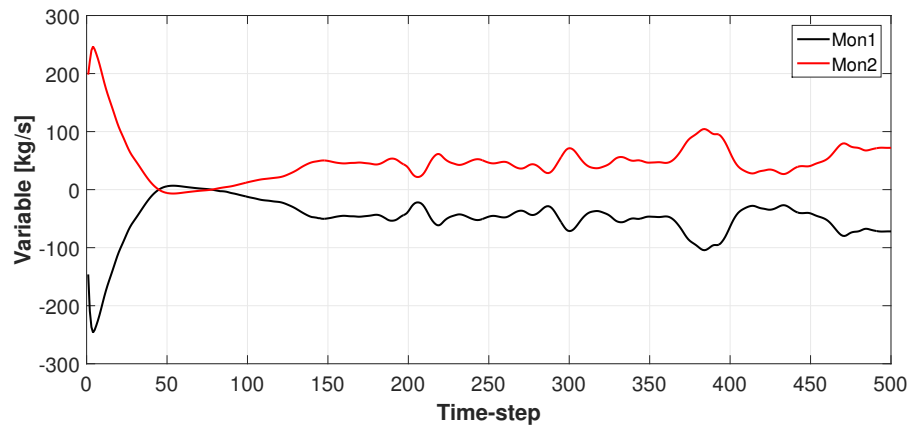


Figure A.6: Monitor points - "1100 Pa" case supplying a cheap value

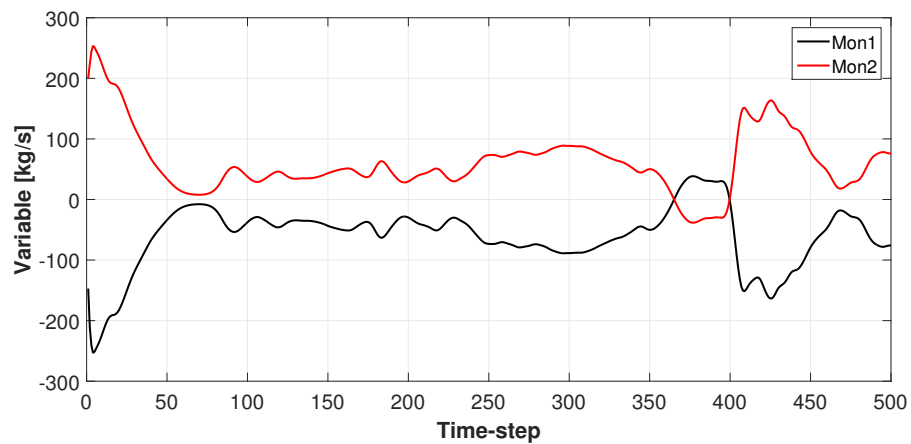


Figure A.7: Monitor points - "1200 Pa" case supplying a cheap value

## A.2 Curves estimated with the co-Kriging model

The curves resulting from the employment of co-Kriging model are shown in the following figures. With regard to the "2 expensive values" cases, Figure A.8-A.11 show that, even though both the expensive and the cheap values are mostly similar in the four cases, only the curve obtained by using five intervals quite properly follows the input values. This is also confirmed by Figure A.12, which shows that the smallest expected mean square error is the one relative to the "5 intervals" curve. This could be a signal that two expensive values are not sufficient to obtain satisfactory results, given that the "5 intervals" curve is actually expected to be the least accurate one. Significantly better results are obtained by the "3 expensive values" cases; the employment of another expensive values helps all the four curves to follow the input values more closely (Figure A.13-A.16). Moreover, Figure A.17 shows that the smaller the number of intervals used for the mean values computation, the higher the mean square error, as initially anticipated.

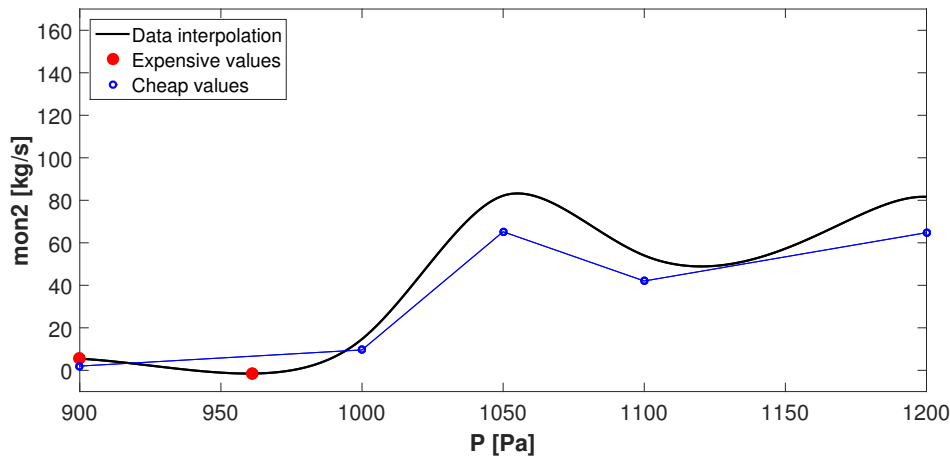


Figure A.8: Co-Kriging model implementation with 5 intervals - 2 expensive values

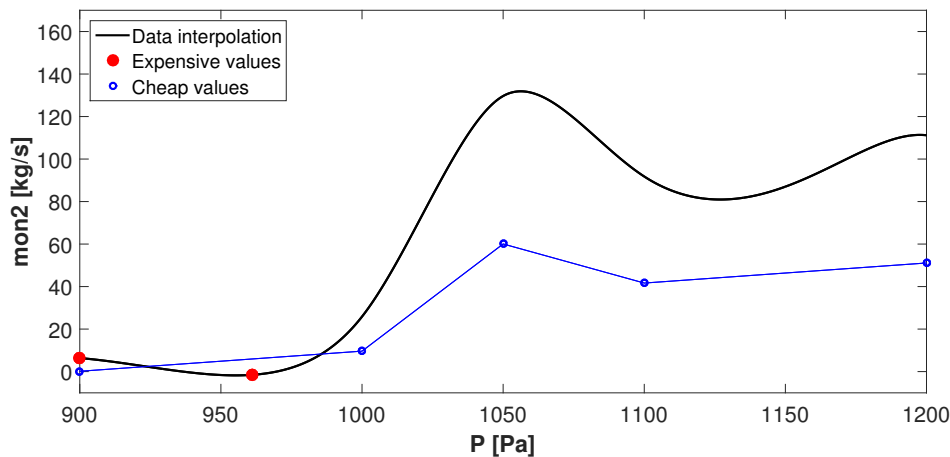


Figure A.9: Co-Kriging model implementation with 10 intervals - 2 expensive values

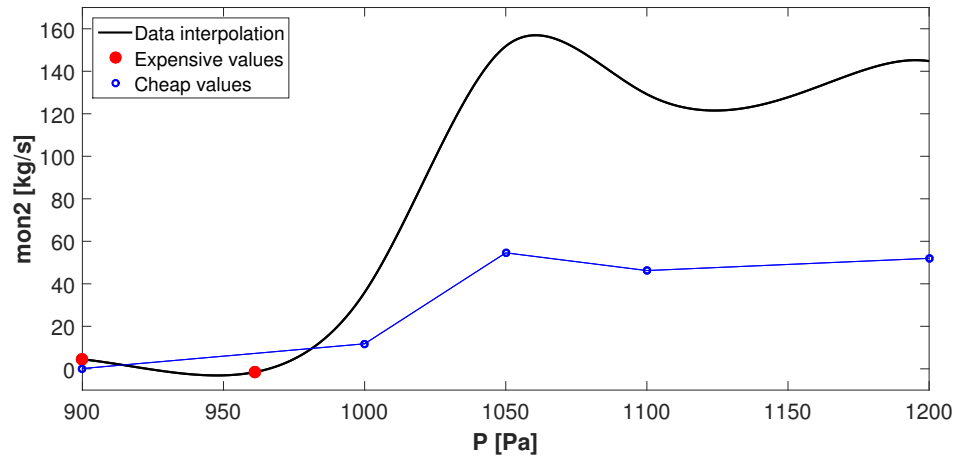


Figure A.10: Co-Kriging model implementation with 30 intervals - 2 expensive values

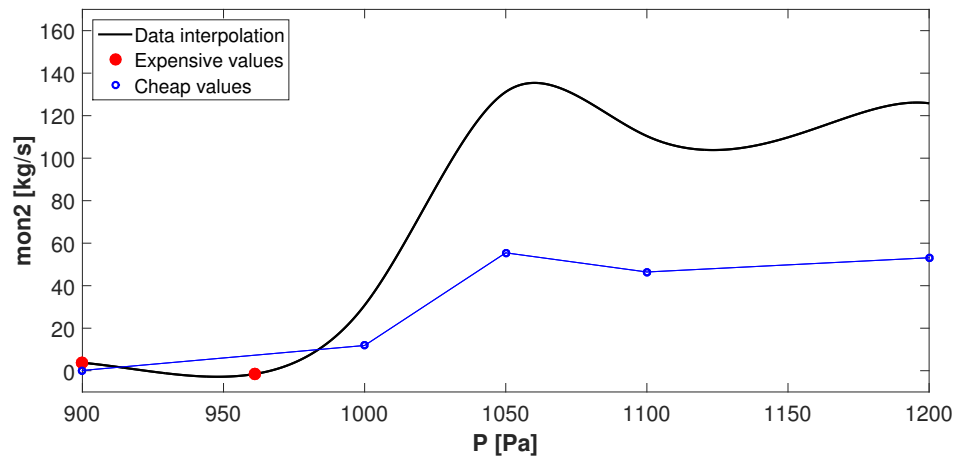


Figure A.11: Co-Kriging model implementation with all values - 2 expensive values

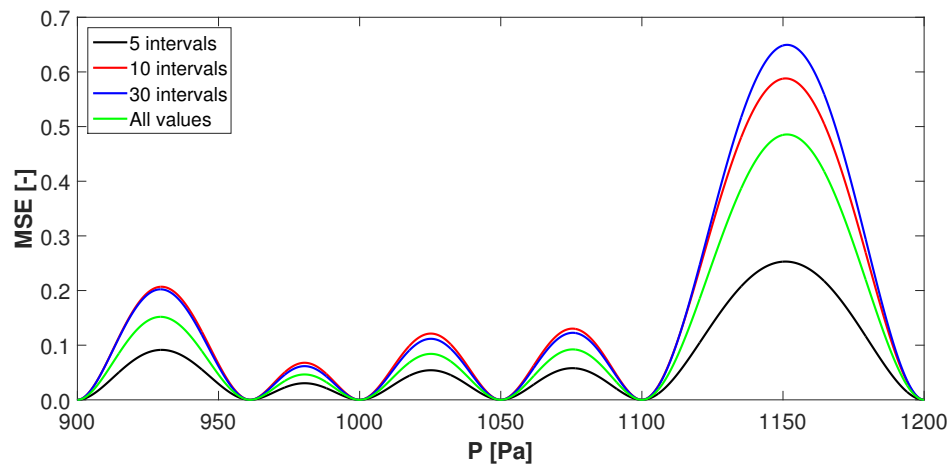


Figure A.12: Mean Square Error - 2 expensive values

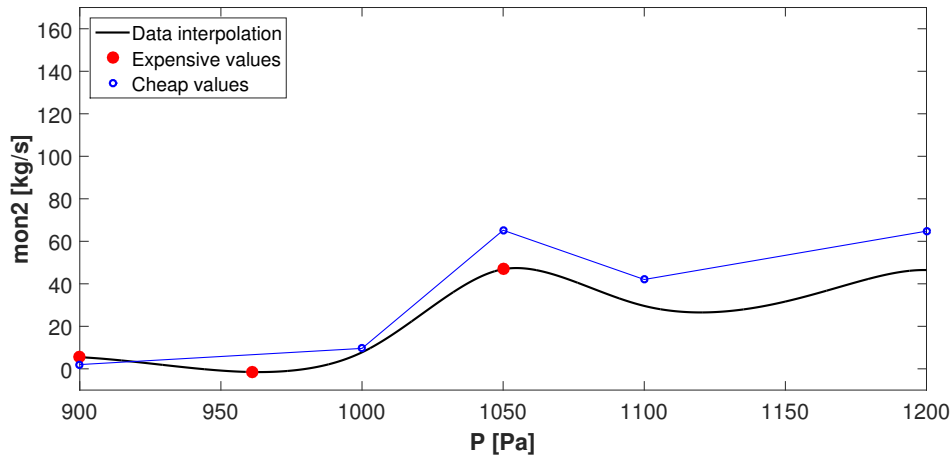


Figure A.13: Co-Kriging model implementation with 5 intervals - 3 expensive values

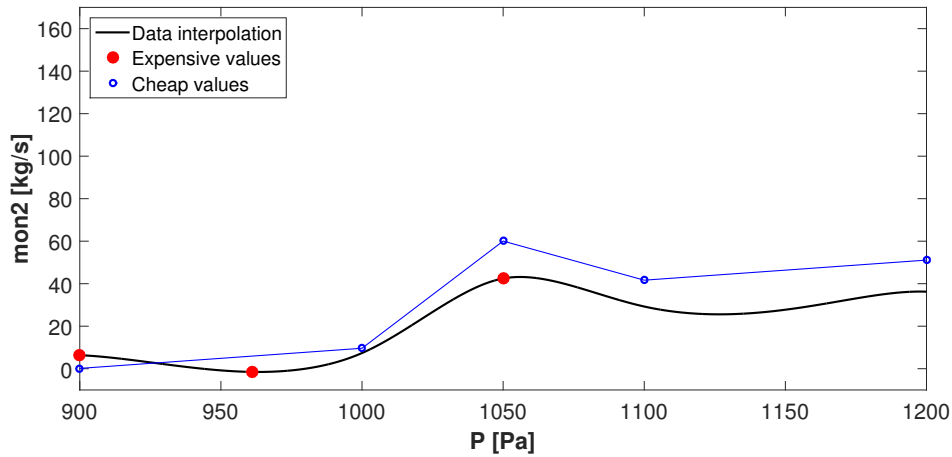


Figure A.14: Co-Kriging model implementation with 10 intervals - 3 expensive values

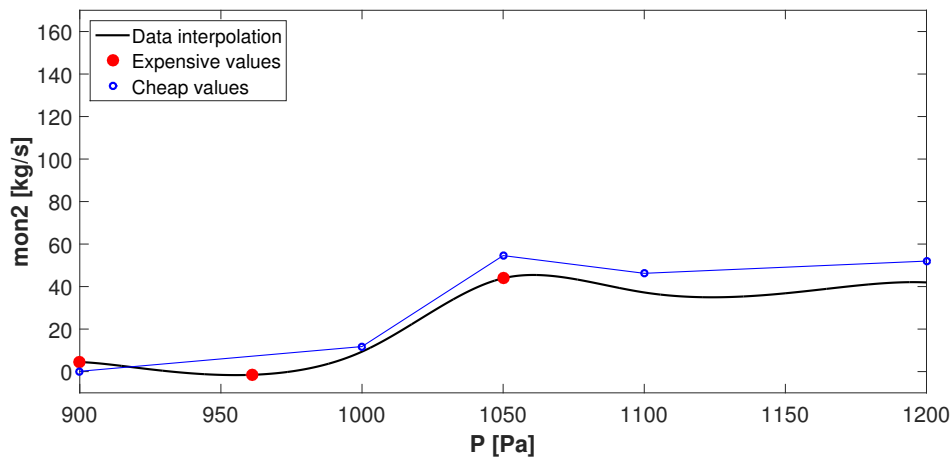


Figure A.15: Co-Kriging model implementation with 30 intervals - 3 expensive values

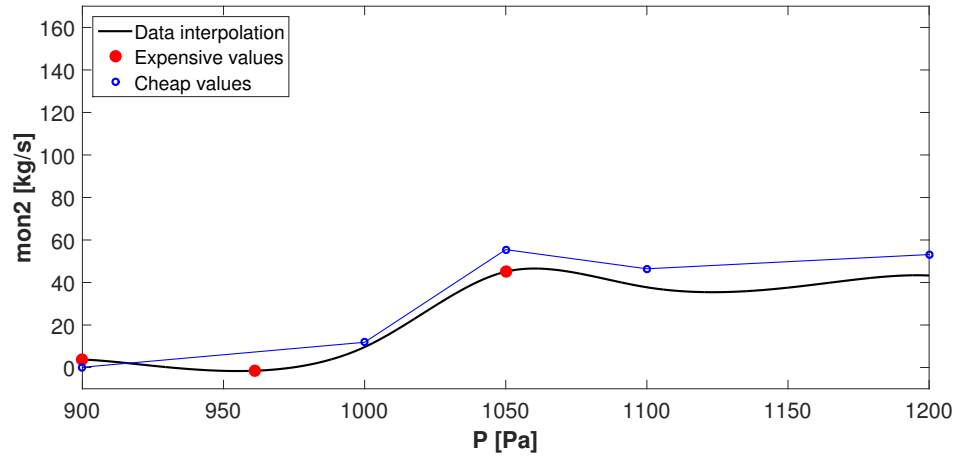


Figure A.16: Co-Kriging model implementation with all values - 3 expensive values

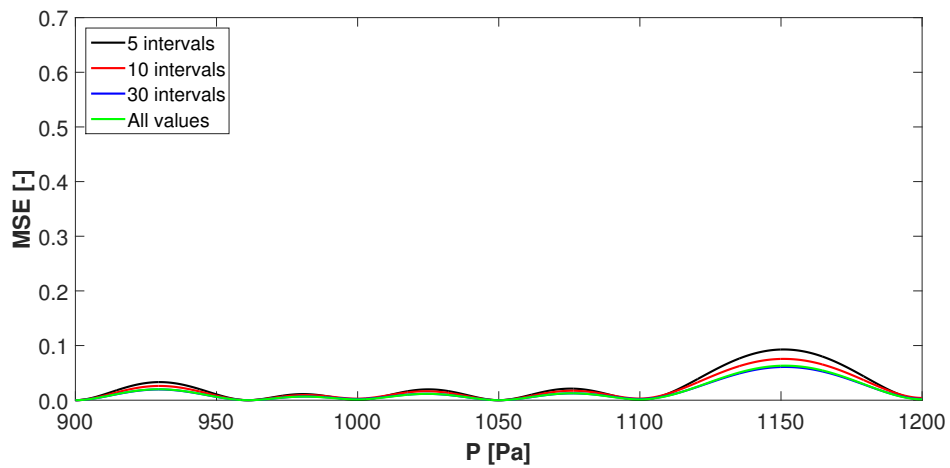


Figure A.17: Mean Square Error - 3 expensive values





## Appendix B

# Comparison between simulations

In Figure B.1, B.2 some planes spaced-out by, respectively, 1.00 and 5.00 m, are represented in order to give an idea of the surfaces position considered for the computation of the values reported in Table B.1, B.2. In both the figures, the first plane on the left is located at  $x = 0.00$  m, at the interface between the nozzle exit and the beginning of the test section. Figure B.3 instead allows us to extrapolate the position of the planes used for the analysis of the  $v$  and  $w$ -component of velocity described in Section 3.6; in this case, the planes are spaced-out by 0.25 m.

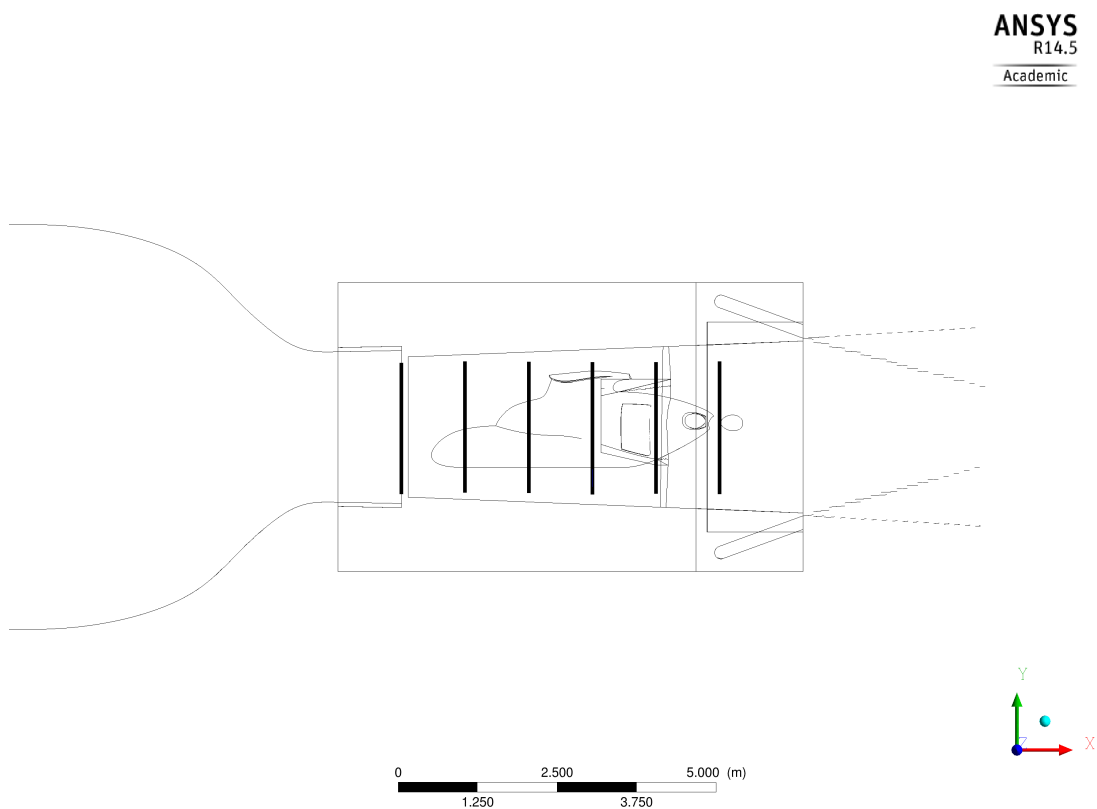


Figure B.1: Planes in x-direction - Test section

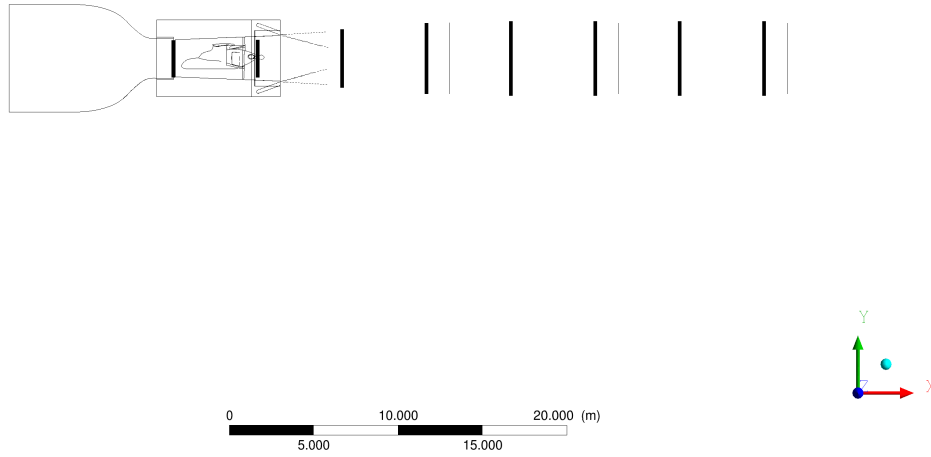


Figure B.2: Planes in x-direction - Wind tunnel

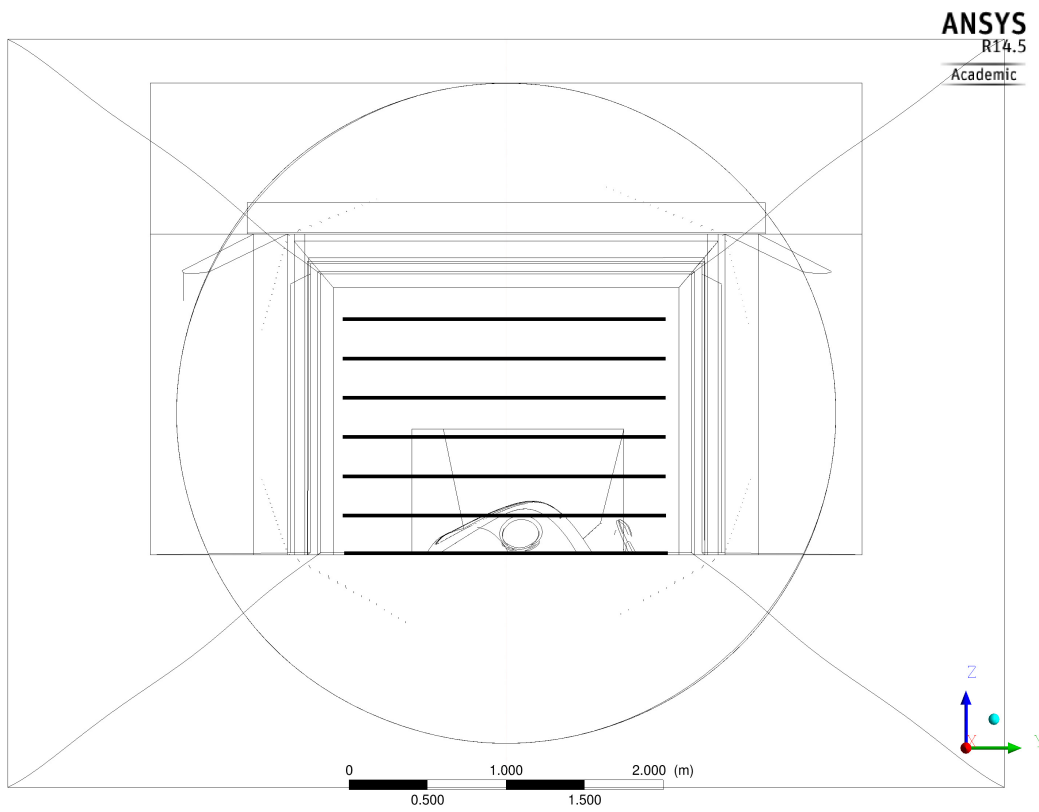


Figure B.3: Planes in z-direction - Test section

## B.1 Pressure and velocity distribution

The values represented in Figure 3.23, 3.24 are also reported in Table B.1, B.2 in order to complete the analysis of pressure and velocity distribution.

Position - x [m]	Pressure [Pa]		
	Mass flow	961.228 Pa	974.405 Pa
0.00	30.39	45.79	37.42
0.25	44.36	60.77	51.88
0.50	53.61	72.79	62.59
0.75	39.44	62.88	51.09
1.00	29.89	57.43	45.45
1.25	35.54	61.97	56.09
1.50	47.27	65.62	73.57
1.75	42.28	50.31	75.00
2.00	27.82	26.66	66.84
2.25	12.56	5.32	56.66
2.50	-18.86	-29.63	29.03
2.75	-26.78	-37.99	22.21
3.00	-24.00	-34.26	23.29
3.25	-12.65	-20.95	30.72
3.50	-5.23	-11.51	32.91
3.75	10.02	5.04	40.71
4.00	45.94	40.77	66.33
4.25	99.80	92.69	108.34
4.50	165.62	155.00	161.98
4.75	215.22	198.25	200.98
5.00	260.39	236.20	239.12
7.50	493.59	439.08	199.65
10.00	621.04	607.31	640.56
12.50	733.84	729.82	723.81
15.00	744.69	794.07	746.19
17.50	750.36	846.48	765.74
20.00	767.36	871.09	785.44
22.50	833.71	892.00	829.47
25.00	895.66	910.50	893.25
27.50	931.40	927.40	934.36
30.00	949.60	941.37	955.16
32.50	959.10	951.51	966.44
35.00	963.57	958.56	972.90

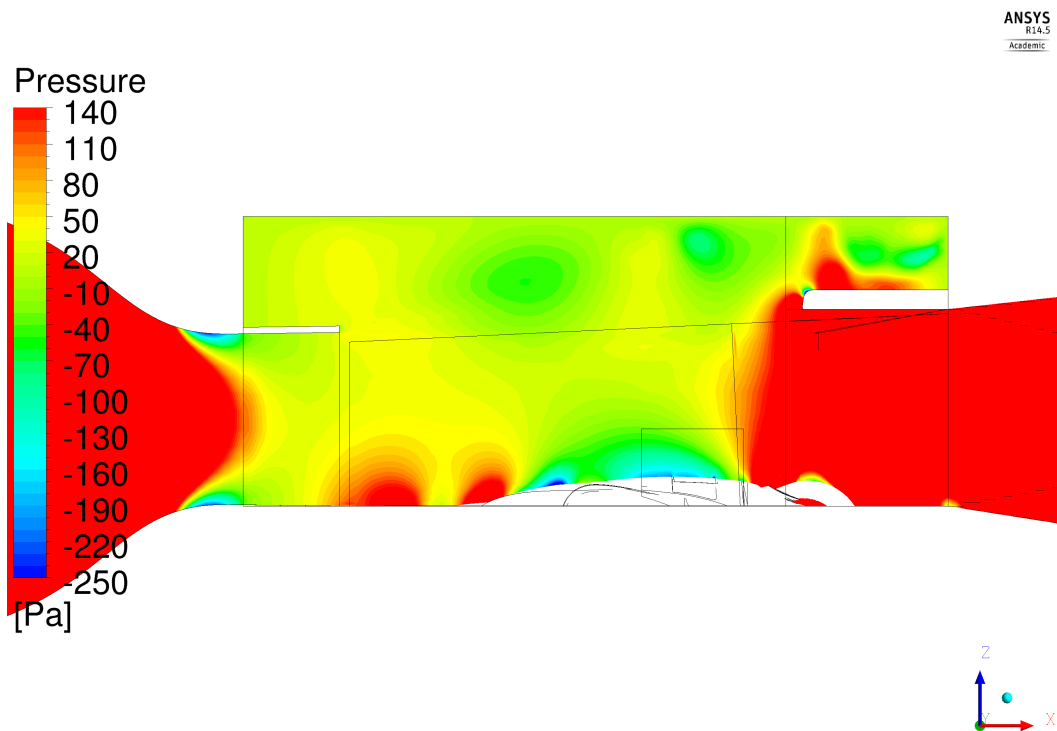
Table B.1: Relative static pressure - Comparison

Position - x [m]	U-velocity [-]		
	Mass flow	961.228 Pa	974.405 Pa
0.00	0.976	0.975	0.975
0.25	0.971	0.971	0.971
0.50	0.968	0.966	0.967
0.75	0.972	0.969	0.970
1.00	0.974	0.971	0.972
1.25	0.972	0.970	0.969
1.50	0.967	0.968	0.963
1.75	0.969	0.971	0.962
2.00	0.972	0.976	0.963
2.25	0.975	0.978	0.964
2.50	0.985	0.986	0.972
2.75	0.987	0.986	0.973
3.00	0.985	0.982	0.971
3.25	0.980	0.976	0.966
3.50	0.977	0.972	0.963
3.75	0.970	0.965	0.957
4.00	0.956	0.952	0.945
4.25	0.936	0.932	0.928
4.50	0.912	0.909	0.907
4.75	0.894	0.893	0.893
5.00	0.879	0.881	0.881
7.50	0.689	0.699	0.695
10.00	0.577	0.574	0.571
12.50	0.435	0.434	0.436
15.00	0.352	0.352	0.352
17.50	0.329	0.325	0.328
20.00	0.328	0.323	0.327
22.50	0.324	0.320	0.325
25.00	0.320	0.318	0.321
27.50	0.317	0.316	0.317
30.00	0.315	0.315	0.316
32.50	0.315	0.314	0.314
35.00	0.314	0.313	0.314

Table B.2: U-component of velocity - Comparison

In the following figures, a comparison between the "Mass flow", the "961.228 Pa" and the "974.405 Pa" cases is presented. First of all, the distribution of relative static pressure and of the u-component of velocity within and outside the wind tunnel test section is shown; subsequently, the same properties are analysed on planes defined on  $x = 2.50$  m,  $x = 7.50$  m and  $x = 20.00$  m; the choice of these planes has been previously motivated in Section 3.6.

**Distribution inside and outside the test section** Pressure fields slightly differ within the test section, in particular in the upper region far from the helicopter surface. On the contrary, the distributions of velocity's u-component are more similar, even though some small differences are present in the upper region; moreover, the region of flow acceleration ending at the diffuser entrance is slightly more extended in the "961.228 Pa" simulation. Some differences in pressure distribution are found outside the test section too; the most significant ones, located in the neighbourhood of  $x = 7.50$  m and of  $x = 20.00$  m, will be analysed in the following paragraphs. With regard to velocity distribution, all the three simulations exhibit the same velocity field in the lower part of the diffuser and of the successive conduct. On the contrary, the flow field is differently simulated in the upper side: this is particularly true as concerns the recirculation area, resulting more limited in the "961.228 Pa" simulation than in the other two cases.



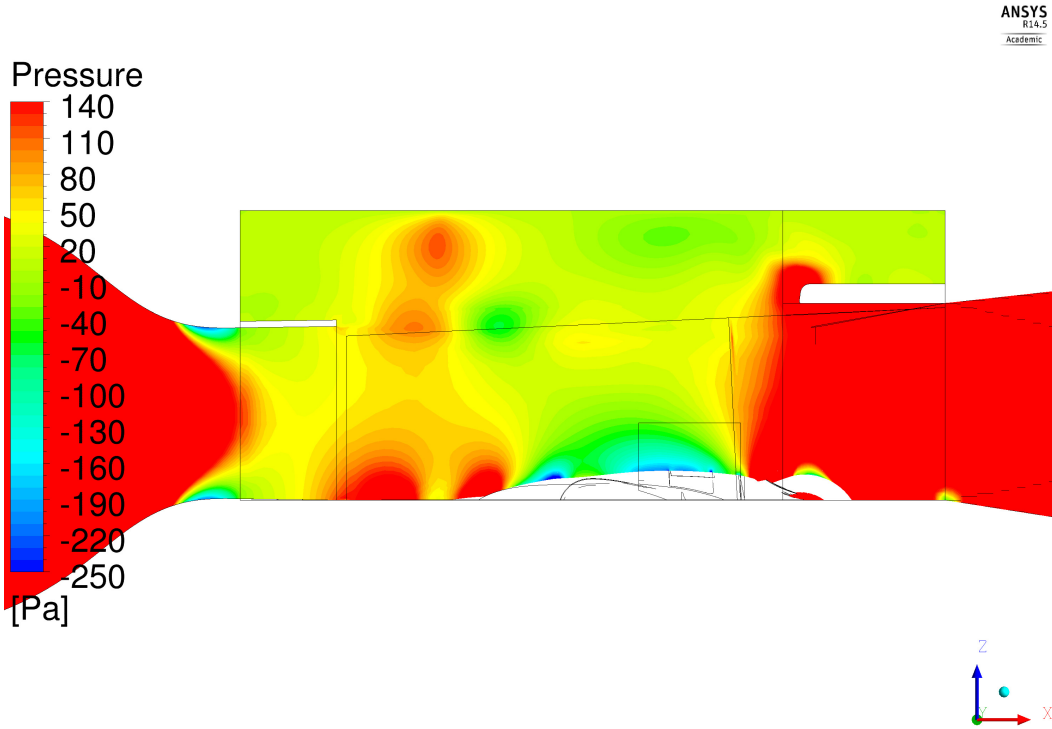


Figure B.5: Relative static pressure distribution in the test section - "961.228 Pa" case

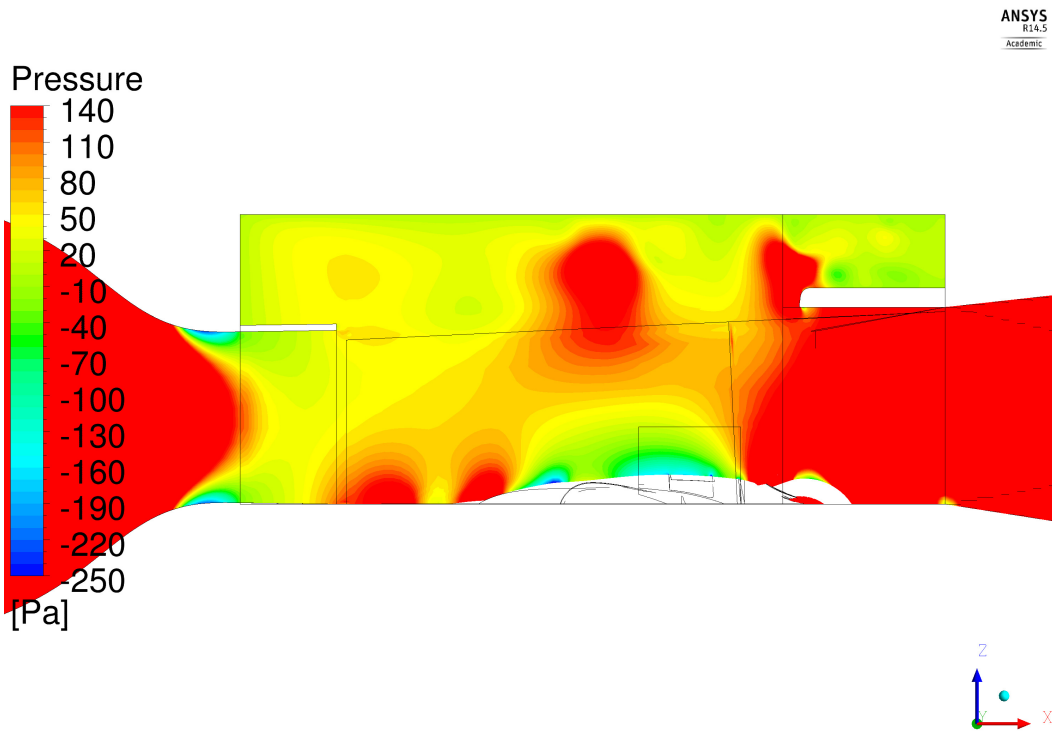


Figure B.6: Relative static pressure distribution in the test section - "974.405 Pa" case

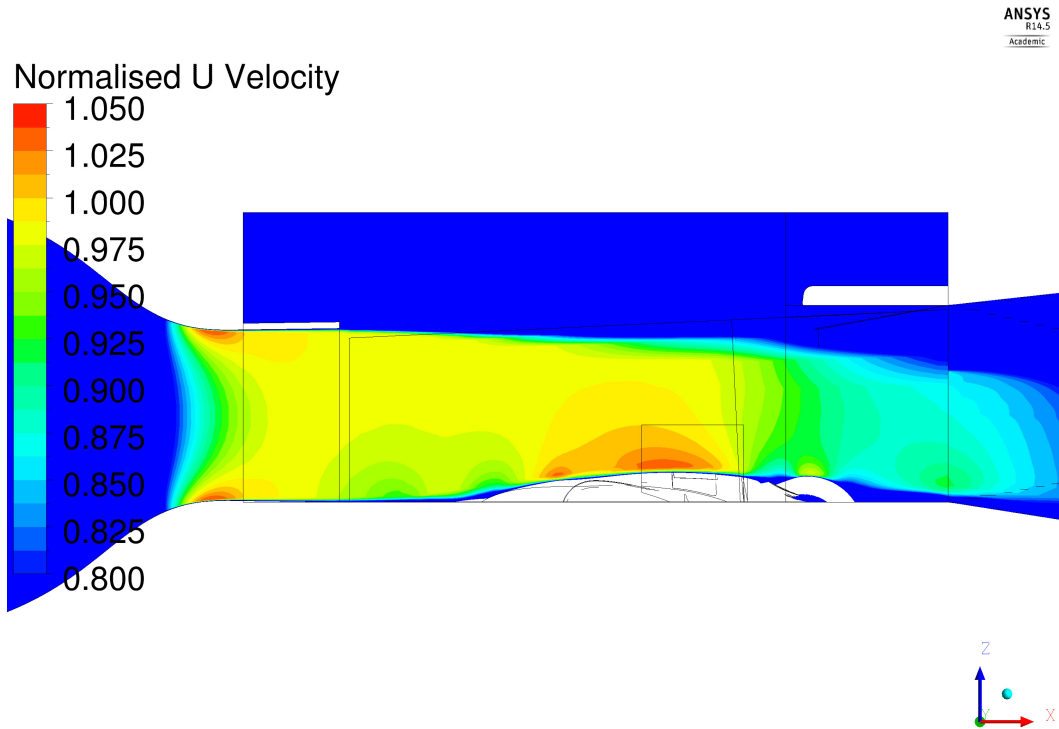


Figure B.7: Velocity u-component distribution in the test section - "Mass flow" case

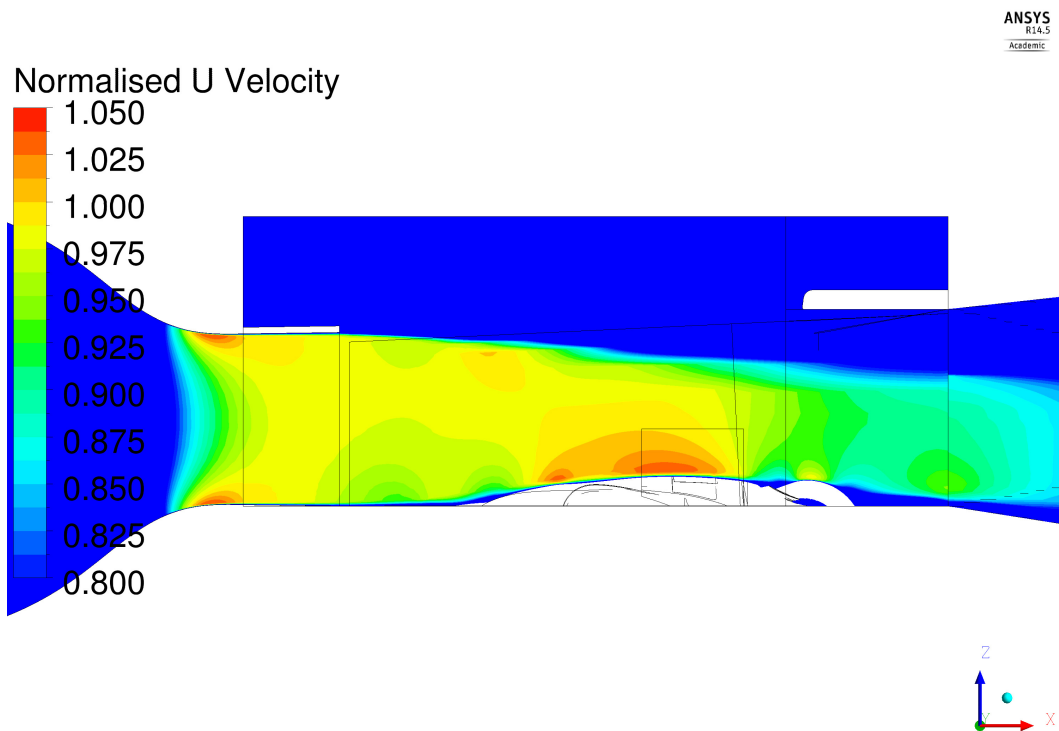


Figure B.8: Velocity u-component distribution in the test section - "961.228 Pa" case

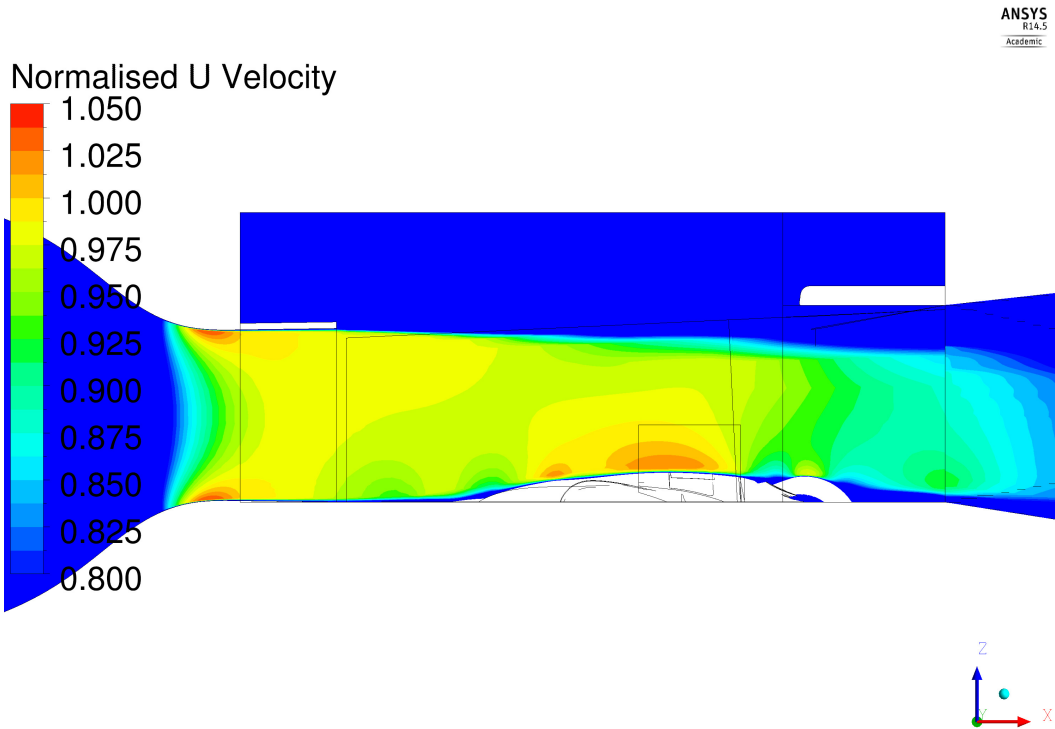


Figure B.9: Velocity u-component distribution in the test section - "974.405 Pa" case

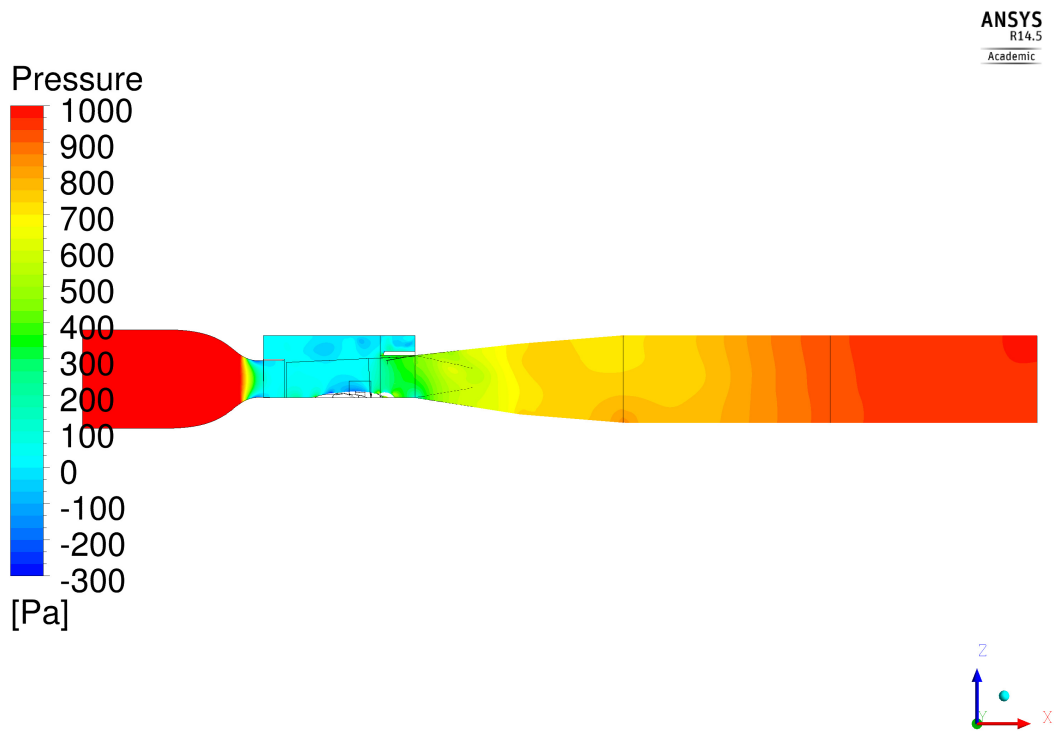


Figure B.10: Relative static pressure distribution in the wind tunnel - "Mass flow" case



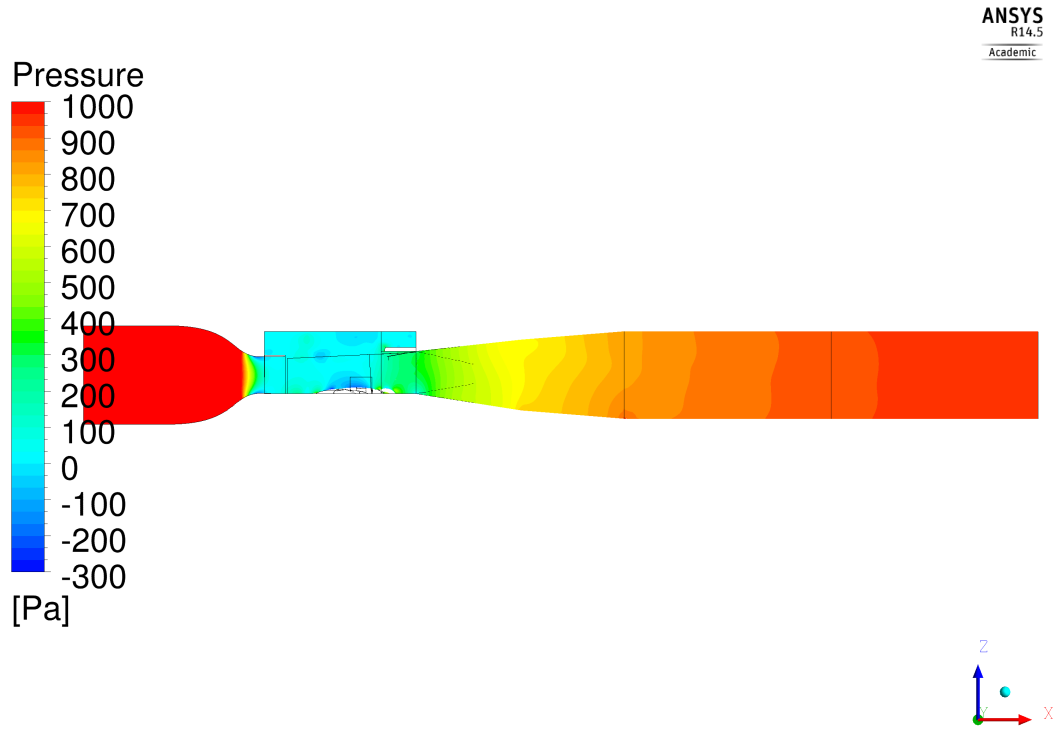


Figure B.11: Relative static pressure distribution in the wind tunnel - "961.228 Pa" case

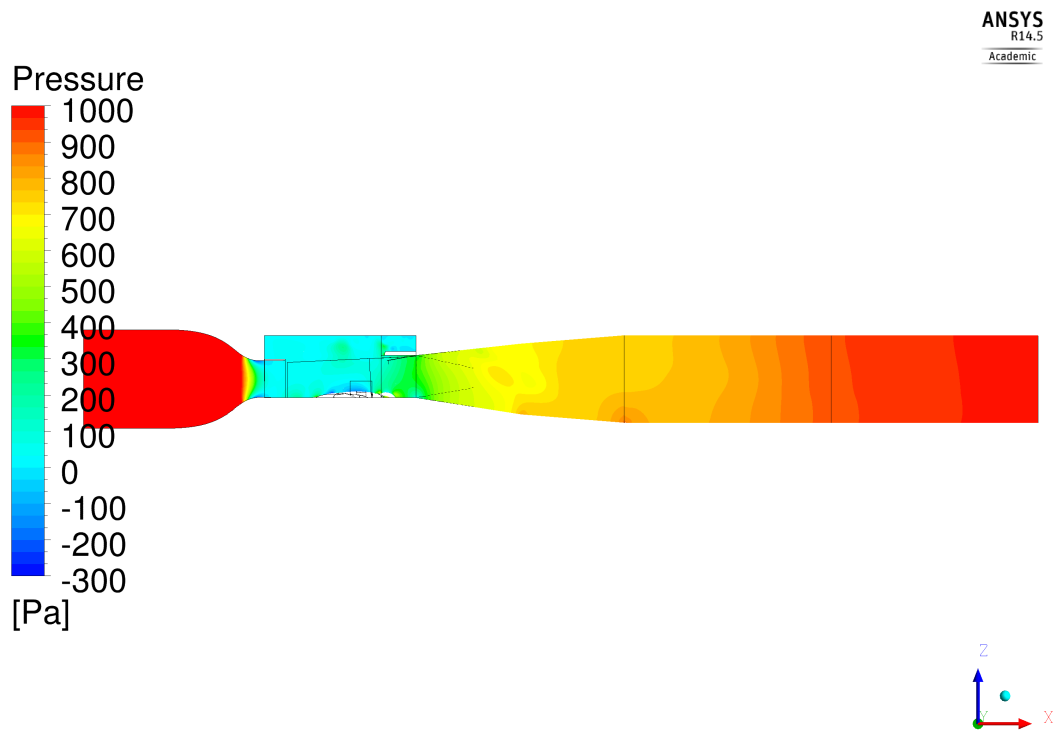


Figure B.12: Relative static pressure distribution in the wind tunnel - "974.405 Pa" case

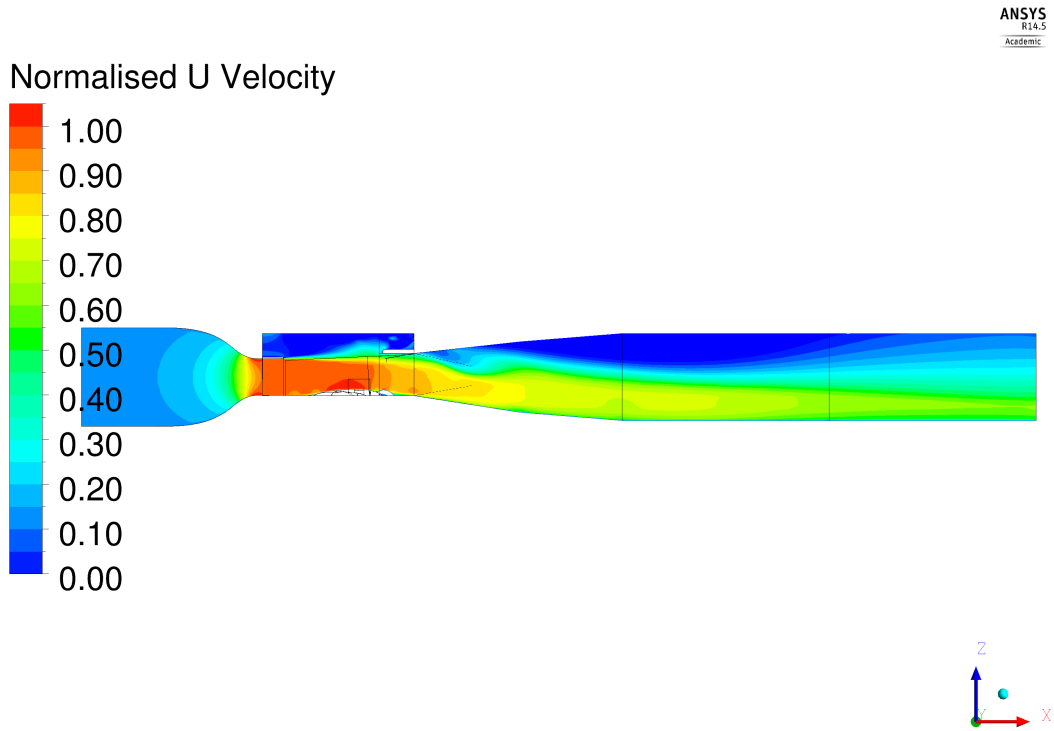


Figure B.13: Velocity u-component distribution in the wind tunnel - "Mass flow" case

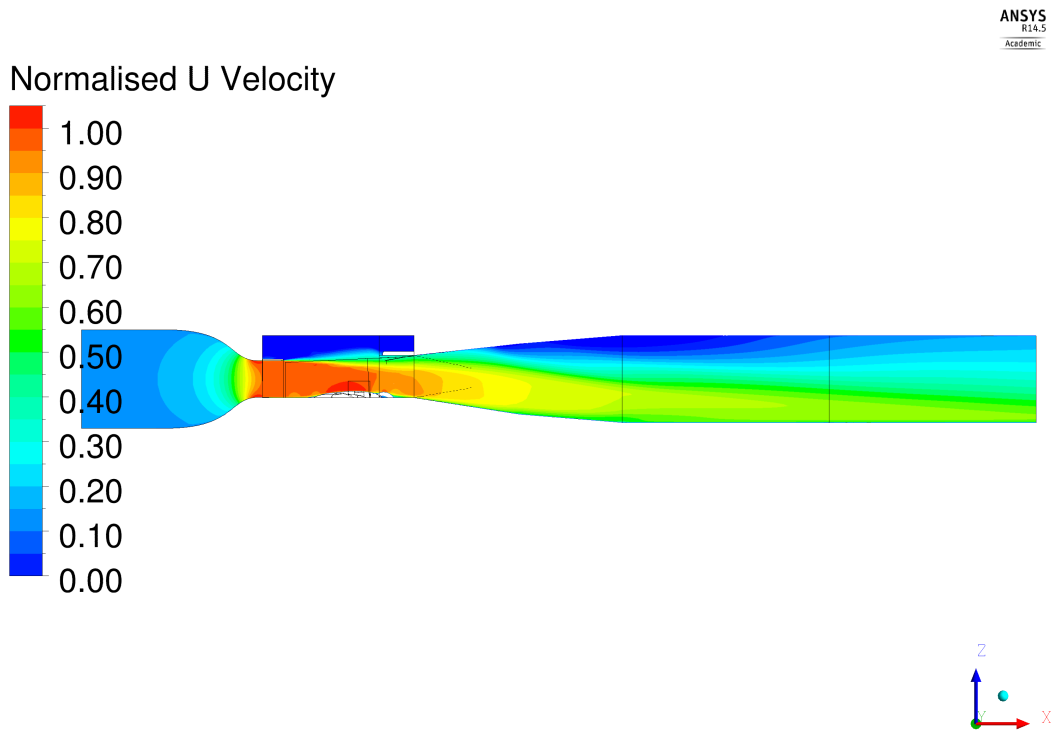


Figure B.14: Velocity u-component distribution in the wind tunnel - "961.228 Pa" case

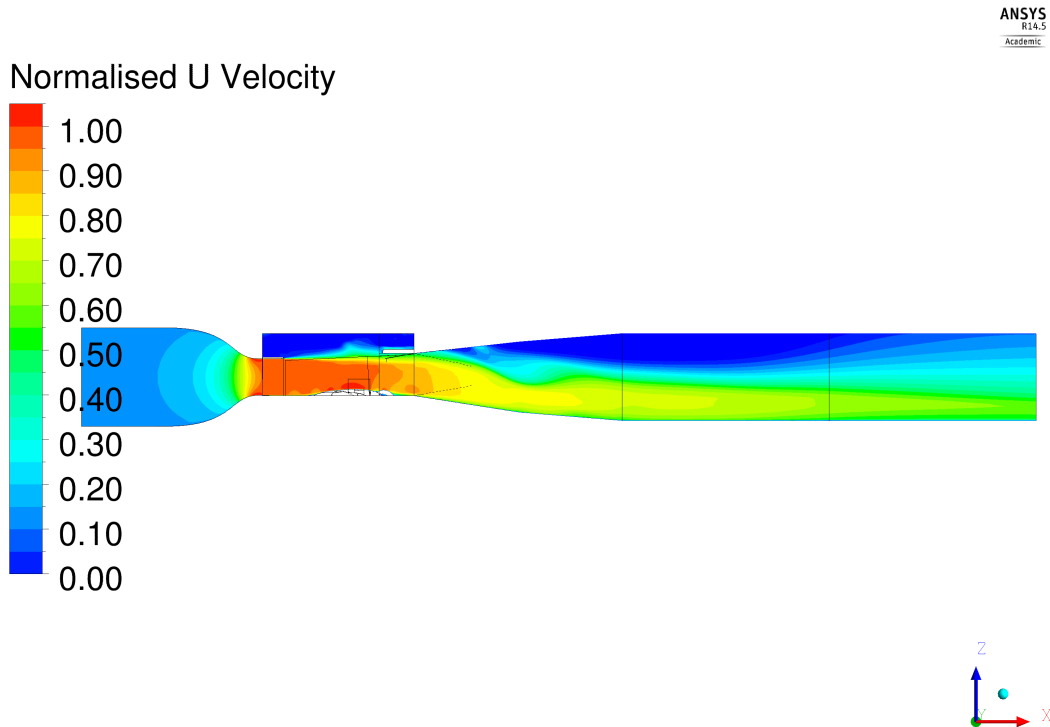


Figure B.15: Velocity u-component distribution in the wind tunnel - "974.405 Pa" case

$x = 2.50 \text{ m}$  "Mass flow" and "961.228 Pa" simulations exhibit a very similar pressure field in this section, in particular close to the helicopter surface. In the upper region the distribution assumes different behaviours: in the first simulation pressure increases moving from the left to the right side of the section, whereas the second simulation shows an opposite trend. The "974.405 Pa" case almost completely differentiates compared to the other two simulations: similar values are obtained only in the region surrounding the mast fairing of the helicopter. With regard to the u-component of velocity, comparable distributions are found in all the three simulations; some differences are present in the upper side of the section, in particular in the "974.405 Pa" case, where the flow is slightly slower.

The discrepancies between the curves representing the pressure trend (Figure 3.25) are caused by different pressure fields in the whole section: significant differences occur especially in the region surrounding the helicopter surface, as Figure B.16, B.17, B.18 demonstrate; analogous considerations can be made for the differences between the curves representing the velocity trend (Figure 3.26), as indicated by Figure B.19, B.20, B.21.

$x = 7.50 \text{ m}$  The pressure values are very different in this section. The "961.228 Pa" case exhibits very low values in the pressure field; "Mass flow" and "974.405 Pa" simulations are characterised by similar pressure values, even though the distributions do not match very well, in particular in the upper side of the section. Nevertheless, the u-component of velocity is very similar. In the "Mass flow" and in the "974.405 Pa" simulations the velocity field is consistent with the pressure distribution, since low pressures correspond to high velocities, and the opposite;

this is not verified in the "961.228 Pa" case, since an almost constant pressure field corresponds to an irregular velocity field.

The pressure distributions analysed justify the discrepancies between the curves represented in Figure 3.23. Even if the pressure fields are not similar at all, the mean values computed in the "Mass flow" and in the "974.405 Pa" cases are anyway very close; with regard to the "961.228 Pa" simulation, the mean pressure calculated on the surface is slightly lower.

$x = 20.00 \text{ m}$  Different pressure fields are simulated in this section; only in the "Mass flow" and "974.405 Pa" cases the pressures are quite similar, whereas those computed in the "961.228 Pa" case are a little higher. All the simulations present a recirculation area in this region of the wind tunnel, even if the comparison between Figure B.31, B.32, B.33 shows that its dimensions are more limited in the second simulation. The distributions of velocity's u-component are quite similar: the comparison between the "Mass flow" and the "974.405 Pa" simulations does not exhibit considerable differences, whereas the "961.228 Pa" case slightly differentiates in the lower side of the section.

The difference between the curves representing the pressure trend in Figure 3.25 is most probably caused by the different dimensions of the recirculation area, that produce significant variations in pressure distribution.

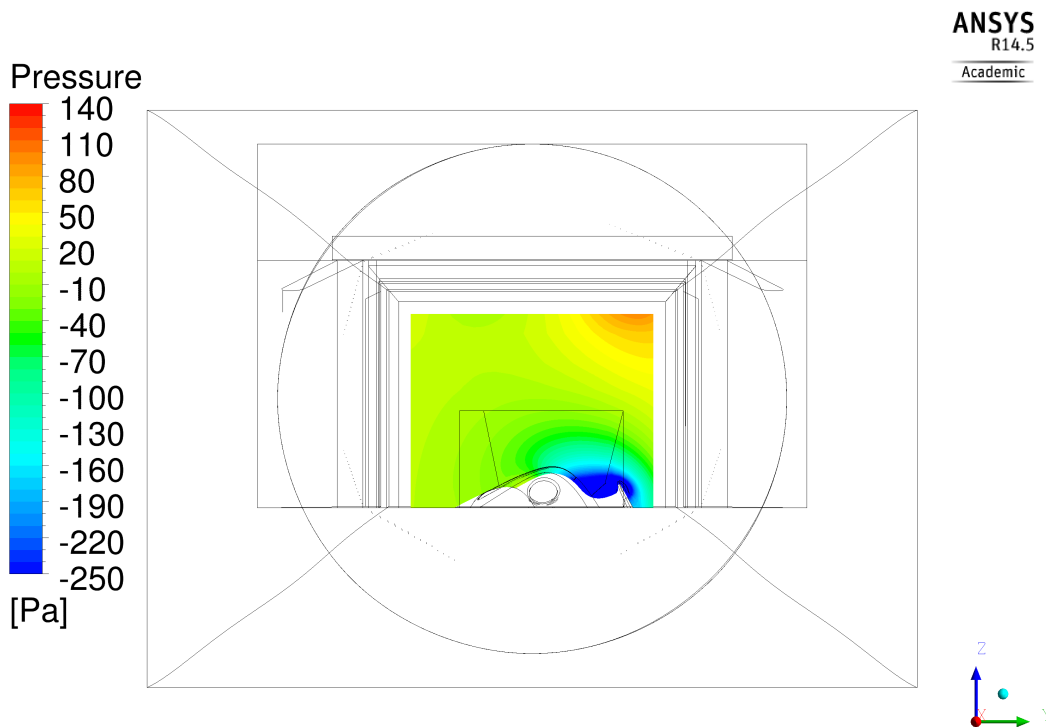


Figure B.16: Relative static pressure distribution at  $x = 2.50 \text{ m}$  - "Mass flow" case

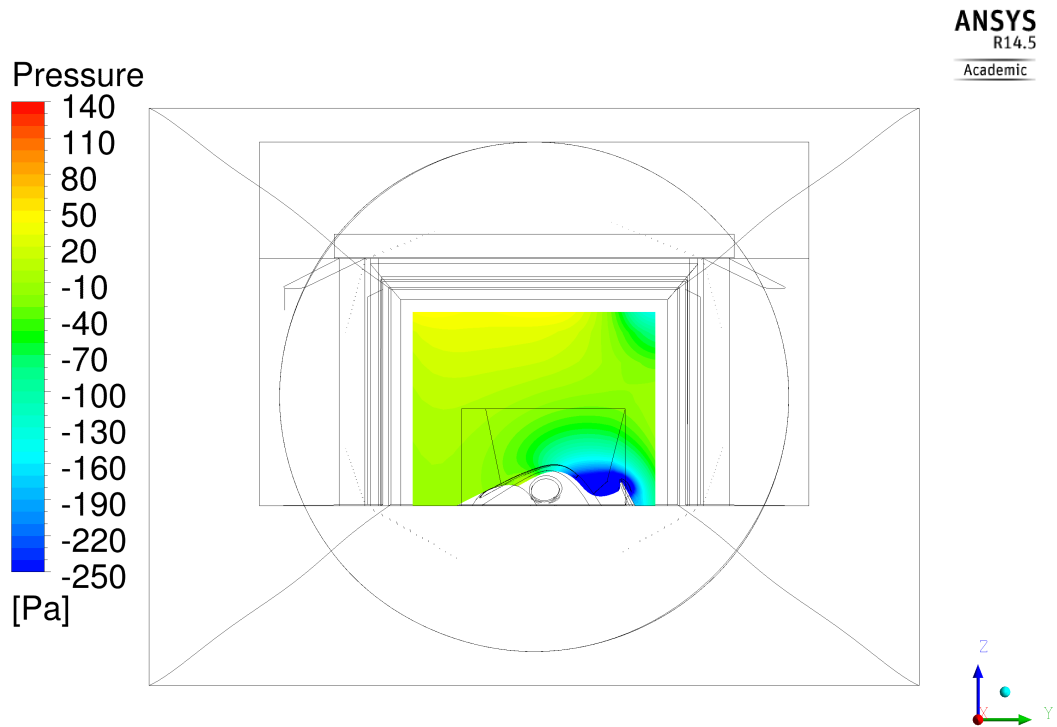


Figure B.17: Relative static pressure distribution at  $x = 2.50$  m - "961.228 Pa" case

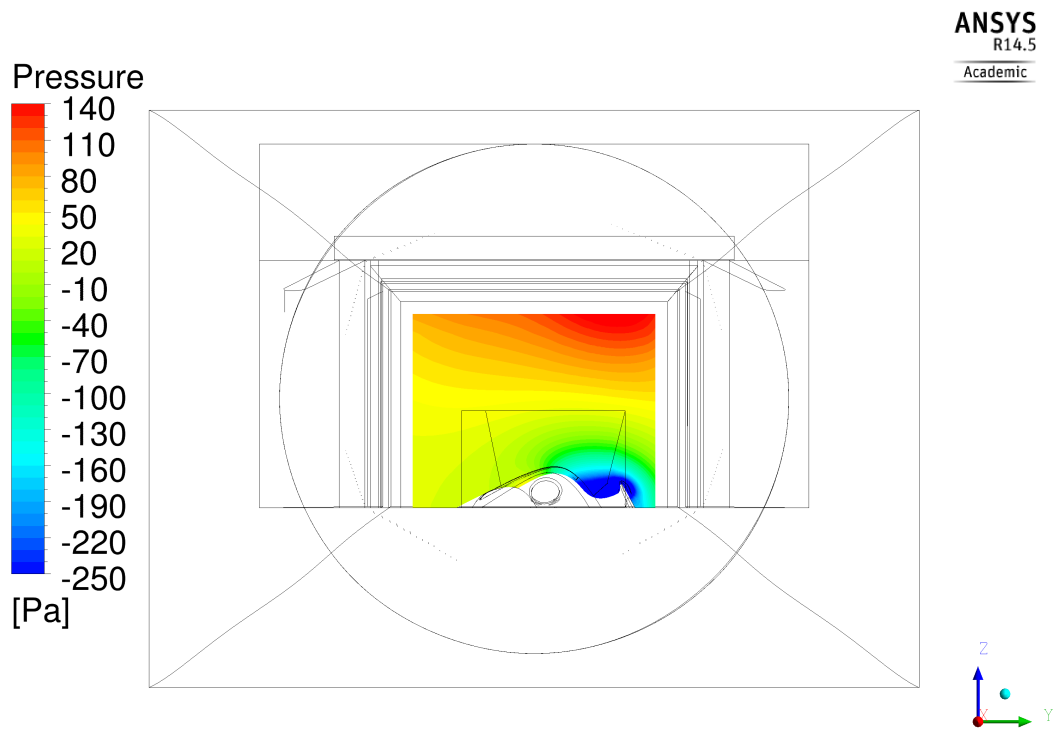


Figure B.18: Relative static pressure distribution at  $x = 2.50$  m - "974.405 Pa" case

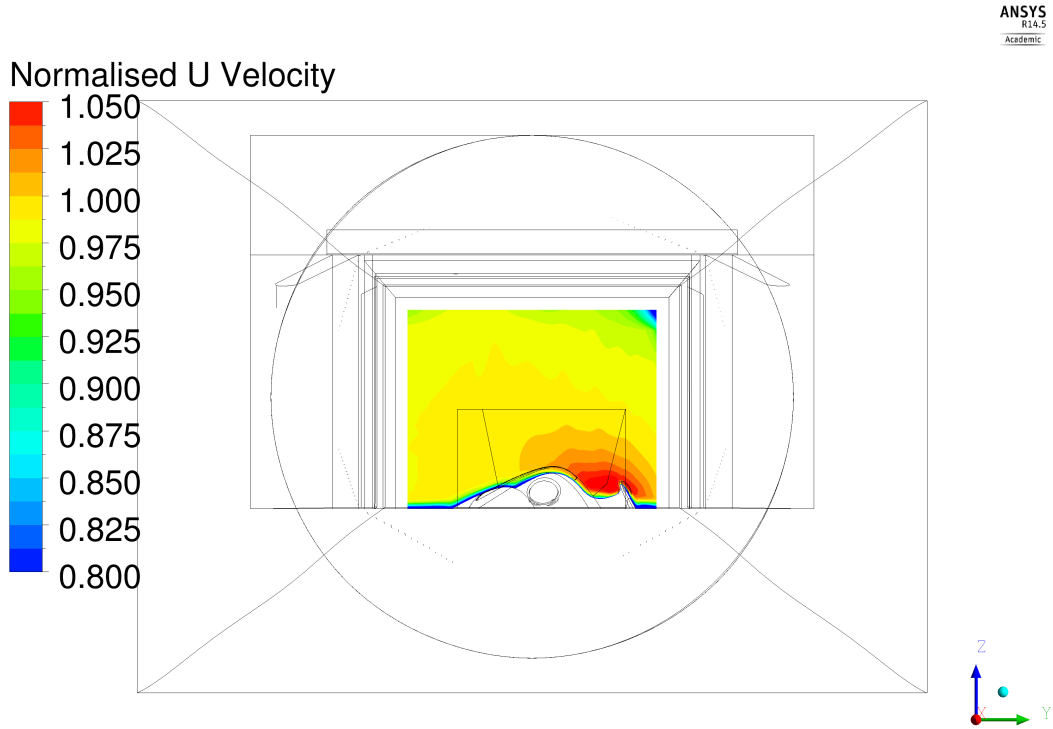


Figure B.19: Velocity u-component distribution at  $x = 2.50$  m - "Mass flow" case

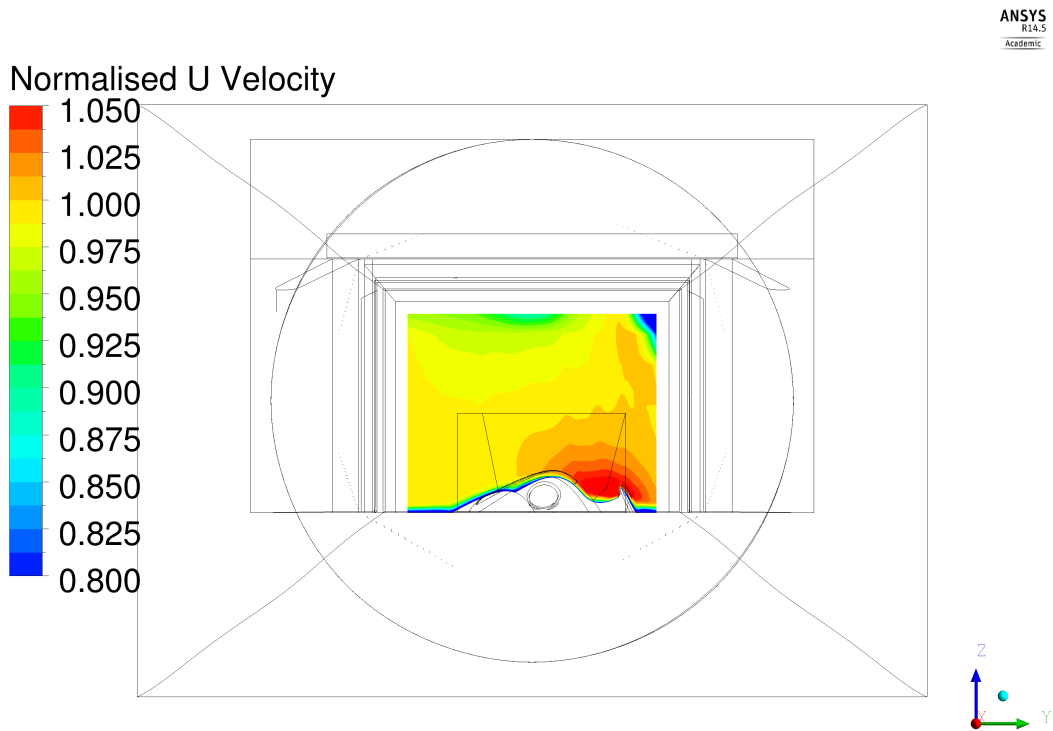


Figure B.20: Velocity u-component distribution at  $x = 2.50$  m - "961.228 Pa" case

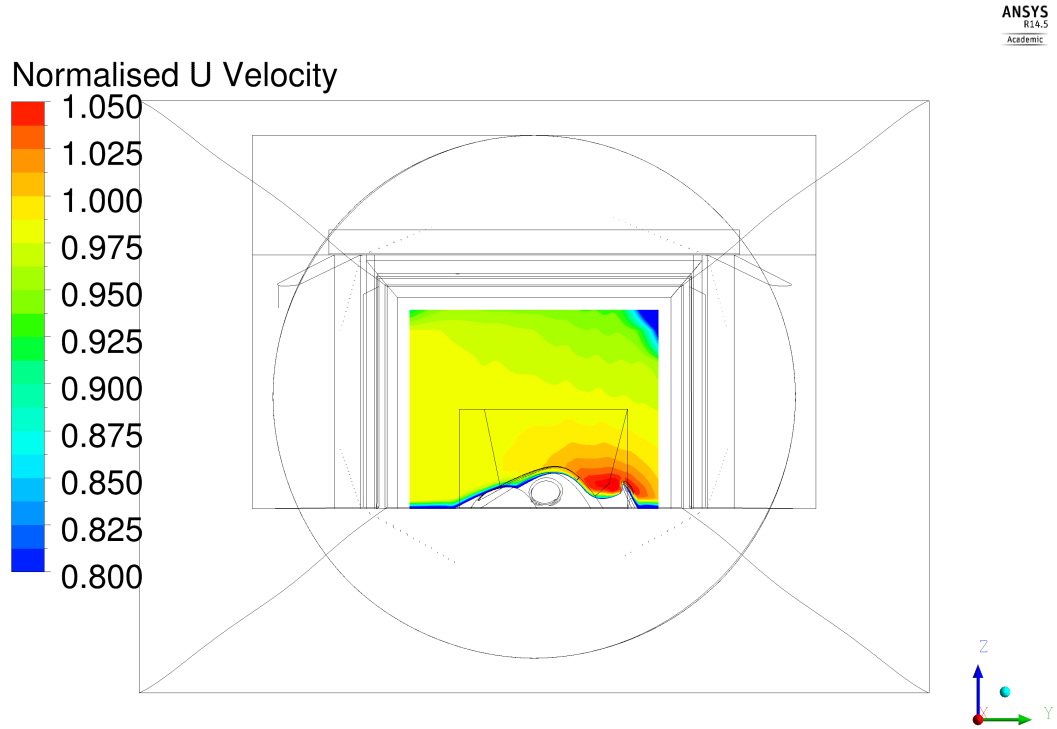


Figure B.21: Velocity u-component distribution at  $x = 2.50$  m - "974.405 Pa" case

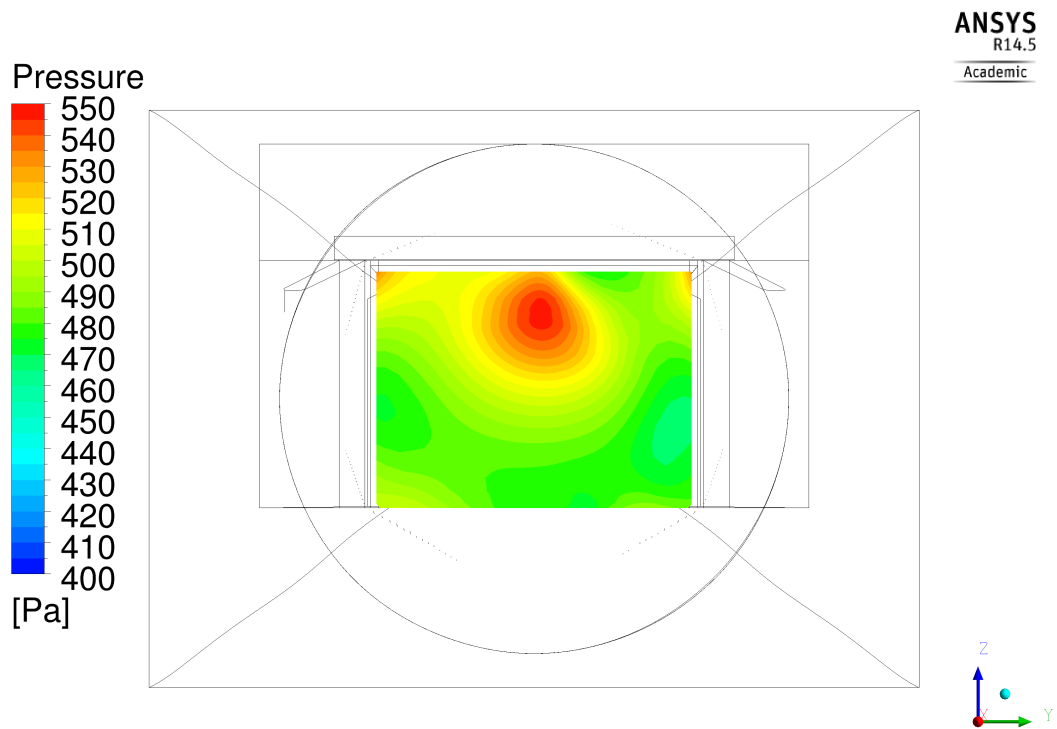


Figure B.22: Relative static pressure distribution at  $x = 7.50$  m - "Mass flow" case

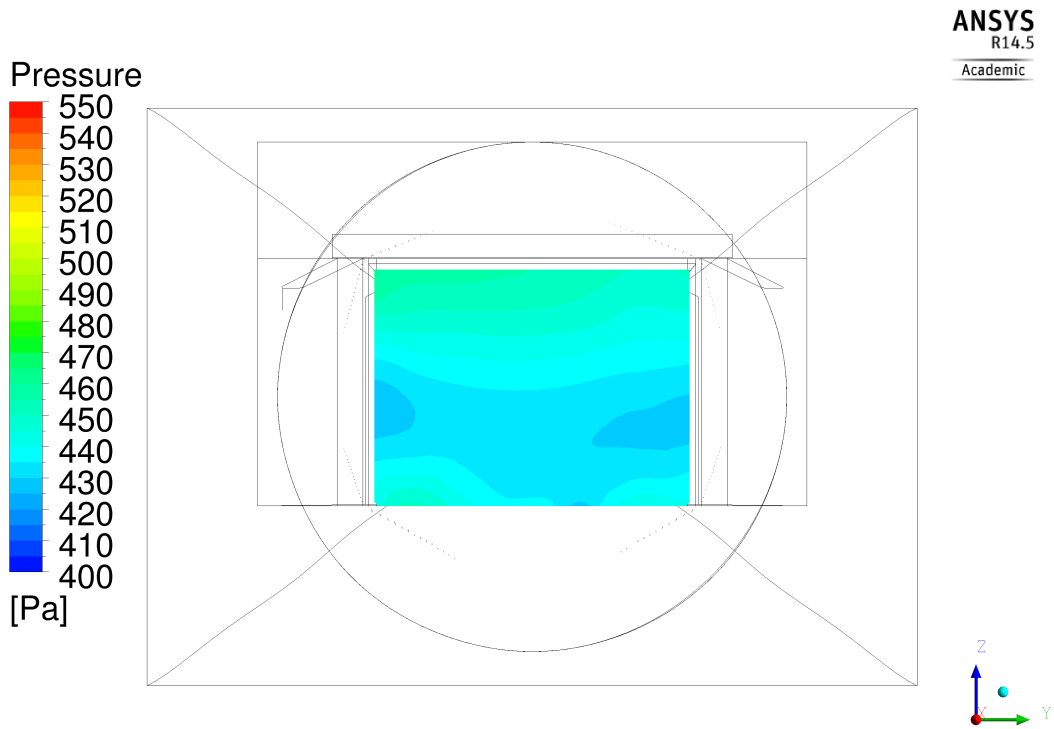


Figure B.23: Relative static pressure distribution at  $x = 7.50$  m - "961.228 Pa" case

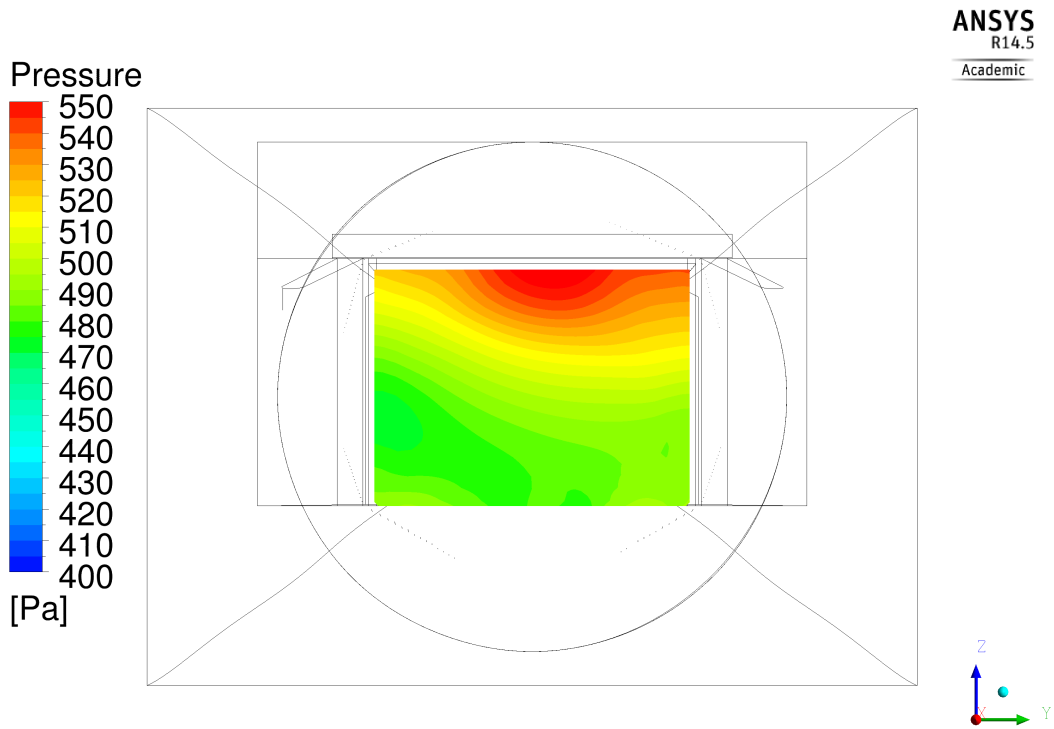


Figure B.24: Relative static pressure distribution at  $x = 7.50$  m - "974.405 Pa" case





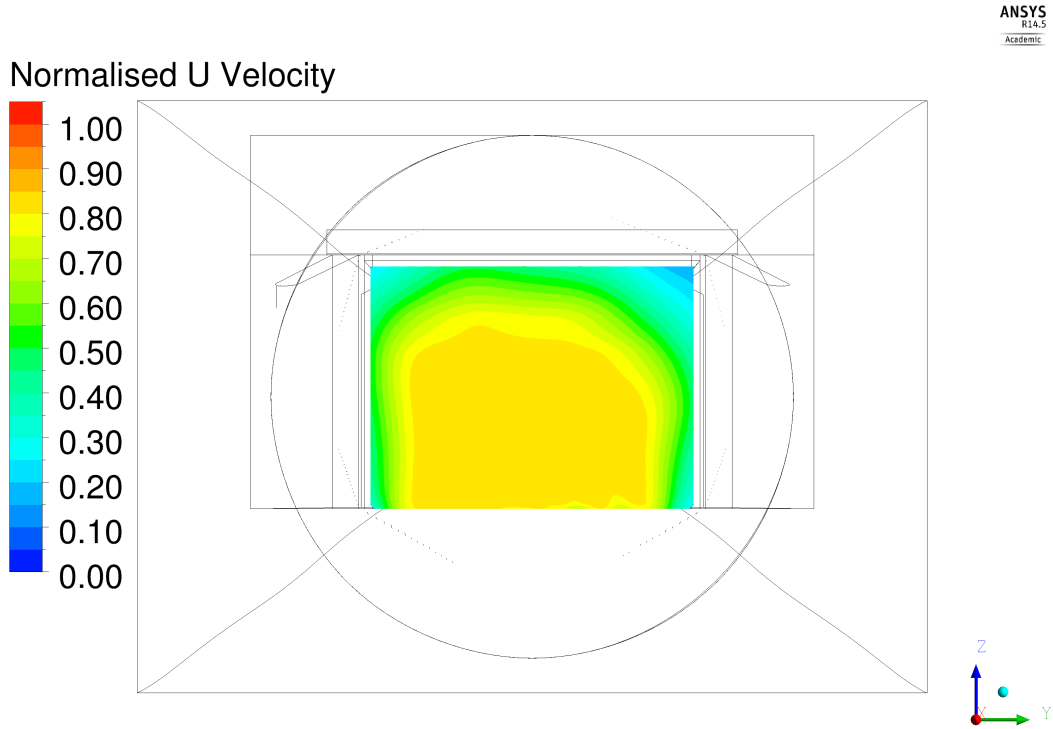


Figure B.27: Velocity u-component distribution at  $x = 7.50$  m - "974.405 Pa" case

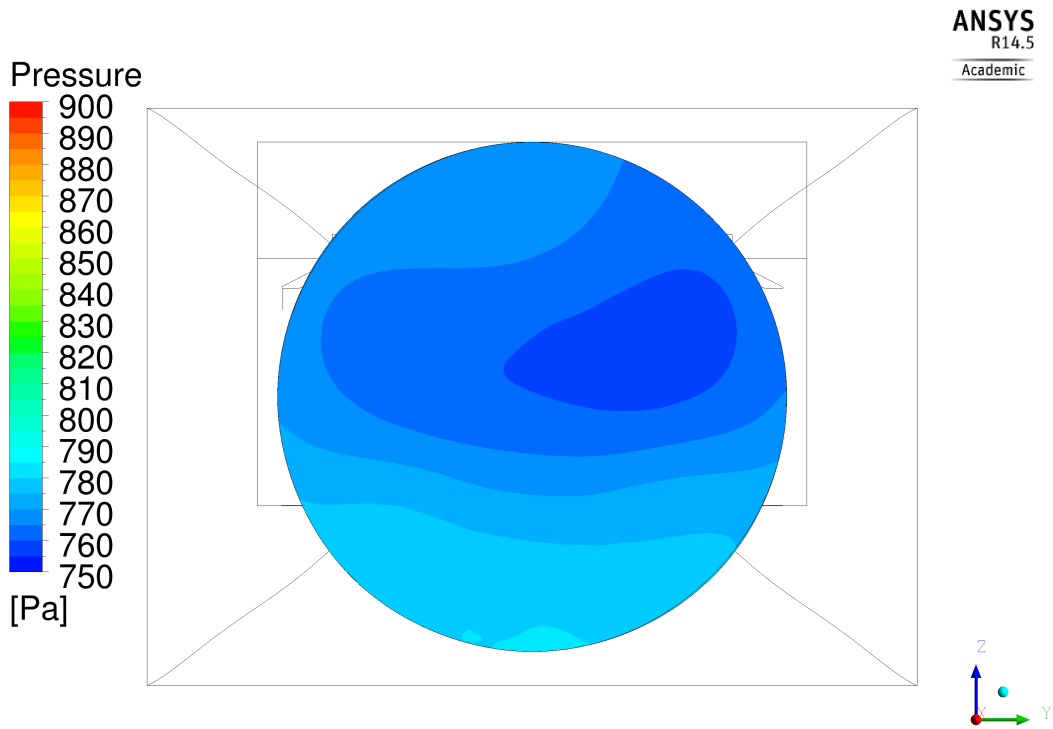


Figure B.28: Relative static pressure distribution at  $x = 20.00$  m - "Mass flow" case

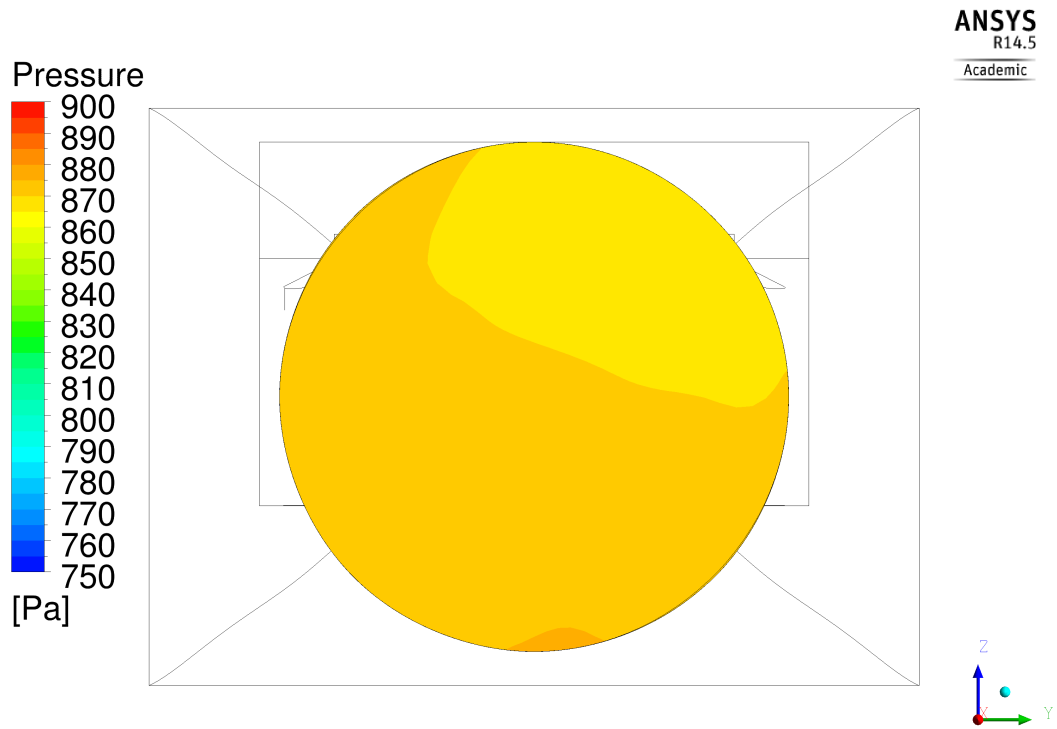


Figure B.29: Relative static pressure distribution at  $x = 20.00$  m - "961.228 Pa" case

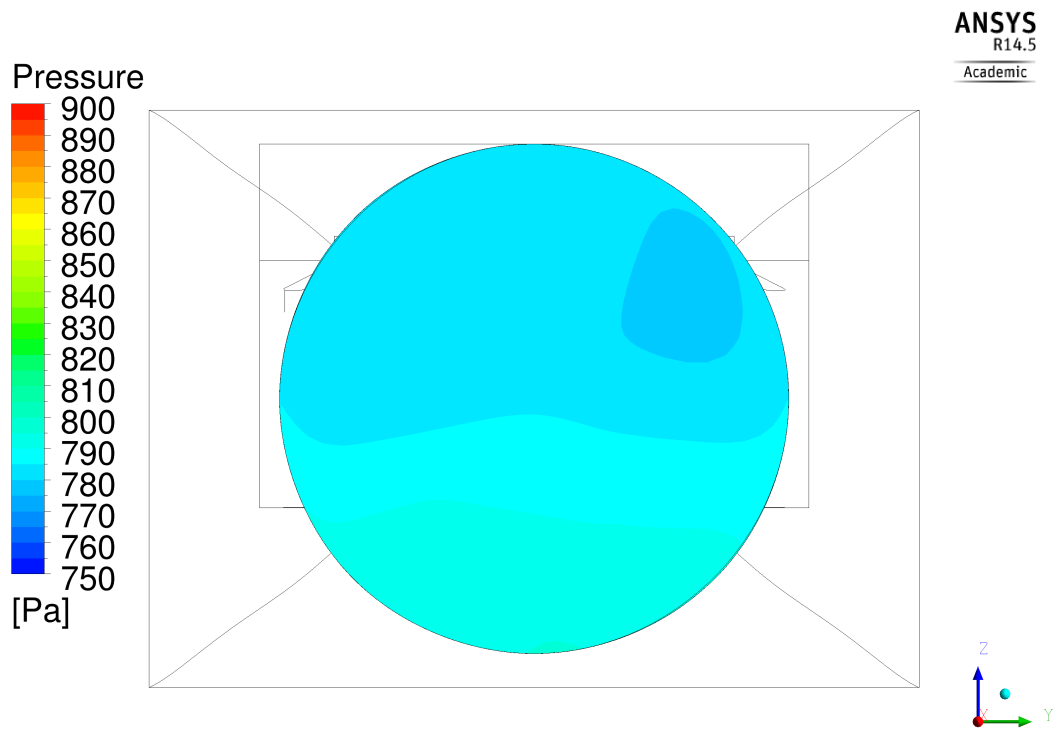


Figure B.30: Relative static pressure distribution at  $x = 20.00$  m - "974.405 Pa" case

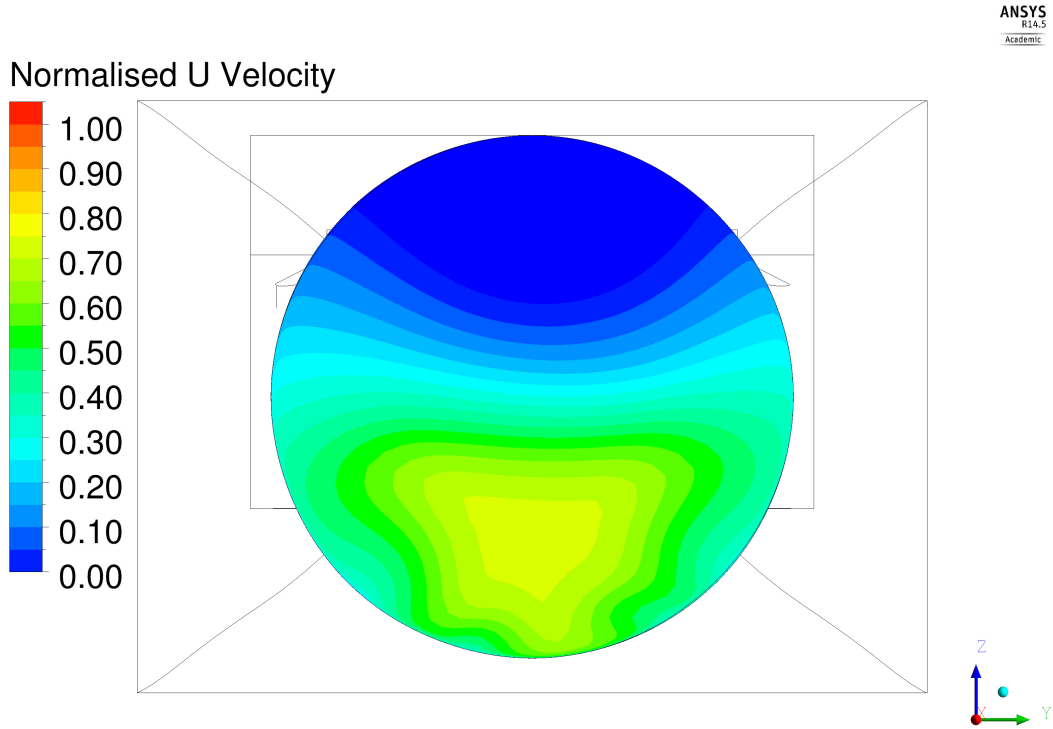


Figure B.31: Velocity u-component distribution at  $x = 20.00$  m - "Mass flow" case

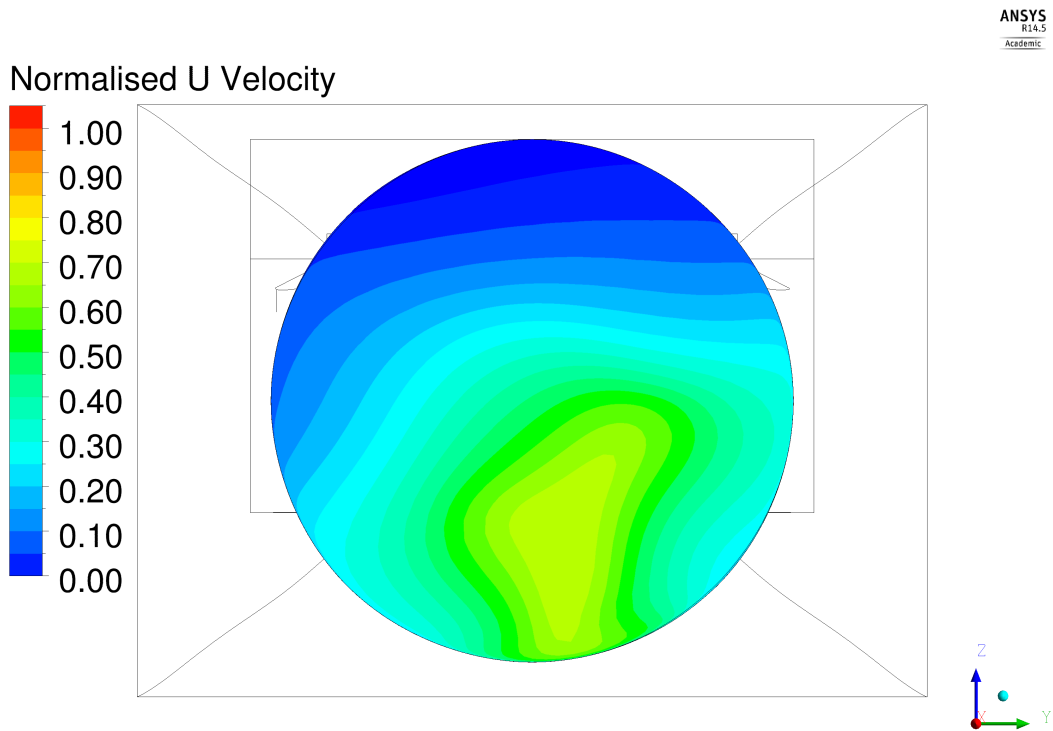


Figure B.32: Velocity u-component distribution at  $x = 20.00$  m - "961.228 Pa" case

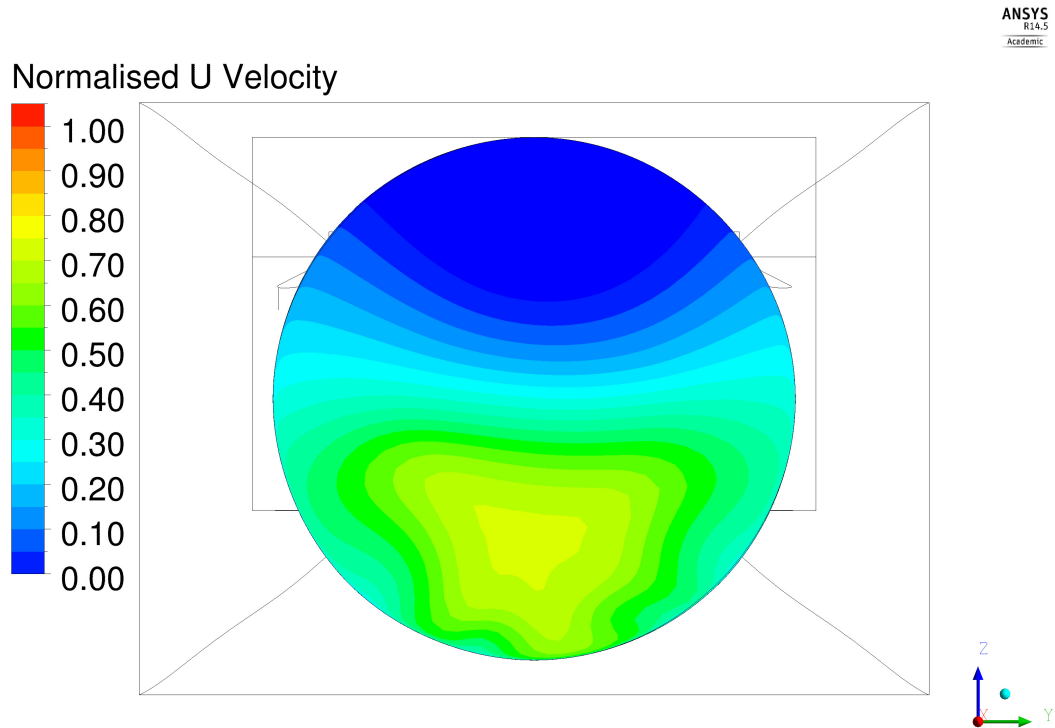


Figure B.33: Velocity u-component distribution at  $x = 20.00$  m - "974.405 Pa" case

## B.2 Pressure and forces acting on the helicopter surface

Forces and moments acting on the helicopter surface are represented in the following histograms, whose values are taken from Table 3.10-3.15; a detailed data description can be found in Section 3.6. Moreover, the  $C_p$  distributions are analysed, performing a comparison between the "Opening" boundary type simulations and the "Mass flow" case. At first sight, no differences are noted in the pressure fields represented in Figure B.40, B.41, B.42; however, some considerations can anyway be made. As a matter of fact, the pressure distributions slightly differ in the central and in the back region of the helicopter surface, in correspondence of the cowling, the cabin and the fairing used in place of the engine air intake. The similarity between the pressure fields is expected, since comparable results are found for force and moment coefficients too.



Figure B.34: Force coefficient - X-axis

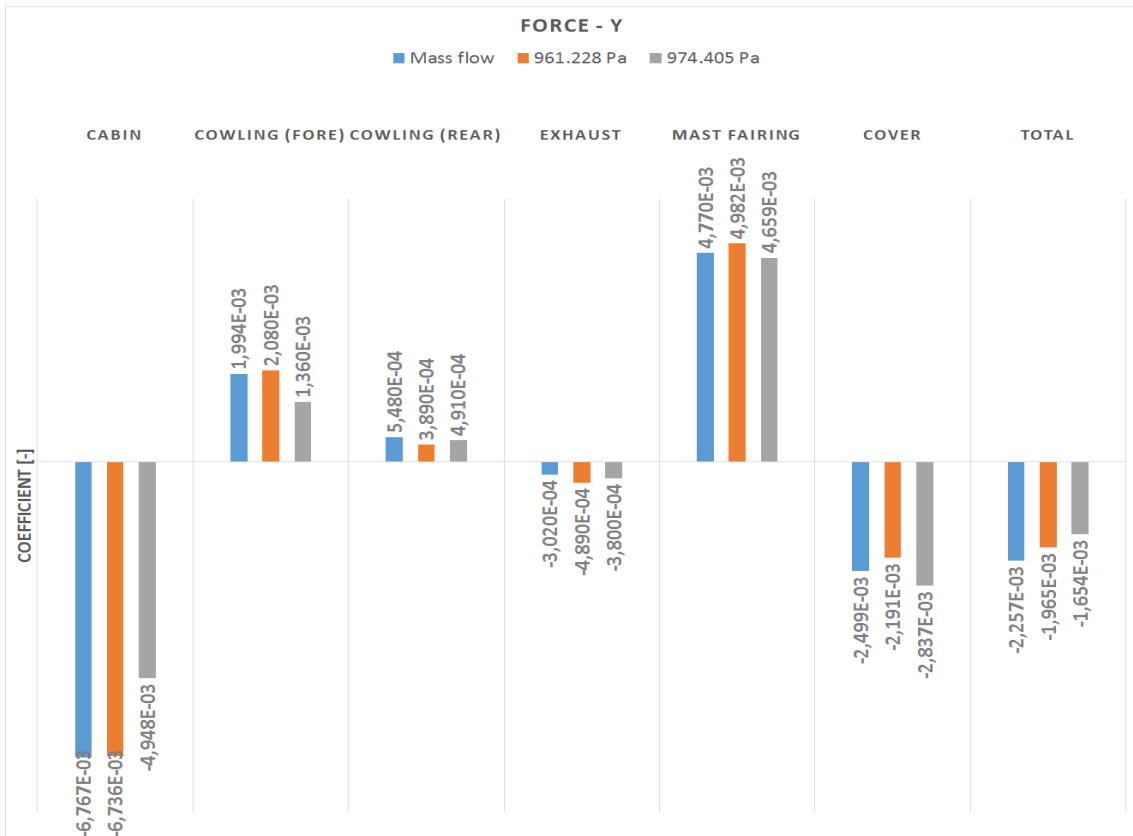


Figure B.35: Force coefficient - Y-axis

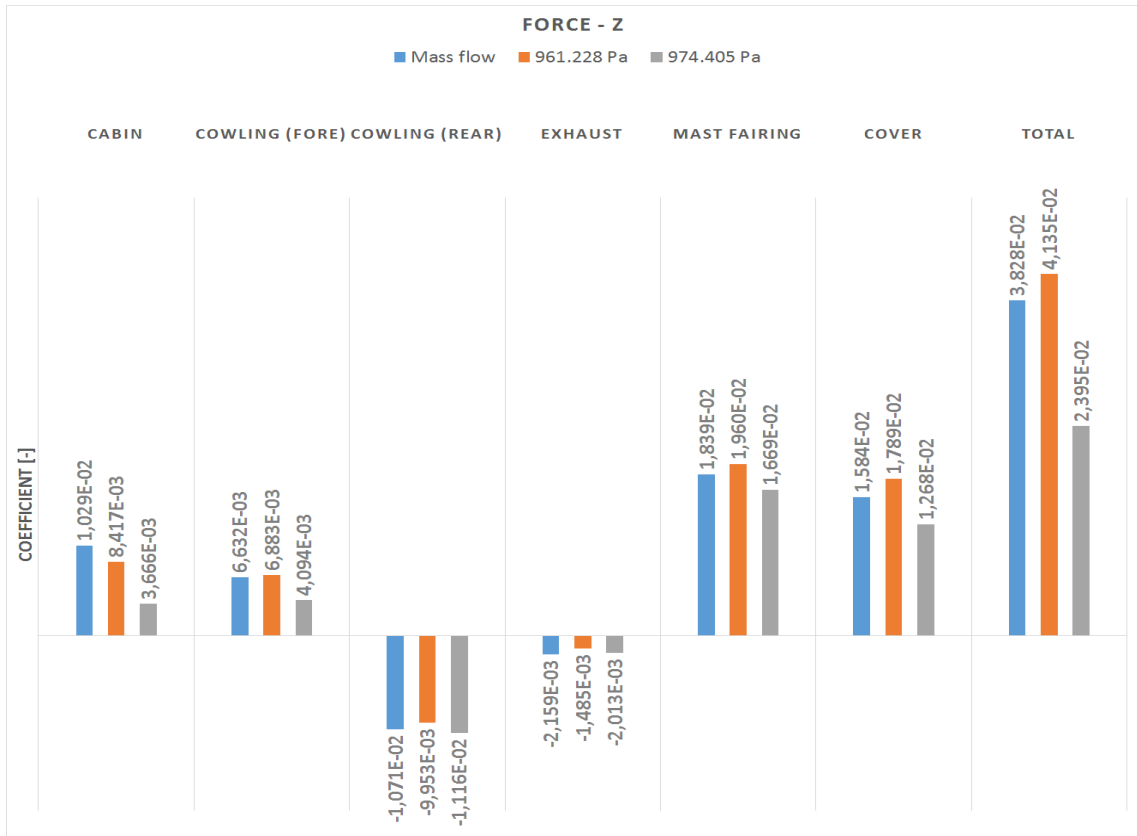


Figure B.36: Force coefficient - Z-axis

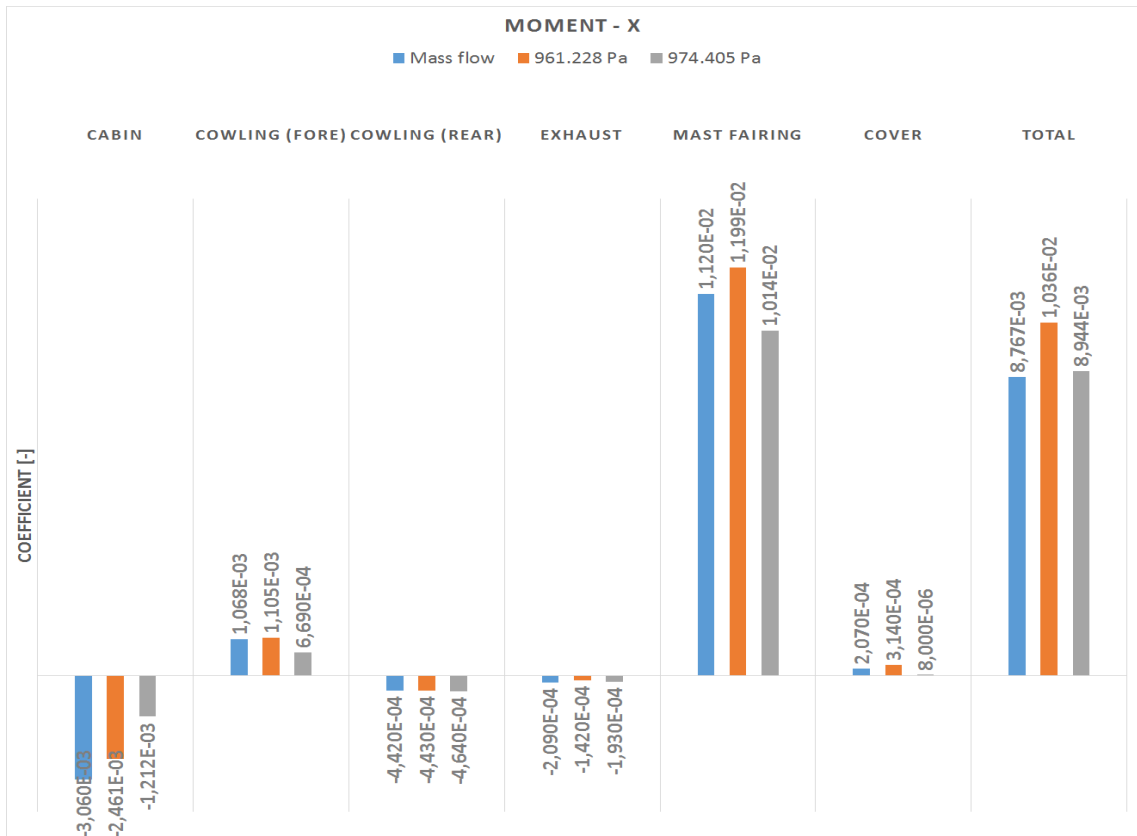


Figure B.37: Moment coefficient - X-axis

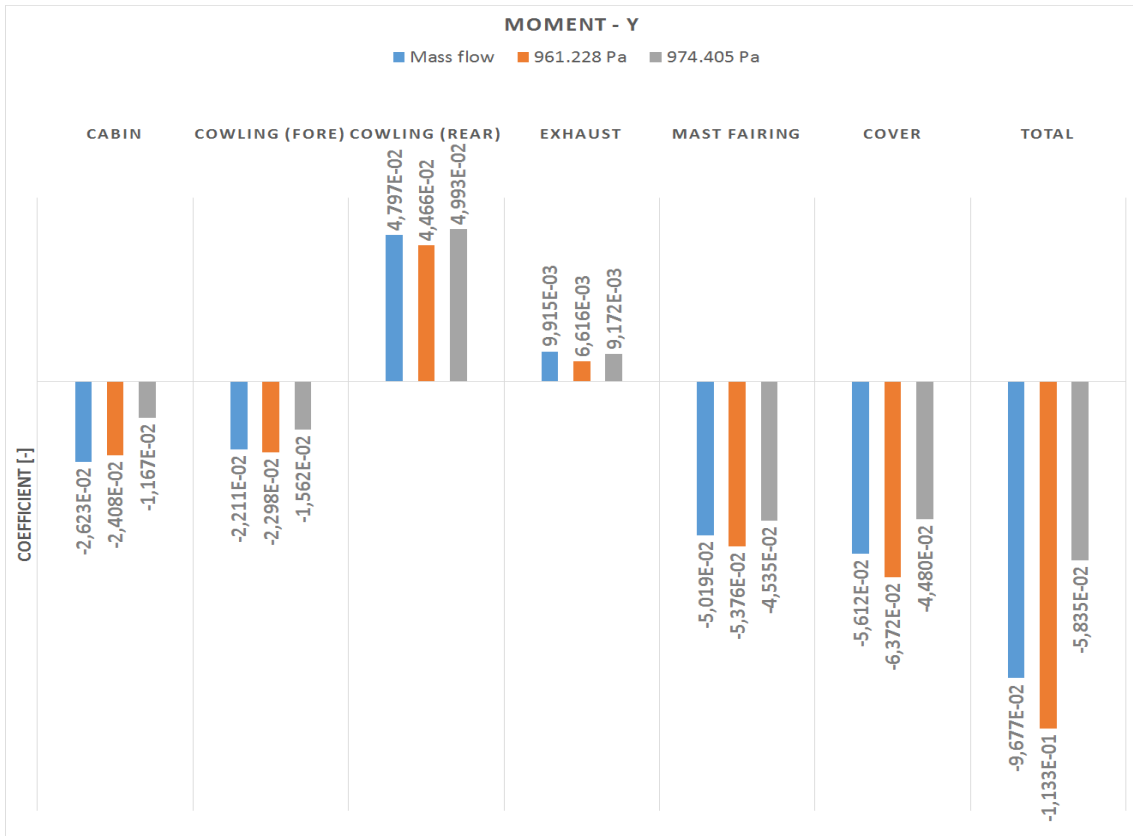


Figure B.38: Moment coefficient - Y-axis

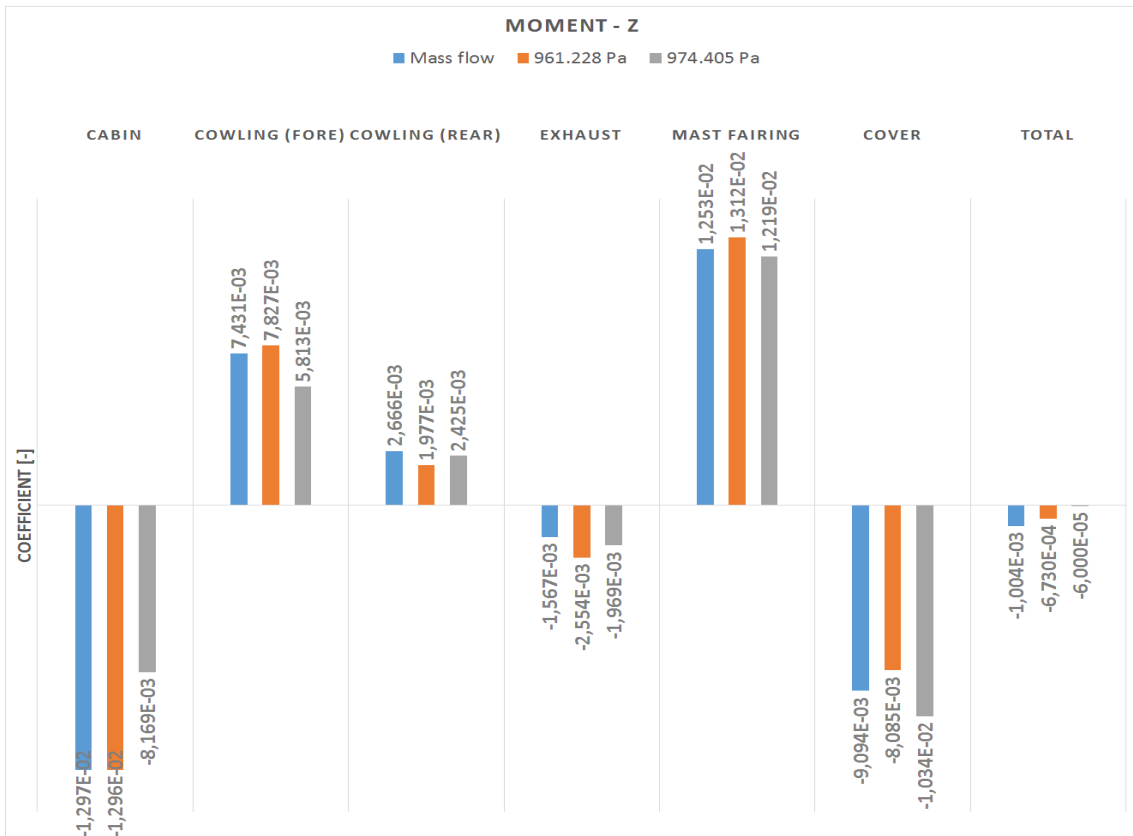


Figure B.39: Moment coefficient - Z-axis



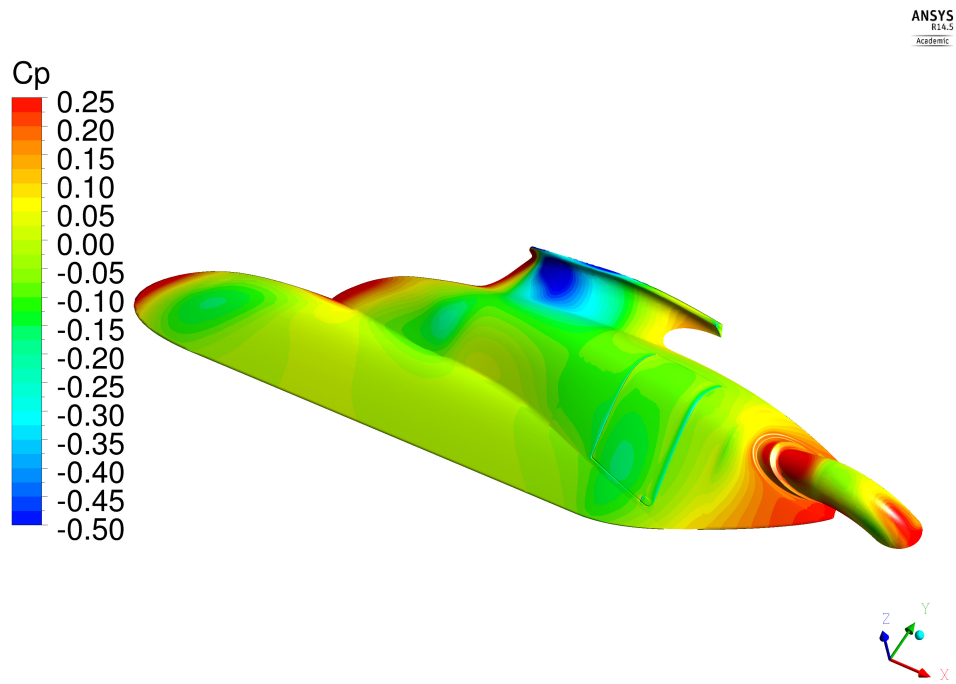


Figure B.40: Pressure field on the helicopter surface - "Mass flow" case

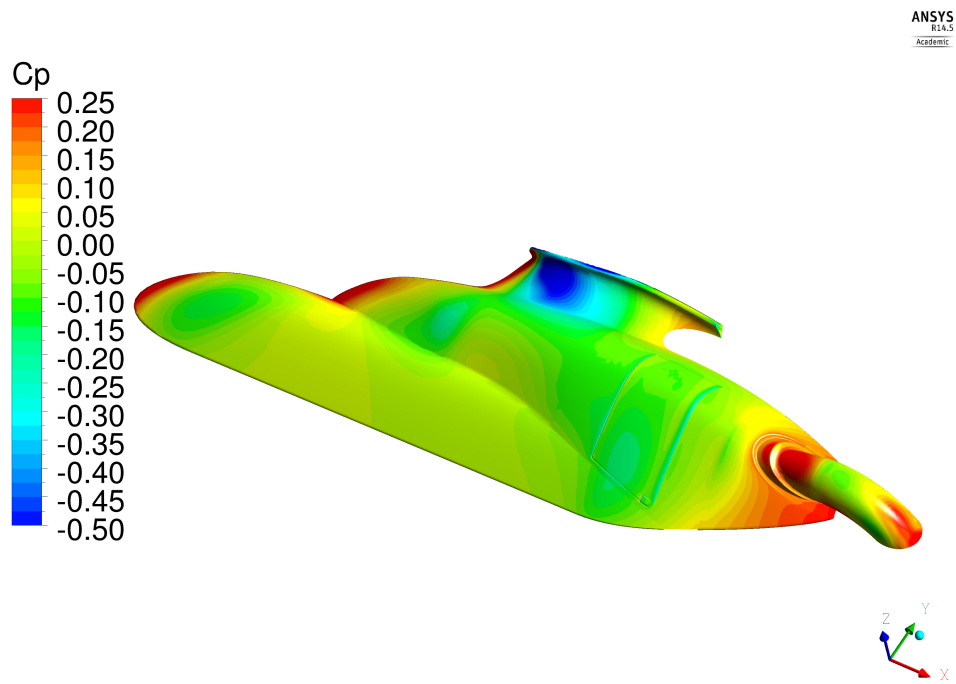


Figure B.41: Pressure field on the helicopter surface - "961.228 Pa" case

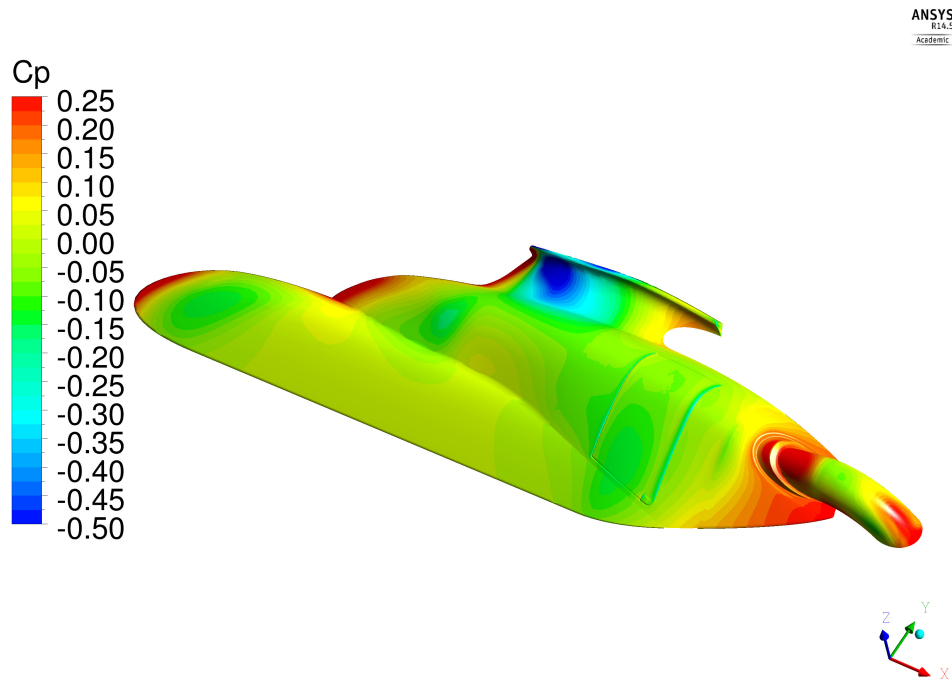


Figure B.42: Pressure field on the helicopter surface - "974.405 Pa" case

## Appendix C

# Loss coefficient model

### C.1 Definition of $K_0$

$$K_0 = \begin{cases} 1.0 & \text{in the case of "new wire screens"} \\ 1.3 & \text{in the case of "circular metal wire not perfectly clean"} \\ 2.1 & \text{in the case of "silk-thread screens"} \end{cases} \quad (\text{C.1})$$

For the analysis described in Chapter 6 only "circular metal wires not perfectly clean" are considered. Anyway, in the following picture the loss coefficient computed for the three different screen typologies is compared; the computation has been performed using the model found in [8], considering  $\theta$  equal to 0 degrees.

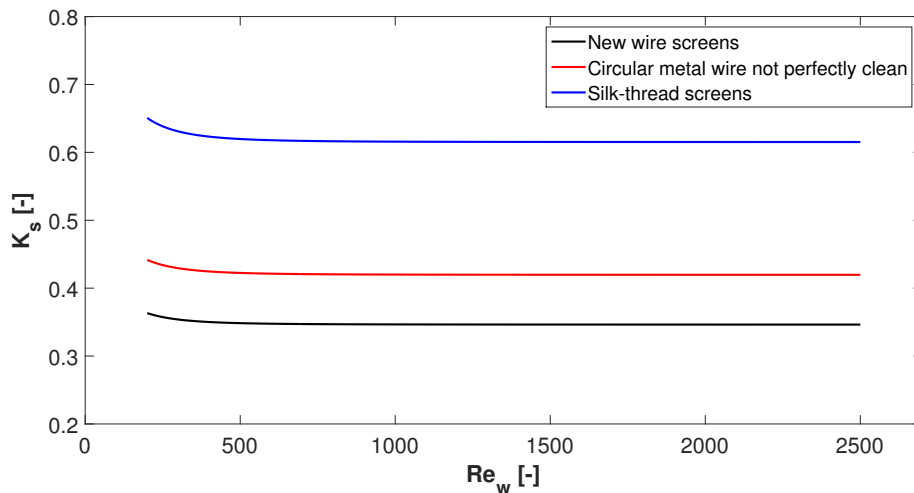


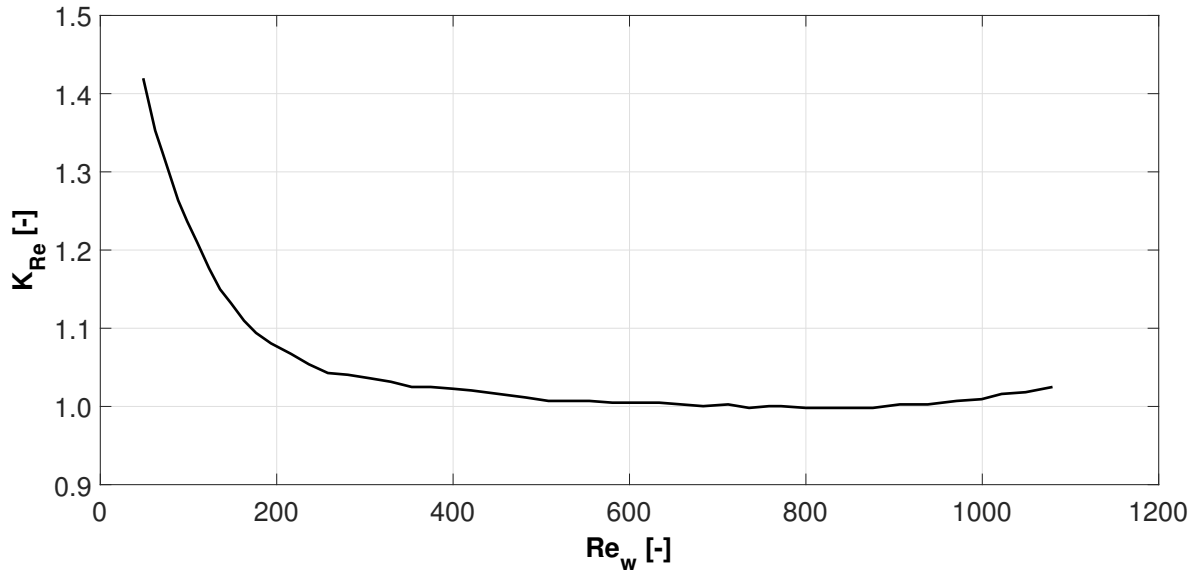
Figure C.1: Comparison between different screen typologies - Loss coefficient

### C.2 Definition of $K_{Re}$

The parameter  $K_{Re}$ , employed to compute the loss coefficient as defined in [19], depends on the screen type considered. It is distinguished between "Circular-wire screens" and "Silk-thread screens"; in both cases,  $K_{Re}$  is defined in such a way that over a certain value the loss coefficient is not influenced by Reynolds number. This is shown in Figure C.2, C.3.

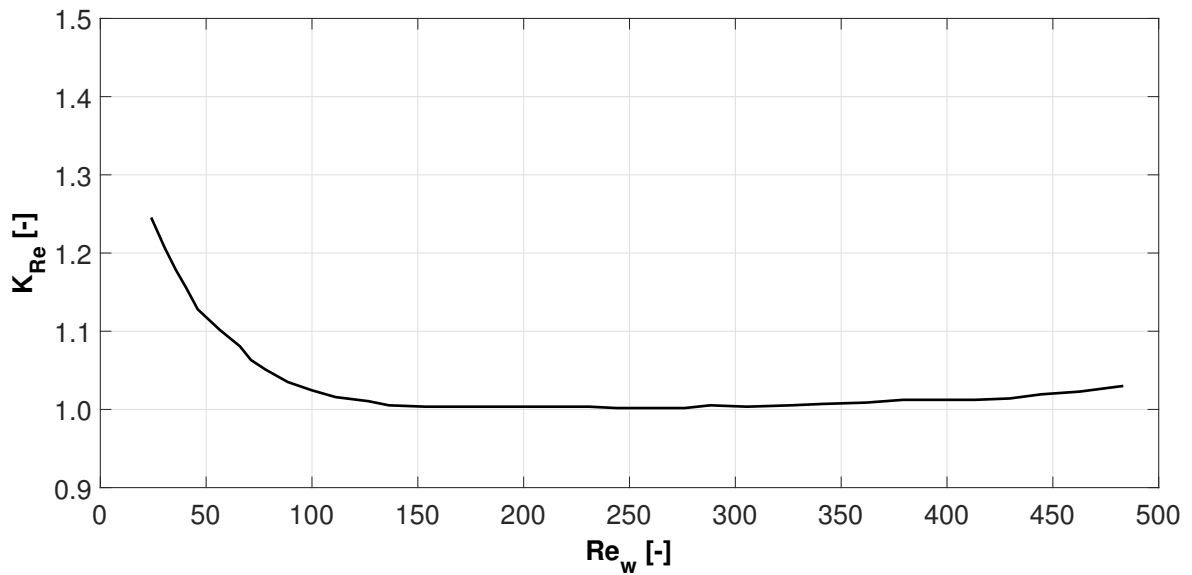
## Circular-wire screens

$$K_{Re} = \begin{cases} \text{see Figure C.2} & \text{if } Re_w \leq 400 \\ 1.0 & \text{if } Re_w > 400 \end{cases} \quad (\text{C.2})$$

Figure C.2:  $K_{Re}$  - Circular-wire screens

## Silk-thread screens

$$K_{Re} = \begin{cases} \text{see Figure C.3} & \text{if } Re_w \leq 150 \\ 1.0 & \text{if } Re_w > 150 \end{cases} \quad (\text{C.3})$$

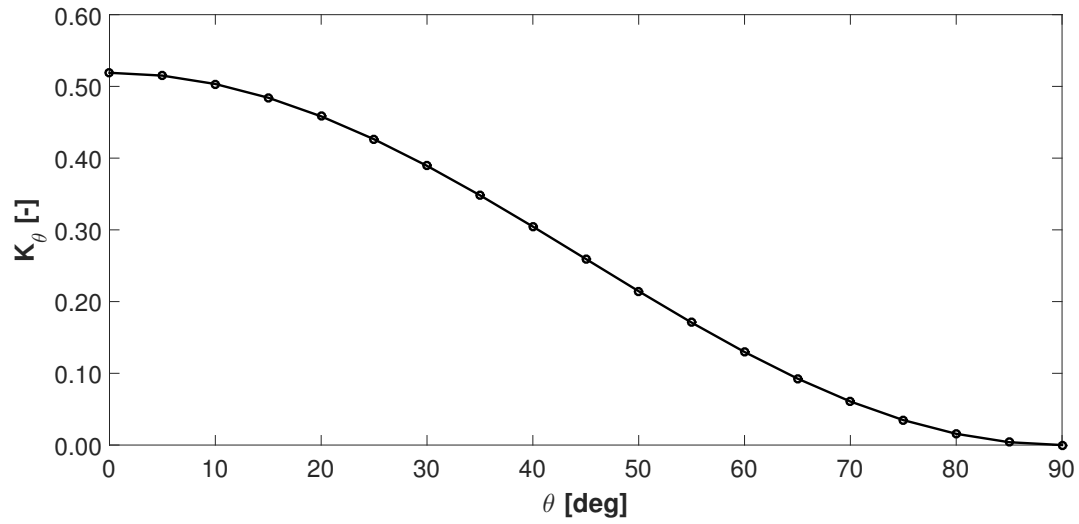
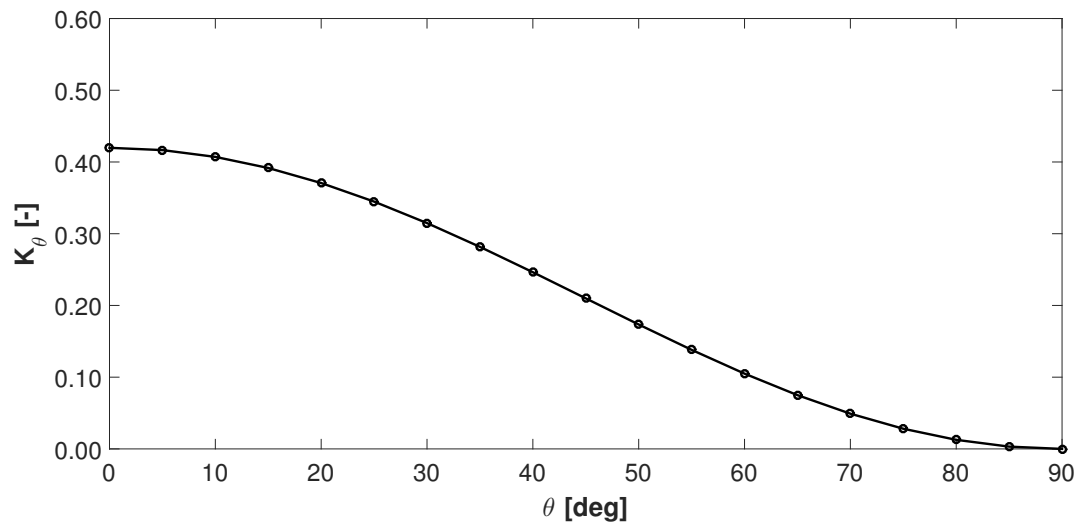
Figure C.3:  $K_{Re}$  - Silk-thread screens

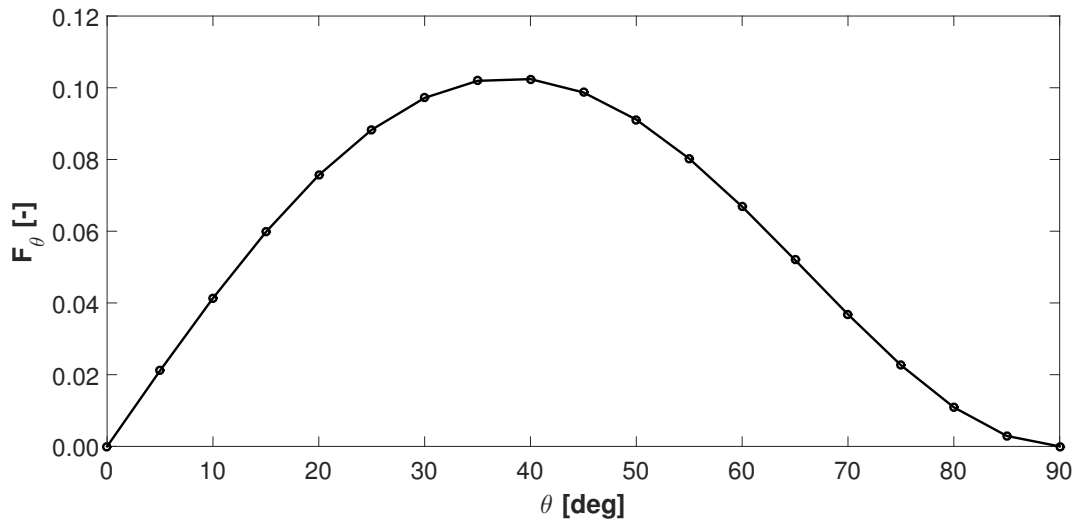
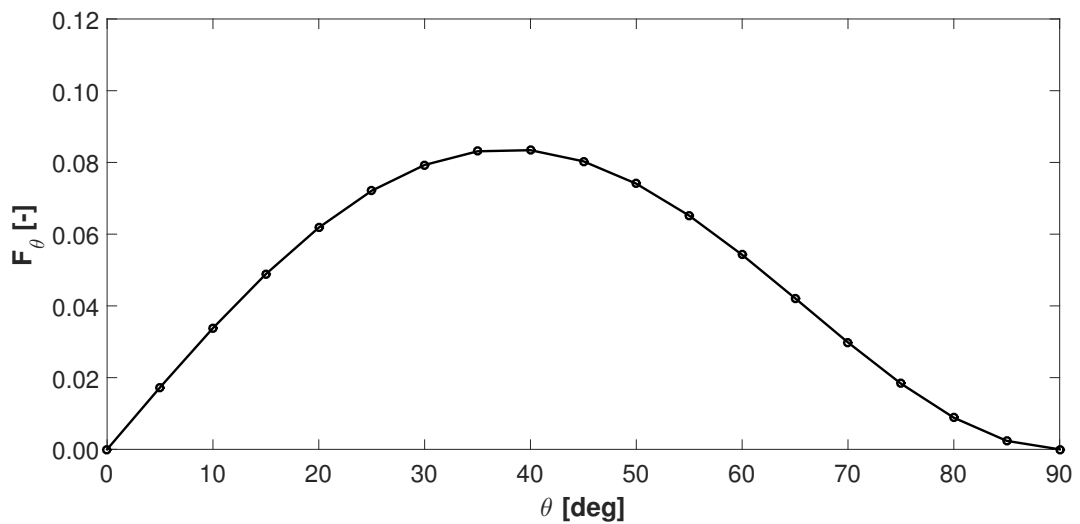
### C.3 Implementation of loss coefficient model

The loss coefficient model described in Chapter 6 is applied to the engine air intake screens; both the normal and the tangential coefficients are calculated. Figure C.4-C.7 represent the trend of  $K_\theta$  and  $F_\theta$  as function of the angle  $\theta$ ; the same values are also shown in Table C.1. The coefficients have been computed using the screen porosities reported in Table 6.1, 6.2 and a Reynolds number equal to 1500; even though the model accuracy is verified only at low  $\theta$  angles, the loss coefficients are calculated on the whole interval defined between 0 and 90 degrees. However, it is suggested that a CFD or an experimental test is performed in order to validate the model when it is used at high  $\theta$  angles.

$\theta$ [deg]	$K_\theta[-]$		$F_\theta[-]$	
	$\beta = 0.720$	$\beta = 0.758$	$\beta = 0.720$	$\beta = 0.758$
0.0	0.519	0.420	0.000	0.000
5.0	0.515	0.419	0.021	0.017
10.0	0.503	0.407	0.041	0.034
15.0	0.484	0.392	0.060	0.049
20.0	0.458	0.371	0.076	0.062
25.0	0.426	0.345	0.088	0.072
30.0	0.389	0.315	0.097	0.079
35.0	0.348	0.282	0.102	0.083
40.0	0.305	0.246	0.102	0.083
45.0	0.259	0.210	0.099	0.080
50.0	0.214	0.174	0.091	0.074
55.0	0.171	0.138	0.080	0.065
60.0	0.130	0.105	0.067	0.054
65.0	0.093	0.075	0.052	0.042
70.0	0.061	0.049	0.037	0.030
75.0	0.035	0.028	0.023	0.018
80.0	0.016	0.013	0.011	0.009
85.0	0.004	0.003	0.003	0.002
90.0	0.000	0.000	0.000	0.000

Table C.1: Loss coefficient model relative to the engine air intake screens

Figure C.4:  $K_\theta$  model - Engine air intake screenFigure C.5:  $K_\theta$  model - Engine screen

Figure C.6:  $F_\theta$  model - Engine air intake screenFigure C.7:  $F_\theta$  model - Engine screen





## Appendix D

# Settings of CFD simulations

In this appendix a description of the settings relative to turbulence and material models employed in the CFD simulations will be given with the purpose of furnishing a more detailed overview of the simulations. All descriptions are taken from [5].

### D.1 Turbulence model

**SST model** Shear Stress Transport (SST) model is indicated for accurate boundary layer simulations. See Section 2.2 for a more detailed description of the model.

### D.2 Material

**Air at 25°C** Air properties are kept constant and evaluated at a temperature of 25°C and at a pressure of 1 atm. This model is indicated when the flow is incompressible, in other words when the Mach number of the fluid is considerably low.

**Air ideal gas** For this model, the density is calculated through the *ideal gas law*; the coefficient  $C_P$  is a function of temperature T.

$$\rho = \frac{wP}{R_0T} \tag{D.1}$$

$$dh = C_p dT \tag{D.2}$$

$$C_P = C_P(T) \tag{D.3}$$



---

# Bibliography

- [1] ACARE - Advisory Council for Aeronautics Research in Europe. Aeronautics and Air Transport: Beyond Vision 2020 (Towards 2050), 2010. [http://ec.europa.eu/research/evaluations/pdf/archive/other\\_reports\\_studies\\_and\\_documents/aeronautics\\_and\\_air\\_transport\\_beyond\\_vision\\_2020.pdf](http://ec.europa.eu/research/evaluations/pdf/archive/other_reports_studies_and_documents/aeronautics_and_air_transport_beyond_vision_2020.pdf).
- [2] ACARE - Advisory Council for Aeronautics Research in Europe. Strategic Research Agenda - Executive summary, October 2014. <http://www.acare4europe.com/sites/acare4europe.org/files/document/ASD-Annex-final-211004-out-asd.pdf>.
- [3] A. Adler. Variation with Mach Number of Static and Total Pressures through Various Screens. Confidential bulletin n.L5F28, NACA - National Advisory Committee for Aeronautics, February 1946.
- [4] ANSYS, Inc., Canonsburg, PA 15317. *ANSYS ICEM CFD User Manual*, 14.5th edition, October 2012.
- [5] ANSYS, Inc., Canonsburg, PA 15317. *ANSYS CFX-Pre User's Guide*, 15.0th edition, November 2013.
- [6] ANSYS, Inc., Canonsburg, PA 15317. *ANSYS CFX-Solver Modeling Guide*, 15.0th edition, November 2013.
- [7] ANSYS, Inc., Canonsburg, PA 15317. *ANSYS CFX-Solver Theory Guide*, 15.0th edition, November 2013.
- [8] J.B. Barlow, W.H. Rae, and A. Pope. *Low-Speed Wind Tunnel Testing*. Wiley-Interscience, Hoboken, New Jersey, USA, 3rd edition, 1999.
- [9] J. Blazek. *Computational Fluid Dynamics: Principles and Applications*. Elsevier, Amsterdam, Netherlands, 2nd edition, 2007.
- [10] G. Bohling. Kriging. The University of Kansas, Kansas Geological Survey, October 2005. <http://people.ku.edu/~gbohling/cpe940/Kriging.pdf>.
- [11] CFD Online. Dimensionless wall distance (y plus), March 2014. [http://www.cfd-online.com/Wiki/Dimensionless\\_wall\\_distance\\_\(y\\_plus\)](http://www.cfd-online.com/Wiki/Dimensionless_wall_distance_(y_plus)).
- [12] CFD Online. Mesh classification, May 2007. [http://www.cfd-online.com/Wiki/Mesh\\_classification](http://www.cfd-online.com/Wiki/Mesh_classification).

- [13] S.W. Cheng, T.K. Dey, and J.R. Shewchuk. *Delaunay Mesh Generation*. CRC Press, Boca Raton, Florida, USA, 1st edition, 2012.
- [14] Clean Sky. "Clean Sky" program. <http://www.cleansky.eu>.
- [15] I. Couckuyt, T. Dhaene, and P. Demeester. *ooDACE Toolbox - A Matlab Kriging Toolbox: Getting started*, June 2013.
- [16] European Commission. European Aeronautics: a Vision for 2020 - Report of the Group of Personalities, January 2001. [http://ec.europa.eu/research/growth/aeronautics2020/pdf/aeronautics2020\\_en.pdf](http://ec.europa.eu/research/growth/aeronautics2020/pdf/aeronautics2020_en.pdf).
- [17] D. Gorissen, K. Crombecq, I. Couckuyt, T. Dhaene, and P. Demeester. A Surrogate Modeling and Adaptive Sampling Toolbox for Computer Based Design. *Journal of Machine Learning Research*, 11: pp. 2051–2055, July 2010.
- [18] F. Heckmeier. Numerische Strömungssimulation für eine Hubschraubersektion mit Triebwerkseinlauf in einer Windkanalmessstrecke. Semester Arbeit, Technische Universität München, 2014.
- [19] I.E. Idel'chik. *Handbook of Hydraulic Resistance*. Jaico Publishing House, Mumbai, India, 3rd edition, 2005.
- [20] innovative-cfd.com. Making sense of cfd grid types. <http://www.innovative-cfd.com/cfd-grid.html>.
- [21] F. Knoth et al. Aerodynamic Analysis of Helicopter Side Intake Variants by Full-Scale Wind Tunnel Measurements. 41st European Rotorcraft Forum, 2015.
- [22] F. Knoth et al. Numerical and Experimental Investigation of Helicopter Engine Air Intakes. 64. Deutscher Luft- und Raumfahrt Kongress, 2015.
- [23] S. Lophaven, H. Bruun Nielsen, and J. Søndergaard. *DACE - A MATLAB Kriging Toolbox*, August 2002.
- [24] O. Makhnin. Lecture 10: Introduction to Kriging. New Mexico Institute of Mining and Technology, Department of Mathematics. <http://infohost.nmt.edu/~olegm/586/HYD10.pdf>.
- [25] B. Mohammadi and O. Pironneau. *Analysis of the K-Epsilon Turbulence Model*. Wiley-Interscience, Hoboken, New Jersey, USA, 1st edition, 1994.
- [26] Technische Universität München. ATHENAI project - Periodic report summary 1, March 2015. <http://cordis.europa.eu/docs/results/619/619819/periodic1-athenai-periodicreport-1-1-with-illustrations.pdf>.
- [27] S.B. Pope. *Turbulent Flows*. Cambridge University Press, Cambridge, United Kingdom, 1st edition, 2000.
- [28] L. Prandtl. Attaining a Steady Air Stream in Wind Tunnels. Technical memorandum n.726, NACA - National Advisory Committee for Aeronautics, October 1933.

- 
- [29] L. Quartapelle and F. Auteri. *Fluidodinamica comprimibile*. Casa Editrice Ambrosiana, Rozzano, Milano, Italy, 1st edition, 2013.
- [30] L. Quartapelle and F. Auteri. *Fluidodinamica incomprimibile*. Casa Editrice Ambrosiana, Rozzano, Milano, Italy, 1st edition, 2013.
- [31] M. Roberts. Air Flow through Woven Stainless Steel Mesh. Applications Team - Energy-Efficient Design Applications, 1999. [http://ateam.lbl.gov/hightech/fumehood/students/su99/roberts/Roberts\\_Fume\\_Hood.pdf](http://ateam.lbl.gov/hightech/fumehood/students/su99/roberts/Roberts_Fume_Hood.pdf).
- [32] J. Scheiman. Comparison of Experimental and Theoretical Turbulence Reduction Characteristics for Screens, Honeycomb, and Honeycomb-Screen Combinations. Technical paper n.1958, NASA - National Aeronautics and Spatial Administration, December 1981.
- [33] G.B. Schubauer, W.G. Spangenberg, and P.S. Klebanoff. Aerodynamic Characteristics of Damping Screens. Technical note n.726, NACA - National Advisory Committee for Aeronautics, January 1950.
- [34] M. L. Stein. *Interpolation of Spatial Data: Some Theory for Kriging*. Springer, 1st edition, 1999.
- [35] Universiteit Gent, INTEC - Department of Information Technology. SUMO - SURrogate MOdeling Lab. <http://www.sumo.intec.ugent.be/>.
- [36] Wikipedia. Delaunay triangulation, January 2015. [http://en.wikipedia.org/wiki/Delaunay\\_triangulation](http://en.wikipedia.org/wiki/Delaunay_triangulation).